Investigation on Cold Spray based Additive Manufacturing of IN 718 Superalloy

Doctoral Thesis

by

Parminder Singh (2019MEZ0008)



DEPARTMENT OF MECHANICAL ENGINEERING INDIAN INSTITUTE OF TECHNOLOGY ROPAR

November 2024

Investigation on Cold Spray based Additive Manufacturing of IN 718 Superalloy

A Thesis Submitted
In Partial Fulfillment of the Requirements
for the Degree of

DOCTOR OF PHILOSOPHY

by

Parminder Singh (2019MEZ0008)



DEPARTMENT OF MECHANICAL ENGINEERING INDIAN INSTITUTE OF TECHNOLOGY ROPAR

November 2024

Parminder Singh: Investigation on Cold Spray based Additive Manufacturing of IN 718 Superalloy Copyright © 2024 by Indian Institute of Technology Ropar All Rights Reserved

DEDICATED

TO

FAMILY & FRIENDS

DECLARATION OF ORIGINALITY

I hereby declare that the work which is being presented in the thesis entitled "Investigation on

Cold Spray based Additive Manufacturing of IN 718 Superalloy" has been solely authored by me.

It presents the result of my own independent investigation/research conducted during the time

period from December 2019 to July 31st 2024 under the supervision of Prof. Harpreet Singh,

Professor, Department of Mechanical Engineering, Indian Institute of Technology, Ropar. To the

best of my knowledge, it is an original work, both in terms of research content and narrative, and

has not been submitted or accepted elsewhere, in part or in full, for the award of any degree,

diploma, fellowship, associateship, or similar title of any university or institution. Further, due

credit has been attributed to the relevant state-of-the-art and collaborations (if any) with

appropriate citations and acknowledgments, in line with established ethical norms and practices. I

also declare that any idea/data/fact/source stated in my thesis has not been fabricated/ falsified/

misrepresented. All the principles of academic honesty and integrity have been followed. I fully

understand that if the thesis is found to be unoriginal, fabricated, or plagiarized, the Institute

reserves the right to withdraw the thesis from its archive and revoke the associated Degree

conferred. Additionally, the Institute also reserves the right to appraise all concerned sections of

society of the matter for their information and necessary action (if any). If accepted, I hereby

consent for my thesis to be available online in the Institute's Open Access repository, inter-library

loan, and the title & abstract to be made available to outside organizations.

Signature:

Name: Parminder Singh

Entry Number: 2019MEZ0008

Program: PhD

Department: Mechanical Engineering

Indian Institute of Technology Ropar

Rupnagar, Punjab 140001

Date:

i

ACKNOWLEDGMENTS

The author would like to express a deep sense of gratitude and esteemed respect to my supervisor Prof. Harpreet Singh, Professor, Mechanical Engineering Department, Indian Institute of Technology Ropar for his impetus, able and continuous guidance throughout my research work. This thesis would not have been possible without his constant support and encouragement. Without their positive support, altitudinous motivation, critical reviewing, timely help it would have been impossible to complete this thesis in the current form. The feeling of kindness and 'never get down' are the noble attributes, which the author learnt from his supervisor and would always try to incorporate them in his character.

I am highly indebted to Prof. Rajeev Ahuja, Director IIT Ropar for providing administrative and academic support including access to different facilities and equipment for the conduct of this research work. The author is highly thankful to all his Doctoral Committee Members, Dr. Ekta Singla, Prof. Harpreet Singh, Dr. Prabhat K. Agnihotri, Dr. Prabir Sarkar and Dr. Pushpendra P. Singh for giving me valuable suggestions from time to time and serving on my committee. The author would also like to acknowledge his Doctoral Committee Members for providing the much-needed continuous encouragement and support. The author is highly indebted to all the faculty members of the Mechanical Engineering Department for their help and support. I am also thankful to Dr. Prabhat K. Agnihotri, Head of the Mechanical Engineering Department, for his help and cooperation. The author would also like to express sincere thanks to Mr. Sukhwinder Singh for the software support in order to perform the modeling and simulation work. The author would also like to acknowledge the support from Mr. Amit Kumar for carrying out SEM/EDS and XRD work respectively. The author would also like to express his gratitude to Dr. Dinesh Siddaiah, Head Librarian, IIT Ropar for his continuous help in arranging and providing reading and reference materials.

The author is highly gratified and thankful to all his labmates of YourLab for their support. The author is also very thankful to close friends Mr. Sukhwinder Singh, Mr. Adityabir Singh and Mr. Jitender, for their continuous motivation, guidance and moral support during the tenure of his work.

The unmatchable support and blessings provided by author's beloved parents; S. Jaswant Singh and Sdn. Jaswinder Kaur could not be expressed in words. The author would like to dedicate his thesis to his highly respectable parents, whose stout faith in God provided implacable support and

boost for the successful completion of his thesis work. The author is highly indebted to his paternal and maternal grandparents S. Phuman Singh, Sdn. Puran Kaur, S. Ajit Singh and Sdn. Paramjit Kaur for the well wishes and extreme love. The author is highly grateful to his brother Sandeep Singh and sister-in-law Rajni for their non-exhaustive moral support. The author would also like to express his gratitude to all his uncles and aunts (S. Jit Singh, S. Gurmit Singh, S. Sukhdev Singh, Sdn. Som Kaur, Sdn. Niranjan Kaur and Sdn. Amarjit Kaur) for their encouragement and continuous support particularly S. Gurmit Singh for his belief in me. The author is thankful to all his cousin brothers and sisters especially his brother S. Balwant Singh who always encouraged me to pursue this work with full dedication and hard work.

Grand acclamation and esteem appreciation is due for the beloved wife of the author, Neelam, who firmly stood by him during all the odd times. She sacrificed her comforts and showed great determination, love and care to ensure that the author meets all the targets during this tenure. A sense of apology for my dear son and daughter, Harwinder Singh and Bavneet Kaur, who probably missed many precious moments of fatherly love and care. The divine presence and enchanting smiles of both of them provided the enormous moral strength and helped in dousing-off much of the tautness and stress.

Above all, the author is highly indebted to almighty God who blessed him with spiritual support, opportunities and fortitude at each and every stage of this work.

(PARMINDER SINGH)

CERTIFICATE

This is to certify that the thesis entitled "Investigation on Cold Spray based Additive

Manufacturing of IN 718 Superalloy", submitted by Parminder Singh (2019MEZ0008) for

the award of the degree of **Doctor of Philosophy** of Indian Institute of Technology Ropar, is a

record of bonafide research work carried out under my guidance and supervision. To the best of

my knowledge and belief, the work presented in this thesis is original and has not been submitted,

either in part or full, for the award of any other degree, diploma, fellowship, associateship or

similar title of any university or institution.

In my opinion, the thesis has reached the standard fulfilling the requirements of the regulations

relating to the Degree.

Signature of the Supervisor

Name: Prof. Harpreet Singh

Department: Mechanical Engineering

Indian Institute of Technology Ropar

Rupnagar, Punjab 140001

Date: / 2024

iv

Cold spray is gaining recognition as a leading additive manufacturing technique due to its low-temperature process, which reduces thermal stresses and preserves the quality of both materials and substrates. Unlike traditional thermal spray methods, cold spray works in a solid state, offering improved material properties, dimensional accuracy, and high-performance coatings with minimal porosity and oxidation. This technique has become increasingly relevant in sectors such as aerospace, automotive, and defense, with ongoing research focused on refining its efficiency, expanding compatible materials, and improving automation and standardization.

This research explores the potential of cold spray for fabricating components from Inconel 718 (IN 718), a superalloy known for its strength, durability, and resistance to high temperatures. Conventional manufacturing techniques for IN 718 face difficulties due to the alloy's toughness and high-temperature forming challenges, such as unwanted phase formation, which can weaken the material. Cold spray, however, offers a promising alternative, as it overcomes these issues while retaining the desired mechanical properties.

In the initial phase of this study, thick layers of pure titanium (Ti) and nickel-chromium alloy (Ni-20Cr) were successfully deposited using cold spray. The performance of these deposits was enhanced through various heat treatments, which allowed for tailoring properties like tensile strength and ductility based on the intended application. This success demonstrated cold spray's potential for creating dense, high-quality layers more efficiently than traditional methods.

The next phase involved optimizing cold spray parameters for fabricating IN 718 pipes. By analyzing the ratio of particle impact velocity to critical velocity, researchers achieved efficient deposition with properties similar to bulk materials. Furthermore, different injection angles were tested, with the 30 deg powder injection angle emerging as the most effective for improving heat transfer, gas temperature uniformity, particle temperature, particle acceleration and reducing cold spray footprint.

Computational fluid dynamics simulations provided deeper insights into the cold spray process, particularly when depositing IN 718 onto stainless steel (SS 304) substrates. These simulations revealed the formation of bow shockwaves at the impact zone, influencing gas attributes, particle behavior and deposition quality. Validation through microstructural analysis confirmed the accuracy of these simulations in understanding how cold spray deposits IN 718 particles.

Finally, optimized cold spray parameters were used to create a 3D IN 718 pipe, exhibiting dense structures with minimal porosity. The deposited material demonstrated microhardness and mechanical properties that closely match those of bulk IN 718. This study confirmed that cold

spray could effectively replace traditional methods for producing IN 718 components, offering superior efficiency and performance while maintaining the integrity of the original material phases.

Cold spray is a cutting-edge additive manufacturing and coating technique that employs highspeed gas to propel powdered particles toward a substrate at low temperatures. Unlike conventional thermal spray methods, this solid-state process prevents particle melting, instead enabling adhesion through plastic deformation upon impact. By preserving the feedstock material's original properties, cold spray minimizes oxidation and thermal stresses, resulting in dense, strong coatings. Its suitability for temperature-sensitive materials like titanium, aluminum, copper, and nickel alloys makes it valuable in applications that requires high-quality coatings with minimal porosity. Cold spray based additive manufacturing (CSAM), is rapidly evolving driven by several pivotal factors. Ongoing research focuses on refining parameters to enhance deposition efficiency and material properties, while advancements in powder metallurgy expand the range of compatible materials. Investments in advanced cold spray systems with automation and precision are boosting throughput and repeatability, making cold spray an integral part of industrial production processes. Integrating cold spray technology into aerospace, automotive, and defense sectors underscores its capability to meet stringent quality standards. Researchers are exploring simultaneous deposition of multiple materials for creating complex, multifunctional components. Leveraging digitalization tools and simulation software optimizes processes and predicts material behavior, complemented by standardization efforts ensuring reliability and uniformity. With these advancements, cold spray technology emerges as a versatile and widely embraced manufacturing solution across various industries. In the context of additive manufacturing, the application of cold spraying technique is very recent. The process appears to be promising due to its unparalleled advantages. However, the applicability of cold spray process for components at industrial length-scale such as energy, aviation, oil and gas, locomotives and healthcare etc. is unknown and needs to be explored to scale-up the process successfully. Moreover, understanding the influence of process parameters on the microstructure evolution, mechanical behavior as well as degradation behavior under simulated operating conditions is critical for advancing this technology in a real sense.

This research aims to develop a comprehensive approach and database for fabricating components using Inconel 718 (IN 718), a precipitation-hardened nickel-chromium-iron-based superalloy renowned for its exceptional mechanical properties across a wide temperature range. IN 718 exhibits outstanding tensile, fatigue, creep, and rupture strength, along with excellent resistance to corrosion and oxidation. However, conventional manufacturing methods face significant challenges with IN 718 due to issues such as excessive tool wear, work hardening, and

low material removal rates during machining. These challenges are compounded by difficulties in high-temperature forming processes caused by the segregation of refractory elements like niobium (Nb) and molybdenum (Mo), leading to Laves phase formation, which compromises material strength and ductility. Advanced manufacturing techniques are necessary for fabricating intricate components from IN 718. Several studies have explored the microstructure of additively manufactured (AMed) IN 718 using various metal additive manufacturing (MAM) processes. However, AMed IN 718 exhibits inferior fatigue performance due to additive manufacturing-induced defects like porosity and subpar surface quality, along with notable variations in microstructure and texture leading to mechanical response anisotropy. Traditional thermal spray techniques result in coatings with high porosity levels. Cold Spray emerges as a promising substitute for additive manufacturing IN 718 components, effectively addressing limitations seen in conventional methods and offering potential enhancements in efficiency and performance.

In this research, our first objective was to establish a proof-of-concept by fabricating thick plates of materials that typically posed challenges in welding, forming, casting, or traditional fabrication methods. To achieve this, we focused on commercially pure Ti and Ni-20Cr alloy. Employing pre- and post-heat treatment procedures, we investigated their effects on structure-property relations. Our initial study involved evaluating thick layers, ranging from 6 to 16 mm, of pure Ti and Ni-20Cr alloy fabricated through high-pressure cold spray process. These layers were then meticulously compared with their conventional as-cast counterparts. The successful deposition of such thick layers underscored the immense potential of cold spray in additive manufacturing of components. Additionally, each heat treatment option enhanced specific properties in the deposits. Depending on the application of the product, a suitable treatment could be selected to achieve desirable properties. For instance, if better tensile strength was required, one could opt for substrate heating (SH) pre-treatment to complement the cold spray process. Conversely, if enhanced ductility with reduced porosity was the goal, hot isostatic pressing (HIP) post-treatment could serve as a suitable supplement to the cold-sprayed deposits. Our comprehensive analyses, encompassing microstructural examinations, mechanical property evaluations, and hightemperature cyclic oxidation studies, consistently indicated that cold spraying offered a viable and promising route for additive manufacturing, particularly for producing thick layers at significantly higher production rates.

In the subsequent study involving the second objective, IN 718, a nickel-based superalloy, was chosen for pipe fabrication. A two-level full factorial design was employed to analyze the velocity ratio (the ratio of particle impact velocity at standoff distance (SoD) to critical velocity) for effective cold spray deposition of IN 718. Cold spraying high-strength materials like IN 718

posed challenges due to limited deformability, impacting coating quality. To achieve properties similar to bulk materials, maintaining a particle impact velocity at SoD above the critical velocity was crucial, with a velocity ratio within the 1.1-2 range for deposition efficiency of 80-100 %. Powder feed rate (PFR) and SoD were kept constant at 30 g/min and 25 mm, respectively. Statistical analysis revealed PFR as a non-significant parameter, while SoD had a minimal positive effect on the velocity ratio. A lower SoD helped maintain a consistent cold spray footprint diameter, ensuring better deposition accuracy and minimizing material oxidation. Thus, meticulous adjustment of process parameters was necessary to achieve elevated particle impact velocities and temperatures, facilitating the formation of maximum well-bonded interfaces between particles and particle-substrate. In our ongoing study, we rigorously explored various cold spray process parameters at both low and high levels using a comprehensive full factorial two-level approach to pinpoint optimized parameters for effective cold spray deposition of IN 718.

In the third objective, we conducted an examination of how different injection angles (90 deg, 30 deg and 0 deg) affected the performance of the cold spray process using IN 718 powder particles and nitrogen gas. The computational modeling including gas flow field simulations and particle trajectory analyses is utilized to understand how these angles influenced various aspects of the process. The chosen turbulence model, $k-\omega$ SST (shear stress transport), was commended for its accuracy in describing turbulent flows, making it suitable for capturing the complex dynamics of gas-particle interaction within the cold spray nozzle. Among the angles tested, the 30 deg injection angle emerged as the most favorable due to several factors. This angle facilitated improved heat transfer, resulting in a higher gas temperature and a more uniform distribution within the gas flow, which was crucial for maintaining consistent deposition quality. Additionally, the 30 deg angle produced higher exit velocities for the nitrogen gas, improving its ability to accelerate and entrain powder particles. Furthermore, the gas dynamics at this angle increased drag forces on the powder particles, aiding in their acceleration and entrainment. As a result, the IN 718 powder particles experienced elevated velocities and temperatures, enhancing their kinetic energy and adhesion upon impacting the substrate. The combined effect of these factors resulted in enhanced deposition efficiency at the 30 deg injection angle, highlighting the importance of angle optimization in achieving desired outcomes, especially in applications requiring precise track generation within complex geometries.

In the fourth objective, a discrete phase computational fluid dynamics analysis was conducted to simulate the gas flow and particle behavior during the cold spray deposition of IN 718 onto an SS 304 pipe. During the analysis, researchers observed a bow shock phenomenon at the impingement

zone where the supersonic jet interacted with the SS 304 substrate pipe. This bow shock caused an increase in gas density and a significant reduction in gas velocity, while the velocity of IN 718 powder particles experienced a relatively smaller decrease. Following this observation, researchers determined the average impact velocity and temperature of the IN 718 powder particles at SoD, serving as crucial input parameters for establishing boundary conditions in single- and multi-particle explicit impact simulation studies of IN 718 onto the SS 304 substrate. Further observations revealed jetting phenomena during the cold spraying process, particularly evident across the D₁₀, D₅₀, and D₉₀ diametric distributions of the IN 718 powder feedstock. Larger particles with diameter above critical diameter underwent notable shape changes due to jetting, contrasting with sub-critical smaller particles that predominantly embedded within the SS 304 substrate. Experimental validation of the coating microstructure, both in single- and multiparticle impact scenarios, underscored the effectiveness of computational fluid dynamics and impact deformation studies in elucidating the underlying processes.

In the last study, researchers utilized optimized cold spray process parameters and calibrated robot configurations, along with tilting turntable settings, to fabricate a 3D standalone pipe. The resulting IN 718 thick pipe deposits measured 6 inches in length, with a nominal bore of 60.3 mm and a thickness of 5 mm respectively. Microstructural analysis revealed deposits characterized by dense structures and minimal porosity. The density, microhardness values and mechanical properties of cold spray additively manufactured (CSAMed) IN 718 thick pipe deposits closely resembled those of bulk IN 718. Notably, no oxide formation was observed in energy dispersive spectroscopy (EDS) analysis, and this was further confirmed through X-ray diffraction (XRD). Additionally, all the phases identified in the powder feedstock were retained in the CSAMed IN 718 thick pipe deposits, indicating the absence of phase transformations during the cold spray process. δ phase precipitates were detected in scanning electron microscopy (SEM) microstructure, which was also confirmed through EDS and XRD analysis. Initial microstructural and mechanical characterization suggested that cold spray could effectively replace conventional processes for fabricating IN 718 pipes, offering numerous advantages.

Keywords: additive manufacturing; cold spray; inconel 718; optimization; computational fluid dynamics; explicit impact simulation; characterization

TABLE OF CONTENTS

DECLARATION OF ORIGINALITY	i
ACKNOWLEDGEMENTS	ii
CERTIFICATE	iv
LAY SUMMARY	V
ABSTRACT	vii
LIST OF FIGURES	xvi
LIST OF TABLES	xxvi
LIST OF PUBLICATIONS	xxviii
LIST OF ABBREVIATIONS	xxix
CHAPTER 1 INTRODUCTION	1
1.1 HISTORICAL BACKGROUND OF ADDITIVE MANUFACTURING TECHNIQUES	2
1.2 OVERVIEW OF THERMAL SPRAY MARKET	8
1.3 RESEARCH MOTIVATION	10
1.4 COLD SPRAY BASED ADDITIVE MANUFACTURING	14
1.5 INCONEL 718 SUPERALLOY	16
1.6 MAIN AIM OF THE RESEARCH WORK	16
1.7 THESIS LAYOUT	17
CHAPTER 2 LITERATURE REVIEW	20
2.1 ADDITIVE MANUFACTURING	20
2.2 METAL ADDITIVE MANUFACTURING TECHNOLOGIES	22
2.2.1 Powder Bed Fusion	23
2.2.1.1 Selective Laser Melting	23
2.2.1.2 Electron Beam Melting	24
2.2.2 Directed Energy Deposition	25
2.2.2.1 Laser based Directed Energy Deposition	26
2.2.2.2 Electron Beam based Directed Energy Deposition	27
2.2.2.3 Arc based Directed Energy Deposition	28
2.3 THERMAL SPRAY: A HISTORICAL PERSPECTIVE ON	29
ADVANCEMENTS	4)
2.4 THERMAL SPRAY BASED ADDITIVE MANUFACTURING	31

TECHNOLOGIES	
2.4.1 Flame Spray	33
2.4.2 High Velocity Oxy-Fuel Process	34
2.4.3 Detonation Gun Spraying	35
2.4.4 Plasma Spraying	36
2.4.5 Cold Spray	37
2.4.5.1 Bonding Mechanism in Cold Spray	39
2.4.5.2 Critical Velocity and Window of Deposition	42
2.5 COMPUTATIONAL FLUID DYNAMICS (CFD) & FINITE	46
ELEMENT ANALYSIS (FEA) OF COLD SPRAY PROCESS	40
2.6 COLD SPRAY BASED ADDITIVE MANUFACTURING (CSAM)	53
2.6.1 Manufacturing Parameters for CSAM	54
2.6.1.1 Propulsive Gas Parameters for CSAM	56
2.6.1.2 Powder Feeder Parameters for CSAM	56
2.6.1.3 Nozzle Parameters for CSAM	57
2.6.1.3.1 Nozzle Traverse Speed	57
2.6.1.3.2 Nozzle Scanning Step	57
2.6.1.3.3 Nozzle Trajectory	58
2.6.2 Properties of CSAM Deposits	58
2.6.3 Defects of CSAM Deposits	59
2.7 OVERVIEW ON ADDITIVE MANUFACTURING OF INCONEL 718	59
2.8 PROBLEM FORMULATION	70
2.8.1 Scope	70
2.8.2 Research Objectives	74
2.8.3 Plan of Study	75
CHAPTER 3 EXPERIMENTAL TECHNIQUES AND PROCEDURES	78
3.1 MATERIALS	78
3.1.1 Proof-of-Concept	78
3.1.1.1 Substrate	78
3.1.1.2 Thick Deposits	79
3.1.1.2.1 Pure Ti Deposits	79
3.1.1.2.2 Ni-20Cr Deposits	80

3.1.2 3D Standalone IN 718 Pipe Deposits	82
3.1.2.1 Substrate	82
3.1.2.2 IN 718 Thick Pipe Deposits	82
3.2 PROCESS PARAMETERS FOR CSAM	85
3.2.1 Proof-of-Concept	85
3.2.1.1 Thick Deposits	85
3.2.1.1.1 Pure Ti Deposits	85
3.2.1.1.2 Ni-20Cr Deposits	86
3.2.2 3D Standalone IN 718 Pipe Deposits	88
3.3 METALLURGICAL CHARACTERIZATION	92
3.3.1 SEM-EDS Analysis	92
3.3.2 X-Ray Diffraction Analysis	92
3.4 MECHANICAL CHARACTERIZATION	93
3.4.1 Microhardness Analysis	93
3.4.2 Nanoindentation Analysis	93
3.4.3 Tensile Testing	93
3.4.4 High Temperature Cyclic Oxidation Study	94
3.5 METHODOLOGY FOR PARAMETRIC OPTIMIZATION FOR	95
COLD SPRAY DEPOSITION OF IN 718 USING MINITAB	73
3.5.1 Factorial Design Approach	95
3.5.2 Data Collection	97
3.6 METHODOLOGY FOR EFFECT OF INJECTION ANGLE ON	
POWDER STREAM AND CARRIER GAS CHARACTERISTICS	99
IN COLD SPRAY DEPOSITION OF IN 718	
3.6.1 Numerical Simulation Methodology	99
3.6.1.1 k-ω SST CFD Model	99
3.6.1.2 Geometry and Computational Domain	102
3.7 METHODOLOGY FOR DISCRETE PHASE COMPUTATIONAL	
FLUID DYNAMICS AND IMPACT DEFORMATION (SINGLE- AND	
MULTI-PARTICLE) STUDY OF COLD SPRAY DEPOSITION OF IN	107
718 POWDER FEEDSTOCK ON SS 304 PIPE WITH EXPERIMENTAL	
VALIDATION	
3.7.1 CFD Simulation Methodology	107

3.7.1.1 k-ω SST CFD Model	107
3.7.1.2 Geometry and Computational Domain	107
3.7.2 Explicit Dynamics Simulation Methodology	110
CHAPTER 4 PROOF-OF-CONCEPT	117
4.1 PURE Ti DEPOSITS	117
4.1.1 Results and Discussion	117
4.1.1.1 Microstructural Analysis	117
4.1.1.2 Mechanical Properties Evaluation	123
4.1.1.3 High Temperature Cyclic Oxidation Study	128
4.2 Ni-20Cr DEPOSITS	135
4.2.1 Results and Discussion	135
4.2.1.1 Microstructural Analysis	135
4.2.1.2 Mechanical Behaviour	138
4.2.1.3 High Temperature Cyclic Oxidation	142
CHAPTER 5 PARAMETRIC ANALYSIS OF COLD SPRAY	147
PROCESS	147
5.1 OPTIMIZING COLD SPRAY PROCESS PARAMETERS	148
5.1.1 Results and Discussion	148
5.1.1.1 Analysis of Variance	148
5.1.1.2 Main and Interaction Effects	150
5.1.1.3 Normal Probability Plot of Residuals	152
5.1.1.4 Optimization	153
5.2 EFFECT OF POWDER INJECTION ANGLE	154
5.2.1 Results and Discussion	154
5.2.1.1 Gas Flow Field Analysis	154
5.2.1.2 Powder Particle Stream Analysis	163
CHAPTER 6 SIMULATION AND CHARACTERIZATION	168
OF IN 718 PIPE	108
6.1 DISCRETE PHASE CFD AND EXPLICIT IMPACT	169
DEFORMATION STUDY	107
6.1.1 Results and Discussion	169
6.1.1.1 Gas Flow Field and Powder Particle Stream Analysis	169
6.1.1.2 Impact Deformation Analysis and Experimental Validation	176

6.1.1.2.1 Single-Particle Impact Analysis	176
6.1.1.2.2 Multi-Particle Impact Analysis	183
6.2 CHARACTERIZATION OF CSAMed 3D STANDALONE IN 718 PIPE DEPOSITS	188
6.2.1 Results and Discussion	188
6.2.1.1 Microstructural Characterization	188
6.2.1.2 Mechanical Properties Evaluation	195
CHAPTER 7 CONCLUSIONS	199
7.1 CONCLUSIONS	200
7.1.1 Proof-of-Concept	200
7.1.2 Parametric Analysis of Cold Spray Process	201
7.1.3 Simulation and Characterization of IN 718 Pipe	203
SCOPE FOR FUTURE WORK	205
REFERENCES	206
BRIEF BIODATA	249

LIST OF FIGURES

Figure No.	Particulars	Page No.
Fig. 1.1	Histogram showing the additive manufacturing market size from the year 2023 to 2033 in USD Billion (https://www.precedenceresearch.com/additive-manufacturing-market)	2
Fig. 1.2	Histogram depicting market share distribution among various coating methods (Viswanathan et al. 2021)	8
Fig. 1.3	Histogram showing cold spray market share in various sectors (Viswanathan et al. 2021)	9
Fig. 1.4	Comparison of cold gas dynamic manufacturing with cold spray and other additive manufacturing techniques (Pattison <i>et al.</i> 2007)	13
Fig. 1.5	Schematic representation of cold spray based additive manufacturing system	15
Fig. 1.6	Thesis layout	17
Fig. 2.1	Unit cost comparison by production volume and complexity in additive manufacturing (AM) vs. traditional manufacturing (TM) (Orme <i>et al.</i> 2017; Fraunhofer 2021; Guo <i>et al.</i> 2024; G. E. Additive 2018)	22
Fig. 2.2	Schematic representation of selective laser melting (Jiao et al. 2018)	24
Fig. 2.3	Diagrammatic view of electron beam melting (Alojaly et al. 2023)	25
Fig. 2.4	Schematic of laser based DED (Sing et al. 2020)	26
Fig. 2.5	Simplified diagram of electron beam based DED (Sing et al. 2020)	27
Fig. 2.6	Basic outline of arc based DED (Alagha et al. 2021)	29
Fig. 2.7	Classification of thermal spray processes on the basis of energy source (Jahani <i>et al.</i> 2018)	32
Fig. 2.8	Taxonomy of thermal spray processes in relation to particle velocity and flame temperature (Ang <i>et al.</i> 2013)	32
Fig. 2.9	Layout of the flame spraying process (Xanthopoulou et al. 2014)	34
Fig. 2.10	Graphical depiction of high velocity oxy-fuel process (Jonda <i>et al.</i> 2020)	35
Fig. 2.11	Illustration of detonation gun spray process (Sundararajan et al. 2013)	36
Fig. 2.12	Schematic of plasma spraying process (Li et al. 2023)	37

Fig. 2.13	Comprehensive diagram of cold spray process (Vardelle et al. 2016)	38
Fig. 2.14	Distinctive characteristics of cold spray (Pathak and Saha 2017)	39
Fig. 2.15	Illustration of adiabatic shear instability phenomena (Assadi <i>et al.</i> 2016)	40
Fig. 2.16	(a) Simulated impact of a copper particle on a copper substrate for the initial velocities of 500 and 600 m/sec. Red arrow shows more pronounced jetting for 600 m/sec; (b) and (c) shows profiles of plastic strain and flow stress along the radial path for impact velocities of 300 and 900 m/s. Higher velocity results in flow stress dropping to zero at the particle-substrate interface indicating towards adiabatic shear instability phenomena; (d), (e) and (f) shows calculated temporal development of plastic strain, temperature and flow stress for various impact velocities (Assadi <i>et al.</i> 2016)	41
Fig. 2.17	Diagrammatic representation of hydrodynamic plasticity phenomena (Hassani-Gangaraj <i>et al.</i> 2018)	42
Fig. 2.18	Graphical representation of material deposition as a function of impact velocity (Hanft et al. 2015)	46
Fig. 2.19	Diagrammatic view of the manufacturing parameters for cold spray based additive manufacturing	55
Fig. 2.20	Schematic showing the research plan	77
Fig. 3.1	A flow chart representing the experimental procedure adopted to develop and characterize thick Ti deposits using CSAM	79
Fig. 3.2	SEM images of the feedstock titanium powder used for cold spray deposition: (a) low magnification; (b) high magnification	80
Fig. 3.3	EDS of the feedstock titanium powder used for cold spray deposition	80
Fig. 3.4	A flow chart representing the experimental procedure adopted to develop and characterize thick Ni-20Cr deposits using CSAM	81
Fig. 3.5	SEM micrographs of as-received Ni-20Cr powder feedstock used for cold spray additive manufacturing at (a) lower and (b) higher magnification	81
Fig. 3.6	EDS spectrum of as-received Ni-20Cr powder feedstock	82
Fig. 3.7	A flow chart showing the experimental procedure adopted to develop and characterize thick IN 718 pipe deposits using CSAM	83

Fig. 3.8	SEM images of as-received IN 718 powder feedstock used for cold spray additive manufacturing at (a) lower and (b) higher magnification	84
Fig 3.9	Particle size distribution of IN 718 powder feedstock	84
Fig. 3.10	Macrographs of cold spray additively manufactured pure Ti thick deposits with IN 718 as a substrate	85
Fig. 3.11	Schematics of the pre-/post-heat treatment operations: substrate heating (SH) and hot isostatic pressing (HIP)	87
Fig. 3.12	Macrographs of the cold spray additive manufactured Ni-20Cr thick deposits: (a) as-sprayed; (b) substrate heated; (c) hot-isostatic pressing treated	88
Fig. 3.13	Detailed representation of optimized robot and tilting turntable parameters for cold spray based additive manufacturing of IN 718 thick pipe deposits	89
Fig. 3.14	Cold spray setup for fabricating IN 718 thick pipe deposits	90
Fig. 3.15	Real-time image showing the fabrication of IN 718 thick pipe deposits in progress	90
Fig. 3.16	Macrographs of cold spray additively manufactured IN 718 seamless pipe (a) top view (b) front view	91
Fig. 3.17	Images showing sectioned cold spray additively manufactured IN 718 pipe during wEDM (a) lower magnification (b) higher magnification	91
Fig. 3.18	Schematic of the convergent-divergent (CD) nozzle used in the CFD analysis of the cold spray deposition of IN 718	98
Fig. 3.19	Validation of CFD model by comparing simulation findings and experimental results	101
Fig. 3.20	Detailed schematic of the three cold spray nozzles with different powder injection angle used in CFD simulation	103
Fig. 3.21	Grid independency results for all three cold spray nozzles with different powder injection angle [90 deg (top), 0 deg (middle) and 30 deg (bottom)]	104
Fig. 3.22	Meshed 2D computational domain of all three cold spray nozzles with different powder injection angle [90 deg (top), 0 deg (middle) & 30 deg (bottom)]	105
Fig. 3.23	Detailed schematic showing the 30 deg powder injection cold spray	108

	nozzle with SS 304 substrate pipe used in CFD simulation	
E:~ 2.24	Commercial convergent-divergent nozzle with 30 deg powder injection	100
Fig. 3.24	used in Plasma Giken ((PCS-100) cold spray system	108
Fig. 3.25	Grid independence testing for the 30 deg powder injection cold spray	109
Fig. 3.23	nozzle with SS 304 substrate pipe	109
Fig. 3.26	Meshed 2D computational domain of the 30 deg powder injection cold	110
Fig. 5.20	spray nozzle with SS 304 substrate pipe used in CFD simulation	110
	Illustration of boundary conditions implemented for impact	
Fig. 3.27	deformation analysis for single-particles of IN 718 powder feedstock	113
	onto an SS 304 substrate	
	Representation of boundary conditions implemented for impact	
Fig. 3.28	deformation analysis for multi-particle of IN 718 powder feedstock	113
	onto an SS 304 substrate	
	Temporal development of maximum effective plastic strain for	
Fig. 3.29	different particle sizes [D_{10} (top), D_{50} (middle) and D_{90} (bottom)] for	114
119. 0.2	impact deformation analysis for single-particles of IN 718 powder	11.
	feedstock onto an SS 304 substrate	
	Temporal development of maximum effective plastic strain for impact	
Fig. 3.30	deformation analysis for multi-particle of IN 718 powder feedstock	115
	onto an SS 304 substrate	
Fig. 3.31	Meshed 2D computational domain for impact deformation of single-	115
8,	particle (D ₅₀) of IN 718 powder feedstock onto an SS 304 substrate	
	Meshed 2D computational domain for impact deformation of multi-	
Fig. 3.32	particle (D ₁₀ , D ₅₀ and D ₉₀ randomly distributed) of IN 718 powder	116
	feedstock onto an SS 304 substrate along with closer view	
Fig. 4.1	Optical images of HIP-treated CSAMed pure titanium deposit around	119
8 ·	the interface at (a) low magnification; (b) high magnification	
	SEM images of HIP-treated CSAMed pure titanium deposit without	
Fig. 4.2	etching at (a) low and (b) high magnification and with etching at (c)	119
	low and (d) high magnification	
Fig. 4.3	EDS mapping of HIP-treated CSAMed pure titanium deposited on IN	120
8- 110	718 substrate	
Fig. 4.4	XRD data of (a) feedstock titanium powder; (b) central region of HIP-	121

	treated CSAMed pure titanium deposit and (c) at interface of the	
	deposited titanium layer and IN 718 substrate	
Fig. 4.5	Cross-sectional microhardness analysis of the HIP-treated CSAMed	125
Fig. 4.3	pure titanium on IN 718 substrate	125
Fig. 4.6	Load-displacement curve of the HIP-treated CSAMed pure titanium	125
Fig. 4.0	deposit obtained through nanoindentation	123
Fig. 4.7	Macro-tensile plot showing engineering stress versus engineering	126
11g. 4.7	strain for the HIP-treated CSAMed pure titanium deposit	120
	Micro-tensile plot showing engineering stress versus engineering strain	
Fig. 4.8	along with the in situ SEM-micrographs at various crack stages for the	127
	HIP-treated CSAMed pure titanium deposit	
	Fractography analysis of the HIP-treated CSAMed pure titanium	
Fig. 4.9	deposit after micro-tensile test at (a) lower and (b) higher	128
	magnification	
	Mass gain per unit area versus number of cycles plot for the HIP-	
Fig. 4.10	treated CSAMed pure titanium deposit subjected to cyclic oxidation in	129
	air at 900 °C	
	Square of mass gain per unit area versus number of cycles plot for the	
Fig. 4.11	HIP-treated CSAMed pure titanium deposit subjected to cyclic	130
	oxidation in air at 900 °C	
Fig. 4.12	Macrographs of the HIP-treated CSAMed pure titanium deposit	130
	subjected to high-temperature cyclic oxidation in air at 900 °C	
	(a) Cross-sectional optical micrograph; (b) cross-sectional	
Fig. 4.13	microhardness analysis of the HIP-treated CSAMed pure titanium	132
	deposit subjected to high-temperature cyclic oxidation in air at 900 °C	
	(a) Surface SEM micrographs; (b) EDS spectrum of the HIP-treated	
Fig. 4.14	CSAMed pure titanium deposit subjected to high-temperature cyclic	133
	oxidation in air at 900 °C	
	EDS mapping of the HIP-treated CSAMed pure titanium deposit	465
Fig. 4.15	subjected to high-temperature cyclic oxidation in air at 900 °C: (a)	133
	titanium; (b) oxygen	
Fig. 4.16	XRD analysis of the HIP-treated CSAMed pure titanium deposit	134
	subjected to high-temperature cyclic oxidation in air at 900 °C	

	Cross-sectional SEM analysis of the CSAMed Ni-20Cr thick plates: (a)		
Fig. 4.17	as-sprayed; (b) substrate heated; (c) hot-isostatic pressing treated, pores	136	
11g. 4.17	in the microstructures are encircled	130	
	Density, apparent surface porosity, and pore size data of the CSAMed		
Fig. 4.18	Ni-20Cr thick plates in as-sprayed, substrate heated, and hot-isostatic	137	
	pressing treated conditions		
Fig. 4.19	EDS spectra of the CSAMed Ni-20Cr thick plates: (a) as-sprayed; (b)	137	
Fig. 4.19	substrate heated; (c) hot-isostatic pressing treated	137	
Fig. 4.20	XRD data of as-received Ni-20Cr powder feedstock and CSAMed Ni-	120	
Fig. 4.20	20Cr thick plates	138	
	Combined load-displacement nanoindentation curves for the CSAMed		
Fig. 4.21	Ni-20Cr thick plates in as-sprayed, substrate heated, and hot-isostatic	141	
	pressing treated conditions		
	Engineering stress vs engineering strain curves for the CSAMed Ni-		
Fig. 4.22	20Cr thick plates in as-sprayed, substrate heated, and hot-isostatic	141	
1 15, 7,22	pressing treated conditions		
	Plot of mass loss/area vs. number of cycles for the CSAMed Ni-20Cr		
Fig. 4.23	thick plate in substrate heated condition (Ni-20Cr-SH) exposed to 50	143	
	cycles of high-temperature cyclic oxidation in air at 900 °C		
	Plot of square of mass loss/area vs. number of cycles for the CSAMed		
	Ni-20Cr thick plate in substrate heated condition (Ni-20Cr-SH)		
Fig. 4.24	exposed to 50 cycles of high-temperature cyclic oxidation in air at 900	143	
	°C		
	Macrographs of the CSAMed Ni-20Cr thick plate in substrate heated		
Fig. 4.25	condition (Ni-20Cr-SH) exposed to 50 cycles of high-temperature	144	
	cyclic oxidation in air at 900 °C		
	Surface SEM image of oxide scale for the CSAMed Ni-20Cr thick		
Fig. 4.26	plate in substrate heated condition (Ni-20Cr-SH) subjected to 50 cycles	145	
g	of high-temperature cyclic oxidation in air at 900 °C		
	EDS analysis of oxide scale for the CSAMed Ni-20Cr thick plate in		
Fig. 4.27	substrate heated condition (Ni-20Cr-SH) subjected to 50 cycles of	145	
_	high-temperature cyclic oxidation in air at 900 °C		
Fig. 4.28	XRD analysis of oxide scale for the CSAMed Ni-20Cr thick plate in	146	

	substrate heated condition (Ni-20Cr-SH) subjected to 50 cycles of		
	high-temperature cyclic oxidation in air at 900 °C		
Fig. 5.1	Main effect plots for velocity ratio	150	
Fig. 5.2	Interaction effect plots for velocity ratio	151	
Fig. 5.3	Pareto chart of standardized effects on the velocity ratio (VR)		
Fig. 5.4	Normal probability plot of residuals		
Fig. 5.5	Velocity contour maps for all three cold spray nozzles with different	156	
11g. 3.3	powder injection angle (a) 90 deg; (b) 0 deg and (c) 30 deg	130	
	Variation of nitrogen gas pressure versus path length for all three cold		
	spray nozzles with different powder injection angle [90 deg (top); 0		
Fig. 5.6	deg (middle) and 30 deg (bottom)] with arrows showing gas flow	157	
Fig. 5.0	through expansion fan along with inset graphs showing pressure	137	
	increase as the gas flow encounters oblique shock waves as depicted		
	through dashed boxes		
	Variation of nitrogen gas temperature versus path length for all three		
	cold spray nozzles with different powder injection angle [90 deg (top);		
Fig. 5.7	0 deg (middle) and 30 deg (bottom)] with arrows showing gas flow	158	
	through expansion fan along with dashed boxes depicting the gas flow		
encountering oblique sho	encountering oblique shock waves		
	Variation of Mach number versus path length for all three cold spray		
	nozzles with different powder injection angle [90 deg (top); 0 deg		
Fig. 5.8	(middle) and 30 deg (bottom)] with arrows showing gas flow through	159	
	expansion fan along with dashed boxes depicting the gas flow		
	encountering oblique shock waves		
	Variation of nitrogen gas velocity versus path length for all three cold		
Fig. 5.9	spray nozzles with different powder injection angle [90 deg (top); 0	160	
	deg (middle) and 30 deg (bottom)]		
Fig. 5.10	Temperature contour maps for all three cold spray nozzles with	161	
119,011	different powder injection angle (a) 90 deg; (b) 0 deg and (c) 30 deg	101	
	Turbulent kinetic energy contour maps for all three cold spray nozzles		
Fig. 5.11	with different powder injection angle (a) 90 deg; (b) 0 deg and (c) 30	162	
	deg		
Fig. 5.12	Particle tracks representing IN 718 powder particle velocity for all	164	

	three cold spray nozzles with different powder injection angle (a) 90		
	deg; (b) 0 deg and (c) 30 deg		
	Variation of average velocity of IN 718 powder particles with path		
Fig. 5.13	length for all three cold spray nozzles with different powder injection	165	
	angle [90 deg; 0 deg and 30 deg]		
	Particle tracks representing IN 718 powder particle temperature for all		
Fig. 5.14	three cold spray nozzles with different powder injection angle (a) 90	166	
	deg; (b) 0 deg and (c) 30 deg		
	Closer view of the particle tracks representing IN 718 powder particle		
Fig. 5.15	temperature in convergent sections for all three cold spray nozzles with	166	
	different powder injection angle (a) 90 deg; (b) 0 deg and (c) 30 deg		
	Variation of average temperature of IN 718 powder particles with path		
Fig. 5.16	length for all three cold spray nozzles with different powder injection	167	
	angle [90 deg; 0 deg and 30 deg]		
Fiσ. 6.1	Contour maps representing Mach number during cold spray deposition	169	
Fig. 6.1	of IN 718 powder feedstock onto an SS 304 substrate pipe	10)	
	Variation of nitrogen gas pressure versus path length in cold spray		
Fig. 6.2	deposition of IN 718 powder feedstock onto an SS 304 substrate pipe	170	
Fig. 0.2	with blue arrow showing increase in pressure due to bow shock		
	phenomenon		
	Variation of nitrogen gas density versus path length in cold spray		
Fig. 6.3	deposition of IN 718 powder feedstock onto an SS 304 substrate pipe	171	
J	with blue arrow showing increase in density due to bow shock		
	phenomenon		
	Variation of Mach number versus path length in cold spray deposition		
Fig. 6.4	of IN 718 powder feedstock onto an SS 304 substrate pipe with blue	172	
	arrow showing drop in Mach number due to bow shock phenomenon		
Fig. 6.5	Variation of average temperature of IN 718 powder particles and		
	nitrogen gas temperature versus path length in cold spray deposition of		
	IN 718 powder feedstock onto an SS 304 substrate pipe with blue	173	
	arrow showing drop in nitrogen gas temperature due to bow shock		
E. C.	phenomenon	154	
Fig. 6.6	Contour maps representing nitrogen gas velocity during cold spray	174	

	,		
	deposition of IN 718 powder feedstock onto an SS 304 substrate pipe		
Fig. 6.7	Contour maps representing nitrogen gas temperature during cold spray	174	
	deposition of IN 718 powder feedstock onto an SS 304 substrate pipe	_,.	
Fig. 6.8	Contour maps representing turbulent kinetic energy during cold spray	174	
11g. 0.0	deposition of IN 718 powder feedstock onto an SS 304 substrate pipe		
Fig. 6.9	Particle tracks representing powder particle velocity during cold spray	175	
11g. 0.7	deposition of IN 718 powder feedstock onto an SS 304 substrate pipe	175	
	Particle tracks representing powder particle temperature during cold		
Fig. 6.10	spray deposition of IN 718 powder feedstock onto an SS 304 substrate	175	
	pipe		
	Variation of average velocity of IN 718 powder particles and nitrogen		
Fig. 6.11	gas velocity versus path length in cold spray deposition of IN 718	176	
Fig. 0.11	powder feedstock onto an SS 304 substrate pipe with blue arrow	170	
	showing drop in nitrogen gas velocity due to bow shock phenomenon		
	Simulated contours of PEEQ for different diameters of IN 718 powder		
Fig. 6.12	feedstock impacting onto an SS 304 substrate (a) D_{10} (13.5 μ m); (b)	177	
	D_{50} (22 μ m); and (c) D_{90} (33.5 μ m)		
	Simulated contours of von-Mises stresses for different diameters of IN		
Fig. 6.13	718 powder feedstock impacting onto an SS 304 substrate (a) D ₁₀ (13.5	179	
115. 0.13	μ m); (b) D_{50} (22 μ m); and (c) D_{90} (33.5 μ m)		
	Simulated contours of temperature for different diameters of IN 718		
Fig. 6.14	powder feedstock impacting onto an SS 304 substrate (a) D_{10} (13.5	180	
	μ m); (b) D_{50} (22 μ m); and (c) D_{90} (33.5 μ m)		
	Single-pass coating cross SEM micrographs showing microstructure of		
	IN 718 powder splats in (a); (b); (c); (d); and (e) with bigger particles		
Fig. 6.15	in dashed yellow rectangles showing jetting formation and white	182	
	arrows depicting smaller particle penetrating deeper inside		
	comparatively softer SS 304 substrate		
Fig. 6.16	Cross SEM micrographs showing microstructure of IN 718 powder		
	splats in (a); (b) and (c) with yellow and white arrows showing	185	
	extrusion and interlocking effects and (d) showing tamping effect		
Fig. 6.17	Simulated contours of (a) PEEQ and (b) von-Mises stresses for multi-	186	
rig. U.1/	particle impact simulation of IN 718 powder feedstock onto an SS 304	100	

	substrate with different diameters D_{10} (13.5 μ m); D_{50} (22 μ m); and D_{90}		
	(33.5 µm) in random distribution		
	Five-pass coating cross SEM micrographs showing microstructure of		
Fig. 6.18	IN 718 powder splats in (b); (c); (d); and (e) in comparison with	187	
	simulation results given in (a) with similar plastic deformation in same	10/	
	colors during multi-particle impact onto SS 304 substrate		
	Cross SEM micrographs of CSAMed IN 718 thick pipe deposits (a)		
Fig. 6.19	500 X; (b) 1 KX; (c) 2 KX; (d) 5 KX; (e) 10 KX; and (f) 15 KX image	189	
	showing δ phase particles		
Fig. 6.20	EDS mapping of CSAMed IN 718 thick pipe deposits	189	
	Top SEM micrographs showing the morphology of deposited IN 718		
Fig. 6.21	powder particles (a); (b); (c) lower magnification and (d); (e); (f)	190	
	higher magnification showing ring of jet type morphology		
Fig. 6.20 E Fig. 6.21 p h Fig. 6.22 S Fig. 6.23 S Fig. 6.24 I Fig. 6.25 I Fig. 6.25 I	EDS spectra of γ matrix and δ phase in CSAMed IN 718 thick pipe	192	
	deposits	192	
Fig 6 23	 500 X; (b) 1 KX; (c) 2 KX; (d) 5 KX; (e) 10 KX; and (f) 15 KX image showing δ phase particles 6.20 EDS mapping of CSAMed IN 718 thick pipe deposits Top SEM micrographs showing the morphology of deposited IN 718 powder particles (a); (b); (c) lower magnification and (d); (e); (f) higher magnification showing ring of jet type morphology 6.22 EDS spectra of γ matrix and δ phase in CSAMed IN 718 thick pipe deposits 6.23 SEM micrograph depicting morphology of δ phase in CSAMed IN 718 thick pipe deposits 6.24 XRD spectra of CSAMed IN 718 thick pipe deposits and as-received IN 718 powder feedstock 6.25 Density and apparent surface porosity of CSAMed IN 718 thick pipe deposits 6.26 Microhardness plot for CSAMed IN 718 thick pipe deposits 	193	
 Fig. 6.18 Five-pass coating cross SEM micrographs showing microstructure of IN 718 powder splats in (b); (c); (d); and (e) in comparison with simulation results given in (a) with similar plastic deformation in same colors during multi-particle impact onto SS 304 substrate Cross SEM micrographs of CSAMed IN 718 thick pipe deposits (a) 500 X; (b) 1 KX; (c) 2 KX; (d) 5 KX; (e) 10 KX; and (f) 15 KX image showing δ phase particles Fig. 6.20	193		
Fig 6 24	XRD spectra of CSAMed IN 718 thick pipe deposits and as-received	104	
	IN 718 powder feedstock	194	
Fig 6 25	Density and apparent surface porosity of CSAMed IN 718 thick pipe	195	
Fig. 6.20 EDS mapping Top SEM in powder part higher magning EDS spectrod deposits Fig. 6.22 SEM micrograph Fig. 6.23 SEM micrograph Fig. 6.24 IN 718 powder part higher magning EDS spectrod deposits SEM micrograph Top SEM in powder part higher magning in powder part highe	deposits	193	
Fig. 6.26	Microhardness plot for CSAMed IN 718 thick pipe deposits	196	
	Micro-tensile plot showing engineering stress versus engineering strain		
Fig. 6.27	along with the in-situ SEM-micrographs at various crack stages for the	198	
	CSAMed IN 718 deposits		
Fig. 6.28	Fractography analysis of the CSAMed IN 718 deposits after micro-		
	tensile test at (a) lower and (b) higher magnification	198	

LIST OF TABLES

Table No.	Particulars				
Table 2.1	Comparison: CSAM Versus Other Fusion-Based Additive Manufacturing Approaches (Yin <i>et al.</i> 2018)				
Table 2.2	Typical Properties of Deposits Affected by CSAM Manufacturing Parameters				
Table 3.1	Chemical composition of IN 718 substrate used in cold spray based additive manufacturing of pure Ti and Ni-20Cr				
Table 3.2	Chemical composition of SS304 substrate pipe used in cold spray based additive manufacturing of IN 718 thick pipe deposits				
Table 3.3	Chemical composition of IN 718 powder feedstock	84			
Table 3.4	Detail of cold spraying process parameters and pre- and post-heat treatment				
Table 3.5	Details of cold spray additively manufactured Ni–20Cr samples				
Table 3.6	Optimized cold spray process parameters for fabrication of IN 718 thick pipe deposits				
Table 3.7	Spraying details for fabricating IN 718 thick pipe deposits				
Table 3.8	Levels of factors studied in cold spray deposition of IN 718				
Table 3.9	Design of experiments with VR calculated using CFD analysis	96			
Table 3.10	Design of experiments with <i>VR</i> calculated using CFD analysis Detail of meshes used in the three cold spray nozzles with different powder injection angle for grid independence study				
Table 3.11	Detail of mesh metrics in the three cold spray nozzles with different powder injection angle used in CFD simulation	105			
Table 3.12	Detail of discrete phase injection properties	106			
Table 3.13	Detail of nitrogen gas used as main and carrier gas	106			
Table 3.14	Detail of meshes used in the 30 deg powder injection cold spray nozzle with SS 304 substrate pipe for grid independence study	109			
Table 3.15	Detail of mesh metrics for the 30 deg powder injection cold spray nozzle with SS 304 substrate pipe used in CFD simulation				
Table 3.16	Detail of explicit impact modeling parameters for impact deformation analysis for single-particles and multi-particle of IN 718 powder	112			

	feedstock onto an SS 304 substrate		
Table 4.1	Microhardness, nanohardness, and elastic modulus data of the CSAMed Ni-20Cr thick plates in as-sprayed, substrate heated, and hotisostatic pressing treated conditions	138	
Table 4.2	Comparison of macro-tensile data of the CSAMed Ni-20Cr thick plates in as-sprayed, substrate heated, and hot-isostatic pressing treated conditions with that of bulk Ni-20Cr alloy	142	
Table 5.1	Analysis of variance	149	
Table 5.2	Model summary	150	
Table 5.3	Optimized solution sets for effective cold spray deposition of IN 718 powder feedstock	154	
Table 5.4	Velocity ratio for Inconel 718 particle size distribution	154	

Journals

- [J1] Singh, P., Singh, S., Singh, H., Calla, E., Grewal, H. S., Arora, H. S., & Krishnamurthy, A. (2023). Characterization and High-Temperature Oxidation Behavior of Ni–20Cr Deposits Fabricated by Cold Spray-Based Additive Manufacturing. *Coatings*, *13*(5), 904.
- [J2] Singh, P., Singh, H., Singh, S., Calla, E., Grewal, H. S., Arora, H. S., & Krishnamurthy, A. (2023). Development, Characterization and High-Temperature Oxidation Behaviour of Hot-Isostatic-Treated Cold-Sprayed Thick Titanium Deposits. *Machines*, 11(8), 805.
- [J3] Two-Level Full Factorial Design Approach for the Analysis of Velocity Ratio for Effective Cold Spray Deposition of Inconel 718. (Status: under preparation).
- [J4] Effect of Injection Angle on Powder Stream and Carrier Gas Characteristics in Cold Spray. (Status: under preparation).
- [J5] Discrete Phase CFD Analysis and Impact Deformation Studies of Cold Spray Deposition of IN 718 on SS 304 Substrate Pipe with Experimental Validation. (Status: under preparation).
- [J6] Development and Characterization of Seamless Inconel 718 Pipe using Cold Spray based Additive Manufacturing Process. (Status: under preparation).

Conference Proceedings

- [C1] Singh, S., Singh, P., Singh, H., & Buddu, R. K. (2019). Characterization and comparison of copper coatings developed by low pressure cold spraying and laser cladding techniques. *Materials Today: Proceedings*, 18, 830-840.
- [C2] Singh, P., Singh, S., & Singh, H. (2023). Flow Visualization and Parameter Suitability in Cold Spray Titanium Deposition: A CFD Approach. In *Advances in Manufacturing Technology XXXVI* (pp. 43-49). IOS Press.

LIST OF ABBREVIATIONS

Letters

Ag -silver

 $A(h_c)$ -contact area Al -aluminium

Al₂O₃ -aluminium oxide or alumina

C -carbon Co -cobalt

CO₂ -carbon dioxide CO_X -carbon oxides

Cp -specific heat capacity at constant pressure

Cr -chromium
Cu -copper

Dcritical -critical particle diameter

D₁₀ -diameter has ten percent smaller and ninety percent larger

D₅₀ -average size

D₉₀ -diameter has ninety percent smaller and ten percent larger

DeltaP -difference between carrier gas and main gas pressure

Dp -particle diameter

 E_{eff} -effective elastic modulus

F1 -empirical factor
F2 -empirical factor

Fe -iron

 F_1 -blending function

He -helium

IN 718 -inconel 718

k -turbulent kinetic energy K_p -parabolic rate constant

Mg -magnesium
Mn -manganese
Mo -molybdenum

 $egin{array}{lll} N_2 & -nitrogen \\ Nb & -niobium \\ Ni & -nickel \\ \end{array}$

Ni-20Cr -nickel-chromium alloy

P -phosphorus

 P_b -generation of turbulent kinetic energy on account of buoyancy

 P_k -generation of turbulent kinetic energy

R_a -average roughness

rpm -revolutions per minute

S -contact stiffness

S -sulfur Si -silicon

SiC -silicon carbide

 S_k -user-defined source term

SO_X -sulphur oxides SS -stainless steel

SST -shear stress transport

t -oxidation time

Ta -tantalum
Ti -titanium

Ti -impact temperature Tm -melting temperature Tr -reference temperature

V -critical velocity (Assadi et al. 2003)

Vcr -critical velocity (Schmidt *et al.* 2006) (please note that this critical

velocity will be referred in this study)

Verosion -erosion velocity

Vp -particle impact velocity at SoD (standoff distance)

VR -velocity ratio

W -tungsten

x -characteristic length

Y -yttrium

Zn -zinc

Zr -zirconium

Greek symbols

 β -Berkovich indenter constant

 ρ -density in kg/m³

 σy -yield strength

 σts -tensile strength

 Δt -characteristic time scale

 ΔW -mass change per total surface area

 γ'' -Ni₃(Nb, Al, Ti)

 γ' -Ni₃(Al, Ti)

 δ -Ni₃(Nb)

γ -solid solution matrix rich in Ni, Cr, and Fe

 λ -thermal conductivity

 ω -specific turbulent dissipation rate

 ϵ -turbulent dissipation rate

 σ_k -turbulent Prandtl number for turbulent kinetic energy

 μ_t -turbulent viscosity

 σ_{ω} -turbulent Prandtl number for specific turbulent dissipation rate

Abbreviations

AF -as-fabricated

ALE -arbitrary lagrangian eulerian

AM -additive manufacturing

AMed -additively manufactured

ANOVA -analysis of variance

APS -atmospheric plasma spray

AS -as sprayed

ASI -adiabatic shear instability

BCC -body-centered cubic

BCT -body-centered tetragonal

CAD -computer-aided design

CAGR -compound annual growth rate

CAM -computer-aided manufacturing

CD -convergent-divergent

CFD -computational fluid dynamics

CGDM -cold gas dynamic manufacturing

CGP -carrier gas pressure

CS -cold spray

CSAM -cold spray based additive manufacturing

CSAMed -cold spray based additively manufactured

DED -directed energy deposition

D-gun -detonation gun

DLD -directed laser deposition

DPM -discrete phase model

DRW -discrete random walk

EBAM -electron beam additive manufacturing

EBM -electron beam melting

EDS -energy dispersive spectroscopy

EOS -equation of state

FDA -food and drug administration

FEA -finite element analysis

FS -flame spray

HCP -hexagonal close-packed

HDPE -high-density polyethylene

HIP -hot isostatic pressing

HPCS -high-pressure cold spray

HT -heat treated

HVOF -high velocity oxy-fuel spray

LENS -laser engineering net shape

LMD -laser metal deposition

LPCS -low-pressure cold spray

LPPS -low-pressure plasma spray

MAM -metal additive manufacturing

MGP -main gas pressure

OFHC -oxygen-free high conductivity

PBF -powder bed fusion

PD -particle diameter

PDEs -partial differential equations

PEEQ -equivalent plastic strain

PFR -powder feed rate

PHed -pre-heated

PS -plasma spray

PU -polyurethane

RANS -Reynolds-averaged Navier-Stokes

SEM -scanning electron microscopy

SH -substrate heating

SLM -selective laser melting

SLS -selective laser sintering

SoD -standoff distance

TKE -turbulent kinetic energy

TLFA -two-level full factorial approach

TM -traditional manufacturing

TRL -technology readiness level

UTM -universal testing machine

UTS -ultimate tensile strength

VPS -vacuum plasma spray

WAAM -wire arc additive manufacturing

w-EDM -wire cut electric discharge machine

XRD -X-ray diffraction

3D -three dimensional

CHAPTER 1

INTRODUCTION

This chapter introduces additive manufacturing and examines its market size. It provides a detailed historical background on various additive manufacturing technologies. The overview of thermal spray processes is discussed, followed by the research motivation for this thesis. Additionally, a concise introduction to the cold spray-based additive manufacturing process and the Inconel 718 superalloy is included. The primary objective of the research work and the layout of the thesis are also outlined.

Manufacturing is crucial for turning raw materials into finished products, which fuels economic growth and fosters innovation across various sectors. Traditionally, manufacturing involved subtractive methods, where material was carved out from a solid block to create the desired shape. However, the introduction of additive manufacturing, or 3D printing, has changed how products are conceived, designed, and made.

Additive manufacturing constructs objects layer by layer, depositing material exactly where it's needed according to a digital plan. This method brings several advantages over traditional manufacturing. Firstly, it allows for the creation of highly detailed and complex shapes that would be difficult or impossible to achieve with subtractive techniques. Secondly, additive manufacturing reduces waste since it only uses the exact amount of material required, unlike subtractive methods which produce a lot of waste. Additionally, it speeds up the process of making prototypes and testing new designs, making it faster to bring products to market. Furthermore, additive manufacturing enables production on demand and locally, which could simplify supply chains and cut down on transportation costs.

On the other hand, traditional manufacturing has its own strengths, like being able to produce large quantities efficiently and having established methods for specific materials and industries. However, it might struggle to adapt to changes in design requirements or efficiently create custom or unique items.

As industries look for ways to be more efficient, flexible, and sustainable in manufacturing, the demand for additive manufacturing is increasing. Its ability to complement or even outperform traditional methods in terms of design flexibility, waste reduction, and adaptability makes it a major force driving innovation and competitiveness in manufacturing.

In 2023, the worldwide additive manufacturing market reached a valuation of USD 17.99 billion. Projections indicate that by 2033, it is anticipated to reach approximately USD 110.13 billion as

shown in Figure 1, reflecting a compound annual growth rate (CAGR) of 19.85 % between 2024 and 2033 (https://www.precedenceresearch.com/additive-manufacturing-market).

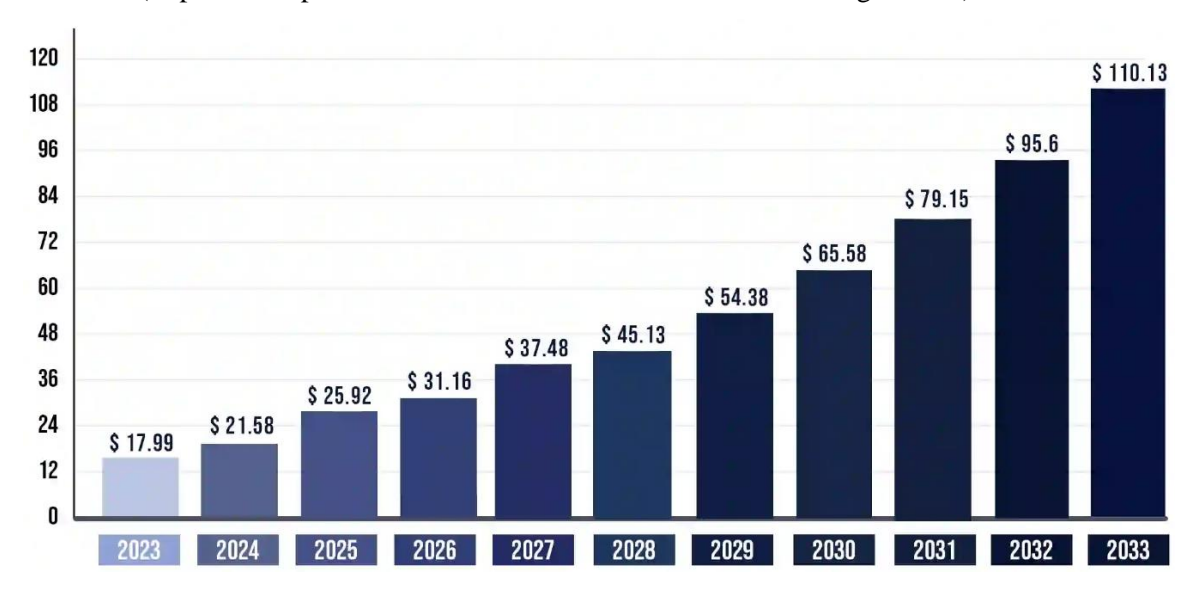


Figure 1.1 Histogram showing the additive manufacturing market size from the year 2023 to 2033 in USD Billion (https://www.precedenceresearch.com/additive-manufacturing-market)

The shipment of 3D printers worldwide totaled 2.2 million units in 2021, with an estimated surge to 21.5 million units by 2030. The market's expansion is attributed to escalating demand for prototyping solutions across diverse sectors, notably healthcare, automotive, and aerospace & defense. Furthermore, the sector's advancement is propelled by intensive research and development efforts in the realm of 3D printing technology.

1.1 HISTORICAL BACKGROUND OF ADDITIVE MANUFACTURING TECHNIQUES

A paradigm shift in the field of manufacturing resulted with the introduction of the concept of additive manufacturing (3D printing) in the late 20th century. Additive manufacturing (AM) involved a transition from the conventional material subtractive (removal) concept to developing integrated components and parts by assimilation of a layer in an incremental fashion (Gibson *et al.* 2021; Guo and Leu 2013). The progress in AM went through an exponential growth from development of stereolithography by Hull in early 1980's (Gibson *et al.* 2021; Hull 1986) to rapid prototyping and casting in early 1990s to use of AM fabricated parts for aerospace use in 2011 (Khorram and Nonino 2017). Compared to conventional manufacturing routes, AM presents many added advantages such as lowering the material wastage, facilitating the fabrication of specialized custom-based and complex components, smart structures and enhanced productivity. In the aviation sector, the use of additive manufacturing can significantly lower the buy-to-fly

ratio. For production of low to moderate quantities, additive manufacturing is a better alternative to existing conventional manufacturing methodologies (Ruffo *et al.* 2006; Hopkinson and Dicknes 2003). The components fabricated using AM technique finds application in almost all types of industrial sectors such as aviation, automobile, energy, healthcare and medical, and oil and gas (Melchels *et al.* 2012). Few examples include, fuel nozzles for aero-engines by General Electric (GE), printing of dental implants and custom prosthetics (Gross *et al.* 2014), tissues, and organs (Schubert *et al.* 2014), customized bicycle components by Raceware Direct, U.K., 15 % saving in energy used in pumping prompted by the new filter design realized by AM for Croft Filter, U.K (Guddati *et al.* 2019). Recently, the U.S. Food and Drug Administration (FDA) approved the 3-D printed pills for treatment of epilepsy. Numerous other examples can be found in (Guo and Leu 2013). Further avenues for AM also include, food processing, and building industry. In Spite of early success, some industries such as Rolls Royce and the nuclear sector have shown some caution for AM considering the lack of research on process and property evaluation related to safety standards (Guo and Leu 2013; Guddati *et al.* 2019).

Among the different variants of AM, commonly used techniques for metals are powder bed fusion (PBF) and direct energy deposition (DED) (Gibson et al. 2021; Guo and Leu 2013; Levy 2010). The prime difference among the two processes is the method of material deposition. In former method, which includes selective laser sintering (SLS)/selective laser melting (SLM), and electron-beam melting (EBM) process the material is deposited in layers followed by consolidation though melting, whereas, in latter method, powder is directly infused into the continuously tracking energy source (eg. laser or electron-beam). Numerous investigations have been reported using either the laser, electron-beam and/or their variants for AM. Murr et al. (2012) reported the results on the several metals and alloys fabricated using laser and electronbeam based AM processes. Among the investigated materials, hardness of the fabricated freeforms was almost similar as derived from both the techniques. However, they were slightly on a lower side in comparison to their wrought and cast counterparts. Highly directional microstructure in many of these developed free-forms with columnar grains were also observed (Murr et al. 2012). Biamino et al. (2011) used EBM to produce dense Ti-based alloy free-form with a porosity content lower than hot-isostatic process. Further, the use of EBM for developing free forms from intermetallic γ-TiAl alloy with high hardness and yield strength was also reported (Murr et al. 2010). However, large amounts of un-melted and partially melted particles along with significant porosity content were detected. Spherical pores with entrapped Ar gas (used for protective environment) were also observed. Lima and Sankare (2014) prepared high aspect-ratio AISI SS316 steel structures using laser-based DED technique. The fabricated structures showed

tensile and flexural strengths (along the build-up direction) similar to the wrought steel, however, the elastic modulus was significantly lower which might be attributed to the presence of cracks, pores and oxidation of the powder particles. Further, these dissimilarity in the elastic modulus might also be the effect of anisotropic microstructure and the presence of high tensile residual stresses playing a dominant role, especially for the high aspect-ratio structures, as also reported by Kahlen and Kar (2001, 2001). Another study (Ma et al. 2013) also reported similar tensile and yield strengths, however, the ductility was significantly reduced from 50 % to 20 %. Dadbakhsh et al. (2012) observed mechanical properties of the fabricated structures are directly related to the thermal residual stresses and bonding strength of the particles. Shah et al. (2014) investigated the effect of process parameters for laser-based DED on microstructural, mechanical, and wear properties of functionally graded materials. The powder flow-rate and energy density were observed to exhibit profound influence on the mechanical strength, hardness and wear resistance. However, Zhang et al. (2014), reported, scan velocity to be a critical parameter controlling the microstructure and mechanical properties, with effect of energy density being minimal. Presence of highly aligned dendritic structure in columnar grains imparts the anisotropic structure in a build-up direction. The orientation and shape of grains is a direct function of the solidification velocity and temperature gradient. Few researchers (Kruth et al. 2004; Osakada and Shiomi 2006) also reported presence of around 10 % porosity for SLM processes even under optimized input power.

The dimensional accuracy of the fabricated parts is also an important parameter. Gu *et al.* (2012) produced near-net-shape products using lasers with a resolution of 130 µm and 400 µm in the scan and build-up directions, respectively. With highly optimized process parameters, Yang *et al.* (2012) attempted to contain the dimensional accuracy of fabricated dental brackets with maximum error compounding to around 38 %. Dimensional distortion and reduced crack-resistance due to residual tensile stresses have been a major concern with SLM and EBM (Kruth *et al.* 2004; Shiomi *et al.* 2004). To confront the problem of cracking and distortion, Abe *et al.* (2001), used dual lasers to modulate residual stresses. Among all the tested configurations, maximum bending strength was observed with positive beam-offset configuration (consolidation with main laser followed by re-melting with another tracing laser). Further, the effects of annealing and heat-treatment were also investigated, however, all the above-mentioned strategies were not able to completely eliminate the residual tensile stresses (Shiomi *et al.* 2004).

The productivity in laser-based systems depends upon the thermal conductivity of the material for a given laser power. Thus, for metals with high thermal conductivity, inadequate melting is often reported. Issues such as uncontrolled melting and fusion of adjacent powder particles were also

reported (Yadroitsev et al. 2007). The problem significantly amplifies in the case of multicomponent systems (Kruth et al. 2004). The difference in the thermal conductivities/absorptivity of the constituent materials in an alloy result in dissimilar melting. Further, fabricated materials using DED processes also face issues such as balling which likely originates due to flow of liquid metal from the melt pool as a result of surface tension (Kruth et al. 2004; Abe et al. 2001; Agarwala et al. 1995). Rombouts et al. (2006) and Chandrasekhar et al. 2013 also discussed the role of surface tension on balling-effect through Rayleigh instability (Rayleigh et al. 1892) and Marconi convection. Comparatively, balling-effect and the associated problems are avoided in solid-state processes such as cold spraying with no melting of the particles involved. Other problems with laser-based systems include propensity to oxidize, high laser reflectivity of metal powders, distorting due to residual stresses that make them significantly more difficult to process than polymers (Guo and Leu 2013; Kruth et al. 2004). Issues such as moderate to poor surface finish, moderate surface resolution, and limitation to conductive materials have been reported for electron-beam based DED. The expulsion of the powder particles due to the repulsive force of negatively charged particles exceeding the gravitational forces, can be a serious issue for fine powders. The accumulated negative charge also tends to repel the incoming electron beam, resulting in a diffused beam (Gibson et al. 2021).

Thermal spraying is a competitive and an established method for layer-by-layer. The potential benefits of thermal spraying have been explored by few researchers for AM. Li *et al.* (2007) reported use of thermal spraying for fabricating the strain gauge for use under high-temperature and harsh working conditions. Longtin *et al.* (2004) successfully demonstrated the use of plasmabased thermal spraying for manufacturing the capacitors, resistors, and sensors with feature resolution of 200 µm.

Cold spray (CS), a derivative of the thermal spraying is a solid-state process and offers numerous benefits over the conventional thermal spraying systems such as plasma, flame and oxy-fuel spray particularly because of its low working temperature (melting of material is avoided) and high kinetic energy of the powder particles (Pattison *et al.* 2007). These operational differences lower the possibility of oxidation of particles (enhancing the splat bonding), porosity content, and leads to refined microstructure. Use of cold spraying provides the benefit of depositing temperature-sensitive material (nanocrystalline and amorphous) and those prone to oxidation (Sova *et al.* 2013). In comparison to the other AM processes, the material deposited using cold spraying has good bonding and high-strength (higher than wrought) due to work-hardening (Lynch *et al.* 2013). Cold spraying has an edge over other AM processes (PBF and DED) and thermal spraying such as HVOF and plasma spraying, due to absence of tensile residual stresses originating from

unavoidable thermal history in these AM processes which lowers the crack resistance of the structure, initiates unwanted phase transformation and geometric distortion (Pattison *et al.* 2007; Champagne and Helfritch 2015; Cavaliere 2014; Devasenapathi *et al.* 2002; Stokes and Looney 2001; Amon *et al.* 1993).

Only a few studies have explored the possibility of use of thermal spraying for AM (Li et al. 2007; Longtin et al. 2004; Stokes and Looney 2001; Patel et al. 2010; Sampath et al. 2003) and those using cold spraying are even smaller (Pattison et al. 2007; Sova et al. 2013; Cavaliere 2014; Cadney et al. 2008; Ortega et al. 2015). Blose et al. (2006) recommend use of cold spraying for costly and difficult to machine materials such as Ti and its alloys. Further post-processing using hot-isostatic pressing helped increase the strength and ductility of the as-sprayed material. Heating the powder was also effective in controlling the porosity. Hall et al. (2006) and Eason et al. (2011) fabricated free-form structures from Al (1 cm thick) and Cu (2.5 cm thick) with high densities (>99.9 %) and tensile strength significantly higher than wrought and cold rolled counterparts (Eason et al. 2012). It was concluded that deposits with small sized particles show higher ductility compared to deposits from coarse powders. The high-impact velocities in cold spraying significantly refined the microstructure compared to the feedstock powder, with nanosized grains observed adjacent to splat boundaries (Eason et al. 2012). The corrosion of the Cu free-forms was also found to be similar to the forged Cu (Choi et al. 2010). Cadney et al. (2008) also explored the possibility of using cold spraying for AM using Zn to develop free-form structure. Pattison et al. (2007) discussed the strategies and possibilities of using cold spraying in combination with real-time machining for fabricating different shapes, and multi-material components using AM.

Although some understanding of the CS process for AM has been developed over a period of time, significant challenges still persist and need to be explored fully for its successful implementation. The type of bonding in the fusion zone of the inter-particle bonding and the dynamic recrystallization therein, and the delamination (crack-growth) process during degradation process through this refined region are few aspects needing attention.

Welding and processing of many materials such as Ti, Cu and Mg etc. are difficult owing to their affinity to oxidation. Thus, cold spray based additive manufacturing presents an ideal alternative to the other manufacturing processes including laser (Pattison *et al.* 2007; Sova *et al.* 2013; Eason *et al.* 2011). The fabrication of materials with high thermal conductivity and reflectance is also a challenging task for SLM and EBM processes, whereas cold spraying is free from such limitations (Thompson *et al.* 2015; Romano *et al.* 2015). Further, compared to laser-based DED processes with its high energy consumption per kg, and high airborne emission of CO₂, SO_x and

NO_x in case of flame and oxy-fuel spray (Thompson *et al.* 2015; Morrow *et al.* 2007), the cold spray is a potential eco-friendly alternative (Villafuerte 2010; Helfritch *et al.* 2015). Cold spraying is also a potential technology for processing difficult to machine materials.

Inconel 718 (IN 718), a nickel-chromium-iron superalloy, is renowned for its exceptional mechanical properties at elevated temperatures, making it a prime choice for demanding applications in aerospace, gas turbines, and nuclear reactors. Its composition allows it to maintain high strength, creep resistance, and fatigue resistance up to 700 °C. However, conventional manufacturing methods face challenges such as tool wear and limited material removal rates, highlighting the need for advanced manufacturing techniques that can effectively address these issues.

AM techniques like SLM and EBM are increasingly employed to produce IN 718 components with unique microstructures. These methods, however, often induce thermal stresses and can lead to the formation of undesirable high-temperature phases, compromising the alloy's mechanical integrity. To mitigate these effects, post-processing treatments such as hot-isostatic pressing (HIP) and solution aging are essential for optimizing microstructure and mechanical properties by promoting uniform alloy distribution and eliminating internal porosity. Yet, even with these treatments, challenges remain, including anisotropic mechanical properties and reduced fatigue performance compared to wrought alloys.

In this context, CS technology emerges as a particularly advantageous alternative for depositing IN 718 coatings or developing 3D standalone components. Unlike traditional thermal spray methods such as atmospheric plasma spray (APS) and high velocity oxy-fuel (HVOF), which typically result in high porosity levels (2.2 % to 3.2 % for APS and 0.5 % to 2.2 % for HVOF), cold spray leverages the kinetic energy of metallic powders propelled by pressurized inert gasses. This method minimizes thermal input, thereby avoiding the thermal degradation and unwanted phase transformations that are especially problematic for high-temperature alloys like IN 718. As a result, cold spray coatings exhibit significantly reduced porosity, often below 2 %, and superior mechanical properties, including adhesion strengths exceeding 900 MPa after heat treatment.

Furthermore, cold spray offers unique benefits for IN 718 that differentiate it from other additive techniques like PBF or DED. While PBF and DED can generate complex geometries and intricate designs, they are also prone to thermal-induced stresses and phase segregation due to high processing temperatures. Cold spray, by contrast, maintains a low-temperature deposition environment that promotes a refined microstructure with improved mechanical properties, including high bonding strength and lower residual stresses. These attributes are particularly advantageous for applications requiring high thermal stability and integrity.

By optimizing process parameters, cold spray can achieve mechanical properties comparable to those of bulk IN 718 materials, making it an effective and reliable technique for high-performance applications in temperature-sensitive environments. Ultimately, the adoption of cold spray technology for IN 718 coatings or standalone not only enhances the material's performance but also contributes to more sustainable manufacturing processes by reducing energy consumption and emissions. This positions cold spray as a leading solution for the deposition of high-temperature alloys, offering a compelling alternative to traditional and other additive manufacturing methods.

1.2 OVERVIEW OF THERMAL SPRAY MARKET

As of 2023, the global thermal spray market is valued at USD 10.46 billion and is projected to grow at a compound annual growth rate (CAGR) of 4.8 % from 2024 to 2030 (https://www.grandviewresearch.com/industry-analysis/thermal-spray-coatings-market).

Figure 1.2 illustrates the market share distribution among various coating technologies, with traditional methods such as plasma spray, flame spray, and HVOF leading the market. These techniques are popular due to their wide range of applications, such as ceramic coatings (plasma spray), cost-effectiveness (flame spray and HVOF), and widespread availability across many countries (Viswanathan et al. 2021).

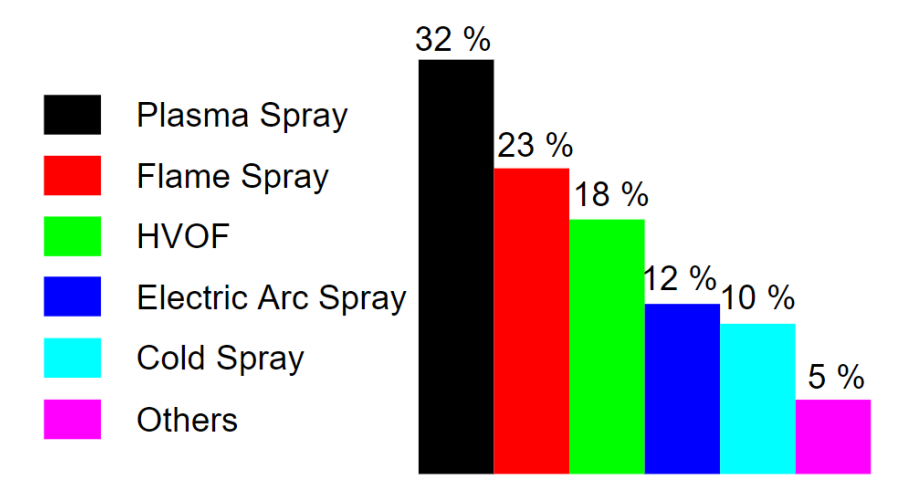


Figure 1.2 Histogram depicting market share distribution among various coating methods (Viswanathan et al. 2021)

CS, a relatively new technology, has captured a 10 % market share, primarily driven by its applications in the transportation, utility, and electronics sectors, as shown in Figure 1.3.

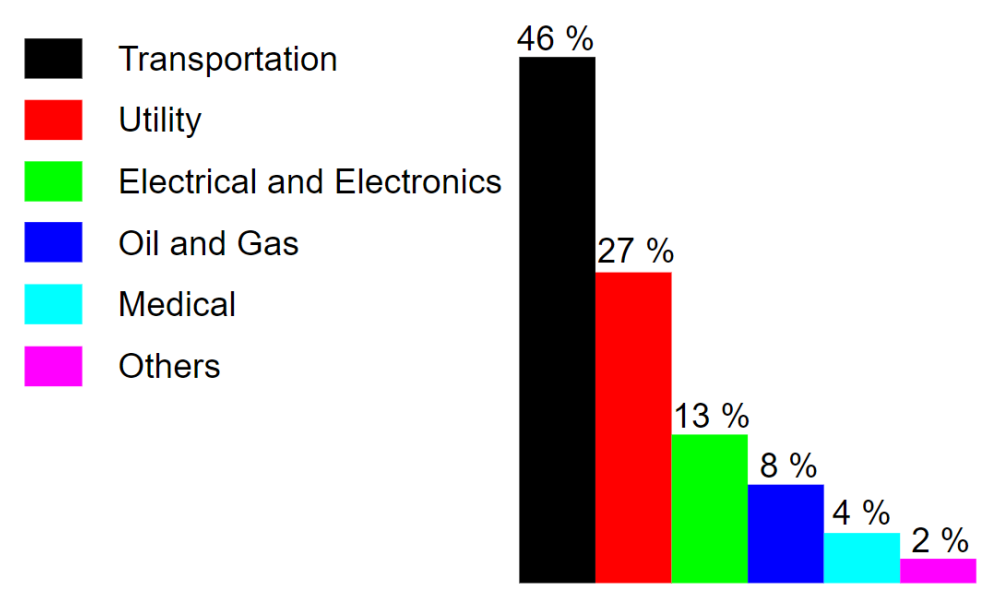


Figure 1.3 Histogram showing cold spray market share in various sectors (Viswanathan et al. 2021)

The major markets for CS are currently in North America and Europe. However, growing demand from other regions is expected to increase its market share in the coming years (Viswanathan et al. 2021).

The global cold spray technology market was valued at USD 943.5 million in 2022 and is projected to grow at a compound annual growth rate (CAGR) of 6.5 % over the forecast period. The increasing demand from the aerospace industry, particularly for repairing lightweight alloys, is expected to drive market growth. Additionally, the expanding electrical and electronics sector in the Asia Pacific region will boost demand. In 2021, the aerospace and defense industry reported total revenues of USD 892 billion, a 2.1 % increase from 2020, with a 11.2 % rise in exports. The aluminum segment led the market in 2022, accounting for 30.6 % of global revenue. Cold sprayed aluminum alloys, including aluminum-silicon alloys, are notable for their high strength, low thermal expansion, and excellent anti-friction properties.

Copper cold spraying is valued for its superior thermal and electrical conductivity, ductility, corrosion resistance, and wear resistance, making it essential in industries such as machinery, electronics, electric power, and energy.

Cold sprayed nickel and its superalloys offer significant benefits, including resistance to hot gasses, energetic material coatings, and high-temperature corrosion. Their diverse capabilities make it suitable for applications in aerospace, automotive, glass, medical, agricultural, roller mills, hydraulic pumps, and component repair industries, driving demand for nickel materials. The titanium segment is anticipated to exhibit a CAGR of 7.5 % during the forecast period.

Titanium is widely used in petroleum, aviation, chemical, medical, sports equipment, construction, aerospace, and automotive industries due to its high strength, excellent biocompatibility, superior corrosion resistance, and low density (https://www.grandviewresearch.com/industry-analysis/cold-spray-technology-market-report).

1.3 RESEARCH MOTIVATION

In simplest terms, Additive manufacturing (AM) is layer by layer building of 3 dimensional components using model data in contrast to material removal by conventional processes such as machining. AM is considered to be one of the most significant developments in manufacturing technologies. It has evolved as a promising technology for synthesizing specialized and complex geometries with reasonable production volume and reduced production time. Looking at the temporal evolution, selective laser sintering (SLS) evolved as the first metal based additive manufacturing technology for a wide range of materials. Selective laser melting (SLM) was developed in an effort to eliminate post-processing of SLS fabricated components. In addition to laser based processes, quite a few other techniques were developed such as electron beam melting and ultrasonic consolidation (Kruth et al. 1998; Gibson et al. 2021; Murr et al. 2012; Bartkowiak et al. 2011). However, these techniques were not able to attract significant importance due to inherent limitations of poor surface quality and low production volumes. Laser based techniques continue to remain at the forefront of additive manufacturing for about a decade due to better process control, superior surface finish and high production volume. Looking on the other side, laser based processes for additive manufacturing have some serious limitations which need immediate cross-examination. Some of these limitations are listed below:

- Since laser based techniques involve melting of powder constituents and their resolidification, significant residual stresses are generated within a splat as well as at intersplat boundaries. Such residual stresses, generated due to sharp thermal gradients are
 likely to deteriorate the mechanical behavior of laser processed components through
 crack initiation and propagation
- Complete consolidation of powders using laser based technology is highly unlikely.
 Powder compaction and consolidation is solely based on temperature dependent diffusion between powder particles rather than driven by any mechanical or gravity forces (Kruth et al. 2007). Lack of efficient consolidation can result in significant pores in fabricated components which makes post-processing nearly inevitable.
- Controlling the flow of liquid metal during laser-based processing is also challenging.

 When a layer of metal solidifies, the curvature on the upper surface can be problematic

for the wetting of subsequent layers and weakens the interface properties. Due to application of high temperature, oxygen contamination is another major concern during laser based manufacturing processes (Kruth *et al.* 2007). Trapped gasses in the powder bed can also interfere with powder consolidation.

• Uncontrolled heat transfer is another major issue for laser based manufacturing, especially when high conductivity powders are used (Kruth *et al.* 2007). The rapid diffusion of heat melts the adjacent material contributing to the distorted geometry. On the other hand, issues related to non-uniform heating may arise when mixtures of different powders with a wide range of thermal conductivity and/or melting temperatures are used. It may lead to vaporization of low melting point material while the constituent with high melting point may remain un-melted.

Thermal spraying with its enriched armory of a range of material deposition processes, is a viable and attractive alternative to the present technologies used in AM. With its advent in the early 20th century, thermal spraying has evolved in both capacity and capability and can potentially be used for depositing all classes and forms (powder, wire) of materials (Pawlowski 2008). The major advantages envisioned with the utilization of thermal spraying in AM includes high deposition rates, no restriction on material that can be sprayed, high kinetic energy of the sprayed materials (highest amongst all known deposition techniques) imparts high structural strength due to induced plastic deformation (Gibson *et al.* 2021; Pattison *et al.* 2007). Attributed to its layer-by-layer building characteristic, thermal spraying may also be considered as an additive manufacturing technique.

Thermal spray techniques reliant on melting, such as plasma spraying, high velocity oxy-fuel spraying, wire flame spraying, powder flame spraying, and detonation spraying, confront several inherent constraints. Firstly, the elevated temperatures involved in melting the feedstock can induce substantial heating of the substrate, potentially causing thermal stress, distortion, or even damage to materials sensitive to heat. Additionally, certain materials may undergo degradation or chemical alterations when subjected to high temperatures, thereby jeopardizing their properties and performance. Moreover, melting processes can give rise to coating porosity, attributable to gas entrapment or incomplete fusion of particles, thereby diminishing coating density and potentially compromising functionality. Furthermore, not all materials are conducive to melting and spraying due to factors such as melting points, thermal characteristics, or chemical reactivity. This limitation may result in uneven melting or phase changes that impair coating quality. Thickness control poses another challenge, as melting processes may struggle to consistently regulate coating thickness, leading to variability that could impact the performance of coated

components. Certain substrate materials, particularly those with low melting points or susceptibility to heat, may not be compatible with thermal spray techniques reliant on melting. Environmental concerns also arise, as melting processes necessitate high-energy heat sources, contributing to energy consumption and emissions of pollutants or greenhouse gasses. Moreover, the complexity and cost of thermal spray equipment for melting processes pose additional hurdles. "Cold spraying" is the most recent entrant to the list of thermal spray techniques. The basic principle of cold spraying technique is to plastically deform the powder particles at relatively much lower temperatures. The metal powder particles are added to the stream of inert gas flowing through a nozzle resulting in supersonic velocities. On account of supersonic velocities in CS, there is increased inter-lamellar cohesion which reduces porosity and lower particle temperatures result in absence of material oxidation or phase altercations. In CS, as the particle velocity exceeds a critical value, the massive particle impact causes rupture of the oxide layer on the substrate surface. This facilitates intimate contact between the powder particle and the substrate under high localized pressure resulting in strong atomic bonds (Pattison et al. 2007). Contrary to other thermal spray techniques, cold spraying operates at significantly low temperatures which enables the development of thick coatings and complex freestanding shapes (Pattison *et al.* 2007).

Recently, by integrating the additive characteristics of CS with the subtractive capabilities of high-speed machining, a novel process was devised for swiftly producing functional engineering components from a variety of materials. This innovative technique is referred to as cold gas dynamic manufacturing (CGDM) (Pattison *et al.* 2007). Comparison of CGDM with cold spray and other additive manufacturing techniques is shown in Figure 1.4.

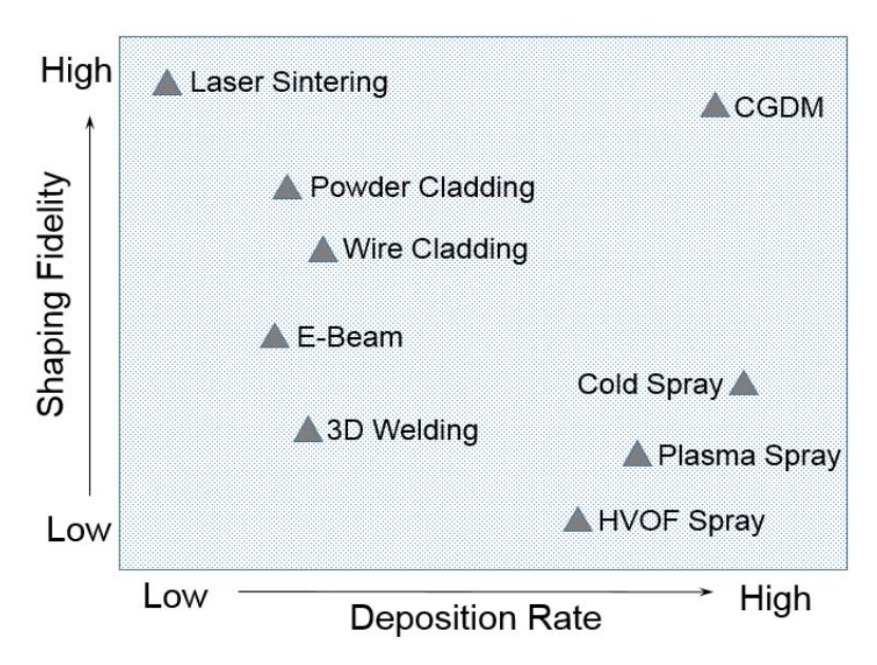


Figure 1.4 Comparison of cold gas dynamic manufacturing with cold spray and other additive manufacturing techniques (Pattison *et al.* 2007)

It can be seen that cold spray technique and CGDM definitely offers high flexibility in terms of fabricating complex shapes with significantly high productivity. CGDM offers noteworthy advantages over laser-based techniques used for additive manufacturing. Since the temperatures involved are low, the components synthesized using CGDM are not subjected to thermal stresses. The microstructure of components synthesized using CGDM is likely to be more homogeneous and refined owing to high strain plastic deformation and absence of high temperature. Powder compaction is driven by high external pressure rather than high temperatures which promotes development of highly dense components. In addition, problems arising due to mismatch of thermal conductivity and melting temperature between different powder constituents can also be avoided.

In the evolving landscape of additive manufacturing (AM), cold spray (CS) technology stands out as a relatively new and promising process. Unlike traditional AM methods that often rely on high-temperature operations, CS operates at much lower temperatures, harnessing the kinetic energy of metallic powder particles propelled at supersonic speeds through an inert gas stream. This unique feature of cold spray provides several unparalleled advantages, making it a strong candidate for the development of advanced industrial components. Despite its potential, the industrial-scale application of cold spray, especially for producing components in fields such as energy, aviation, oil and gas, locomotives, and healthcare, remains underexplored. For this technology to be a viable solution at an industrial level, a deeper understanding of its process parameters,

microstructural evolution, mechanical behavior, and degradation under simulated conditions is essential.

The motivation for this research stems from the challenges associated with manufacturing high-performance components from IN 718, a nickel-based superalloy renowned for its exceptional high-temperature strength, creep resistance, and fatigue performance. These properties make IN 718 indispensables for critical applications in the aerospace, energy, and power generation sectors. However, traditional manufacturing methods for IN 718 face significant challenges:

- 1. Machining Difficulties: The hardness and high strength of IN 718 cause rapid tool wear, making machining costly and time-intensive.
- 2. Thermal Processing Issues: Processes involving high temperatures can lead to the formation of unwanted acicular δ -phases, which embrittle the material and degrade mechanical properties.
- Phase Segregation: The non-uniform distribution of elements such as niobium can result
 in localized phase transformations, compromising the alloy's mechanical behavior and
 overall performance.

These challenges necessitate the exploration of alternative manufacturing methods capable of producing IN 718 components with precision and reliability. Cold spray technology presents itself as a compelling solution. The proposed research seeks to bridge critical scientific gaps to position cold spray as a viable additive manufacturing process for industrial-scale applications. This will involve a detailed parametric study to optimize IN 718 deposition, advanced CFD modeling of gas flow field simulations and particle trajectory analyses onto an SS 304 substrate, and the development of fully dense, standalone IN 718 components. Through comprehensive characterization of their microstructural and mechanical properties, this research will propel cold spray into the forefront of AM technologies, making it an important tool for complex industrial applications.

1.4 COLD SPRAY BASED ADDITIVE MANUFACTURING

CS technology has traditionally been utilized as a high-volume coating method for applications such as thick coating deposition, corrosion protection, and dimensional restoration and repair. Its ability to create highly dense deposits without theoretical thickness limits positions CS as a promising technique for AM. When compared to conventional powder bed fusion methods like selective laser melting/sintering (SLM/SLS), direct energy deposition (DED), and electron beam melting (EBM), CS offers several distinct advantages for AM applications as discussed in the previous section. With the help of the current state-of-the art robotic arm manipulators, multiple

scanning strategies can be adopted as per requirement to improve the deposition accuracies. Employing more than one manipulator further increases design flexibility, enabling the fabrication of complex 3D components.

The cold spray based additive manufacturing (CSAM) system is illustrated in Figure 1.5, which begins with highly pressurized gas, typically nitrogen (N₂) or helium (He), stored in cylinder pallets. This gas serves both as the main and carrier gas.

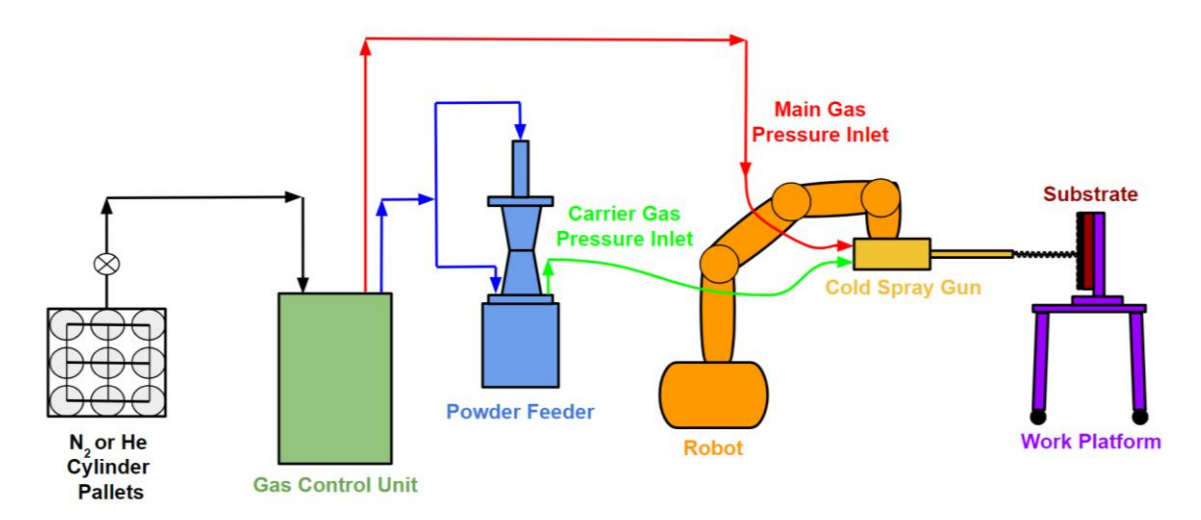


Figure 1.5 Schematic representation of cold spray based additive manufacturing system

Within the gas control unit, the gas is split into two streams: one is directed to the cold spray gun where it is heated by an internal heater, and the other is sent to the powder feeder. The powder particles are transported to the convergent-divergent nozzle by the carrier gas, which remains at ambient temperature. As the gas exits the De Laval nozzle, it accelerates the powder particles to supersonic speeds, causing them to impact the target substrate on the work platform with high velocity. The CS gun is mounted on a robotic arm which is programmed to maneuver along the desired path (Patel et al. 2021). The substrate fixed on the tilting turntable (or work platform) further adds to the degree of freedom of the CSAM system.

Recent research has investigated the use of CS technology in additive manufacturing, focusing on materials such as nickel-aluminum, pure aluminum, zinc, and titanium alloys. However, there is still limited data on the microstructural and mechanical properties of freestanding objects created using CS. Traditionally, CS deposits have been used in non-structural applications. As CS technology progresses towards producing load-bearing structural components, it is essential to validate the performance of CS deposits under both static and cyclic loading conditions.

1.5 INCONEL 718 SUPERALLOY

Inconel 718 (IN 718) is precipitation-hardened nickel-chromium-iron based superalloy modified with niobium known for its exceptional mechanical properties across a wide range of temperatures. IN 718 demonstrates outstanding tensile, fatigue, creep, and rupture strength, coupled with excellent resistance to corrosion and oxidation (Alkhimov et al. 1994; Kosarev et al. 2003). The microstructure of IN 718 comprises a γ solid supersaturated solution matrix abundant in Ni, Cr, and Fe, along with precipitates of coherent phases such as metastable γ'' Ni₃(Nb, Al, Ti) and γ' Ni₃(Al, Ti). δ stable phase Ni₃(Nb) is an important precipitating phase for the IN718 alloy which is incoherent with the γ fcc matrix. After heat treatment, precipitation and elongation of the δ phase happen, replacing the γ'' phase near grain boundaries due to high Nb concentration. This process is crucial for controlling grain growth and enhancing mechanical properties (Grujicic et al. 2004; Pattison et al. 2007; Gilmore et al. 1999; Dykhuizen and Neiser 2003). IN 718 poses formidable challenges across various aspects of its processing using conventional methods, including excessive tool wear, work hardening, low material removal rates during room temperature machining. Additionally, high-temperature forming processes may encounter difficulties due to segregation of refractory elements such as Nb and Mo (Li and Li 2005; Grujicic et al. 2003). Segregation of niobium during high-temperature production results in Laves phase formation. Laves phase undermines material strength, ductility, fatigue, and creep rupture properties by depleting essential elements for precipitation strengthening and promoting crack initiation and propagation (Sonar et al. 2021). The necessity for employing advanced manufacturing techniques becomes even more apparent when fabricating components made from IN 718 superalloy.

1.6 MAIN AIM OF THE RESEARCH WORK

The research explores cold spray technology across multiple objectives. It begins by establishing the viability of cold spray in additive manufacturing through the fabrication of thick deposits using challenging materials like pure titanium and Ni-20Cr alloy. Various pre- and post-heat treatment operations are performed on these thick deposits. Microstructural characterization, mechanical properties evaluation, and high-temperature cyclic oxidation studies help to understand the structure-property relationships. Further studies optimize cold spray parameters for specific materials, such as the IN 718 superalloy, focusing on pipe fabrication. Computational modeling and experimental validation reveal the effects of injection angles on cold spray performance, powder particle attributes, and gas dynamics during deposition. Finally, the fabrication of a 3D standalone pipe demonstrates the capability of cold spray to produce

components with dense structures, minimal porosity, and mechanical properties that closely resemble bulk materials. Overall, the research highlights cold spray as a promising additive manufacturing technology, offering significant advantages in production efficiency and component quality.

1.7 THESIS LAYOUT

The thesis is organized as shown in Figure 1.6.

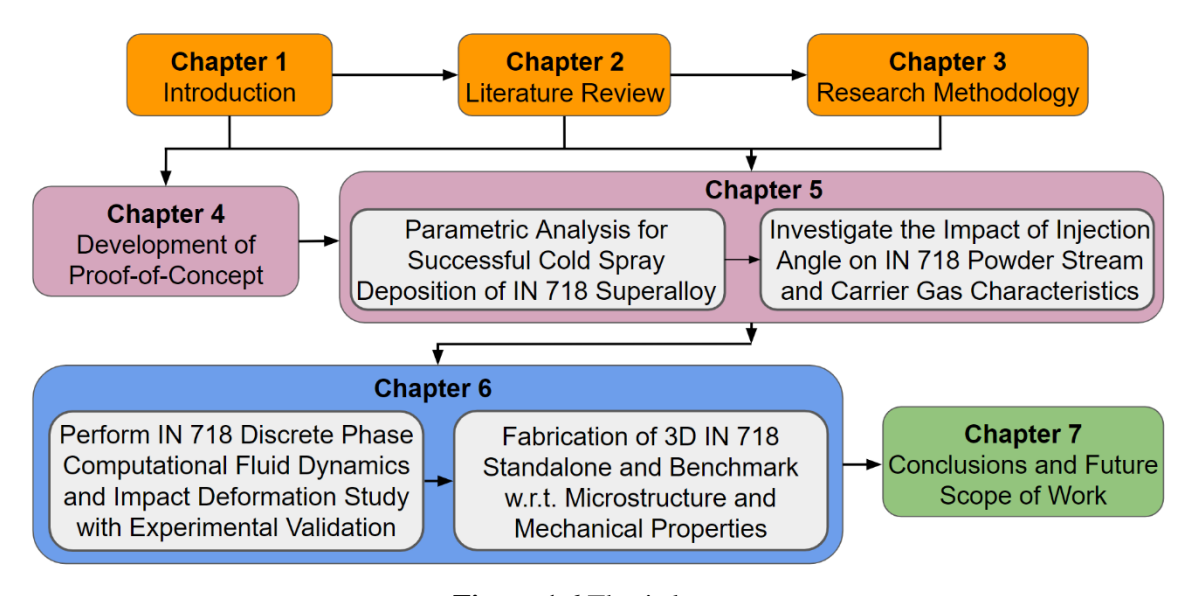


Figure 1.6 Thesis layout

The research aims to assess the potential of cold spray technology in additive manufacturing, focusing on fabricating thick deposits and pipe of challenging materials.

Chapter 1: Introduction

This chapter establishes the groundwork for the thesis, presenting background context, introducing primary subjects, elucidating the inspiration for conducting the research, outlining clear objectives, structuring the thesis, and emphasizing significant contributions.

Chapter 2: Literature Review

This chapter provides a methodical assessment of previous endeavors in additive manufacturing with a focus on difficult-to-process materials, covering a range of additive manufacturing technologies. Additionally, it investigates current research into computational fluid dynamics (CFD) analysis of the cold spray process and studies concerning particle impact deformation, identifying significant gaps in research. Utilizing these identified gaps, research objectives are formulated.

Chapter 3: Research Methodology

This chapter outlines a systematic methodology employed to attain the specified objectives, presented in a stepwise manner.

Chapter 4: Establishing Cold Spray based Additive Manufacturing Process for Fabricating Thick Standalone Geometries: A Proof-of-Concept Study

In this chapter, we aim to demonstrate the feasibility of cold spray technology for additive manufacturing of challenging materials like pure Ti and Ni-20Cr alloy. By employing pre- and post-heat treatment procedures, we examine their impact on structure-property relations. Thick layers ranging from 6 to 16 mm are fabricated through high-pressure cold spray process and compared with conventional as-cast counterparts. Successful deposition of these thick layers highlights the potential of cold spray in additive manufacturing.

Chapter 5: Parametric Analysis for Successful Cold Spray Deposition of IN 718 Superalloy

The first part of the chapter rigorously explores various cold spray process parameters at both low and high levels using a comprehensive full factorial two-level approach to pinpoint optimized parameters for effective IN 718 depositions. Cold spraying high-strength materials like IN 718 poses challenges due to limited deformability, impacting coating quality.

In the subsequent part, we examine how different injection angles (90 deg, 30 deg, and 0 deg) affect the performance of a cold spray process using IN 718 powder particles and nitrogen gas. We use computational modeling, including gas flow field simulations and particle trajectory analyses, to understand the influence of angle on the process. The chosen turbulence model, k- ω SST, accurately describes turbulent flows, making it suitable for capturing gas-particle interaction dynamics.

Chapter 6: Discrete Phase Computational Fluid Dynamics with Impact Deformation Studies of Cold Spray Deposition of IN 718 and Fabrication of 3D IN 718 Standalone and Benchmark wr.t. Microstructure and Mechanical Properties

In the first part, we conduct a discrete phase computational fluid dynamics analysis to simulate gas dynamics and particle behavior during cold spray deposition of IN 718 powder feedstock onto an SS 304 substrate pipe. We determine the average velocity and temperature of the powder particles for establishing boundary conditions in impact deformation studies. The single- and multi-particle impact deformation results closely align with the microstructure of cold spray additively manufactured (CSAMed) IN 718 deposits.

In the next chapter, we use optimized cold spray and robot parameters, along with tilting turntable settings, to fabricate a 3D standalone pipe. The resulting IN 718 thick pipe deposits measure 6 inches in length, with a nominal bore of 60.3 mm and a thickness of 5 mm. Microstructural analysis reveals dense structures with minimal porosity. CSAMed IN 718 thick pipe deposits exhibit density, microhardness values and mechanical properties similar to bulk IN 718, with no oxide formation observed in the deposits. Additionally, all phases identified in the powder feedstock are retained in the deposit, indicating no phase transformation during the cold spray process. These findings suggest that cold spray has the potential to replace conventional methods in manufacturing IN 718 pipes.

Chapter 7: Conclusion and Future Scope

In this chapter, we present the conclusions drawn from the current research study and offer insights into potential directions for future research endeavors.

CHAPTER 2

LITERATURE REVIEW

This chapter provides an extensive examination of metal additive manufacturing technologies, emphasizing directed energy deposition (DED) and powder bed fusion (PBF). It also discusses thermal spray based techniques such as arc spray (AS), flame spray (FS), plasma spray (PS), detonation gun (D-gun) spray, high velocity oxy-fuel (HVOF) spray, and cold spray (CS), with a special focus on cold spray based additive manufacturing (CSAM). Key factors in CSAM, such as propulsive gas conditions (pressure, temperature, type), powder feeder settings (feed rate), and nozzle parameters (traverse speed, scanning step, standoff distance, spray angle, trajectory), are examined for their impact on coating quality. The chapter makes a comparative evaluation of CSAM with other techniques. The chapter also reviews research on computational fluid dynamic studies and impact deformation analyses in cold spray process to understand the deposition dynamics and their effect on final product properties. The literature on Inconel 718 additive manufacturing is reviewed, noting that rapid solidification leads to a microstructure with a supersaturated γ matrix, Laves phase, and limited γ'' and γ' particles. Heat treatment is crucial to dissolve the Laves phase and optimize γ'' and γ' precipitation. Additive manufacturing defects like porosity negatively impact the creep behavior and introduce anisotropy in mechanical response due to microstructure and texture variations. Elevated thermal residual stresses and phase transformations further compromise mechanical integrity. Cold spray is also an ecofriendly process that presents an effective alternative to other thermal spray techniques for its low-temperature process, reduced thermal stresses, high bonding strength and enhanced material properties. It produces a refined microstructure with lower oxide content and porosity, making it suitable for temperature sensitive and high thermal conductivity applications.

2.1 ADDITIVE MANUFACTURING

Additive manufacturing (AM) builds objects layer by layer from 3D model data generated using CAD (computer-aided design), employing a common feedstock like powder or wire in contrast to traditional subtractive methods. The feedstock used is melted or fused by a heat source, following a digitally defined path, and solidifies to create the final shape. The benefits of using additive manufacturing parts include shorter lead times, reduced buy-to-fly ratios, lower costs, the ability to design and produce complex lightweight structures, and the integration of multiple components into a single piece. These advantages result in improved performance while staying within budget and schedule constraints, thus enhancing both programmatic and technical risk management

(Angrish 2014; Shapiro *et al.* 2016). Metal additive manufacturing's design flexibility allows for material distribution optimization, reducing weight while meeting mechanical and performance standards. It also enables the combination of parts, decreasing costs and risks associated with multiple components and minimizing potential joint failures. Additionally, by leveraging mechanical, thermal, and other optimization techniques, additive manufacturing can produce high-performance parts that surpass conventional manufacturing capabilities, incorporating intricate internal features like conformal cooling channels in combustion chambers or turbine blades (Snyder and Thole 2019; Kerstens *et al.* 2021). The AM excels in high complexity and reduced lead times as compared with traditional manufacturing (TM).

Improved understanding of process parameters has mitigated quality impacts in AM. Parameters like power, scan speed, and hatch spacing influence component quality, affecting surface roughness, residual stress and porosity. This knowledge rooted in materials characterization enhances the Process-Structure-Properties relation thus improving performance (Murr *et al.* 2012). However, AM still faces challenges such as limited materials, uncertain properties, design constraints, post-processing needs, and waste generation in the form of support structures if applicable. Additionally, it demands advanced design skills for complex, lightweight components and stringent quality control for certification (Bikas *et al.* 2016). As access to AM machines expands, it still trails traditional manufacturing methods, prompting the need for supply chain advancement. Post-processing poses significant challenges for AM, necessitating specialized thermal treatments, cleanliness procedures, and surface enhancements to refine rough surfaces. This includes tasks such as powder removal, support and baseplate removal, thermal processing, hot-isostatic pressing (HIP), surface polishing, and often final machining (Yadroitsev *et al.* 2021; Yadroitsev *et al.* 2018).

Despite the drawbacks outlined, there are distinct scenarios where AM proves highly suitable for different applications, offering evident technical superiority compared to conventional manufacturing techniques as depicted in Figure 2.1. The unit cost comparison by production volume and complexity is shown for AM and TM both.

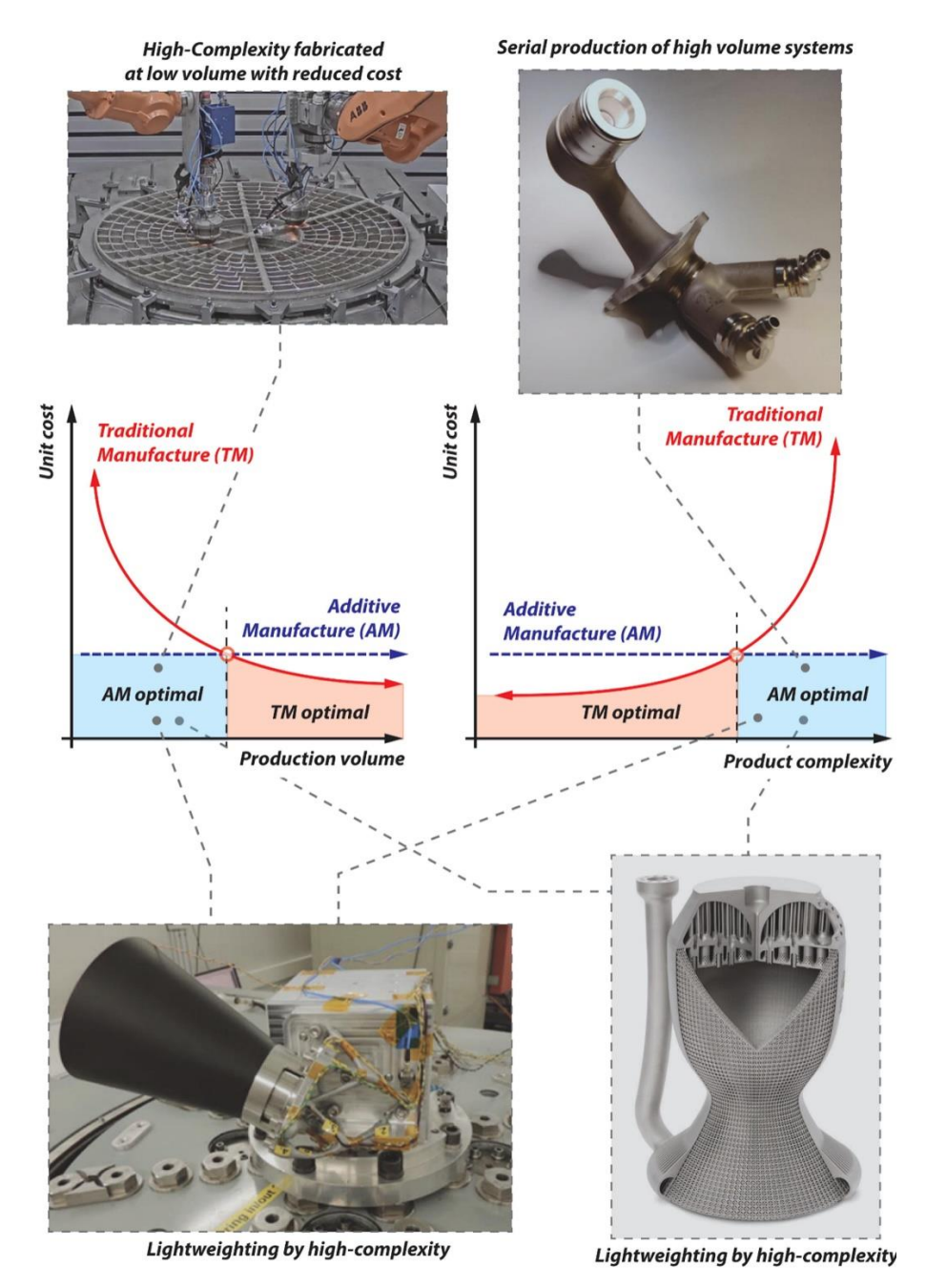


Figure 2.1 Unit cost comparison by production volume and complexity in additive manufacturing (AM) vs. traditional manufacturing (TM) (Orme *et al.* 2017; Fraunhofer 2021; Guo *et al.* 2024; G. E. Additive 2018)

2.2 METAL ADDITIVE MANUFACTURING TECHNOLOGIES

Additive manufacturing, as defined by the international standard ISO/ASTM 52900 (ASTM 2015), encompasses seven process categories, such as directed energy deposition (DED) and powder bed fusion (PBF), enabling the production of metal components with nearly full density. Usually, either a laser or an electron beam is employed to selectively melt or sinter the feedstock

(powder or wire). While other process categories exist, they are not extensively discussed due to their ongoing evolution and lower technology readiness levels (TRL) (Deb *et al.* 2018).

2.2.1 Powder Bed Fusion

In the metallic materials domain, powder bed fusion (PBF) encompasses techniques like selective laser sintering (SLS), selective laser melting (SLM), and electron beam melting (EBM). These methods follow a similar manufacturing process: depositing metal powder over the powder bed and solidifying each subsequent layer of the part using a welding beam or laser. Because of the loose powder, most PBF techniques necessitate the inclusion of support structures to uphold overhanging geometries within the part design. SLS and SLM diverge in terms of the energy applied to solidify the metal powder: SLS raises the powder particles to their sintering temperature, whereas SLM melts the powder particles. EBM functions similarly but utilizes an electron beam unit to heat parts. These methods are favored for their capability to produce intricate parts with minimal geometrical tolerances compared to extrusion based MAM techniques (Neikov 2019).

2.2.1.1 Selective Laser Melting

SLM represents a powder based additive manufacturing technique enabling the production of three-dimensional functional parts from CAD data. Following a similar path to SLS, SLM entails complete melting of the powder rather than sintering or partial melting. Commencing with the deposition of a thin layer of powder, typically 50 to 75 µm thick, onto a substrate platform, a high-power fiber laser scans the powder surface, generating heat that melts the powder particles, forming a molten pool. After scanning each layer, the platform descends by a single-layer thickness in the z-axis, and a new layer of powder is deposited. This process iterates until the entire build is finished. Once the fully dense part is formed, loose powders are removed, necessitating completion within an inert gas atmosphere like argon to eliminate oxygen from the building chamber. Subsequently, the substrate is extracted from the build chamber, and supports are carefully removed (Shirazi et al. 2015). The schematic representation of the process is shown below in Figure 2.2. Copper, aluminum, stainless steel, tool steel, chromium, titanium and superalloy powders have all been employed in the SLM process. Creation of large components is very difficult as it is inconvenient and inefficient due to build volume restrictions in the SLM working chamber, even though the bulk of wasted powders may be recycled for further AM procedures. There is some material loss during the melting when powders get degraded or oxidized and are no longer recyclable (Song et al. 2021). The SLM process does pose limitations when it comes to constructing arbitrarily shaped designs. Currently, producing overhanging

geometries or horizontal struts presents a challenge, primarily attributed to the inadequate heat conduction in the powder bed beneath the newly solidified layers of exposed powders (Rashed 2019).

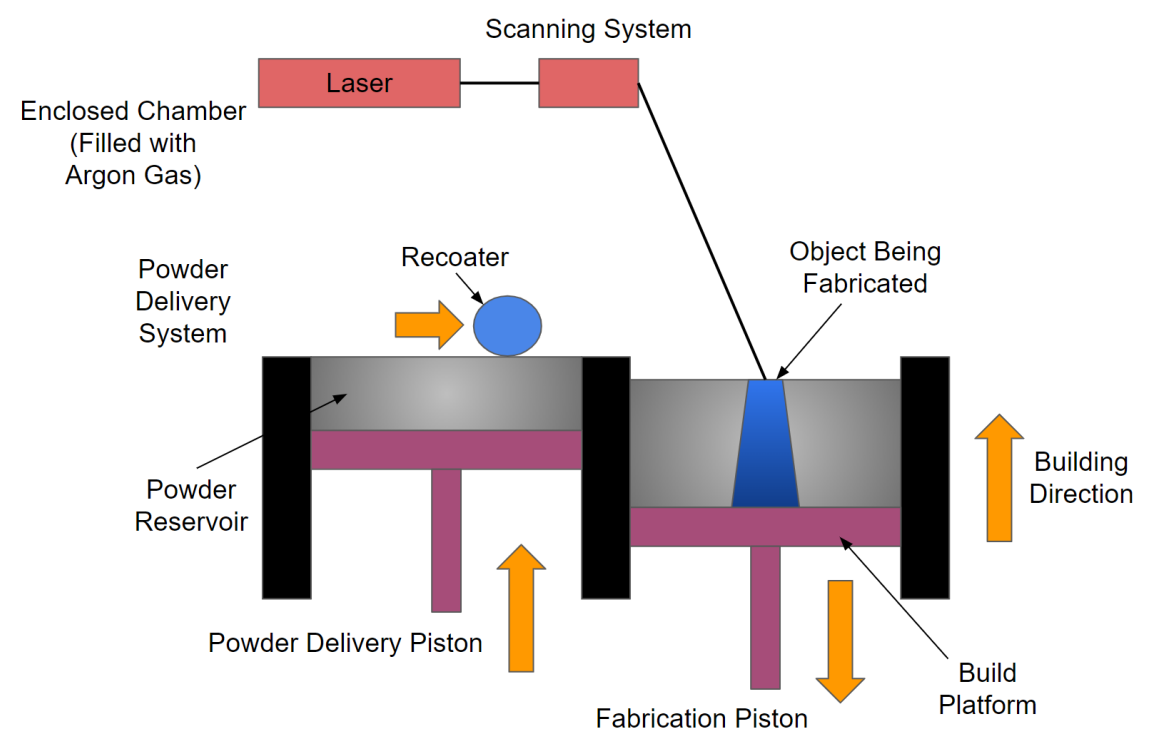


Figure 2.2 Schematic representation of selective laser melting (Jiao *et al.* 2018)

2.2.1.2 Electron Beam Melting

EBM is a form of AM that was first developed in 1997. This is one of the most modern technologies which employs a computer-controlled electron gun to make 3D objects out of metal powder like other AM processes. An electron beam generated from a tungsten filament provides the energy for the melting processes. Figure 2.3 displays a detailed diagram. Layer by layer of metal powder is melted in a strong vacuum to produce the desired output. The powder bed is held at high temperatures (>870 K), and overnight cooling durations are required when the build job is completed to cool the powder bed. Beam power, beam scanning velocity, beam focus, beam diameter, beam line spacing, plate temperature, preheat temperature (including the number of repetitions, speed, and power of the beam), contour strategies, and scan strategies are the process parameters that are involved in the EBM process. Only a few materials (Ti grade 2, Ti6Al4V, Inconel 718, CoCrMo) are used in EBM since optimizing the process parameters is considerably more challenging than the SLM process. Brittle materials can be processed using EBM, which is often not possible with SLM. It is normal to expect brittle materials, such as intermetallics, to

exhibit poor thermal expansion and contraction tendencies. These materials are not able to accommodate the internal stresses as a result of the solidification process, hence leading to formation of cracks. Because EBM may be used to create fully dense parts, it is very popular in the aerospace, medical or orthopedic implant, and automotive industries (Zhang *et al.* 2018).

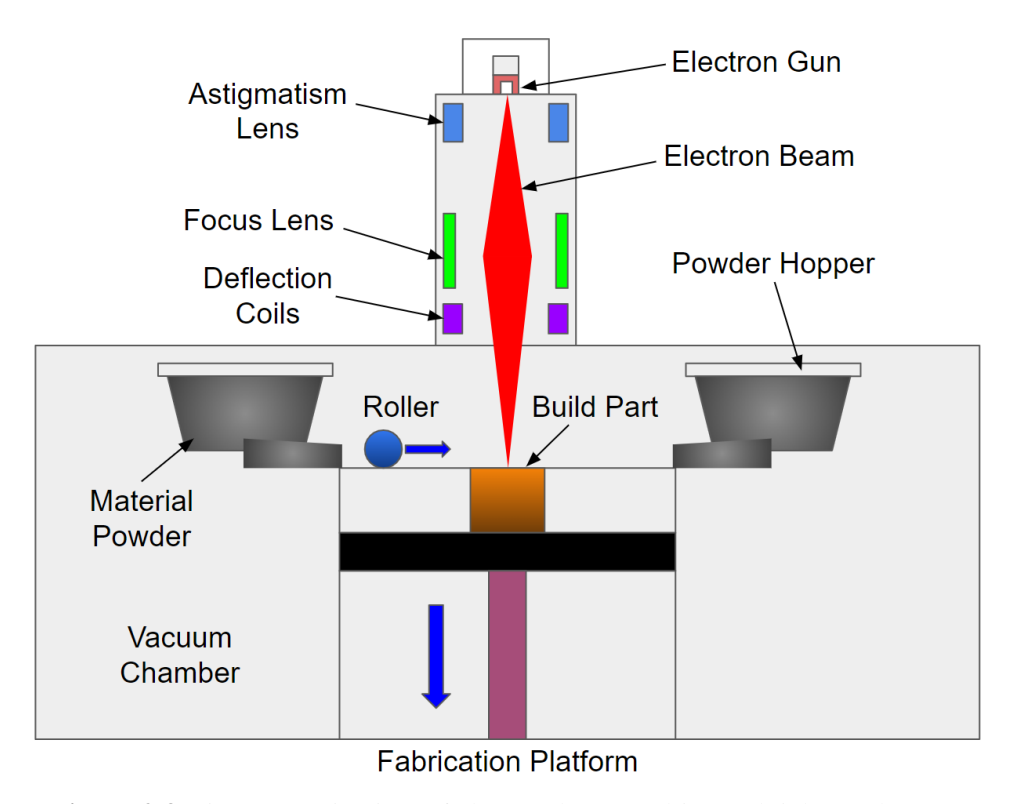


Figure 2.3 Diagrammatic view of electron beam melting (Alojaly *et al.* 2023)

2.2.2 Directed Energy Deposition

In contrast to powder bed processes, directed energy deposition (DED) techniques involve locally depositing feedstock material by feeding powder or wire directly into the melt pool, created by an energy source like electrical arcs, lasers, or electron beams (Uriondo *et al.* 2015). The materials primarily processed using this technique include aluminum, tantalum, titanium and its alloys, stainless steel, tungsten, cobalt, copper, tin, nickel, niobium, and Inconel. Since DED doesn't rely on a powder bed, it offers advantages in geometrical freedom compared to other AM methods and isn't constrained by build size limitations. Consequently, very large components can be manufactured using this technique. DED machines are commonly employed in repairing high-value existing components such as turbine blades. However, DED typically exhibits lower resolution (with minimum feature sizes of about 1 mm) compared to powder bed based technologies, making it suitable for larger components with reduced resolution or where post-processing machining operations are feasible (Pereira *et al.* 2021; Yu *et al.* 2012). The maximum

build dimensions resemble those of laser based PBF, with the most recent versions boasting a circular build diameter of 350 mm and a height of 380 mm. These machines commonly utilize larger feedstock powder sizes, leading to increased roughness values. Nonetheless, these systems have undergone significant development and provide comparatively swift build times owing to their high-power capabilities and rapid electron beam scanning (Sola and Nouri 2019).

DED is sometimes referred to as laser metal deposition (LMD), direct light fabrication or 3D laser cladding due to the changes in the energy source and intended usage (Singh et al. 2021).

2.2.2.1 Laser based Directed Energy Deposition

Laser based DED systems, such as Optomec's laser engineering net shape (LENS) DED system, employ a laser as the primary energy source. A hermetically sealed space filled with argon is required for the LENS process in order to maintain extremely low amounts of oxygen and moisture. As a result, oxidation is avoided and the part is kept clean. The material deposition nozzle receiving the metal powder material directly advances to the following layer after depositing a single-layer. The machine is creating the entire part by adding successive layers. The component is given the necessary finishing through machining and heat treatment. Direct energy deposition (DED) using a laser is well-established as a coating method to improve parts' wear resistance as well as a repair process in various application fields (Svetlizky *et al.* 2020; Izadi *et al.* 2020; Zhai *et al.* 2019; Rzeszotarska *et al.* 2023). The process schematic is shown below in Figure 2.4.

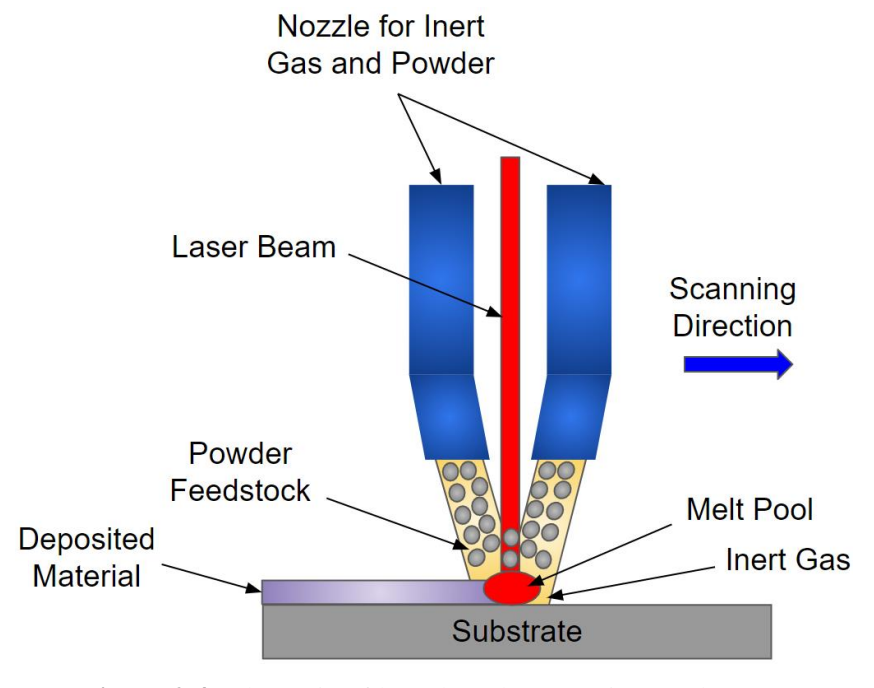


Figure 2.4 Schematic of laser based DED (Sing *et al.* 2020)

2.2.2.2 Electron Beam based Directed Energy Deposition

The electron beam based DED system operates with a high-power electron beam gun and a wire feed mechanism within a vacuum environment (as shown in Figure 2.5). In this process, the electron beam generates a small molten pool on the substrate, into which the wire is fed, depositing material at the precise location. As the electron beam moves away due to the translation of the substrate or gun, the molten pool solidifies quickly. A computer program manages the electron beam, wire feed, and translation/rotation parameters to fabricate near-net shape objects within a vacuum chamber. After achieving this near-net shape, the part undergoes heat treatment and machining. The process's scalability is mainly constrained by the vacuum chamber's size, allowing for the production of components ranging from millimeters to several meters (Osipovich et al. 2023; Sun et al. 2021; Li et al. 2023; Sames 2015; Baufeld et al. 2017). Sciaky, Inc. pioneered the wire feed electron beam process in the mid-1960s and refined it in the 1990s to produce knife-edge seals for jet engines. By 2000, the electron beam additive manufacturing (EBAM) process was developed to help manufacturers create large, high-value metal parts more efficiently, reducing both time and costs. Sciaky introduced the EBAM process as a service in 2009, naming it electron beam direct manufacturing (Baufeld et al. 2017; Cheng and Chou 2015; Madhavadas et al. 2022).

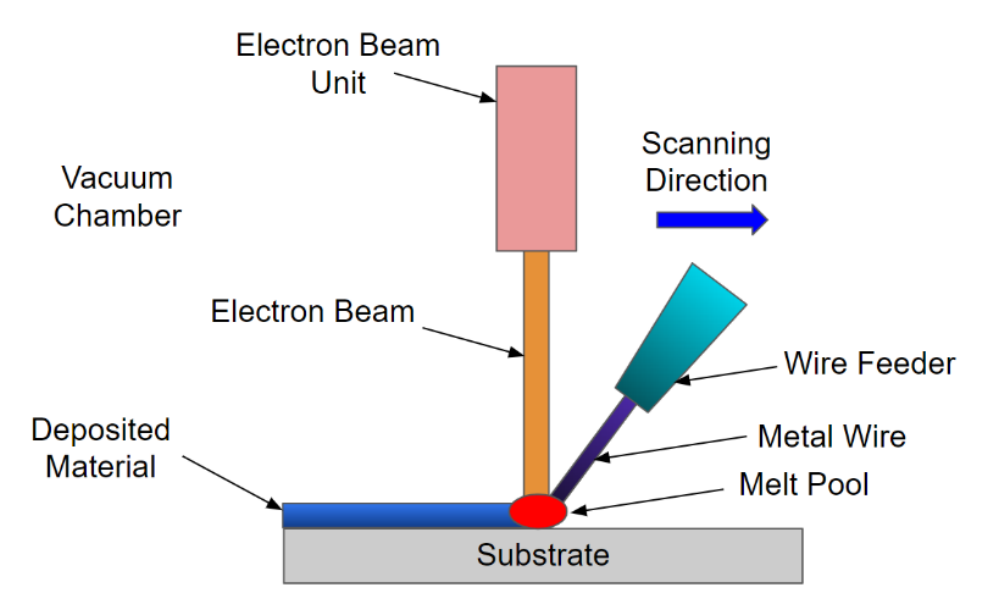


Figure 2.5 Simplified diagram of electron beam based DED (Sing *et al.* 2020)

EBAM is currently the fastest metal additive manufacturing technology, boasting deposition rates between 3.18 and 9.07 kg of metal per hour, depending on the material and part characteristics (Vafadar *et al.* 2021; Madhavadas *et al.* 2022). In comparison, the highest reported deposition

rate for laser-based wire feed is 2.9 kg per hour. Standard SLM and EBM metal powder AM methods produce between 0.1 and 0.2 kg per hour, while blown powder techniques (powder-fed laser directed energy deposition methods) achieve a maximum rate of 2.27 kg per hour (Valentin *et al.* 2019; Jackson *et al.* 2016; Murr 2018; Yan and Yu 2015).

Moreover, EBAM can produce large-scale metal structures exceeding 6 meters in length with minimal material waste (Wei *et al.* 2020; Vafadar *et al.* 2021). A significant feature of Sciaky's EBAM technology is the ability to use multiple wire feed nozzles with a single electron beam gun. This capability allows for the simultaneous feeding of two or more different metal alloys into a single molten pool, enabling the production of "graded" or "super alloy" components or ingots under independent program control (Negi *et al.* 2020; Baufeld *et al.* 2016; Osipovich *et al.* 2023).

2.2.2.3 Arc based Directed Energy Deposition

Wire arc additive manufacturing (WAAM) is a wire based directed energy deposition (DED) technique that utilizes an electrical arc to melt the wire feedstock and deposit material layer by layer to form a part as represented in Figure 2.6. Compared to electron beam and laser sources, the use of an electrical arc offers several advantages. One significant advantage of WAAM is its low capital investment, as WAAM systems can be assembled from open-source equipment and components readily available from various suppliers in the well-established welding industry (Anzalone *et al.* 2013; Cunningham *et al.* 2018; Derekar 2018). Additionally, WAAM does not require a vacuum environment, unlike electron beam methods (Milewski and Milewski 2017), which reduces setup and ramp-down times and prevents over-aging in precipitation-hardened materials (Sames *et al.* 2017). Although electron beam DED methods avoid atmospheric contamination without the need for inert shielding gas, they are prone to element depletion and evaporation during processing (Taminger and Hafley 2003).

WAAM also provides higher fusion efficiency compared to laser-based methods (Jackson et al. 2016), especially beneficial for reflective metal alloys with poor laser coupling efficiency, such as aluminum, copper, and magnesium (Gu et al. 2012; Guo et al. 2016). WAAM typically achieves layer heights of 1–2 mm, surface waviness of 500 µm, and deposition rates up to 10 kg/hr, making its productivity and material deposition comparable to laser-based and electron beambased DED approaches (Williams et al. 2016; Cunningham et al. 2018). Repairing metal components like rails, rotors, and dies that are prone to wear during use is another use for WAAM. Manually fixing them is a tedious and labor-intensive activity.

Post processing is necessary for the majority of WAAM procedures. This is a crucial step in

addressing the residual stresses and surface roughness caused by WAAM. After printing, a stress relief treatment is used to lessen the part's residual stresses. To decrease the chance of early failure and improve the part's performance and lifespan, this treatment is carried out at a high temperature. Occasionally, a specific heat treatment is used to improve the material's qualities. The second-most significant post-processing phase in WAAM is surface finishing. Every WAAM component is built in layers, which is visible from the outside. It is crucial to use a finishing process like milling or grinding in order to maximize fatigue life, tensile behavior, and corrosion resistance (Suárez *et al.* 2022).

Research and development have enhanced WAAM's capabilities, allowing it to process a variety of materials effectively. For instance, aerospace titanium alloy Ti-6Al-4V (Martina *et al.* 2013) and nickel bronze (Ding *et al.* 2016) have been successfully produced with static mechanical properties close to those of wrought and cast materials (Pan *et al.* 2018).

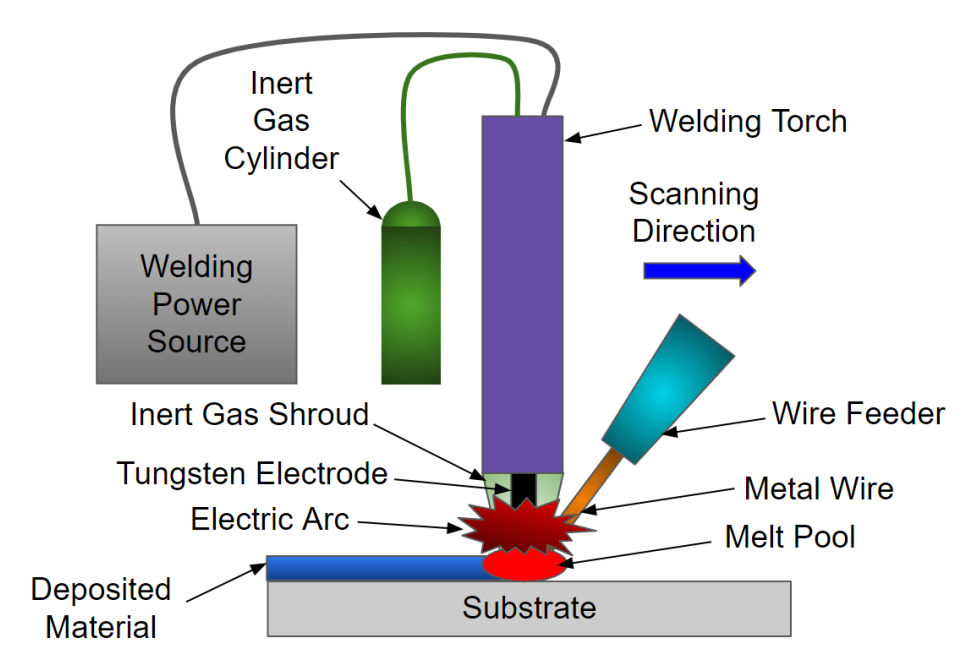


Figure 2.6 Basic outline of arc based DED (Alagha *et al.* 2021)

2.3 THERMAL SPRAY: A HISTORICAL PERSPECTIVE ON ADVANCEMENTS

In the early 1900s, Dr. Max Ulrick Schoop of Zurich made a significant discovery, observing that "a stream of molten particles impinging upon themselves" could form a coating, laying the foundation for thermal spraying. During this era, engineers were exploring the use of high-pressure gas to break liquids into tiny particles or powders. Dr. Schoop's findings led to the development of the first thermal spray method. Collaborating with his German engineering colleagues, Felix Meyer and Franz Herkenrath, Dr. Schoop devised techniques and tools for

creating coatings from molten and powdered metals. This progress culminated in the establishment of the first stationary metal spraying factory in 1910 (Siegmann and Abert 2013).

In 1912, Dr. Schoop and his team further advanced thermal spraying by inventing the first device for spraying solid metal in wireform. This method, known as metallizing, involved feeding a wire rod into an intense, concentrated flame surrounded by a stream of compressed gas. The molten metal would then atomize and propel onto a surface, creating a coating (Siegmann and Abert 2013).

The outbreak of World War II in 1939 spurred the growth of the American thermal spray industry, with members of the International Thermal Spray Association playing a pivotal role in providing urgently needed "metallizing" for replacement parts in industrial equipment. By the war's end in 1945, metallizing had gained widespread recognition as a vital industrial process. Today, metallizing is commonly referred to as oxy-fuel or flame spraying (Fauchais and Vardelle 2012; Irissou *et al.* 2008).

A series of advancements in thermal spraying have made it more cost-effective compared to its early stages. However, the introduction of plasma spraying in the 1960s marked a significant technological leap forward. This method involves melting and applying metal coatings to a substrate using powder feedstock and high-temperature plasma. Plasma spraying expanded the range of surface applications for thermal spray coatings, making them much more versatile than previous iterations (Fauchais and Montavon 2007; Sampath *et al.* 2013; Mauer *et al.* 2011).

A major breakthrough occurred in the 1980s with the introduction of high velocity oxy-fuel (HVOF) spraying. This process produces a high-pressure, high-temperature flame that can propel melted powder feedstock at very high speeds by igniting fuel (such as hydrogen, acetylene, or propane) and oxygen. The resulting coating is exceptionally dense and firmly bonded (Bakan *et al.* 2017; Anusha *et al.* 2023; Henao *et al.* 2019).

New thermal spraying processes have emerged due to inherent limitations in conventional thermal methods such as plasma spraying, HVOF spraying, and flame spraying. The high temperatures associated with these approaches can lead to undesired metallurgical changes, including oxidation and grain growth, which can adversely affect coating adhesion to the substrate, as well as porosity and substrate degradation (Pan *et al.* 2016; Talib *et al.* 2003; Berger 2015; Gonzalez *et al.* 2016).

The cold spray (CS) process, a recent addition to the thermal spray domain, relies on kinetic energy (300-1500 m/s) rather than thermal energy. This approach helps overcome the limitations associated with thermal energy. CS is capable of depositing coatings with low porosity, high bond and cohesive strength, and higher deposition yield (Vaz *et al.* 2023; Champagne *et al.* 2021;

Viscusi *et al.* 2019). In the following section, we will delve into the various thermal spray processes in general and explore the cold spray process in detail.

2.4 THERMAL SPRAY BASED ADDITIVE MANUFACTURING TECHNOLOGIES

Thermal spray processes encompass a range of coating techniques used to apply metals, polymers, ceramics, and other materials onto various substrates (Ang and Berndt 2014). Additionally, these methods facilitate the fabrication of large components that cannot be economically or technically produced through powder metallurgy (Berger 2007). Thermal spray processes use a variety of feedstock materials, such as wires, powders (including metals, ceramics, and polymers), and liquids (such as suspensions and solution precursors), to produce coatings on solid substrates capable of withstanding high temperatures (Prashar et al. 2021; Mittal and Paul 2022). Thermal spray processes are classified on the basis of the energy source as displayed in Figure 2.7. These methods are primarily highly effective in developing coatings that resist wear, erosion, corrosion, and abrasion (Yin et al. 2019). Thermal spraying is also employed to enhance various surface properties, such as lubricity, electrical conductivity, and insulation (Tejero-Martin et al. 2019). The family of thermal spraying techniques includes several processes, such as arc spray (AS), flame spray (FS), plasma spray (PS), detonation gun (D-gun) spray, high velocity oxy-fuel (HVOF) spray, and cold spray (CS) (Boulos et al. 2021). These processes involve propelling feedstock particles in molten, semi-molten, or solid states towards a substrate. Upon impact, the particles undergo flattening, rapid cooling, and solidification to form a coating (Lavernia and Srivatsan 2010; Gan and Berndt 2015). The parameters of the spray process, such as velocity, temperature, and particle size, influence the interaction between the spray particles and the flame, as well as the deposition quality of the coatings (Kumar and Kumar 2021; Oksa et al. 2011). Furthermore, chemical reactions, like the oxidation of metal alloys during heating, can alter the chemical phases and compositions of the feedstock, thereby imparting new properties to the coatings (Kumar and Kumar 2021).

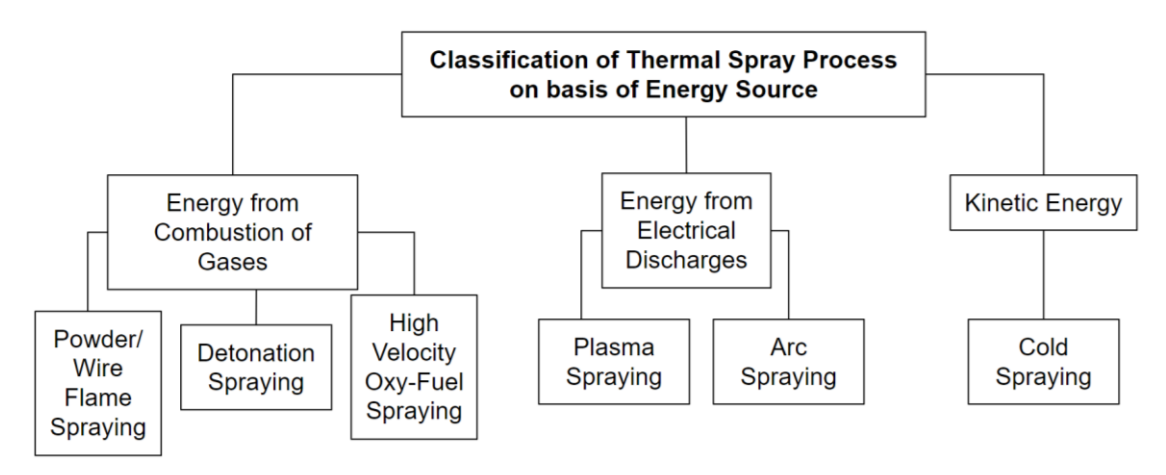


Figure 2.7 Classification of thermal spray processes on the basis of energy source (Jahani *et al.* 2018)

Thermal spray processes can be categorized based on the velocity of the spray particles and the deposition temperatures (Talib *et al.* 2003; Ang *et al.* 2014), as illustrated in Figure 2.8.

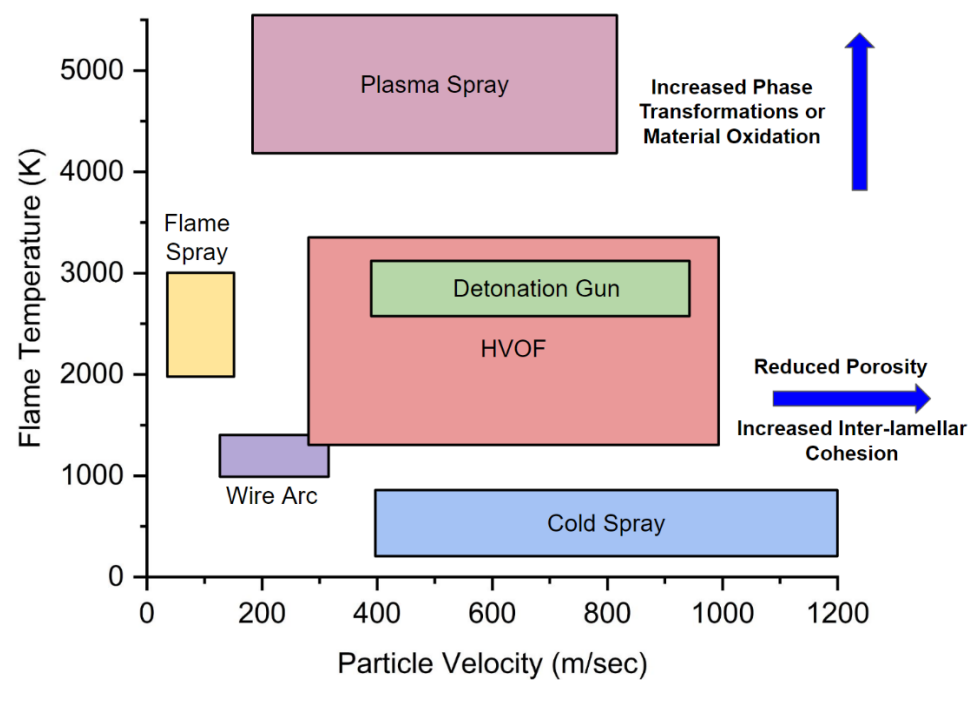


Figure 2.8 Taxonomy of thermal spray processes in relation to particle velocity and flame temperature (Ang *et al.* 2013)

The smallest structural unit of thermal spray coatings is called a splat. Splats are created by the impact of individual particles and serve as the fundamental building blocks of the coating (Ang and Berndt 2014). The adhesion of these particles to the substrate occurs through metallurgical

and mechanical bonding. As these particles continuously deposit along the substrate's lateral surface, they form a lamellar microstructure (Li *et al.* 2022; Tiamiyu *et al.* 2021).

Choosing the appropriate thermal spray process for a specific application depends on various factors, including operational requirements, substrate geometry, degradation severity, deposition rate, and the cost of the coating process or equipment (Dorfman 2018; Fauchais and Vardelle 2012). Additionally, the temperature of the heat source is crucial in determining the suitable thermal spray method. HVOF is categorized as high-velocity techniques operating at moderate temperatures ranging from 2000 to 4000 °C (Milanti *et al.* 2016; Matikainen *et al.* 2015). Conversely, cold spray relies on the mechanical deformation properties of metallic powders at lower temperatures, typically below 800 °C and near the recrystallization temperatures. This method is predominantly suitable for ductile materials such as aluminum, copper, and zinc (Walker 2018; Viscusi *et al.* 2019). Plasma spray, on the other hand, is a high-temperature process known for producing dense coatings, particularly applicable to ceramics (Gill and Tucker 1986; Heimann 1996). Arc and flame spray processes are characterized by relatively lower speeds, with arc spray capable of achieving high throughputs and producing thick coatings (Boulos *et al.* 2021).

Despite the numerous advantages offered by thermal spray processes for material deposition, a limitation lies in their line-of-sight nature. Only areas visible to the spray gun can be coated, leaving small and deep cavities on the target surface inaccessible. However, this limitation can be addressed with the availability of nozzle attachments or miniaturized spray guns designed to overcome such obstacles (Schwartz 2010; Merchant and Hewitt 1997). Another challenge in using thermal spray processes for coating is the risk of coating unintended areas. This issue can be mitigated through the implementation of suitable masking strategies, effectively covering the areas where coating is not desired (Vardelle *et al.* 2016; Ashokkumar *et al.* 2022).

2.4.1 Flame Spraying

Flame spraying utilizes an oxyacetylene flame to melt target materials ranging from several metals, polymers, and some ceramic substances (Fauchais *et al.* 2014; Pawlowski 2008). This method was the first thermal spraying process, originating from modifications made to oxyacetylene torches. Flame spraying can be categorized into two types based on the form of the feedstock material: Wire Flame and Powder Flame (Fauchais *et al.* 2014; Schwartz 2010). Powders are typically fed through a central passage using carrier gasses such as argon or nitrogen, or they can be gravity-fed from a canister mounted directly on the spray gun (Talib et al. 2003). The powder material melts in the combustion flame due to the heat of the chemical reaction

between oxygen and fuel. The compressed air then atomizes the molten material and propels it towards the prepared substrate surface at speeds between 50 and 300 m/s (Fauchais *et al.* 2014). The schematic for the flame spraying process is presented in Figure 2.9.

This process is effective for applying economical coatings, often characterized by high levels of oxides and porosity, and can produce a rough surface finish. These features can impact the coating's properties, such as hardness and corrosion resistance. The flame temperature in flame spraying typically ranges from 2,800 °C to 3,200 °C (Fauchais and Vardelle 2012; Tejero-Martin *et al.* 2019).

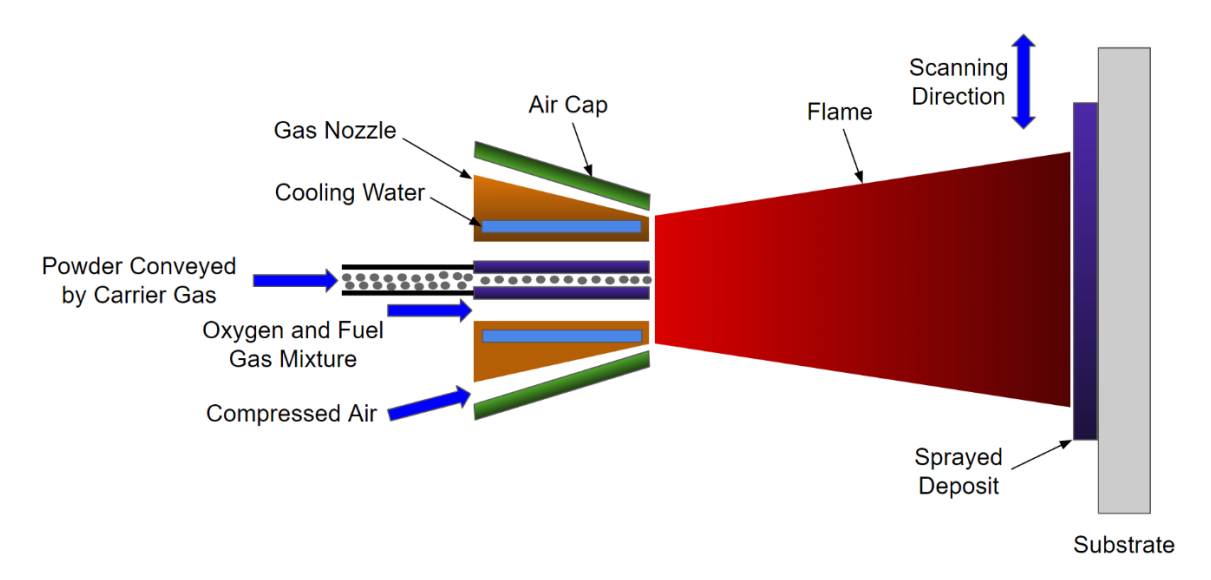


Figure 2.9 Layout of the flame spraying process (Xanthopoulou *et al.* 2014)

2.4.2 High Velocity Oxy-Fuel Process

High velocity oxy-fuel (HVOF) employs a fuel (commonly kerosene or hydrogen) and oxygen mixture ignited in a combustion chamber under precisely controlled conditions. The combustion gasses are accelerated through a converging-diverging nozzle at extremely high speeds, reaching up to Mach 7 as illustrated in Figure 2.10 (Anusha *et al.* 2023). Powders (such as tungsten carbide, nickel-chrome alloys, and chrome carbides) are injected into the high-temperature gas stream, where they soften from the heat and strike the substrate at very high velocities (approximately Mach 2) with substantial kinetic energy. HVOF is widely accepted in demanding industries such as oil and gas, steel mills, power generation, valves, and pumps, particularly as a hard chrome replacement (Ben Mahmud 2018; Dorfman 2018). This process produces dense, durable coatings that can be ground with silicon carbide or, in some cases, diamond-polished for a high-quality finish. The dense coatings applied by HVOF provide excellent protection against corrosion and erosion, often outperforming traditional hard chrome plating (Hulka 2013). For

instance, HVOF-coated ball valves in the oil and gas industry can last up to ten times longer than chrome-plated ones, effectively resisting corrosive crude oil, water, mud, and sand (Vernhes *et al.* 2013). These coatings can achieve hardness levels up to 1400 HV, low porosity below 1 %, and bond strengths over 80 MPa, all while maintaining a low substrate temperature to prevent metallurgical changes (Singh *et al.* 2023; Kumar *et al.* 2023).

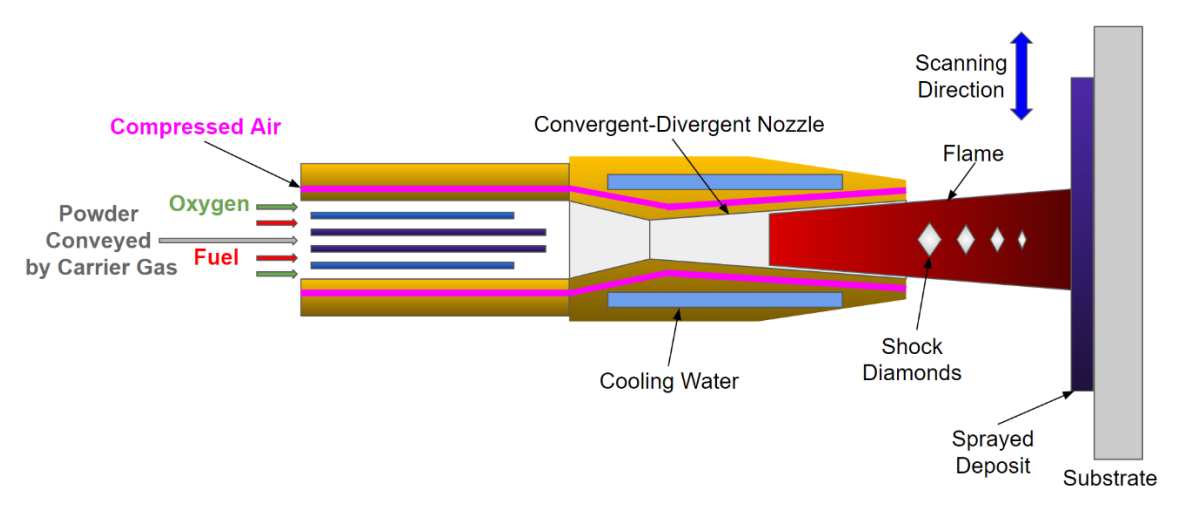


Figure 2.10 Graphical depiction of high velocity oxy-fuel process (Jonda *et al.* 2020)

2.4.3 Detonation Gun Spraying

The detonation gun spraying process is a type of thermal spraying where the coating material in powder form is heated and accelerated by high-pressure, high-temperature gasses produced from the controlled explosive combustion of a precisely measured mixture of gasses, typically oxygen and acetylene (Gu *et al.* 2020; Boulos *et al.* 2021). Developed in Russia and introduced by Union Carbide employees Gfeller and Baiker in the early 1950s (Anish *et al.* 2016), this process uses a barrel about 1 meter in length with one end closed. A spark plug ignites the gas mixture, causing repeated explosions within the closed section of the barrel (Kadyrov 1996). After each detonation, the barrel is purged with a brief burst of nitrogen. This crucial step prevents the residual heat from causing premature combustion of the new fuel mixture, which could lead to an uncontrolled reaction. Additionally, a small amount of inert nitrogen gas is introduced between successive fuel and feedstock mixtures to prevent backfiring. The detailed diagram is shown in Figure 2.11. D-guns generally operate at firing rates ranging from 1 to 10 Hz.

The state of the powder particles upon impact with the substrate depends on the material being coated. Metals such as aluminum, nickel, and copper are fully molten, ceramics like Al₂O₃ and Cr₂O₃ remain solid, and multi-component powders such as WC-Co and Cr₃C₂-NiCr experience partial melting of their low-melting binder phases (Sundararajan *et al.* 2013). The temperatures

can reach up to 3000 °C, and particle velocities can reach up to 1000 m/s (Kadyrov and Kadyrov 1995). The process is effective for coating a variety of materials, including metals, alloys, and cermets, and produces dense coatings with minimal thermal degradation and lower oxide content compared to other thermal spray methods (Dorfman 2018; Tucker Jr 2013).

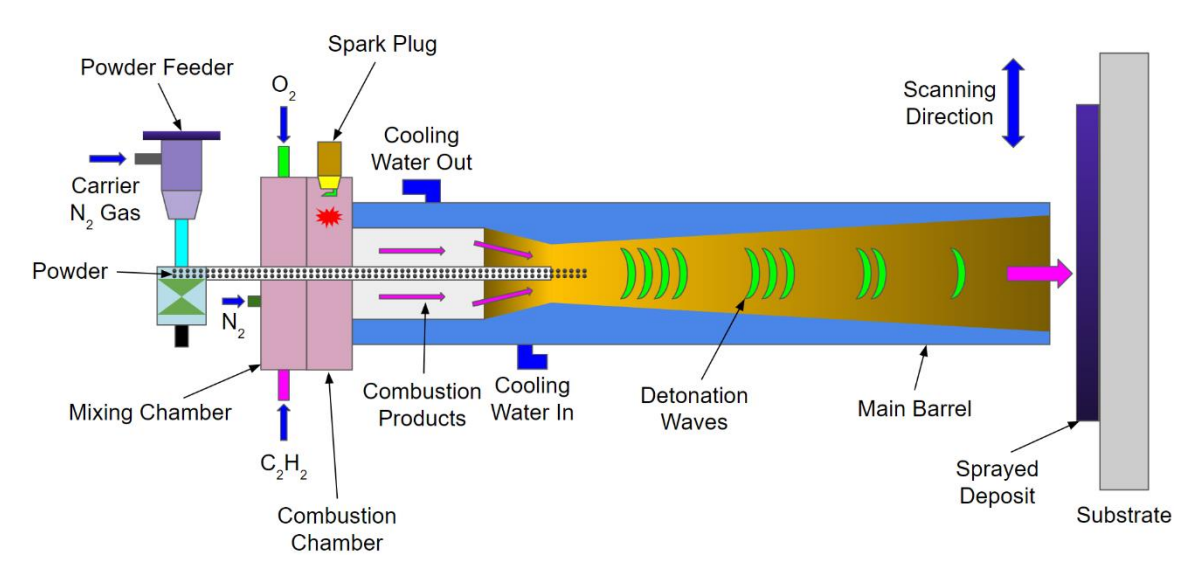


Figure 2.11 Illustration of detonation gun spray process (Sundararajan et al. 2013)

2.4.4 Plasma Spraying

Plasma spray is a well-known electrical-thermal spray technique that utilizes a partially ionized conductive medium known as "plasma" to melt powdered feedstock material and project it onto a target surface. A typical plasma spray gun consists of two electrodes: a tungsten cathode, shaped like a bullet, and a copper anode that encases it. Both electrodes are cooled with water, and an insulator ensures they remain electrically separated. The copper anode also serves as a nozzle to direct the hot plasma jet (Hui *et al.* 2007; Vardelle *et al.* 1993).

To generate a plasma jet, an inert plasma-forming gas—commonly argon or nitrogen, often mixed with helium or hydrogen—is introduced into the annular space between the electrodes. An electric arc ionizes the gas, creating a high-temperature, electrically conductive plasma. This plasma jet expands and exits the open end of the anode, forming a fast-moving jet. Depending on the configuration of the anode, the plasma jet can be either supersonic or subsonic. The feedstock material, introduced as a powder into the plasma jet, melts and is propelled towards the substrate as seen in Figure 2.12 (Vardelle *et al.* 1993). A notable variant of plasma spraying is vacuum plasma spray (VPS), also referred to as low-pressure plasma spray (LPPS). LPPS systems operate at chamber pressures ranging from 5 to 20 kPa (37 to 150 Torr). Prior to the coating process, the chamber is evacuated to eliminate all air and then refilled with an inert gas, such as argon, to

achieve the desired operating pressure. VPS/LPPS techniques are capable of producing coatings of superior quality, with densities approaching theoretical limits, minimal porosity, and very low oxide content. Due to the complexity and high cost of the equipment, these methods are predominantly used in the aerospace and biomedical industries (Montavon *et al.* 1995; Gruner 1984; Scrivani *et al.* 2003).

In plasma spraying, the heat source is an electric arc struck between two non-consumable electrodes. The gas flow past the arc blows the plasma through a nozzle, with plasma temperatures reaching 10,000–20,000 °C, higher than those used in other spray methods. Common gasses include hydrogen, nitrogen, argon, or helium (Boulos *et al.* 2023).

The cladding material, typically in powder form but sometimes as wire, is fed into the arc, where it melts and is transported to the workpiece by the plasma jet. The high temperature of the plasma allows for the spraying of ceramics and metal oxides with high melting points. Due to the expense of plasma spraying equipment, it is less frequently used for simpler materials with lower oxidation sensitivity. Its primary use is in applying non-metallic coatings to metallic substrates to create electrically insulating layers (Kim *et al.* 2017; Unabia *et al.* 2018).

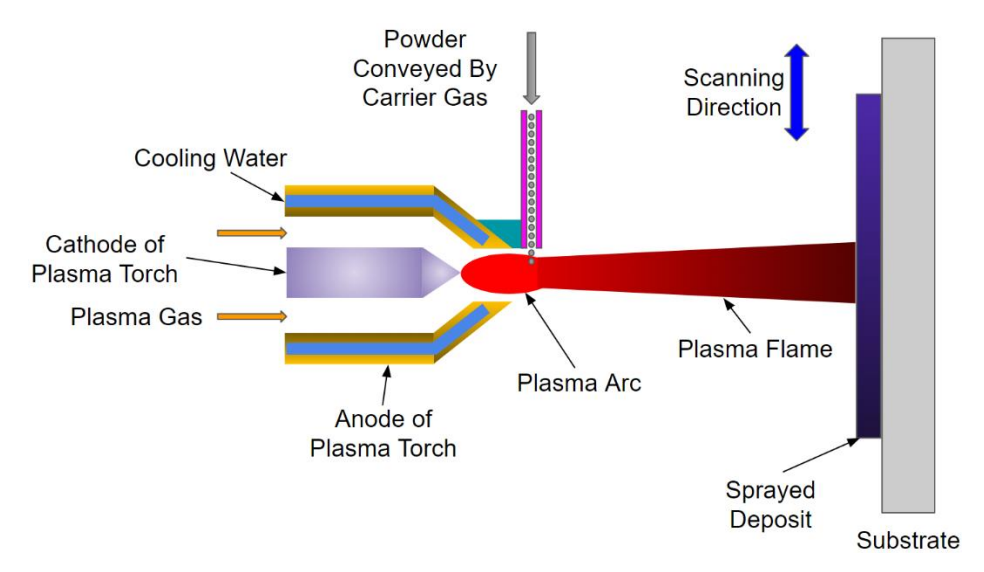


Figure 2.12 Schematic of plasma spraying process (Li et al. 2023)

2.4.5 Cold Spray

Cold Spray is a modern spray coating technique that emerged in the mid-1980s at the Theoretical and Applied Mechanics Institute in the former Soviet Union. Professor Anatolii Papyrin and his team came up with the idea while studying models in a wind tunnel exposed to a flow of gas and copper particles traveling at supersonic speeds. When these particles reached velocities surpassing a critical value (known as V_{cr}), they began depositing on the surface of the substrate.

Realizing the potential of this phenomenon, the researchers saw an opportunity to use this technology for applying coatings. They proved the effectiveness of the Cold Spray technique for various purposes by successfully depositing a wide range of pure metals, metal alloys, and composites onto different substrate materials (Alkhimov *et al.* 2001; Karthikeyan 2005). Cold Spray is renowned for its capability to achieve high strain rates (10⁷ s⁻¹ to 10⁹ s⁻¹) and deposit materials without melting. This process involves accelerating very small metallic or composite powder particles (5 to 100 μm) to supersonic speeds (500–1200 m/s) by using a converging-diverging (De Laval) nozzle and striking them onto a substrate. This impact leads to significant plastic deformation, enabling the particles to bond with the substrate in a solid state (Akisin *et al.* 2022; Dykhuizen and Smith 1998). The detailed representation of the cold spray method is shown in Figure 2.13.

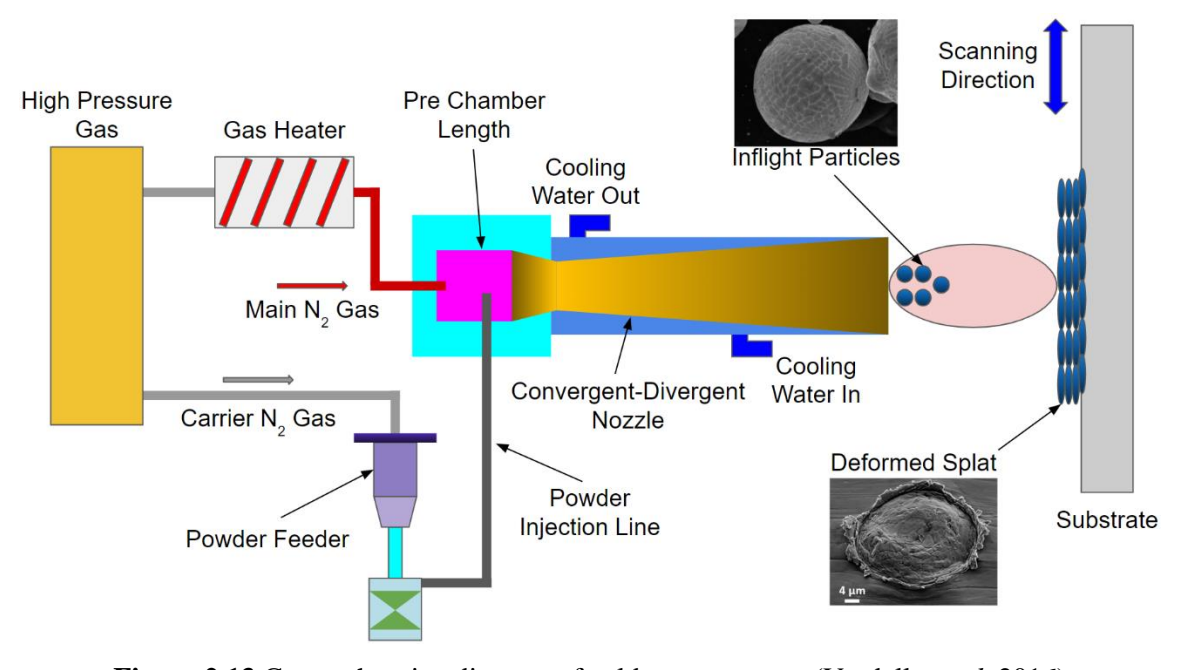


Figure 2.13 Comprehensive diagram of cold spray process (Vardelle et al. 2016)

Cold spray technology can be divided into high-pressure cold spray (HPCS) and low-pressure cold spray (LPCS) systems, based on the operating pressure. HPCS systems, which can operate at pressures up to 50 bar, typically use compressed helium (He) or nitrogen (N₂) as the operating gas. In contrast, LPCS systems operate at pressures up to 20 bar, and primarily use compressed air as the operating gas (Winnicki *et al.* 2021; Vadla and Doom 2018).

The capabilities of Cold Spray extend to both surface engineering and additive manufacturing, as outlined in Figure 2.14, which also illustrates the range of materials suitable for cold spraying (Pathak and Saha 2017).

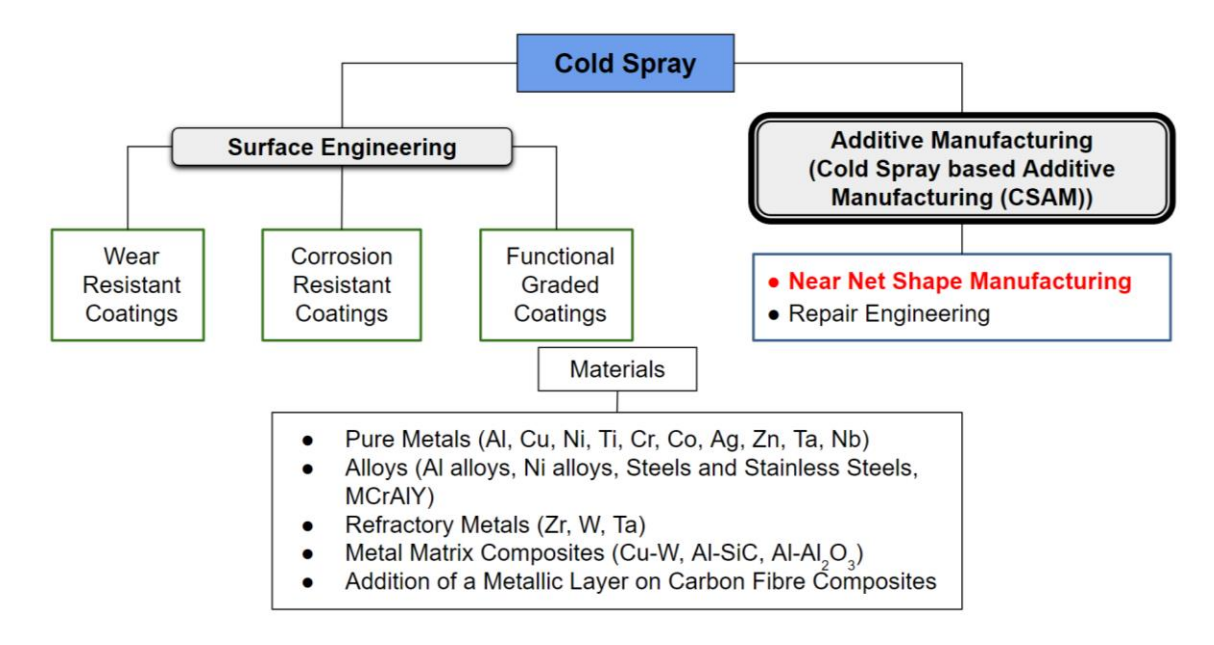


Figure 2.14 Distinctive characteristics of cold spray (Pathak and Saha 2017)

2.4.5.1 Bonding Mechanism in Cold Spray

Cold spray technology harnesses the kinetic energy of feedstock powder, unlike traditional methods such as arc, flame, and plasma spraying, which predominantly utilize the thermal energy of the feedstock (Oyinbo and Jen 2019; Melentiev and Lubineau 2021). In cold spray, adhesion between the feedstock and substrate is driven by high strain rate plastic deformation phenomena (Nastic *et al.* 2021). Various factors influence particle bonding in cold spray, including thermomechanical variables like flow stress, plastic strain, temperature, and pressure at the interface, as well as geometrical factors such as crater depth, contact surface area, and width. These factors are significantly impacted by changes in particle impact velocity. Understanding these fundamental quantities and conditions is essential for establishing bonding criteria (Imbriglio and Chromik 2021; Moridi *et al.* 2014; King *et al.* 2015).

In cold gas spraying, particle bonding is believed to result from extensive plastic deformation and associated phenomena at the interface. This bonding mechanism is similar to those seen in processes such as explosive cladding or shock wave powder compaction, both of which have been extensively studied for their bonding mechanisms and applications. In explosive cladding, effective bonding occurs within specific ranges of impact angles, velocities, and material properties, often characterized by the formation of an outflowing jet of material at the contact zone (Assadi *et al.* 2003; Adaan-Nyiak and Tiamiyu 2023). Just a few millimeters from the interface, one can observe regions with severe deformation, highly elongated grains, recrystallized grains, and occasionally resolidified microstructures. However, melting and

resolidification are typically confined to a layer less than a micrometer thick at the interface (Assadi *et al.* 2016).

The widely accepted theory of adiabatic shear instability (ASI) was proposed by Assadi *et al.* (2016), who employed a finite element modeling approach to investigate this phenomenon and determine the critical velocity of copper. The critical velocity represents the threshold at which ASI occurs, facilitating successful bonding of the feedstock to the substrate. According to Assadi, when particles impact the surface at velocities equal to or greater than the critical velocity, a significant temperature increase at the interface ensues due to the supersonic collision. The resultant high plastic strain at the interface can induce softening through adiabatic heating. This thermal softening effect may prevail over strain rate hardening effects at higher velocities as demonstrated in Figure 2.15, leading to adiabatic shear instability at the interface.

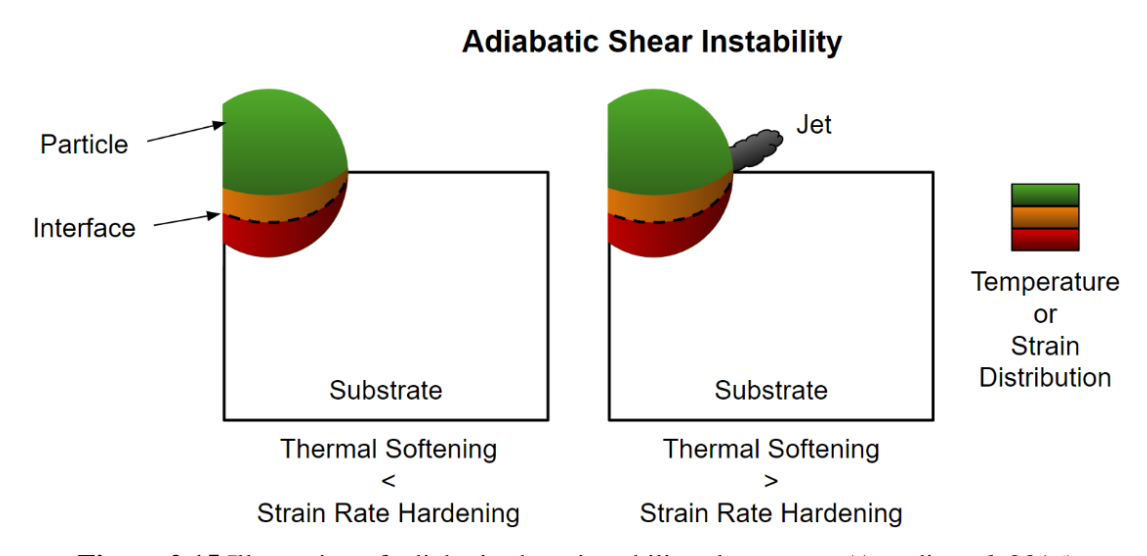


Figure 2.15 Illustration of adiabatic shear instability phenomena (Assadi et al. 2016)

With a considerable magnitude of plastic strain at the interface, the material's shear strength diminishes to values near zero, primarily due to the dominance of thermal softening over hardening effects as shown in Figure 2.16 (b), 2.16 (c) along with temporal development of strain, temperature and stress in Figure 2.16 (d), 2.16 (e) and 2.16 (f). It is important to mention that increasing the particle velocity will result in more pronounced jetting as shown by the red arrow in Figure 2.16 (a) (Assadi *et al.* 2016).

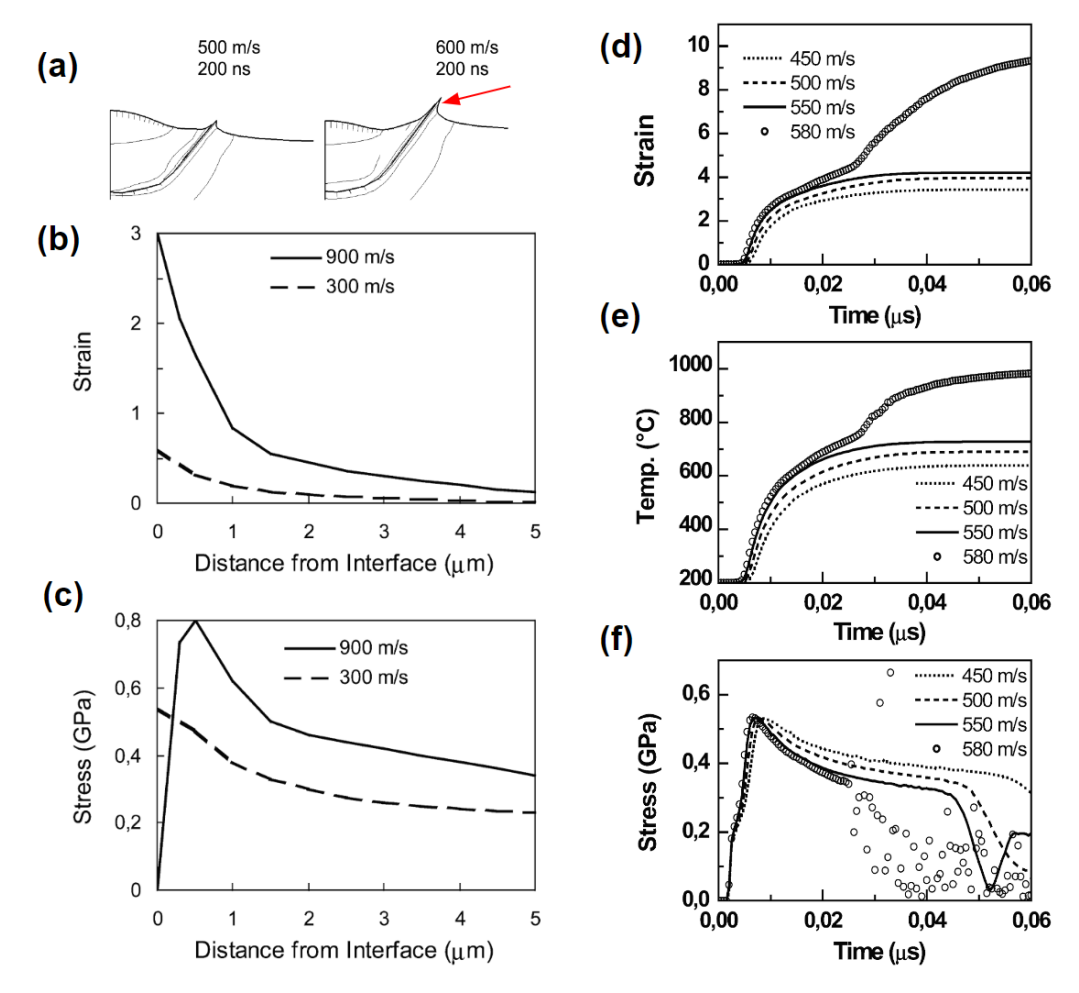


Figure 2.16 (a) Simulated impact of a copper particle on a copper substrate for the initial velocities of 500 and 600 m/sec. Red arrow shows more pronounced jetting for 600 m/sec; (b) and (c) shows profiles of plastic strain and flow stress along the radial path for impact velocities of 300 and 900 m/s. Higher velocity results in flow stress dropping to zero at the particle-substrate interface indicating towards adiabatic shear instability phenomena; (d), (e) and (f) shows calculated temporal development of plastic strain, temperature and flow stress for various impact velocities (Assadi *et al.* 2016)

Hassani-Gangaraj *et al.* (2018) contested the bonding mechanism proposed by Assadi *et al.* (2016), suggesting that adiabatic shear instability (ASI) may not be necessary for bonding. Instead, they proposed their hydrodynamic plasticity theory, wherein they explained that during supersonic impact of a powder particle, non-uniform compressive pressure waves develop in both the particle and substrate. As the shock velocity increases the edge velocity as illustrated in Figure 2.17, hydrodynamic stresses surpass the material's flow strength, leading to material jetting phenomena occurring at the interface.

Additional bonding mechanism theories, such as interlocking (Champagne *et al.* 2016), oxide layer breakup (Li *et al.* 2010), and interface amorphization (Ko *et al.* 2016), have been proposed. However, these mechanisms have not received as much attention as adiabatic shear instability (ASI) and hydrodynamic plasticity.

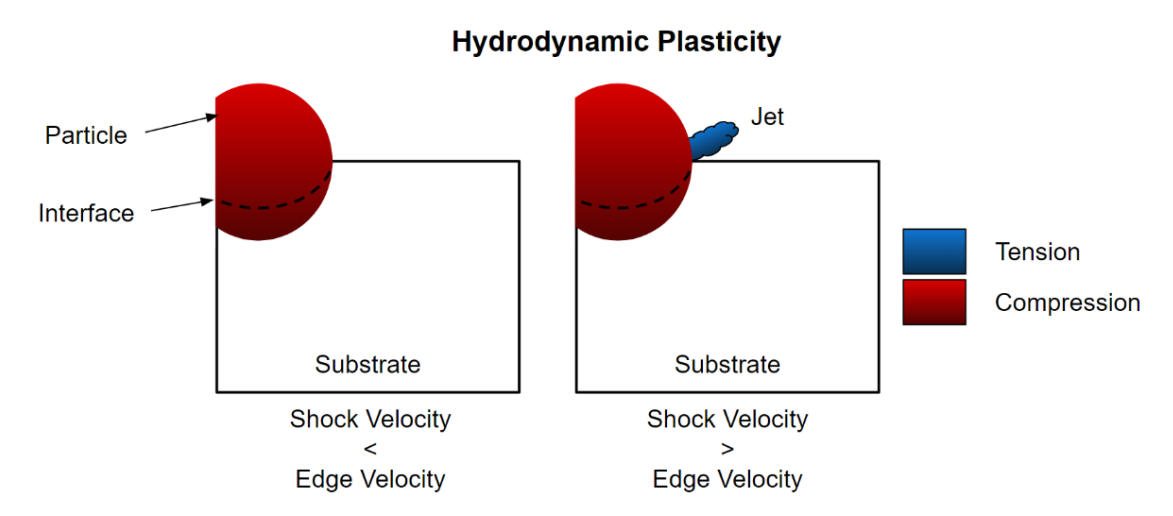


Figure 2.17 Diagrammatic representation of hydrodynamic plasticity phenomena (Hassani-Gangaraj *et al.* 2018)

Mechanical bonding involves physical interlocking and deformation of particles upon impact, enhancing adhesion (MacDonald *et al.* 2018). Hussain *et al.* (2009) proposed that the metal jetting resulting from the impact of incoming copper particles leads to the formation of lips of aluminum, partially enveloping the copper particles. Adiabatic shear instability (ASI) indirectly influences mechanical bonding by altering conditions at the particle-substrate interface, such as promoting particle flattening and interlocking through plastic deformation and localized heating (Bruera *et al.* 2023; Adaan-Nyiak and Tiamiyu 2023).

Metallurgical bonding relies on atomic diffusion and solid-state welding processes. Particles remove surface oxide layers through jetting, facilitating the creation of true metallurgical bonds (Cai *et al.* 2018). ASI indirectly impacts metallurgical bonding by creating conditions favorable for atomic diffusion and intermixing between deposited particles and the substrate material (Adaan-Nyiak and Tiamiyu 2023). The intense plastic deformation and localized heating associated with ASI promote atomic diffusion and enhance interfacial interactions, facilitating metallurgical bond formation (Nikbakht *et al.* 2024; Imbriglio and Chromik 2021).

2.4.5.2 Critical Velocity and Window of Deposition

In cold spraying, successful particle bonding requires localized deformation and adiabatic shear instabilities at high impact velocities, known as the critical velocity (Assadi et al. 2003; Schmidt

et al. 2003; Stoltenhoff et al. 2002). Numerical analyses can identify these instabilities and help calculate the critical velocity based on material properties and process parameters. Assadi et al. (2003) used numerical simulations to determine how various material properties affect the critical velocity, summarizing these effects into a concise expression presented in SI units.

$$V = 667 - 0.014 \,\rho + 0.08 \,(Tm - Tr) + 10^{7} \,(\sigma y) - 0.4 \,(Ti - Tr) \qquad \text{eq}(2.1)$$

Where V is the critical velocity in m/sec ((Assadi $et\ al.\ 2003$), ρ is the density in kg/m³, σy is the yield strength of the powder material in N.m², Tm and Ti is the melting and impact temperature of the powder particle in K whereas Tr is the reference temperature of 293 K. Equation (2.1) is useful for estimating the impact of minor changes in material and process parameters on the critical velocity. However, its applicability is limited to materials with properties similar to those of the reference material, namely copper. Assadi $et\ al.\ (2003)$ work does not consider particle size as an influential factor. However, various reports suggest that particle size can affect the critical velocity (Blazynski 2012; Papyrin $et\ al.\ 2003$; Van Steenkiste and Smith 2004). One explanation for this variation is the differing surface-to-volume ratios, where smaller particles have more adsorbents or oxides, which can impede bonding. Additionally, differences in heat conduction length scales and size-dependent variations in strain rate hardening may also contribute to the observed differences in critical velocities. Furthermore, the experimental findings were fitted using a simple yet physically sound expression as given by Equation (2.2), enabling convenient estimation of critical velocity across various metallic materials (Schmidt $et\ al.\ 2006$) by taking into account mechanical and thermal balance simultaneously.

$$Vcr = \sqrt{\frac{F1. 4.\sigma ts. \left(1 - \frac{Ti - Tr}{Tm - Tr}\right)}{\rho} + F2.Cp. (Tm - Ti)}$$
 eq(2.2)

Where Vcr represents critical velocity in m/sec (Schmidt et~al.~2006) (please note that this critical velocity will be referred in this study) taking into account both mechanical and thermal balance, σts is the tensile strength of the powder feedstock in N.m⁻², Tm and Ti represent the melting and impact temperatures of the powder particle in K, respectively, while Tr denotes the reference temperature of 293 K. ρ is the density in kg/m³, Cp signifies specific heat capacity at constant pressure in J·kg⁻¹·K⁻¹ whereas FI and F2 implies empirical factors.

Another significant impact effect in cold spraying occurs when the impact velocity surpasses a certain threshold, leading to a transition from plastic impact to hydrodynamic penetration. This transition results in strong erosion caused by the impacting particles. The velocity at which

deposition transitions to erosion, dependent on material and temperature, is termed the erosion velocity Verosion. The threshold for erosion due to particle penetration is experimentally established through impact tests. The calibration factors F1 and F2 are derived by aligning these experimental results with corresponding calculations (Schmidt $et\ al.\ 2006$).

The simulations indicated that material deformation in the bond zone could reach strain rates of up to 10^9 /s and strains of 10 or higher. A material deemed "sprayable" should sustain such extreme conditions of plastic flow without fracturing. Additionally, the simulations provided estimates of heating and cooling rates, with cooling rate being particularly crucial. In the bond zone, the cooling rate needed to balance low enough to promote shear instability yet high enough to allow the interface to solidify and complete the bonding process before particle rebound. Furthermore, the bond strength needed to withstand elastic "spring-back" forces to prevent particle detachment (Blazynski 2012; Schmidt *et al.* 2006).

Analytical descriptions of material deformation and heat transfer indicated that particle size can influence attainable interface temperatures, strain rates, and stress. In very small particles, shear instabilities may be impeded by high cooling rates resulting from intense temperature gradients within a small particle volume. This demonstrates that adiabatic shear instabilities cannot be automatically assumed to be adiabatic in small dimensions. The occurrence of these instabilities requires significant adiabatic straining. When the cooling rate in highly strained regions approaches the heating rate, shear instabilities are hindered or completely prevented. Additionally, smaller particles exhibit higher strain rates and more profound strain-rate hardening. Viscous shear strength in the jetting region is also higher for smaller dimensions, hindering localized deformation and increasing critical velocity. Furthermore, smaller particles experience higher quench rates during production and possess intrinsically higher strength due to finer microstructure, such as Hall-Petch hardening. Their higher surface-to-volume ratios may also result in higher impurity content, with surface contaminants like oxide shells significantly influencing bonding, potentially leading to an increased critical velocity for finer particles. For very small particles, the heat dissipation occurs extremely rapidly, leading to significantly lower maximum interface temperatures compared to larger particles. Small particles do not exhibit signs of shear instability. In contrast, larger particles, when impacting at high velocities, reach maximum interface temperatures near their melting points. Due to slower cooling rates, these larger particles remain at high temperatures for extended periods. Considering that particle bonding occurs through a diffusion process, the quality of the bond is likely influenced by the thermal history of the contact zone and possibly by the contact pressure. To evaluate shear instability, a threshold is used where bonding is considered sufficient if 20 % of the particlesubstrate interfaces exceed a temperature of 1000 K. This bonding criterion is employed to determine the critical velocities. Numerical simulations clearly indicate that heat conduction significantly impacts bonding in cold spraying. This effect can also be described analytically. The depth of heat diffusion can be estimated using Equation (2.3), where Δt represents the characteristic time scale, calculated based on particle diameter (Dp) and particle impact velocity at SoD (standoff distance) (Vp), and x represents the characteristic length, which depends on particle diameter. The value of particle impact velocity is analytically determined by taking a particle diameter of 25 μ m as the reference (Schmidt *et al.* 2006).

$$x = \sqrt{k \cdot \triangle t}, \quad k = \frac{\lambda}{Cp \cdot \rho}, \quad \Delta t = \frac{Dp}{Vp}, \quad x = \frac{Dp}{6}$$
 eq(2.3)
$$Dcritical = 36 \cdot \frac{\lambda}{Cp \cdot \rho \cdot Vp}$$
 eq(2.4)

Where λ represents the thermal conductivity of the powder particle in Wm⁻¹K⁻¹, ρ is the density in kg/m³, Cp signifies the specific heat capacity at constant pressure in J·kg⁻¹·K⁻¹. The material-dependent velocity for bonding should approximate this value. The characteristic length, chosen as an arbitrary fraction of the particle diameter, is used to calibrate this equation. Solving Equation (2.3) for particle diameter results in Equation (2.4), which defines a 'critical' particle diameter (*Dcritical*). For particles larger than this critical diameter, thermal diffusion is sufficiently slow to enable localized shear instability at the surface of an impacting spherical particle. Consequently, smaller particles would not achieve the necessary conditions for bonding (Schmidt *et al.* 2006).

In the cold spray process, particle temperature can be significantly elevated, with most influential factors being temperature-dependent. The region below the critical velocity (Vcr) indicates either a lack of bonding or minor erosion. The onset of jetting formation takes place at the velocity equivalent to critical velocity. As the velocity goes on increasing further leads to more pronounced jetting. The region above the erosion velocity (Verosion) signifies severe erosion or, for soft particles impacting a hard substrate, no deposition (Ozdemir 2023; Kim 2017). The range between Vcr and Verosion defines the sprayability window as illustrated in Figure 2.18. The deposition efficiency of ductile materials increases exponentially when the impact velocity past the Vcr (Hanft et al. 2015).

Kamaraj and Radhakrishnan (2019) devised coating diagrams for the cold spray process, using particle velocity and temperature as the primary coordinates. These diagrams incorporate contours representing velocity ratios at values of 0.5, 0.8, 1.0, 1.5, 2.0, and 2.5. These contours

serve as a predictive tool for estimating deposition efficiency, cohesive strength, and particle flattening ratio by establishing relationships between these properties and the velocity ratio. The expression for the velocity ratio (VR) is represented by the Equation (2.5) given below.

$$Velocity\ Ratio\ (VR) = \frac{Particle\ impact\ velocity\ at\ SoD\ (Vp)}{Critical\ velocity\ (Vcr)} \qquad eq(2.5)$$

In order to get very good deposition efficiency in the range of 80-100 %, velocity ratio should fall within the span of 1.1-2. Velocity ratios exceeding a value of 2 pose a risk of causing erosion to the substrate material and a decrease in the deposition efficiency. Therefore, it is of paramount importance to emphasize the optimization of cold spray process parameters, ensuring they are finely tuned to align with the specific velocity ratio, as this directly impacts the integrity and longevity of the coating or thick deposits (Kumar *et al.* 2017; Raletz *et al.* 2006).

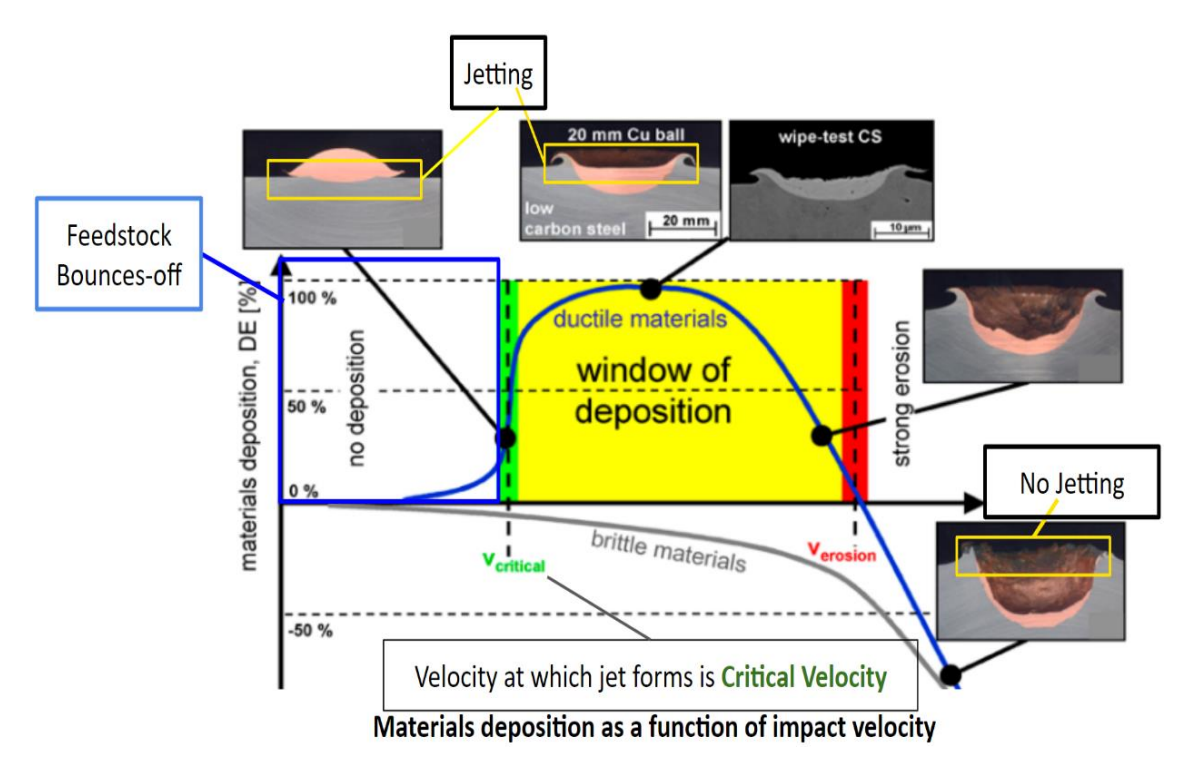


Figure 2.18 Graphical representation of material deposition as a function of impact velocity (Hanft et al. 2015)

2.5 COMPUTATIONAL FLUID DYNAMICS (CFD) & FINITE ELEMENT ANALYSIS (FEA) OF COLD SPRAY PROCESS

CFD and FEA have become essential tools for understanding and optimizing the cold spray process, offering detailed insights that enhance experimental findings. This overview examines

the key contributions and discoveries from CFD and FEA studies in the cold spray process, underscoring their importance in advancing this technology.

One of the seminal studies in CFD modeling of cold spray processes was carried out by Grujicic et al. (2004). They utilized CFD to simulate the gas flow and particle acceleration within a cold spray nozzle, providing foundational insights into the velocity and temperature distributions of particles within the supersonic gas jet. Assadi et al. (2003) contributed significantly to this comprehension by integrating CFD with particle trajectory calculations. Their research clarified the interconnection between gas dynamics and particle behavior, with a specific emphasis on the critical velocity required for successful deposition. They provided a theoretical framework for predicting the critical velocity based on material properties and process parameters. Meanwhile, Tabbara et al. (2011) conducted CFD analyses on nozzles with different cross-sectional shapes (square, elliptical, and circular) to investigate the effects of upstream powder injection on particle acceleration and distribution. These research works emphasized the critical role of nozzle design and gas flow parameters in attaining the necessary particle velocities for effective deposition. Ning et al. (2010) established a 2D CFD model for low pressure cold spray process employing both nitrogen and helium, which showed good agreement with the experimental findings using Schlieren imaging. They found that helium exhibited separation near the nozzle exit, potentially impacting the uniformity of particle velocity. The study highlighted the importance of drag coefficient in predicting particle velocities, with promising results for non-spherical particles using the Haider and Levenspiel correlation. Zahiri et al. (2014) calibrated a 3D CFD $k-\epsilon$ type model against the thermal history of the substrate exposed to the cold spray supersonic jet. They assessed the model's performance using measured temperature data for a titanium substrate subjected to cold spray nitrogen at 800 °C and 3 MPa, providing insights into critical parameters like domain meshing method, turbulence, and dissipation coefficients during spraying. Furthermore, they accounted for heat transfer and radiation effects in the de Laval nozzle employed in the experiments. Vadla and Doom (2018) analyzed step-drilled, conical, and curved nozzles using the SST (shear stress transport) turbulence model. They observed that the stepdrilled nozzle induced shock formation in the divergent section, causing significant fluctuations in pressure, temperature, and velocity. This nozzle also produced the lowest jet velocity both in the divergent section and at the substrate. In contrast, the curved nozzle performed best due to its design, which allowed for significant gas expansion and a smooth transition from convergent to divergent sections, avoiding sharp corners. Caruso et al. (2018) created a 3D RANS model for the low-pressure CS process, incorporating turbulence with the realizable model. They examined the particle impact through both one-way and two-way coupling approaches, concluding that the twoway coupling yielded more precise outcomes. They emphasized the importance of considering solid-gas interactions, highlighting that neglecting them could compromise accuracy. Li *et al.* (2012) and Karimi *et al.* (2006) created numerical models to examine gas flow and powder particle paths. Additionally, Zavalan and Rona (2023) introduced a Method of Characteristics-based design workflow for cold spray nozzles, which optimized the convergent-divergent nozzle through multiphase CFD. The optimized nozzle exhibited higher particle velocity (8-9 %), reduced variability (3.8 %), and improved particle deposition uniformity (22.6 %). Additionally, gas flow quality was enhanced, resulting in 75.6 % more dispersion of metal particles, potentially boosting deposition efficiency by 150 %.

Stoltenhoff et al. (2002) demonstrated through CFD simulations and spray tests that achieving adhesion necessitates powder particles exceeding 570 m/s for spherical copper powder. They employed nitrogen gas and 5-25 µm particles in order to achieve deposition efficiency over 70 %, yielding coatings with low porosity and oxygen content akin to the original powder feedstock. Chavan et al. (2019) conducted investigation on the influence of nozzle throat crosssection on coating microstructure and properties. Three nozzles with identical design Mach numbers but varying h/L (ratio of nozzle width at exit to divergent portion length) ratios were utilized. The nozzle with the smallest throat area exhibited inferior properties and microstructure, attributed to particle velocity distribution influenced by viscous boundary layer effects. The study reinforced Alkhimov et al. (2001) recommendations regarding nozzle design, highlighting the importance of h/L ratio greater than 0.02 for optimal coating performance and energy efficiency. Li and Li (2005) employed a discrete phase model to investigate the flow dynamics within cold spray, uncovering substantial impacts of parameters such as nozzle expansion ratio, particle dimensions, gas composition, operational pressure, and temperature on particle acceleration. Their results emphasized the importance of an expansion ratio of 6.25 for efficient particle acceleration at a standoff distance of 30 mm, achievable with both nitrogen (N₂) and helium (He) propellants, and a divergent section length of 40 mm. Winnicki et al. (2015) carried out numerical and experimental analyses on cold spray (CS), with a focus on spherical and dendritic copper particles. Analytical calculations and experimental measurements showed that spherical particles reached velocities of around 500 m/s, while dendritic particles attained speeds of about 550 m/s due to their irregular shapes causing increased drag force. Larger particles were more affected by gas pressure, whereas smaller particles were primarily influenced by temperature. Varadaraajan and Mohanty (2017) studied the influence of radial injection angle on the spatial distribution of powder particles exiting the CS nozzle. Lupoi and Neill (2011) studied four nozzle configurations, each with different acceleration channel lengths and powder injector geometries.

When powder was released axially and upstream of the nozzle throat, particle trajectories dispersed widely instead of staying centered, with particle stream size comparable to nozzle exit cross-section diameter upon impact. CFD analysis attributed this phenomenon to high gas turbulence near the nozzle throat and particle deflections from channel walls. Narrower beam formation was achievable with smaller diameter injectors and downstream injection of the powder. Neo et al. (2022) investigated the varying particle velocity across a broad spectrum of spray distances and powder feed rates during the cold spraying of Inconel 625. They experimented with standoff distances ranging from 3 to 40 cm, observing that the highest average velocity of 781 m/s occurred at a spray distance of 8 cm. Additionally, they noted that increasing the powder feed rate had minimal influence on particle velocity. Ning et al. (2007) investigated the effects of particle size and morphology on in-flight particle velocity and deposition efficiency, finding that irregularly shaped particles had higher velocities than spherical ones. Irregular particle velocity decreased from 390 to 282 m/s as size increased from 20 to 60 µm. Critical velocities were about 425 m/s for spherical copper particles and over 550 m/s for irregular ones. Preheating irregular particles at 390 °C for 1 hour reduced their critical velocity to 460 m/s. Larger particles exhibited lower critical velocities. Meng et al. (2011) examined the impact of gas temperature on the properties of cold sprayed 304 stainless steel coatings. They observed that porosity decreased from 6 % \pm 0.5 % at 450 °C to 2 % \pm 0.3 % at 550 °C, resulting in a denser coating structure. The cohesive strength of the coatings increased from 56 ± 4 MPa at 450 °C to 73 ± 3 MPa at 550 °C. Additionally, all coatings demonstrated enhanced corrosion resistance compared to the interstitial-free steel substrate. Sova et al. (2018) conducted experimental and numerical analyses, determining that a micronozzle with a 0.5 mm throat, 1 mm exit diameter, and 20 mm length was suitable for cold spray deposition of aluminum powder, achieving a spray spot diameter of no more than 1.7 mm. However, they found that the impact velocity of particles was lower, leading to reduced coating adhesion strength and increased porosity. Li et al. (2012) examined the gas and particle dynamics in the steady cold spray process, validating their simulations with experimental data from supersonic impinging jets. They discovered that the highest particle impact velocity occurred at a Stokes number of around one, and found that overexpanded nozzles were preferable due to their lower chamber pressure and slightly higher impact velocity. By employing a normal-shock model, they estimated particle impact speed based on the distance between the bow shock and the substrate, though further validation was required for overexpanded jets. Meyer et al. (2016) employed a 2D-axisymmetric Eulerian-Lagrangian model to study the effect of feed rate on particle acceleration. They used Stellite-6 (high density alloy) having spherical shape, and Alumina (lower density ceramic) with irregular morphology.

They found that increasing the feed rate significantly reduced mean particle acceleration during spraying, with both materials showing similar susceptibility to mass loading effects. The denser material exhibited more than twice the reactivity of the ceramic under volumetric loading conditions. These investigations underscored the significance of fine-tuning the parameters to optimize the cold spray process resulting in higher particle velocities, thereby enhancing deposition efficiency.

Samareh and Dolatabadi (2007) investigated the impact of substrate presence on gas flow in low-pressure cold spray nozzles via 3D CFD simulations. They revealed that standoff distance, shape, and gas interactions significantly influenced particle deposition. The optimal standoff distance which helped in minimizing stagnation pressure to 330 kPa was 10 mm from the nozzle exit. Cylindrical substrates induced less particle deviation but lower impact velocities than flat plates. High-pressure gradients and shocks particularly affected smaller particles (<25 µm), influencing their deposition and coating quality. Yin et al. (2012) employed a CFD code to examine how substrate size affects supersonic flow, particle acceleration, and temperature distribution in cold spray. Their findings showed that smaller substrate diameters resulted in higher particle impact velocities due to reduced bow shock formation. Additionally, they found that thicker substrates exhibited lower temperatures, indicating a need for higher inlet conditions during preheating. Ozdemir et al. (2019) introduced a computational method for simulating continuous heat generation in cold spray deposition at the macroscale, employing multicomponent finite volume methods and validated with literature data. It proved useful for controlling thermal energy distribution in coatings, particularly for thermally sensitive materials like those in electronics. The study showed that higher deposition rates resulted in slower substrate temperature rise due to fast dissipating thermal energy from particle impact. Also, in coatings and additive manufacturing, the thermal model monitored heating and cooling rates to detect potential failures caused by thermal expansion mismatches. Garmeh et al. (2023) investigated the impact of introducing an offset to the nozzle-substrate hole configuration on flow and particle conditions upon impact. They discovered that shifting the nozzle away from the hole's center reduced pressure inside the hole. This offset increased deposition in deeper holes, particularly along the edges, aiding in filling undeposited areas. Additionally, they found that reducing the hole diameter or increasing the hole depth significantly decreased the deposition rate.

The integration of CFD with other simulation techniques, such as finite element analysis (FEA), has enabled more comprehensive studies of the cold spray process. For example, Li *et al.* (2009) studied how simulation settings affect particle behavior in CS using ABAQUS/Explicit for

copper material (OFHC), highlighting the need for precise adjustments to accurately simulate processes like metal jetting, adiabatic shear instability, oxide film effects, and particle-substrate adhesion. Li and Gao (2009) employed ABAQUS/Explicit for three-dimensional modeling of particle impact behavior in cold spraying for copper and other materials. They evaluated various settings for material damage, ALE (arbitrary lagrangian eulerian) adaptive meshing, distortion control, and contact interaction. Their findings indicated that simulations with material damage effectively handled element distortion and provided more accurate results. Mesh size had less impact on results when material damage was included. While particle size had minimal effect on particle morphologies, it affected element failure at contact interfaces. Song et al. (2018) investigated residual stresses in a single-particle splat (Ti-6Al-4V) formed during the cold spray process, utilizing numerical simulations and direct measurements. They observed that insufficient temperatures around the south pole hindered diffusion, resulting in weakened bonding. Large compressive residual stresses were found near the top of the powder particle due to intense shock waves, while tensile residual stresses emerged near the bonding interface, attributed to adiabatic shear and material jetting. Minor compressive stresses were also noted at the south pole, with slight tensile stresses at the very top, indicating stress equilibrium. Benenati and Lupoi (2016) explored how varying incident angles affected the size of the compressive zone and residual stress, noting a correlation with density and yield stress. They observed that stress profiles at the interface remained continuous for the same material cases, while discontinuities arose due to differing mechanical properties. Moreover, they determined that depositing successive layers with a perpendicular relative orientation (90 degrees) resulted in a final product with reduced residual stress. Cavaliere and Silvello (2018) used finite element modeling to analyze particle behavior based on gas temperature, pressure, and particle properties. They repaired an IN 718 panel with a 30° V-notch using pure Ni particles via cold spray. The crack behavior of the V-notched sheets under bending loads was investigated through FEA and mechanical experiments. Sun et al. (2018) examined how the deposition characteristics of cold sprayed IN 718 particles on IN 718 substrates varied with different surface conditions. They suggested that heating the substrate positively influenced metallurgical bonding by increasing plastic dissipation energy and reducing flow stress and elastic strain energy. Moreover, they examined that at a substrate temperature of 450 °C, the maximum stress value and temperature at the contact were lower due to less particle deformation occurring under this condition. Estejab and Khalkhali (2023) used ABAQUS Explicit 2018 to explore HDPE and PU particle deposition on polymeric substrates. Unlike HDPE on PU, PU on HDPE caused more deformation in PU particles, with significant substrate deformation and increased contact area. For like-on-like HDPE deposition at room temperature, a critical velocity of 300 m/sec led to local melting of the semi-crystalline polymer. However, at 100 °C, deposition failed due to excessive plastic deformation exceeding a threshold of 6. PU particle deposition resulted in lower stress and temperatures compared to HDPE. Ghelichi et al. (2011) developed a 3D finite element model to compute the critical velocity in cold spray coating, employing Abaqus 6.9-1 Explicit for numerical analysis and Python 2.4-1 for processing Abaqus outputs and conducting numerical tests to detect shear instability and critical velocity. The results were in good agreement with experimental results. This improved accuracy was credited to a specific mathematical approach for identifying shear instability. Saleh et al. (2014) analyzed cold spray particle deposition using the SPH (smooth particle hydrodynamics) modeling method, uncovering particle interactions and layer adhesion through "micro-welding," where particles bonded via thin molten bands. Microstructural studies and modeling supported the kinetic origin of the heat source. The Johnson-Cook model and Mie-Grüneisen EOS (equation of state) effectively represented adhesive interactions among CS particles, allowing the study of microscopically thick coatings. The model accurately reproduced particle shape and stress states, validated against experimental data. It showed significant plastic deformation at the particle periphery, where localized heating likely facilitated adhesion. Ghelichi et al. (2014) developed a two-step simulation approach to determine the final residual stress state, considering grit blastinginduced stresses, particle size distribution, random impact positions, and particle velocity and temperature. The first step employed FEA/Explicit simulation, while the second incorporated annealing effects using the Zenner-Wert-Avrami method based on experimental data. The model's accuracy was validated through XRD measurements, which showed good agreement with experimental data, except at the substrate surface due to unmodeled particle bonding. Longer coating times and higher process temperatures significantly relieved residual stress, whereas shorter times and lower temperatures resulted in less stress relief. Loke et al. (2021) investigated the impact of spray angle on Al6061 alloy coating deposited on Al6061 substrate, employing experimental and modeling approaches. Single-splat deposition simulations indicated peak shear stresses at 60-65° angles, declining sharply beyond 70°, with highest interfacial PEEQ (equivalent plastic strain) strains at 50°. Experimental tensile adhesion tests showed maximal bond strength at 60° and lowest at 90°, correlating with simulations revealing decreased interfacial-bonded material with increasing spray angle. Neutron and x-ray diffraction confirmed equi-biaxial stress state in coatings, with higher compressive residual stresses at 50° spray angle, aligning with FEA results indicating increased shear stress as spray angle decreased below 70°. Chen et al. (2016) observed that in the perpendicular case, an outward metal jet was formed along the entire rim of the deposited particle, sinking into the substrate to create an inverted cone shape.

When the spray angle was reduced to 75°, a metal jet formed only on one side, along the tangential direction, leaving a noticeable gap between the particle and substrate on the other side due to the tangential velocity component. King *et al.* (2010) explored copper particle impact on aluminum during cold spray deposition, revealing localized deformation and higher interfacial temperatures on aerospace alloy 7050 compared to softer commercially pure aluminum. At low velocities on the harder substrate, deformation was evenly shared between particle and substrate. Penetrative regime was reached at higher velocities on 7050 alloy. Jetting in particles was suppressed due to substrate deformation absorption of impact energy, enhancing deposition efficiency at high velocities. Adiabatic shearing in the crater wall caused temperature rise to melting point, confirming experimentally observed melting and formation of intermetallic phase CuAl₂ due to eutectic melt diffusion.

2.6 COLD SPRAY BASED ADDITIVE MANUFACTURING (CSAM)

Cold spray technology has found extensive application across diverse industries, spanning aerospace, automotive, energy, medical, marine, and more, primarily for coating purposes. These coatings offer effective protection against high temperatures, corrosion, erosion, oxidation, and chemical damage (Guo *et al.* 2022; Kumar 2022). In recent times, cold spray has emerged as a promising additive manufacturing technique for creating both standalone metal components and restoring damaged ones. This advancement not only brings a fresh perspective to traditional additive manufacturing methods but also widens the scope of applications for cold spray technology (Li *et al.* 2018; Yin *et al.* 2018). As a newcomer to the additive manufacturing domain, Cold spray based additive manufacturing (CSAM) inherits the advantages of cold spray while presenting unique benefits compared to fusion-based techniques like selective laser melting (SLM), electron beam melting (EBM), and laser metal deposition (LMD). A comparison given in Table 1 reveals CSAM's strengths, notably shorter production times, scalability to larger product sizes, enhanced flexibility, and suitability for repairing damaged components. Notably, CSAM excels in processing high-reflectivity metals such as copper and aluminum, which pose challenges for laser-based methods (Yin *et al.* 2018).

Currently, CSAM is primarily used to fabricate components with rotational symmetry, such as cylinder walls, tubes, and flanges. It can also create complex structures like array fin heat exchangers, metal labels, and 2D codes with the assistance of well-designed mandrels, spindles, or masks (Yin *et al.* 2018). CSAM's versatility extends to repairing damaged components across various industries, notably aerospace, due to its flexibility and ability to preserve the original properties of the substrate material. This method significantly reduces costs compared to

component replacement. While still an emerging technology, CSAM has garnered increasing attention for its applications and research efforts in recent years (Ashokkumar *et al.* 2022; Hegab *et al.* 2023; Kahhal *et al.* 2024; Prashar and Vasudev 2021).

Table 2.1 Comparison: CSAM Versus Other Fusion-Based Additive Manufacturing Approaches (Yin *et al.* 2018)

	CSAM	SLM	EBM	LMD	
Powder Feed Mode	Direct Deposition	Powder Bed	Powder Bed	Direct Deposition	
Feedstock Limitations	Difficulty Processing High Hardness and Strength Metals	Difficulty Processing High Reflectivity and Poor Flowability Metals	Unsuitable for Non-Conductive and Low Melting Temperature Metals	Difficulty with High Reflectivity Metals	
Powder Melting	No	Yes	Yes	Yes	
Product Size	Large	Limited	Limited	Large	
Dimensional Accuracy	Low	High	High	Medium	
Mechanical Properties (AF)	Low	High	High	High	
Mechanical Properties (HT)	High	High High		High	
Production Time	Short	Long	Long	Long	
Equipment Flexibility	High	Low	Low	Low	
Suitable for Repair	Yes	No	No	Yes	

2.6.1 Manufacturing Parameters for CSAM

The quality of the deposition process in CSAM is heavily influenced by various manufacturing parameters, including propulsive gas conditions (such as pressure, temperature, and type), powder feeder settings (powder feed rate), and nozzle parameters (traverse speed, scanning step, standoff distance, spray angle, and trajectory) as depicted through detailed schematic in Figure 2.19. These

factors play a crucial role in determining the quality of the deposited material (Prashar and Vasudev 2021; Li et al. 2020).

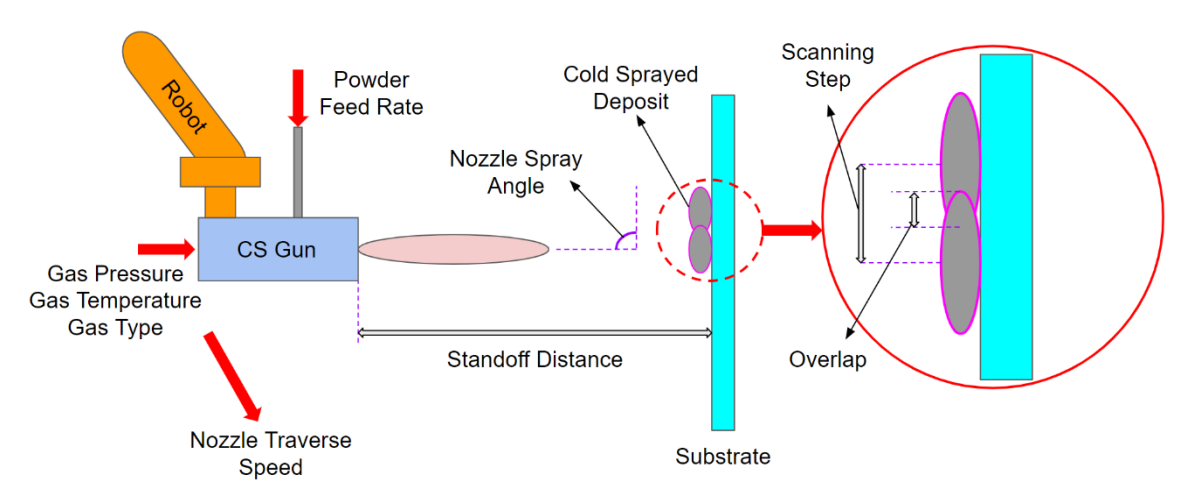


Figure 2.19 Diagrammatic view of the manufacturing parameters for cold spray based additive manufacturing

Table 2 provides an overview of typical deposit properties and their correlation with manufacturing parameters. A comprehensive understanding of these parameters is essential for devising optimal CSAM manufacturing strategies and ensuring high-quality products.

Table 2.2 Typical Properties of Deposits Affected by CSAM Manufacturing Parameters

	Porosity	Deposit Strength	Adhesion	Residual Stress	Deposition Efficiency
Gas pressure ↑	↓	↑	1	1	↑
Gas temperature ↑	↓	↑	1	↑	↑
Gas molecular weight ↑	1	↓	↓	1	↓
Powder feed rate ↑	↑	\downarrow	\downarrow	1	\downarrow
Traverse speed ↑	1	↑	1	↓	↑
Scanning step	×	×	×	×	×
Standoff distance ↑	0	0	0	0	0
Spray angle ↑	↓	1	1	1	1
Trajectory	×	×	×	×	×

^{&#}x27;↑' increase, '↓' decrease, 'o' relevant but no common view, '×' no data available

2.6.1.1 Propulsive Gas Parameters for CSAM

Propulsive gas parameters stand out as the most critical factors in CSAM manufacturing, directly influencing particle impact velocity and consequently, deposit properties. Typically, gasses like helium, nitrogen, and air are employed, with gas pressure and temperature ranging from 0.5 to 6.0 MPa (5 bar to 60 bar) and 25 to 1000 °C, respectively. Elevated gas pressure, temperature, or lower molecular weight lead to higher particle impact velocities (Yin et al. 2016). Helium usage yields the highest particle velocities, albeit at a higher cost. Increasing gas temperature proves more effective than raising gas pressure (Yin et al. 2016). The consensus in the cold spray community supports the notion that higher particle impact velocities enhance deposit properties. Experimental studies affirm that boosted velocities improve deposition efficiency, reduce porosity, enhance deposit strength, and promote adhesion due to fewer inherent defects and enhanced metallic bonding (Vilardell et al. 2015; Bagherifard and Guagliano 2020). Higher impact velocities result in increased deposit hardness, albeit with higher residual stress due to intensified plastic deformation (Luzin et al. 2011; Shayegan et al. 2014; Cavaliere and Silvello 2015). However, elevated gas temperatures mitigate residual stress through in-situ annealing, minimizing the impact of temperature increase on residual stresses (Ghelichi et al. 2014; Luo et al. 2014; Sun et al. 2020; Li et al. 2020).

2.6.1.2 Powder Feeder Parameters for CSAM

The powder feed rate is defined as the quantity of powder introduced into the cold spray nozzle per unit time. It is a critical parameter in CSAM that influences deposit properties in three primary ways. Firstly, the powder feed rate greatly influences the flow stream through the nozzle, thereby affecting particle velocity (Meyer et al. 2017; Meyer et al. 2016; Ozdemir et al. 2017). As the feed rate increases, strong gas-particle interactions reduce particle velocity, resulting in higher porosity and decreased deposition efficiency, hardness, and tensile strength. However, typical CSAM feed rates of 10-30 g/min have a minimal effect on particle velocity (Ozdemir et al. 2017). Secondly, the feed rate affects the thickness and profile of the deposit. Higher rates produce thicker deposits with sharper profiles, similar to the effect of nozzle traverse speed, requiring consideration of both parameters together (Pattison et al. 2007; Sova et al. 2013). Lastly, high feed rates can cause localized residual stresses between the deposit and substrate, leading to potential delamination (Ozdemir et al. 2017; Taylor et al. 2006). Therefore, maintaining a moderate powder feed rate is essential for achieving optimal deposit properties in CSAM.

2.6.1.3 Nozzle Parameters for CSAM

2.6.1.3.1 Nozzle Traverse Speed

Nozzle traverse speed directly affects the spray duration and the amount of feedstock powder impacting the target surface per unit time, influencing the deposit thickness and cross-sectional profile of a single-track deposit (Ozdemir *et al.* 2017; Sova *et al.* 2013; Fang *et al.* 2010; Kotoban *et al.* 2017; Tan *et al.* 2017). Generally, a lower nozzle traverse speed results in a thicker, sharper deposit, similar to the effect of a higher powder feed rate (Pattison *et al.* 2007; Sova *et al.* 2013). This variation in deposit thickness and profile is due to the different amounts of feedstock powder released per unit time and area, with both lower traverse speeds and higher feed rates releasing more powder. The change in track profile is also influenced by the flow characteristics of the propulsive gas through a supersonic nozzle, where particle velocity and deposition efficiency are higher at the center than at the edges, creating a Gaussian-shaped cross-section (Champagne *et al.* 2011; Tabbara *et al.* 2011; Yin *et al.* 2014). The sloped sides of the deposit affect the deposition efficiency of subsequent layers, leading to steeper slopes with decreased traverse speed and increased feed rate. Therefore, in CSAM applications, controlling the thickness and profile of a single-track deposit requires careful coordination of nozzle traverse speed and powder feed rate (Pattison *et al.* 2007; Sova *et al.* 2013).

Nozzle traverse speed significantly affects the microstructure and properties of the deposit. As traverse speed decreases, deposit density increases, but mechanical properties such as elastic modulus, deposit strength, and adhesion strength with the substrate decline (Tan *et al.* 2017; Rech *et al.* 2014; Moridi *et al.* 2014). Higher traverse speeds lead to increased porosity (Tan *et al.* 2017). At the lowest speeds, deposits may delaminate from the substrate due to low adhesion strength and high residual stresses (Ozdemir *et al.* 2017; Tan *et al.* 2017). Studies have also reported frequent delamination at low traverse speeds and high powder feed rates (Ozdemir *et al.* 2017). Additionally, lower traverse speeds cause higher temperatures in the deposit and substrate due to the high-temperature impinging jet, which aids the deposition process but induces thermal stresses at the interface (Tan *et al.* 2017; Yin *et al.* 2015).

2.6.1.3.2 Nozzle Scanning Step

In CSAM, deposits are formed by nozzle scanning across the target surface in a pre-defined trajectory, layering line by line. This process creates a deposit by stacking multiple single-track deposits, often using an overlapping strategy where adjacent tracks overlap. The interval between the centerlines of two tracks, known as the scanning step, significantly affects the uniformity of deposit thickness and surface morphology. Typically, the scanning step is set to half the single-

track width to ensure a flat surface (Kumar and Pandey 2022; Yin and Lupoi 2021). However, recent findings suggest that a more precise selection of the scanning step can yield a smoother surface. For instance, using a self-developed software called Toolkit, researchers found that a 4 mm scanning step resulted in more consistent deposit thickness than a 7 mm step, highlighting the importance of scanning step optimization in CSAM (Cai *et al.* 2014). Despite this, studies on the impact of varying scanning steps are limited, and further research is needed to fully understand its effects on deposit properties.

2.6.1.3.3 Nozzle Trajectory

The nozzle trajectory in CSAM is the path followed by the nozzle during the process, crucial for ensuring homogeneous deposit density and properties. On flat surfaces, a simple zig-zag pattern is typically used due to its ease and effectiveness in creating uniform deposits (Rech *et al.* 2014). For complex curved surfaces, however, maintaining consistent standoff distance, spray angle, and nozzle traverse speed is essential to prevent inhomogeneity (Lynch *et al.* 2013). Trajectory planning for such surfaces is often done using CAD/CAM software on an off-line programming platform to accurately control nozzle parameters and adapt to surface topography (Yin *et al.* 2018). A recent study introduced a novel spiral trajectory for repairing damaged aluminum coupons, where the nozzle traverse speed varied inversely with crater depth to produce a uniform deposit. This approach resulted in a final flat repaired surface with minimal excess material, though it could lead to nonhomogeneous microstructure due to varying traverse speeds (Chen *et al.* 2017). Despite the potential benefits, research on nozzle trajectory strategies remains sparse, necessitating further exploration and innovation in this area.

2.6.2 Properties of CSAM Deposits

Numerous studies have investigated the properties of CSAM deposits. Typically, as-fabricated CSAM deposits contain compressive residual stress due to peening stress accumulation between layers (Luzin *et al.* 2011; Suhonen *et al.* 2013). This stress can be alleviated through post-spray annealing (Coddet *et al.* 2015; Coddet *et al.* 2014). Initially, these deposits exhibit inferior mechanical properties, such as lower ductility, electrical conductivity, and thermal conductivity, compared to bulk materials or fusion-based additive manufacturing materials, owing to inherent defects in cold sprayed deposits (Bagherifard *et al.* 2017). However, appropriate heat treatments can significantly enhance these mechanical properties, bringing them to levels comparable to bulk materials.

2.6.3 Defects of CSAM Deposits

CSAM deposits commonly exhibit defects such as micro-pores and inter-particle boundaries, resulting from insufficient particle plastic deformation and poor inter-particle bonding during deposition. These defects are particularly prevalent in as-fabricated deposits with low particle impact velocity and significantly impair mechanical properties. For CSAM copper deposits, micro-pores are rarely present, even at low impact velocities, due to copper's excellent ductility and low strength-to-density ratio (Raoelison *et al.* 2016). Consequently, inter-particle boundaries are the primary defects affecting copper deposits. In contrast, materials like steel, Ni-based superalloys and titanium, with higher hardness or strength-to-density ratios, frequently exhibit micro-pores in addition to inter-particle boundaries (Meng *et al.* 2011; Goldbaum *et al.* 2011). Both types of defects negatively impact the mechanical properties (yield strength, ultimate tensile strength and elongation) of these deposits. Studies have shown that increasing particle impact velocity to enhance plastic deformation or applying post-heat treatments to induce recrystallization can mitigate the adverse effects of these defects (Huang *et al.* 2015; Ito and Ogawa 2014; Gärtner *et al.* 2006; Stoltenhoff *et al.* 2006; Borchers *et al.* 2005; Sudharshan *et al.* 2007; Sundararajan *et al.* 2010; Winnicki *et al.* 2017; Sundararajan *et al.* 2013).

Increasing particle impact velocity is the most straightforward method to reduce micro-pores and enhance inter-particle bonding in CSAM deposits (Assadi *et al.* 2003; Bae *et al.* 2009; Gärtner *et al.* 2006). Higher impact velocities increase particle deformation, preventing micro-pore formation, and promote chemical reactions at inter-particle boundaries, resulting in improved metallurgical bonding (Bae *et al.* 2009; Assadi *et al.* 2003; Gärtner *et al.* 2006).

Heat treatment is also effective in reducing deposit defects, particularly at inter-particle boundaries (Huang *et al.* 2015; Ito and Ogawa 2014; Gärtner *et al.* 2006; Stoltenhoff *et al.* 2006; Borchers *et al.* 2005; Sudharshan *et al.* 2007; Sundararajan *et al.* 2010; Winnicki *et al.* 2017; Sundararajan *et al.* 2013). After annealing, recrystallization within particles and across interparticle boundaries repairs these defects. This process transforms the grain structure into fine equiaxed grains, making the inter-particle boundaries less visible or even completely eliminating them (Huang *et al.* 2015; Li *et al.* 2006).

2.7 OVERVIEW ON ADDITIVE MANUFACTURING OF INCONEL 718

Inconel 718 (IN 718) is a precipitation-hardened superalloy based on nickel-chromium-iron, modified with niobium (Sonar *et al.* 2021). It is renowned for its exceptional mechanical properties across a broad temperature range, making it ideal for high-strength, creep-resistant, and fatigue-resistant applications up to 700 °C (Behera and Behera 2022). This alloy is notable for its

good weldability due to sluggish precipitation kinetics and is highly valued for its superior high-temperature strength, resistance to fatigue, wear, and hot corrosion. These properties, coupled with its favorable weldability, render IN 718 suitable for high-temperature applications in aircraft, gas turbines, turbocharger rotors, nuclear reactors, liquid-fueled rockets, and other structural and corrosive environments (Hosseini and Popovich 2019; Nnaji *et al.* 2020; Kumar *et al.* 2021).

The microstructure of IN 718 consists of a γ solid solution matrix rich in Ni, Cr, and Fe, along with precipitates of coherent phases such as metastable γ'' Ni₃(Nb, Al, Ti) and γ' Ni₃(Al, Ti). The stable δ phase Ni₃(Nb) is crucial for controlling grain growth and enhancing mechanical properties, as it replaces the γ'' phase near grain boundaries due to high Nb concentration during heat treatment (Kumar *et al.* 2021; Dehmas *et al.* 2011; Manikandan *et al.* 2019; Strondl *et al.* 2008). Conventional processing methods for IN 718 pose significant challenges, including excessive tool wear, work hardening, and low material removal rates during room temperature machining (Mahesh *et al.* 2021; De Bartolomeis *et al.* 2021). High-temperature forming processes can also be problematic due to the segregation of refractory elements like Nb and Mo, leading to the formation of the Laves phase, which undermines material strength, ductility, fatigue, and creep rupture properties by depleting essential elements and promoting crack initiation and propagation (Radhakrishna *et al.* 1997; Sonar *et al.* 2021; Li *et al.* 2018).

The need for advanced manufacturing techniques becomes evident when fabricating complex components from IN 718. Various studies have explored the microstructure of additively manufactured (AMed) IN 718 in both as-deposited and post-heat treated states using different metal additive manufacturing (MAM) processes such as selective laser melting (SLM) (Nadammal *et al.* 2017; Popovich *et al.* 2017; Mostafa *et al.* 2017; Wang *et al.* 2016; Pröbstle *et al.* 2016), electron beam melting (EBM) (Strondl *et al.* 2008; Kirka *et al.* 2016; Sames *et al.* 2014; Kirka *et al.* 2017; Deng *et al.* 2017), directed energy deposition (DED) (Unocic *et al.* 2014; Tayon *et al.* 2014), and directed laser deposition (DLD) (Qi *et al.* 2009; Zhao *et al.* 2008; Parimi *et al.* 2014; Tian *et al.* 2014; Liu *et al.* 2013; Liu *et al.* 2011). The as-built SLM IN 718 microstructures typically features a laminar structure with prominent columnar γ dendrites in the X and Y planes and an equiaxial structure in the Z-plane, indicating rod-shaped grains elongated in the Z-direction (Wang *et al.* 2016; Gong and Chou 2016; Gong *et al.* 2015). This columnar structure extends through multiple layers due to partial remelting of previous layers and heterogeneous nucleation of γ dendrites, known as epitaxial growth (Wang *et al.* 2016; Gong and Chou 2016; Gong *et al.* 2015).

The crystallographic texture of AMed IN 718 is influenced by local heat flow directions and competitive grain growth in one of the six (001) preferred growth directions of the fcc structure

(Gribbin *et al.* 2019). The texture can range from strong cube texture to fiber texture or even random texture, depending on process parameters such as power input and scanning strategy (Strondl *et al.* 2011; Parimi *et al.* 2012). The (001) texture is particularly beneficial for high-temperature creep-fatigue applications and can be utilized as a design parameter to develop site-specific load-adaptive properties (Popovich *et al.* 2017).

Porosity is another critical feature of powder-based AMed IN 718. Ensuring the final product's density and the absence of cracks is crucial for acceptance. Circular-shaped pores typically result from gas entrapment in the molten metal, while irregular-shaped 'lack of fusion' pores arise from incomplete feedstock fusion during manufacturing. Cracks may result from AM-induced residual stresses or from solidification or liquation cracking (Qi *et al.* 2009; Sames *et al.* 2014).

The microstructure of AMed IN 718 varies along the building height due to the height-dependent thermal profile (Parimi *et al.* 2012; Wang *et al.* 2016; Wang and Chou 2015; Sames *et al.* 2014; Deng *et al.* 2018). The bottom layers, in direct contact with the build substrate plate, experience higher cooling rates, resulting in finer dendrites compared to the coarser columnar dendrites in the top layers (Gong and Chou 2016; Gong *et al.* 2015). Micro-segregation in AMed IN 718 is primarily manifested as Nb and Mo-rich Laves phase (Liu *et al.* 2013; Aydinöz *et al.* 2016; Ma *et al.* 2015). Lower cooling rates at the top layers usually lead to a higher percentage of Laves phase, which can form a thick and continuous network (Gong and Chou 2016; Gong *et al.* 2015). Generally, the high cooling rates in AMed processes result in a microstructure that is significantly finer than that of cast materials (Liu *et al.* 2011). While cast IN 718 shows macro-segregation of Nb and Mo elements, the as-built AMed alloy's microstructure is characterized by a supersaturated solid solution with inter-dendritic micro-segregation (Chlebus *et al.* 2015). Process parameters such as heat input, scanning rate, and scanning strategy significantly influence the microstructure of AMed IN 718, directly impacting the local mechanical properties (Parimi *et al.* 2014; Zhong *et al.* 2005; Jia and Gu 2014).

The complex solidification and cooling process during AMed inhibits efficient precipitation of strengthening phases, resulting in non-equilibrium phases, micro-segregation, and high residual thermal stresses in the as-deposited build (Zhang *et al.* 2015; Gribbin *et al.* 2016). Post-heat treatment processes are typically employed to improve the microstructure and mechanical properties of AMed IN 718 builds.

The AMS 5664E standard for IN 718 includes a hot-isostatic pressing (HIP) step before homogenization to close existing pores and flaws by plastic flow (Popovich *et al.* 2017). After HIP, the material undergoes solution or homogenization treatments to control δ and Laves phase precipitation, followed by aging steps to form strengthening phases (Slama and Abdellaoui 2000).

In AMed IN 718, the as-built microstructure typically contains brittle Laves and δ phases due to micro-segregation of Nb and Ti (Zhang *et al.* 2015; Deng *et al.* 2018; Li *et al.* 2018). Solution heat treatment aims to dissolve these phases and homogenize the distribution of Ti, Al, and Nb, facilitating effective precipitation of γ' and γ'' during subsequent aging treatments (Zhang *et al.* 2015; Raghavan *et al.* 2017; Deng *et al.* 2017).

For wrought IN 718 (AMS 5663), typical post-heat treatment includes solution annealing at 980 °C for 1 hour followed by double aging at 720 °C for 8 hours and 620 °C for 8 hours (Benn and Salva 2010; Zhang *et al.* 2015). However, this temperature may not fully dissolve Laves and other micro-segregated phases in AMed IN 718 (Tucho *et al.* 2017), leading to Nb-rich areas and enhanced δ phase formation at the expense of γ' and γ'' (Li *et al.* 2018). Therefore, higher solution/homogenization temperatures (around 1080 °C) are recommended for AMed IN 718 to ensure uniform Nb distribution and prevent acicular δ phase precipitation during subsequent solution treatment (Zhao *et al.* 2008; Benn and Salva 2010; Kuo *et al.* 2017; Zhang *et al.* 2015; Kuo *et al.* 2017).

Without homogenization, solution treatment leads to Nb-enriched areas and acicular δ phases within and at grain boundaries (Zhang *et al.* 2015). Conversely, a solution treatment following homogenization results in needle-shaped δ precipitates at grain boundaries (Zhang *et al.* 2015; Deng *et al.* 2018; Li *et al.* 2018; Cao *et al.* 2018; You *et al.* 2017), which pin the boundaries and impede grain growth and sliding during high-temperature exposure (Li *et al.* 2018). Post-homogenization/solution treatment, γ' and γ'' strengthening phases form during aging, improving strength and ductility. For example, a double aging treatment after homogenization at 1080 °C can yield superior mechanical properties compared to wrought IN 718 (Zhang *et al.* 2015; Deng *et al.* 2018; Li *et al.* 2018; Cao *et al.* 2018; You *et al.* 2017).

HIP, widely used in the casting industry, is also employed for AMed IN 718 to remove internal porosity and flaws (Chang 2009). The HIP process, involving high-pressure and temperatures between 1150 °C and 1280 °C, causes recrystallization, significant microstructural changes, and dissolution of Laves and δ phases (Unocic *et al.* 2014; Brenne *et al.* 2016; Popovich *et al.* 2019; Seede *et al.* 2018; Lee *et al.* 2006). Treatment duration depends on component size, and temperatures above ~1200 °C can cause excessive grain growth (Rao *et al.* 2006).

Grain size and morphology differ significantly between AMed IN 718 treated with solution treatment alone and those undergoing combined homogenization and solution treatments. Solution treatment alone results in partial recrystallization and fine grain size, while the combined approach leads to extensive recrystallization and serrated grain boundaries due to needle-shaped δ

precipitates, which enhance creep properties by restricting grain boundary sliding (Popovich *et al.* 2017; Zhang *et al.* 2015; Popovich *et al.* 2019).

High-temperature homogenization (>1100 °C) or HIPing causes complete recrystallization, eliminating deposition layer boundaries and reducing anisotropy by removing the preferential (001) texture along the building direction (Popovich *et al.* 2019; Raza *et al.* 2018; Bird and Hibberd 2009).

SLM IN 718 under different heat treatment conditions shows varying microstructures. Rapid solidification and high cooling rates during SLM inhibit the precipitation of strengthening phases, leading to lower mechanical strengths in the as-built condition (Strondl *et al.* 2008; Unocic *et al.* 2014; Pröbstle *et al.* 2016; Sames *et al.* 2014). Direct aging (720 °C for 8 hours + 620 °C for 8 hours) precipitates γ' and γ'' but does not alter dendrite size or Laves phase morphology. Solution treatment allows efficient γ' and γ'' precipitation during aging. Solution treatment at 930 °C leads to significant fine δ plate precipitation, while higher temperatures dissolve δ phase, improving the overall microstructure and mechanical properties (Pröbstle *et al.* 2016; Zhang *et al.* 2015; Qi *et al.* 2009; Chlebus *et al.* 2015).

Numerous studies have examined the tensile behavior of AMed IN 718 across different methods, such as DLD (Qi et al. 2009; Zhao et al. 2008; Liu et al. 2011; Kuo et al. 2017), SLM (Popovich et al. 2017; Soller et al. 2016; Wang and Chou 2017; Trosch et al. 2016; Tillmann et al. 2017; Raghavan et al. 2017; Kuo et al. 2017; Brenne et al. 2017; Xia et al. 2016; Smith et al. 2016), and EBM (Kirka et al. 2016; Cakmak et al. 2016; Strondl et al. 2011; Kirka et al. 2017; Deng et al. 2017).

Notably, as-built IN 718 is rarely used without precipitation hardening treatment, making heat-treated properties more relevant. The as-built alloy shows lower strength but higher ductility due to the lack of γ' and γ'' precipitation hardening phases. Comparison of SLM and EBM as-built IN 718 indicates higher strength for EBM, likely due to in-situ precipitation hardening at higher processing temperatures (Deng 2018). Most reported strength values for AMed IN 718 falls between those of cast and wrought alloys, with AM showing superior strength to cast due to finer microstructure (Brenne *et al.* 2016) and inferior properties to wrought due to porosity (Pröbstle *et al.* 2016; Wang *et al.* 2012; Gribbin *et al.* 2016).

Tensile anisotropy in AMed IN 718 reveals higher ductility but lower yield/ultimate strength and elastic modulus for samples loaded parallel to the build direction, attributed to $\langle 001 \rangle$ texture and columnar grain morphology (Popovich *et al.* 2017; Benn and Salva 2010; Ni *et al.* 2017; Saint *et al.* 2016; Chlebus *et al.* 2015; Amato *et al.* 2012; Smith *et al.* 2016; Deng *et al.* 2017). The elastic

modulus is significantly lower in the build direction, and string-like pores aligned parallel to the build direction may reduce strength in the perpendicular direction (Deng *et al.* 2017).

The anisotropy in ductility is linked to different cracking mechanisms in tensile loading, with columnar grain boundaries facilitating damage accumulation and failure (Ni *et al.* 2017). Studies show spatial dependency of tensile properties within AMed builds, with varying observations for EBM and SLM due to process differences (Kirka *et al.* 2016; Deng *et al.* 2017).

Low-temperature solution treatment enhances strength while reducing ductility, whereas HIP improves ductility at the cost of strength. Aging treatments increase strength but reduce ductility due to γ' and γ'' precipitation (Unocic *et al.* 2014; Raghavan *et al.* 2017; Zhang *et al.* 2015; Smith *et al.* 2016). High-temperature annealing enhances ductility with minor strength loss, and AMed IN 718 shows a more pronounced strength drop at high temperatures compared to wrought alloy (Trosch *et al.* 2016).

Spatial hardness variation depends on the specific AM technique and process parameters, with higher hardness often reported at the bottom of builds due to repetitive heating cycles (Stevens *et al.* 2017; Tian *et al.* 2014; Wang *et al.* 2016; Zhang *et al.* 2011). Minimal differences in hardness are observed between planes parallel and perpendicular to the build direction (Stevens *et al.* 2017; Konečná *et al.* 2016; Gribbin *et al.* 2016; Strondl *et al.* 2011). AM process parameters significantly impact hardness, with increased input energy affecting Laves phase formation and γ'' precipitation. Fine microstructures from AM processes enhance hardness, but post-process heat treatment is necessary to meet the minimum hardness requirements of wrought IN 718 (Stevens *et al.* 2017; Parimi *et al.* 2012; Wang *et al.* 2012).

Fatigue behavior studies of AMed IN 718 for different AM processes generally indicate inferior fatigue endurance compared to wrought alloys, especially at lower stress amplitudes due to stress concentrations from pores. Surface condition significantly affects fatigue performance, with machined specimens showing much longer endurances than as-fabricated ones. Surface defects and process-induced pores are primary factors in reduced fatigue life (Johnson *et al.* 2017; Kelley *et al.* 2016; Johnson *et al.* 2016; Brenne *et al.* 2016; Aydinöz *et al.* 2016).

Anisotropy in fatigue response shows lower endurance for samples loaded parallel to the build direction. Proper heat treatments, such as HIP and surface machining, can improve fatigue properties to levels comparable to wrought IN 718. However, surface defects remain a critical factor in fatigue performance (Kelley *et al.* 2016; Konečná *et al.* 2016).

Strain-controlled fatigue tests reveal similar trends, with AMed IN 718 exhibiting inferior endurance due to defects. Cyclic deformation behavior includes initial hardening followed by softening and brittle failure. Elevated temperature fatigue tests indicate varying endurance

depending on stress amplitudes and heat treatment, with post-process treatments enhancing high-temperature fatigue life by dissolving brittle phases and forming grain boundary restrictions (Johnson *et al.* 2017; Sui *et al.* 2017; Popovich *et al.* 2018; Konečná *et al.* 2016; Aydinöz *et al.* 2016; Gribbin *et al.* 2016; Kirka *et al.* 2017). Micro-lattice of AMed IN 718 structures show lower endurance compared to dog bone specimens due to poor surface finish and stress concentration at intersections, highlighting the importance of internal surface quality for fatigue performance (Huynh *et al.* 2016).

Creep properties of AMed IN 718 have been studied across various manufacturing methods: directed laser deposition (DLD) (Zhao *et al.* 2008; Kuo and Kakehi 2017), selective laser melting (SLM) (Hautfenne *et al.* 2017; Kuo *et al.* 2017; Brenne *et al.* 2017; Pröbstle *et al.* 2016; Brenne *et al.* 2016; Xu *et al.* 2018; Xu *et al.* 2018; Kuo *et al.* 2018) and electron beam melting (EBM) (Kuo *et al.* 2018; Strondl *et al.* 2011; Shassere *et al.* 2018). Comparative studies with wrought IN 718 show mixed results; some (Kuo and Kakehi 2017; Kuo *et al.* 2017; Xu *et al.* 2018; Xu *et al.* 2018; Kuo *et al.* 2018) indicate inferior creep properties for AM variants, while others (Brenne *et al.* 2017; Pröbstle *et al.* 2016; Shassere *et al.* 2018) report superior performance. These discrepancies arise due to variations in manufacturing processes, heat treatments, and surface conditions.

Pröbstle *et al.* (2016) linked the superior creep properties of SLM IN 718, particularly in the primary creep regime, to processing-induced sub-grains. Additional factors such as enhanced niobium availability for γ'' precipitation hardening, solid solution strengthening, and the presence of smaller δ precipitates also contribute to improved performance under compressive loads (Brenne *et al.* 2017; Pröbstle *et al.* 2016).

Conversely, Strondl *et al.* (2011) attributed shorter creep rupture times in EBM IN 718 to process-induced porosity leading to premature failure. Xu *et al.* (2018) found that as-built SLM IN 718 exhibited poor creep performances due to surface defects and unfavorable microstructures, although heat and surface treatments significantly enhanced creep rupture times. Kuo *et al.* (2018) compared the creep responses of SLM and EBM IN 718 with wrought alloys, reporting shorter rupture durations for both AM variants. Heat treatment plays a crucial role in creep performance.

The δ phase significantly impacts the creep behavior of AMed IN 718. While small amounts of needle-shaped δ precipitates at grain boundaries can control grain boundary sliding and improve low-stress, high-temperature creep performance, non-optimal heat treatments may lead to extensive γ'' transformation to δ , forming precipitation-free zones and accelerating creep void formation (Kuo *et al.* 2017; Kuo *et al.* 2018).

Anisotropy in creep behavior has been noted, with better performance for specimens loaded parallel to the build direction (Hautfenne *et al.* 2017; Kuo *et al.* 2017; Strondl *et al.* 2011). Inferior performance in perpendicular loading is linked to δ phase presence at grain boundaries perpendicular to the stress direction, facilitating rapid creep cavity formation (Hautfenne *et al.* 2017; Strondl *et al.* 2011). EBM builds exhibit more significant anisotropy due to their larger, elongated grains and strong $\langle 001 \rangle$ texture, leading to better creep performance when loaded parallel to the build direction. Shassere *et al.* (2018) found that HIPed EBM IN 718 with large columnar grains loaded parallel to the build direction outperformed wrought alloys and samples loaded perpendicularly.

Porosity and residual stress are significant issues in AMed parts, affecting their mechanical integrity. Porosity in AMed IN 718 arises from various mechanisms, including insufficient melting, shrinkage during cooling, entrapped processing gas, and pre-existing voids in powder feedstock (Qi et al. 2009; Schaak et al. 2016). Strategies to reduce porosity include optimizing AM process parameters and post-process treatments (Qi et al. 2009). Valdez et al. (2017) demonstrated the impact of porosity on mechanical properties, showing that higher porosity levels lead to premature crack formation, low ductility, and inferior stress rupture properties. Porosity also affects the endurance of materials under cyclic loading conditions (Zhao et al. 2008; Tillmann et al. 2017; Schaak et al. 2016). Gas-containing pores in high-temperature applications, like turbine blades, can cause internal stress and accelerate crack formation (Tillmann et al. 2017; Schaak et al. 2016).

The distribution of porosity within a build depends on AM process parameters, with varying trends reported in the literature (Parimi *et al.* 2012; Parimi *et al.* 2014; Amsterdam and Kool 2009). Increased heat energy or pre-heating generally reduces porosity by forming larger melt pools with lower viscosity, allowing better fusion and gas escape (Qi *et al.* 2009; Sames *et al.* 2014). However, excessive heat input can cause turbulent melt pools, increasing gas-contained porosity (Parimi *et al.* 2014; Sames *et al.* 2014; Huynh *et al.* 2016).

Hot-isostatic pressing (HIP) is a post-processing technique used to close internal porosity, but it is less effective for gas-containing pores or those near the surface (Schaak *et al.* 2016; Aydinöz *et al.* 2016). Encapsulation can help close surface-adjacent pores during HIP (Aydinöz *et al.* 2016). Residual stress, resulting from high-temperature gradients during AM processes, significantly affects mechanical integrity. The techniques for measuring residual stress include X-ray and neutron diffraction, layer removal, and Vickers indentation (Cao *et al.* 2013; Liu *et al.* 2011; Tillmann *et al.* 2015; Lu *et al.* 2015). Residual stresses depend on AM process type and

parameters, with EBM generally producing lower residual stresses due to high pre-heating temperatures (Raghavan *et al.* 2016; Sochalski-Kolbus *et al.* 2015; Prabhakar *et al.* 2015).

Pre-heating the substrate affects cooling rates and residual stress development (Tucho *et al.* 2017; Feng *et al.* 2017; Gribbin *et al.* 2016; Sames *et al.* 2014). EBM's higher pre-heating temperature significantly reduces residual stresses (Sames *et al.* 2014). Layer thickness, heat input, and overlap rate also influence residual stresses, with increased overlap rates generally reducing residual stresses (Cao *et al.* 2013; Mukherjee *et al.* 2017). Residual stresses impact mechanical integrity characteristics like fatigue performance, fracture toughness, and crack growth behavior (Mukherjee *et al.* 2017). They also drive static recrystallization during post-process heat treatment, affecting grain size distribution (Cao *et al.* 2013; Liu *et al.* 2011; Zhang *et al.* 2015).

The mentioned processes have inherent limitations; rapid solidification in AMed IN 718 creates a microstructure featuring a supersaturated γ matrix, along with the presence of Laves phase and limited γ'' and γ' particles. Essential heat treatment is imperative to dissolve the Laves phase and optimize the precipitation of γ'' and γ' . In comparison to the wrought alloy, the fatigue performance of AMed IN 718 is inferior due to defects from additive manufacturing and subpar surface quality. Moreover, additive manufacturing-induced defects like porosity significantly impede the creep behavior of AMed IN 718 under tensile creep conditions. Additionally, the microstructure and texture of AMed IN 718 exhibit notable variations between directions parallel and perpendicular to the building direction, leading to mechanical response anisotropy. Furthermore, the presence of elevated thermal residual stresses and phase transformations compromises the mechanical integrity of AMed IN 718 (Qi *et al.* 2009; Slama and Abdellaoui 2000; Pröbstle *et al.* 2016; Zhao *et al.* 2008; Parimi *et al.* 2014; Bird and Hibberd 2009; Zhang *et al.* 2015; Feng *et al.* 2017).

Traditional thermal spray techniques, such as plasma (Ramesh *et al.* 2011) or flame spraying (Lyphout *et al.* 2012; Lyphout *et al.* 2011; Lyphout *et al.* 2014), melt Inconel 718 powders propelled towards substrates, forming coatings ranging from a few hundred microns to 2.7 mm thick. However, these methods often result in high porosity levels, ranging from 2.2 % to 3.2 % for atmospheric plasma spray (APS) (Ramesh *et al.* 2011) and 0.5 % to 2.2 % for high velocity oxy-fuel (HVOF) spray (Lyphout *et al.* 2012; Lyphout *et al.* 2011; Lyphout *et al.* 2014). Research indicates that HVOF coating adhesion strength (72.2–124.7 MPa) is influenced by powder velocity and temperature, with higher velocities associated with lower porosity but higher oxide content (Lyphout *et al.* 2012). Moreover, Young's modulus of Inconel 718 coatings varies between surface and cross-section measurements, both lower than that of the Inconel 718 coupon (Lyphout *et al.* 2014).

Recent advancements in cold spray (CS) technology have enabled the deposition of IN 718 coatings, leveraging the kinetic energy of metallic powders while minimizing thermal input (Schmidt et al. 2006). Micron-sized metallic powders propelled by pressurized inert gasses like N₂ or He, reach supersonic velocities upon impact with substrates, inducing severe localized plastic deformation and adiabatic shear instability at the powder-substrate/powder-powder interface if velocities surpass a critical threshold (Vcr) (Wang and Zhang 2013). Impact velocities below Vcr result in powder rebounding off the substrate, while excessively high velocities (greater than $2 \times Vcr$) cause substrate erosion instead of adhesion. Vcr is influenced by factors like powder materials, size, temperature, and substrate composition, highlighting the need for precise control over spray parameters (Wang and Zhang 2013). Cold spray is known for its lowtemperature process, reducing thermal stresses and improving material properties (Xu et al. 2021). It creates a refined microstructure with lower oxide and porosity, suitable for temperaturesensitive and high thermal conductivity applications (Zhang et al. 2021). It offers high bonding strength, faster deposition rates, and enables the fabrication of complex geometries without size limitations. Additionally, it is a potentially eco-friendly process having reduced energy consumption and emissions.

Karthikeyan et al. (2004) were among the first to showcase the practicality of depositing IN 718 using the CS technique back in 2004. Their work laid a foundational understanding of the process parameters and feasibility of achieving successful IN 718 coatings through cold spraying. Mauer et al. (2017) provided a comprehensive analysis by comparing the experimentally derived particle velocities of IN 718 powder which is cold sprayed using varied particle sizes with values predicted through model calculations. Ma et al. (2019) produced IN 718 alloy coating via cold spraying, employing diverse propelling gasses. Their findings indicate superior adhesive strength when using helium instead of nitrogen. Additionally, the research reveals a direct relationship between the adhesive strength and the pressure of the propelling gas. Kim et al. (2015) highlighted a significant challenge in creating thick deposits via CS, primarily attributed to the accumulation of compressive residual stresses across the coating's depth. Bagherifard et al. (2017) conducted a comparison between the microstructure and mechanical characteristics of IN 718 samples manufactured by CS in as-built and aged states. They also examined as-built selective laser melting (SLM) samples. The findings indicated that the aged CS samples exhibited elevated tensile strength compared to the as-built SLM samples. Also, the attained properties were close to bulk IN 718 properties.

Wong et al. (2013) investigated the impact of particle velocity and post-heat treatment on the tensile strength and ductility of cold sprayed coatings. Coatings sprayed at higher particle velocity

showed lower porosity (1.9-2.7 %) than those at lower velocity (3.2-3.8 %), with porosity unaffected by subsequent heat treatment. Notably, heat treatment at 1250 °C for 1 hour caused significant interparticle metallurgical bonds in the higher velocity coatings, likely due to sintering effects and high initial impact velocities. This resulted in enhanced ductility, with Inconel 718 coatings sprayed at 787 m/s and heat-treated at 1250 °C achieving a ductility of 24.7 % and a tensile stress of 763.6 MPa, approximately 62 % of the bulk material's strength.

Singh *et al.* (2018) studied the effect of coating thickness on residual stress and adhesion strength in cold sprayed IN 718 coatings on IN 718 substrates using N₂ as a propelling gas. They found that mechanical properties improved with increasing thickness, approaching the bulk value of IN 718. Residual stresses were predominantly compressive, influenced by peening during deposition, with a potential for relaxation via dynamic recovery and recrystallization. Compressive residual stress decreased with thicker coatings. Adhesion strength decreased with increasing thicknesses, predicted using the energy-release-rate criterion and influenced by residual stress. Predicted values closely matched measured ones, decreasing with thicker coatings in the presence of residual stresses, independent of thickness when residual stresses were absent.

Singh *et al.* (2017) examined how substrate roughness and spray angle affect the deposition of cold sprayed IN 718. Using N₂ as a carrier gas at 950 °C and 4 MPa, dense coatings (≈98 % density) were successfully applied to IN 718 substrates. The study found that substrate roughness significantly impacts deposition efficiency and particle deformation, with smoother substrates showing less localized plastic deformation. An optimal roughness of about 3 μm was suggested. Deposition efficiency and coating density were greatly influenced by substrate roughness and spray angle, while Vickers hardness remained unaffected. Deposition efficiency is reduced with a decrease in spray-angle, while the coating porosity and coating roughness show an inverse trend. Coating roughness was more dependent on spray angle, with standoff distance having minimal effects.

Ma *et al.* (2019) studied the microstructural and mechanical properties of high-performance cold sprayed IN 718 alloy coatings using N₂ and He as propelling gasses. They found that higher gas temperatures or pressures increased particle velocity, with He providing greater acceleration, resulting in deeper embedding and more deformation of particles on substrates. N₂-processed coatings had reduced porosity at higher pressures, with a minimum of 1.84 % at 7 MPa, while He-processed coatings were nearly fully dense at 0.21 % porosity. Adhesive strength improved with higher gas pressures, reaching 132.6 MPa for N₂ at 7 MPa and 582 MPa after heat treatment, and 435.4 MPa for He in the as-sprayed state, increasing to 899.4 MPa post-heat treatment. Both types exhibited brittle behavior in tensile tests, with elongation below 0.6 %, but He-sprayed

coatings had higher UTS due to better inter-particle bonding and lower porosity. Post-heat treatment significantly improved UTS, elongation, and Young's Modulus, with fracture morphology showing metallurgical bonding features.

Pérez-Andrade *et al.* (2019) explored the optimization of IN 718 thick deposits through cold spray processing and annealing. Analysis of powder microstructures and properties proved crucial in selecting appropriate spray parameters and predicting deposit qualities. As-sprayed deposits exhibited porosities <2 % with clear particle deformation features. Enhanced formation of $M_{23}C_6$ carbides and δ phase was noted in HIP-annealed conditions due to higher dislocation density induced by deformation at increased process gas temperatures. The complex balance of residual stresses was attributed to thermal and peening effects, as well as random particle packing conditions and temperature variations between the substrate and deposited layers. Porosity results suggested that a solution + aging treatment was adequate for achieving deposit porosities below 1 %, rendering HIPing treatment non-mandatory.

Zhang *et al.* (2021) compared the deposition of Inconel 718 coatings using CS and APS. In this investigation, PG 718 powders were employed for CS, while Amdry 718 powders were used for APS, with each technique optimized for best performance. The CS coatings retained the morphology, composition, and crystallinity of the original PG 718 powders, resulting in higher hardness (510.4–527.3 HV_{200g}, 8.2 GPa) and compressive residual stress (-30.5 \pm 12.5 MPa), although they were denser (0.2–0.5 %) and more brittle. Conversely, APS coatings were more porous (0.8–1.5 %), with grains aligned in lamellar structures and lower hardness (227.5–252.2 HV_{200g}, 3.9 GPa), but exhibited higher tensile residual stress (254.4 \pm 33.3 MPa). Adhesion strength was marginally higher for APS (76.4 \pm 6.1 MPa) compared to CS (74.0 \pm 12.1 MPa), and APS also demonstrated superior tensile strength and ductility. Solution heat treatment was found to reduce the compressive stress and hardness of CS coatings, thereby improving their ductility.

2.8 PROBLEM FORMULATION

2.8.1 Scope

In preceding sections, an extensive and thorough review of literature concerning various metal additive manufacturing technologies and thermal spray based processes has been presented. This review has specifically focused on their applicability to challenging materials, such as the nickel based superalloy Inconel 718. The discussion has encompassed the various limitations and issues associated with different types of additive manufacturing. Notably, the cold spray based additive manufacturing process is highlighted for its efficiency in producing specialized components, characterized by relatively fast production times and minimal defects like porosity or material

oxidation. Despite its advantages, there has been limited investigation into the use of the cold spray based additive manufacturing process for the fabrication of 3D shapes of IN 718 superalloy. This is primarily due to the alloy's limited deformability, as well as the microstructural changes and phase transformations that occur during the process. Furthermore, the review has included detailed analyses of computational fluid dynamics and impact deformation in the context of the cold spray process. Based on this comprehensive literature survey, several critical research gaps have been identified, indicating areas where further study is needed. The research gaps could be broadly classified into two main categories as shown below:

1. Gas Dynamics and Particle Deformation

a. The detailed description of the bonding mechanism, critical velocity, and window of deposition underscores the importance of ensuring that the particle impact velocity at SoD (Vp) exceeds the critical velocity (Vcr) for proper jetting formation. The region below *Vcr* indicates insufficient bonding or minor erosion. Jetting formation begins at the velocity equivalent to Vcr, and as the velocity increases, the jetting becomes more pronounced. The region above the erosion velocity (Verosion) signifies severe erosion. Effective jetting formation is crucial for the bonding of powder particles to the substrate and to each other. The velocity ratio (VR) is a key indicator of deposition efficiency, and a parametric analysis of the cold spray process conditions on VR is essential to determine the most suitable parameter set for the IN 718 superalloy. To achieve a high deposition efficiency, ranging from 80-100 %, VR should be within 1.1-2. Velocity ratios exceeding 2 risk causing erosion to the substrate material and decreasing deposition efficiency. Therefore, it is crucial to optimize the cold spray process parameters, ensuring they are finely tuned to achieve the specific VR that directly impacts the integrity and longevity of the coating or thick deposits.

Hypothesis: Optimizing VR within the range of 1.1 to 2 will enhance deposition efficiency and bonding quality of IN 718 superalloy coatings, while minimizing substrate erosion and improving the overall integrity of the deposited material.

b. A comprehensive survey of the literature on CFD studies of the cold spray process has been conducted. However, a thorough analysis of gas dynamics and particle trajectories has not been explored. It is essential to investigate the effects

of highly turbulent flow on the velocity and temperature of IN 718 powder particles. Additionally, the impact of fluctuations in flow characteristics due to shock waves has not been examined. The literature lacks studies on how changes in powder injection angle affect heat transfer and temperature distribution. Specifically, the effect of varying powder injection angles on the average particle impact temperature and velocity of IN 718 superalloy powder remains unexplored. Moreover, there is no research on how different injection angles influence particle distribution after exiting the nozzle. Furthermore, the impact of a circular substrate on gas attributes and the resultant particle impact velocity and temperature of IN 718 superalloy also needs investigation. These gaps highlight the necessity for in-depth research to understand the interaction between turbulent flow, shock waves, injection angles, and substrate presence, which could significantly enhance process control and improve the performance of IN 718 coatings or thick deposits.

Hypothesis: Variations in powder injection angles significantly affect the average particle impact temperature, velocity, and distribution of IN 718 superalloy particles, which in turn influence the coating quality and performance.

c. Several studies have investigated impact deformation analysis following the collision of powder particles with both the substrate and each other. However, none have established a direct connection between optimizing outcomes from CFD analysis—specifically, particle impact temperature and velocity of IN 718 superalloy—and their use as inputs for impact deformation studies involving single- and multiple particles. Additionally, there have been limited efforts to correlate findings from impact simulations with experimental results using scanning electron micrographs. These gaps underscore the need for research that integrates CFD-optimized parameters with impact deformation studies and validates these findings through experimental observation. Such efforts could significantly advance understanding and control of the cold spray process for IN 718 superalloy applications.

Hypothesis: The integration of CFD-optimized parameters, specifically particle impact temperature and velocity, will provide a more accurate predictive model for impact deformation in IN 718 superalloy particles during collisions.

2. Fabrication of 3D Standalone Inconel 718 Thick Deposits

a. An extensive literature review on the additive manufacturing of IN 718 superalloy has been conducted. Metal additive manufacturing technologies and traditional thermal spray based processes used for IN 718 face significant challenges, including limited deformability, microstructural changes, and phase transformations. Cold spray based additive manufacturing offers crucial advantages over these methods. However, there is limited literature specifically addressing the additive manufacturing of IN 718 superalloy. There is a critical need for research focused on fabricating thick deposits of IN 718 for industrial use, utilizing optimized parameters set. This gap underscores the necessity for further investigation into cold spray processes tailored to IN 718, ensuring that they meet industrial standards for quality, efficiency, and reliability. Addressing these research gaps could significantly advance the application of cold spray technology in producing robust IN 718 components for various industrial applications.

Hypothesis: Optimizing cold spray process parameters will lead to improved mechanical properties and microstructural integrity of thick deposits of IN 718 superalloy, making them suitable for industrial applications.

b. The literature review highlights the microstructural changes and phase transformations in IN 718, a superalloy with a γ solid supersaturated solution matrix rich in Ni, Cr, and Fe. It contains coherent precipitates such as metastable γ" (Ni₃(Nb, Al, Ti)) and γ' (Ni₃(Al, Ti)). The δ stable phase (Ni₃(Nb)), which is incoherent with the γ fcc matrix, is crucial for the alloy. During the post-heat treatment, the δ phase precipitates and elongates, replacing the γ" phase near grain boundaries due to high Nb concentration. It is helpful in controlling grain growth and enhancing mechanical properties. Studies on additively manufactured IN 718, in both as-deposited and post-heat treated states using various metal additive manufacturing processes, reveal inherent limitations. Rapid solidification in AMed IN 718 results in a supersaturated γ matrix, the presence of the Laves phase, and limited γ" and γ' particles. Heat treatment is necessary to dissolve the Laves phase and optimize γ" and γ' precipitation. Compared to wrought alloy, AMed IN 718 shows inferior fatigue performance due to additive manufacturing defects and poor surface quality. Defects like porosity hinder the

creep behavior of AMed IN 718 under tensile creep conditions, while elevated thermal residual stresses and phase transformations further compromise its mechanical integrity. Traditional thermal spray techniques, such as HVOF, plasma and flame spraying, melt Inconel 718 powders and propel them towards substrates, often resulting in high porosity levels and oxide content. Recent advancements in CSAM enable the deposition of 3D standalone IN 718 thick deposits. Microstructural characterization, chemical composition analysis, phase analysis, density determination, porosity, microhardness analysis and mechanical property evaluation needs to be performed for investigating the developed IN 718 thick deposits using CSAM. These analyses will collectively provide a comprehensive understanding of the quality, performance, and suitability of the IN 718 thick deposits fabricated using CSAM for industrial applications.

Hypothesis: Optimized cold spray based additive manufacturing of IN 718 can produce dense, thick deposits with controlled microstructure and phase stability, minimizing defects and enhancing mechanical integrity, thus achieving industrial-grade properties superior to conventional methods.

2.8.2 Research Objectives

The primary objective of this study is to investigate cold spray based additive manufacturing of IN 718 superalloy. Based on research gaps identified through a comprehensive literature review, the following research objectives have been established for this work.

- 1. To establish cold spray based additive manufacturing for fabricating thick standalone geometries: A Proof-of-Concept Study.
- 2. To perform parametric analysis for successful cold spray deposition of IN 718 superalloy.
- 3. To investigate the impact of injection angle on powder stream and carrier gas characteristics in cold spray deposition of IN 718 superalloy.
- 4. To perform discrete phase computation fluid dynamics and impact deformation (single- & multi-particle) study of cold spray deposition of IN 718 powder feedstock on SS 304 substrate pipe with experimental validation.
- 5. To develop 3D standalone IN 718 thick deposits using cold spray based additive manufacturing and benchmark with respect to microstructure, microhardness

and mechanical properties.

2.8.3 Plan of Study

In this study, the research plan followed is given as under:

- 1. The study aimed to establish cold spray based additive manufacturing (CSAM) for fabricating thick standalone deposits using materials that are difficult to weld, form, and fabricate, including pure Ti (which is also temperature-sensitive) and Ni-20Cr. The choice to initially use Ti and Ni-20Cr as coating materials for proof-of-concept studies was strategic. Titanium was selected due to its highly pyrophoric nature when deposited using other thermal spray techniques. By employing cold spray, the study aimed to assess the capability of this method to safely and effectively deposit Ti, even using irregularly shaped particles, showcasing the process's advantages in minimizing oxidation and maintaining material properties. Ni-20Cr was chosen for its relevance in high-temperature and corrosive environments, similar to IN 718, but with simpler processing requirements. Studying Ni-20Cr first allowed for the evaluation of particle impact, bonding mechanisms, and deposition quality without the complexities inherent to IN 718. These initial materials provided foundational insights into cold spray performance, including particle behavior, bonding, and defect minimization, serving as a preparatory step before transitioning to the more challenging IN 718. The microstructure, mechanical properties and high-temperature cyclic oxidation behavior of bulk materials manufactured through CSAM were evaluated, with investigations into the influence of pre- and post-heat treatment techniques such as hot-isostatic pressing and substrate heating. Given that microstructure significantly influences material properties, the objective was to identify the most effective and efficient methods for fabricating materials with desired structural properties. To develop a proof-of-concept, two studies focusing on the cold spray deposition of thick deposits of pure Ti and Ni-20Cr were conducted. The accumulated knowledge and capabilities were then utilized to develop industryrelevant real-life components of IN 718 superalloy owing to its widespread applicability and the challenges they present during processing.
- 2. A parametric analysis was conducted for the successful cold spray deposition of IN 718 superalloy using a two-level full factorial approach (TLFA) with Minitab. This method investigated the effects of various cold spray process parameters, including main gas pressure inlet, main gas temperature inlet, deltaP (the difference between

carrier and main gas pressure inlet), powder particle flow rate, standoff distance, and powder particle diameter, on the velocity ratio (VR). VR, being a crucial indicator of deposition efficiency, was used as the output response for optimizing the process parameters. The cold spray process parameters were optimized according to the average size (D_{50}) of the IN 718 superalloy powder, and their effectiveness was also evaluated for other particle distributions. TLFA proved to be particularly valuable for analyzing the effects of independent variables and their interactions.

- 3. The effect of injection angle on the powder stream and carrier gas characteristics in the cold spray deposition of IN 718 superalloy was examined using the optimized set of process parameters. Cold spray nozzles with diverse powder injection angles were numerically modeled using IN 718 as the powder feedstock and nitrogen as the process gas. Gas flow field simulations and particle trajectory analyses were conducted for various injection angles, employing the k-ω SST (shear stress transport) model.
- 4. A discrete phase CFD study was conducted to analyze the impact deformation (both single- and multi-particle) of IN 718 powder feedstock deposited on a SS 304 substrate pipe, followed by experimental validation. The optimized cold spray process parameters were employed in the CFD modeling. The particle impact velocity and temperature at the standoff distance (SoD) were used as inputs for the impact deformation analysis. This analysis was further validated using scanning electron microscopy (SEM) micrographs of single and multiple IN 718 particles.
- 5. To support the manufacturing process, fixtures were developed, and robotic programming was implemented, facilitating the precise deposition of thick IN 718 layers on pipe substrate using cold spray technology. Following the deposition process, microstructural characterization, chemical composition analysis, phase analysis, density measurement, porosity assessment, microhardness and mechanical testing were performed to thoroughly evaluate the quality, performance, and suitability of the IN 718 thick deposits for industrial applications.

This methodical approach, as illustrated in the research plan schematic Figure 2.20, integrates material selection, advanced analytical techniques, and practical manufacturing solutions to address the complexities through cold spray additive manufacturing for IN 718 superalloy, ultimately aiming to enhance its industrial application and performance.

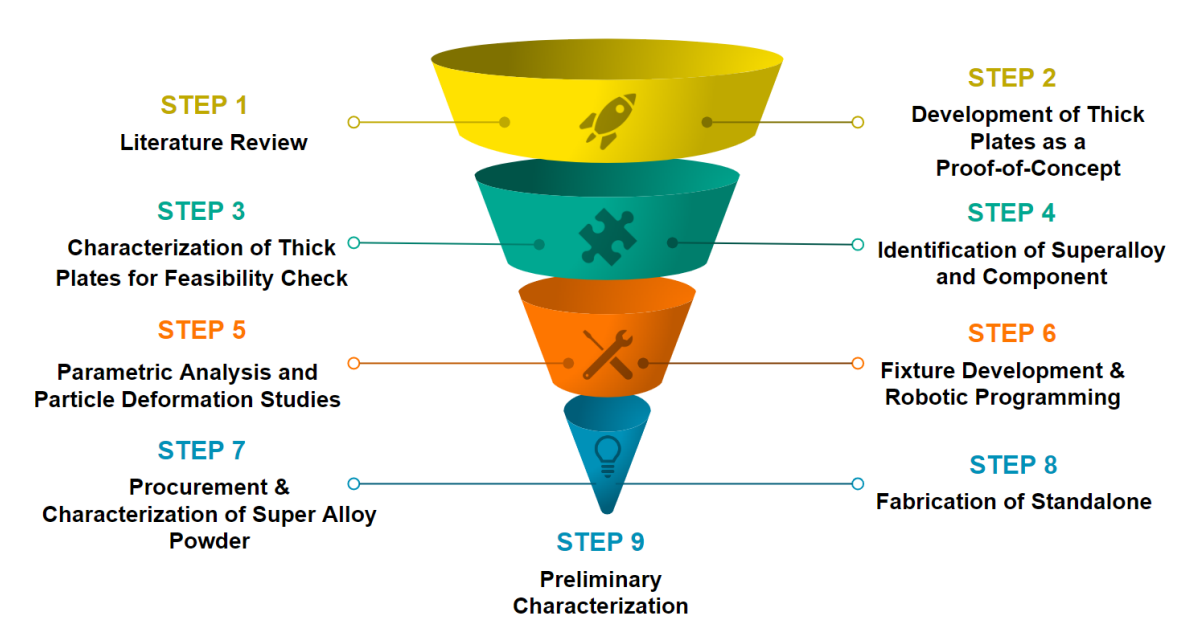


Figure 2.20 Schematic showing the research plan

CHAPTER 3

EXPERIMENTAL TECHNIQUES AND PROCEDURES

This chapter details the experimental techniques and procedures employed for the development and characterization of cold spray based additive manufacturing of pure Ti and Ni-20Cr thick deposits, demonstrating proof-of-concept, as well as the creation of a 3D standalone IN 718 thick pipe deposit. This chapter will also include the discussion regarding the methodology used for the two-level full factorial approach (TLFA), CFD numerical modeling, and impact deformation analysis. These methods were applied to optimize cold spray process parameters, investigate the effect of powder injection angle on the powder stream and carrier gas characteristics, and conduct discrete phase computational fluid dynamics and impact deformation (single- and multi-particle) studies of cold spray deposition of IN 718 powder feedstock onto an SS 304 substrate pipe.

3.1 MATERIALS

3.1.1 Proof-of-Concept

3.1.1.1 Substrate

To develop thick deposits of materials such as pure Ti and Ni-20Cr as a proof-of-concept, IN 718 was used as the substrate material. The chemical composition of IN 718 is detailed in Table 3.1. An as-cast IN 718 block, sourced from Rajasthan Metals (Bangalore, India), was machined to the required dimensions. Using a wire cut electric discharge machine (w-EDM) (Electronika, India), samples measuring 50 mm x 20 mm x 3 mm were cut from the block. The average roughness (R_a) of the top surface for cold spray deposition on all samples was measured at 5 μ m. This measurement was obtained using a surface roughness tester (Mitutoyo, Gurgaon, India) after the w-EDM process.

Table 3.1 Chemical composition of IN 718 substrate used in cold spray based additive manufacturing of pure Ti and Ni-20Cr

Elements	Ni	Cr	Fe	Nb	Mo	Al	Ti	Mn	Cu	C,S,P
Percentage (Wt%)	51.4	17.4	20.1	5.1	3.07	1.66	0.83	0.02	0.02	0.4

3.1.1.2 Thick Deposits

3.1.1.2.1 Pure Ti Deposits

The flowchart as depicted in Figure 3.1 represents the experimental procedure adopted to develop and characterize thick Ti deposits fabricated using cold spray based additive manufacturing process. Pure titanium powder (Praxair Surface Technologies, Indianapolis, IN, USA), ranging in size from 11 to 45 µm, and having an irregular shape was employed as a feedstock material. Scanning Electron Microscopy (SEM) (Jeol, 6610LV, Japan) micrographs of pure Ti feedstock powder are demonstrated in Figure 3.2 (a) and 3.2 (b). It can be seen that particles are having an irregular morphology with an angular particle shape. The Energy Dispersive Spectroscopy (EDS) (Oxford, 51-ADD0013) examination of the powder revealed the existence of only the Ti phase (99.95%), as displayed in Figure 3.3. The carbon traces in the EDS data could be attributed to the carbon tape used during analysis to avoid the charging effect of electrons.

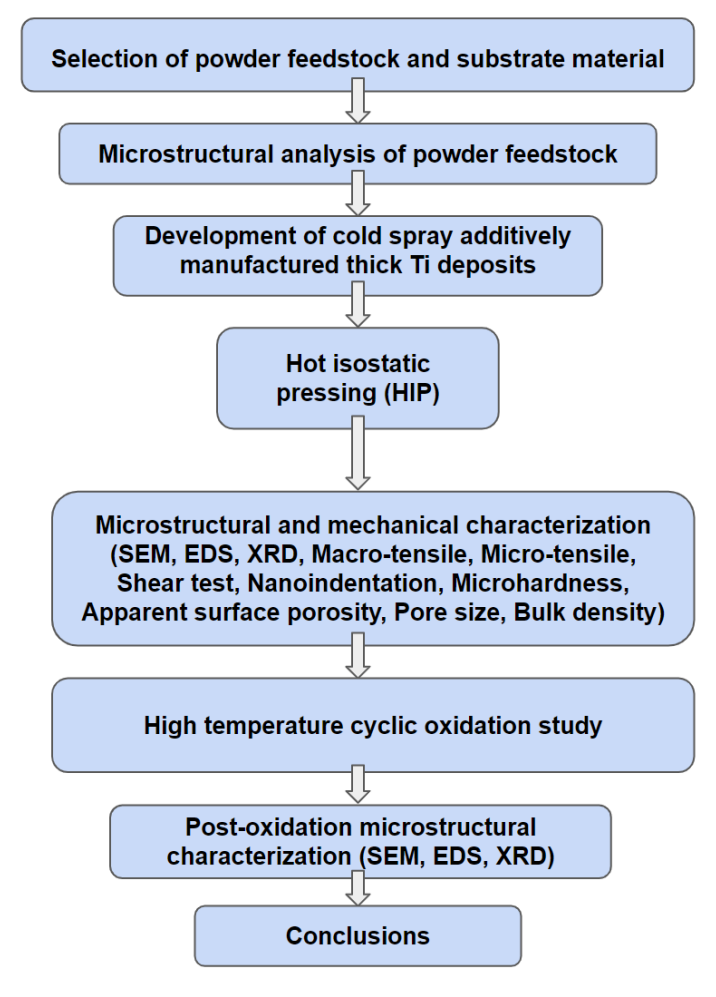


Figure 3.1 A flow chart representing the experimental procedure adopted to develop and characterize thick Ti deposits using CSAM

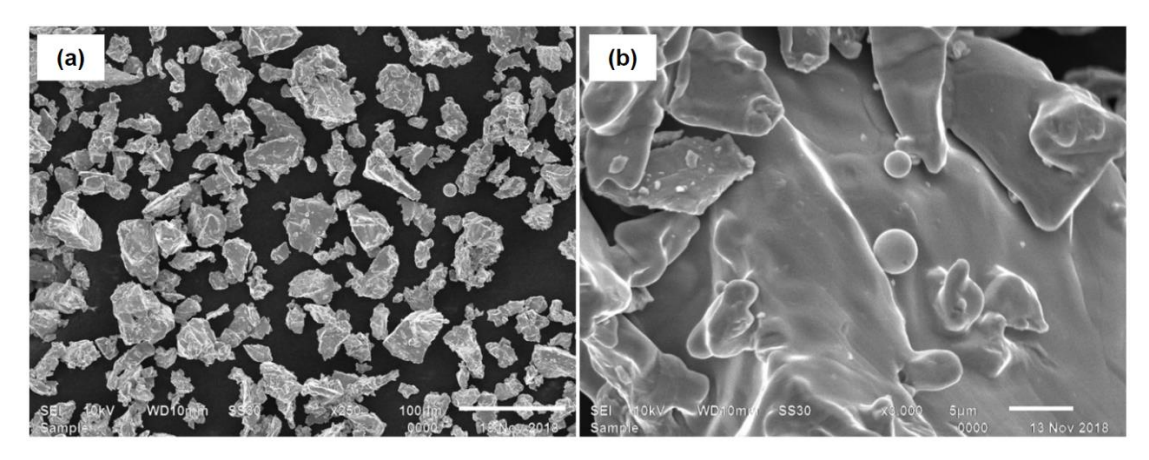


Figure 3.2 SEM images of the feedstock titanium powder used for cold spray deposition: (a) low magnification; (b) high magnification

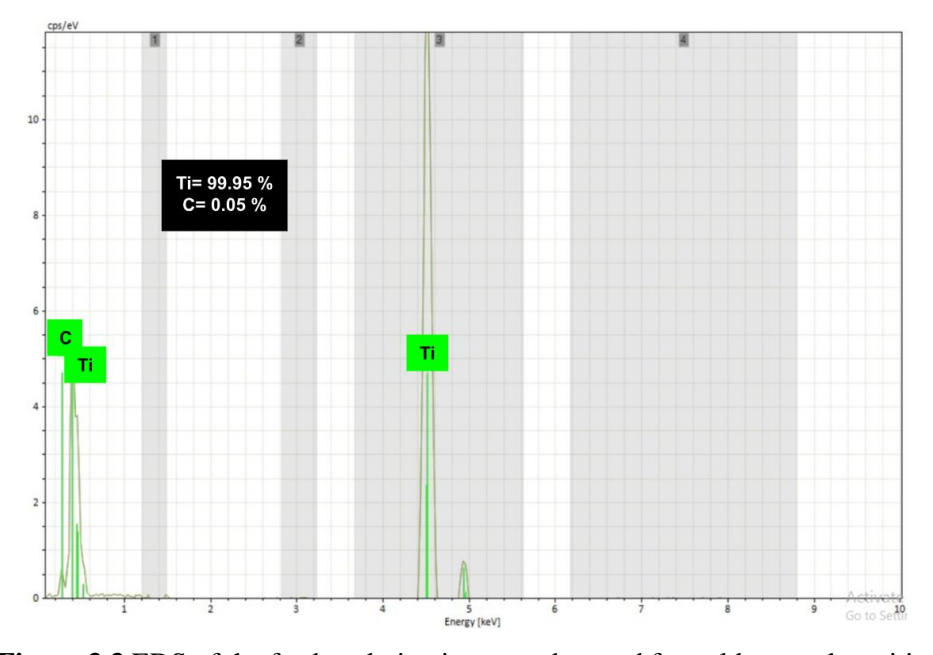


Figure 3.3 EDS of the feedstock titanium powder used for cold spray deposition

3.1.1.2.2 *Ni-20Cr Deposits*

The flowchart depicting the experimental procedure followed to develop and characterize Ni-20Cr thick deposits using different pre-/post-heat treatment techniques is shown in Figure 3.4. The feedstock material was commercially available Ni-20Cr powder with a particle size in the range of 5-45 μ m (Praxair Surface Technologies, Indianapolis, IN, USA). SEM images of the powder feedstock are displayed in Figure 3.5 (a) and 3.5 (b) respectively showing spherical morphology of the powder particles. EDS investigation revealed the elemental composition displaying Ni as 77 % and Cr as 23 %. There was no presence of oxide in the powder feedstock as illustrated in Figure 3.6.

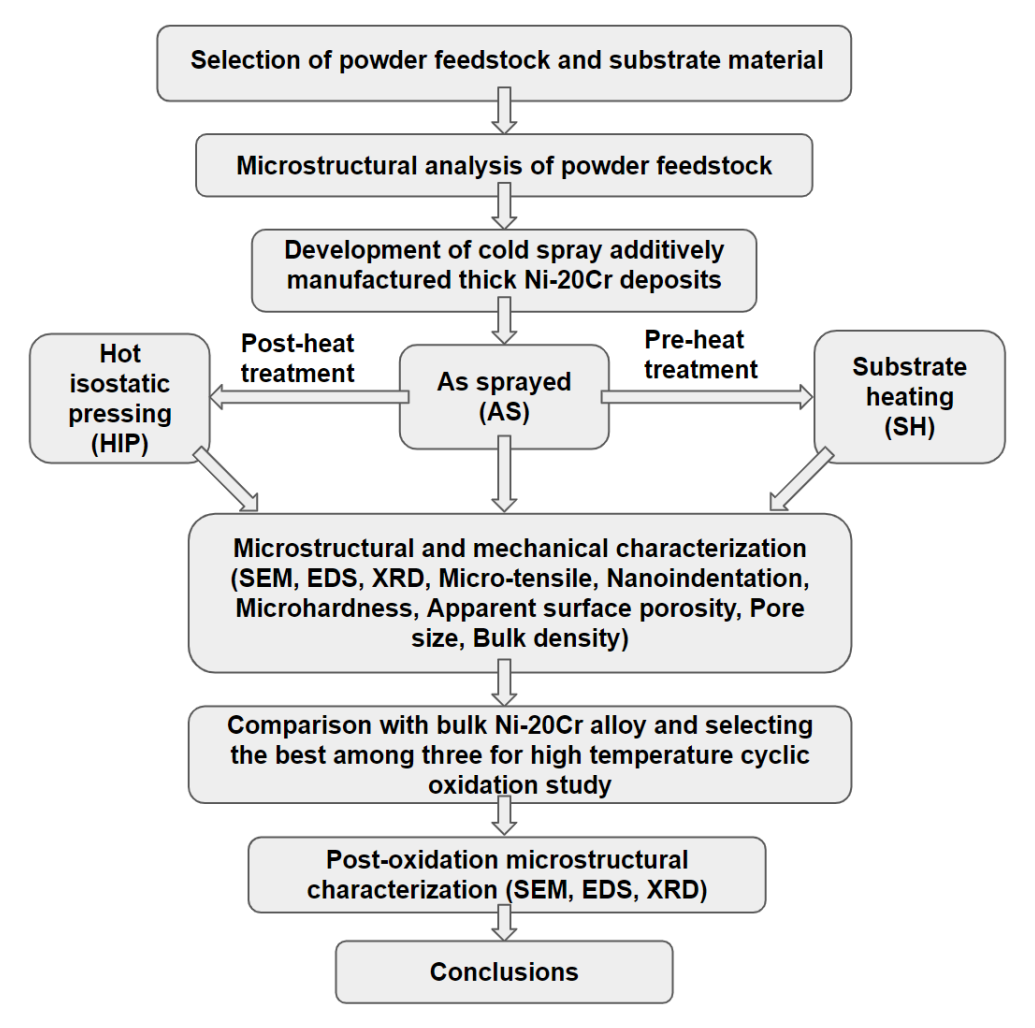


Figure 3.4 A flow chart representing the experimental procedure adopted to develop and characterize thick Ni-20Cr deposits using CSAM

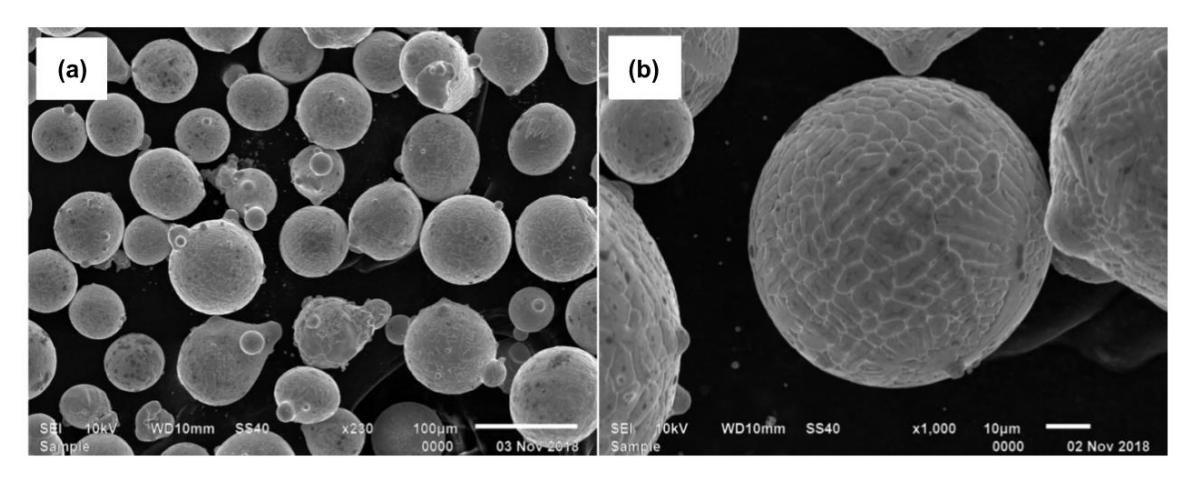


Figure 3.5 SEM micrographs of as-received Ni-20Cr powder feedstock used for cold spray additive manufacturing at (a) lower and (b) higher magnification

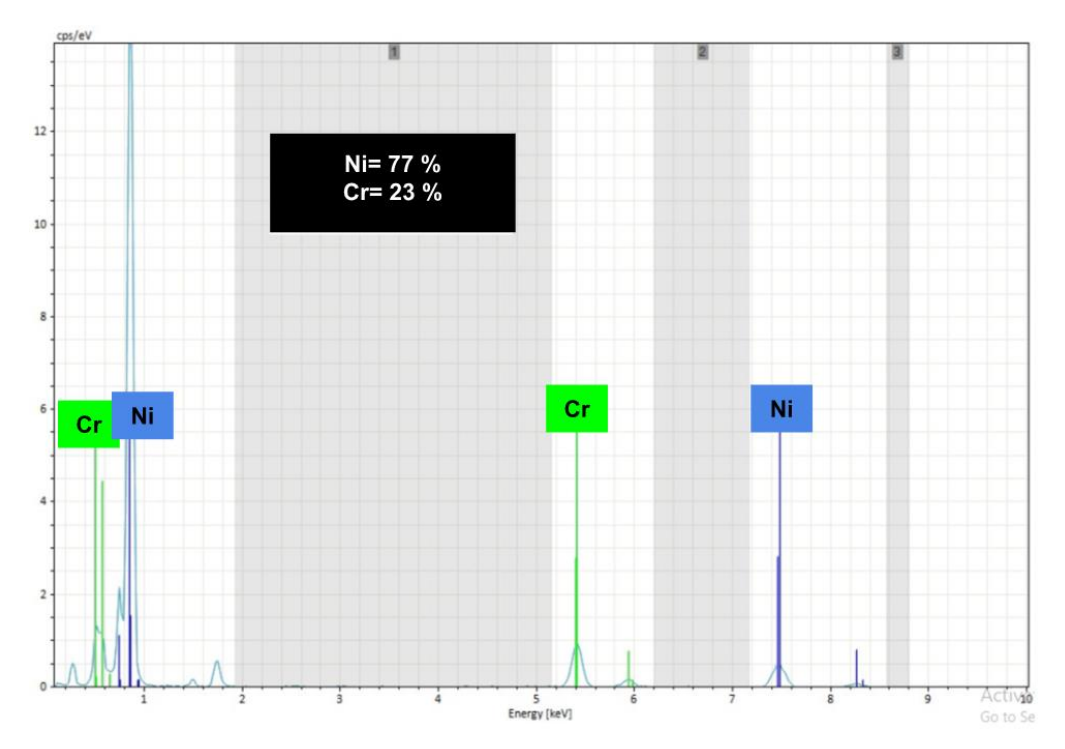


Figure 3.6 EDS spectrum of as-received Ni-20Cr powder feedstock

3.1.2 3D Standalone IN 718 Pipe Deposits

3.1.2.1 Substrate

For the development of 3D standalone IN 718 thick pipe deposit, SS 304 substrate material was chosen. SS 304 pipe was procured from Ludhiana Metal Industries (Ludhiana, India). The chemical composition of the as-received SS 304 substrate material is provided in Table 3.2. The average roughness (R_a) of the curved surface of the as-received SS 304 substrate pipe, designated for cold spray deposition of IN 718, measured 6 μ m. This measurement was conducted using a surface roughness tester from Mitutoyo located in Gurgaon, India.

Table 3.2 Chemical composition of SS304 substrate pipe used in cold spray based additive manufacturing of IN 718 thick pipe deposits

Elements	C	Si	Mn	P	S	Ni	Cr	Fe
Percentage (Wt%)	0.08	1	2	0.04	0.03	8-10.5	18-20	Balance

3.1.2.2 IN 718 Thick Pipe Deposits

The flowchart as represented in Figure 3.7 demonstrates the experimental procedure followed for the development and characterization of the 3D standalone IN 718 thick pipe deposits. The

feedstock is commercially available IN 718 powder (Praxair Surface Technologies, Indianapolis, IN, USA). SEM images of the powder feedstock showing spherical morphology of all IN 718 powder particles, are depicted in Figure 3.8 (a) and 3.8 (b) respectively.

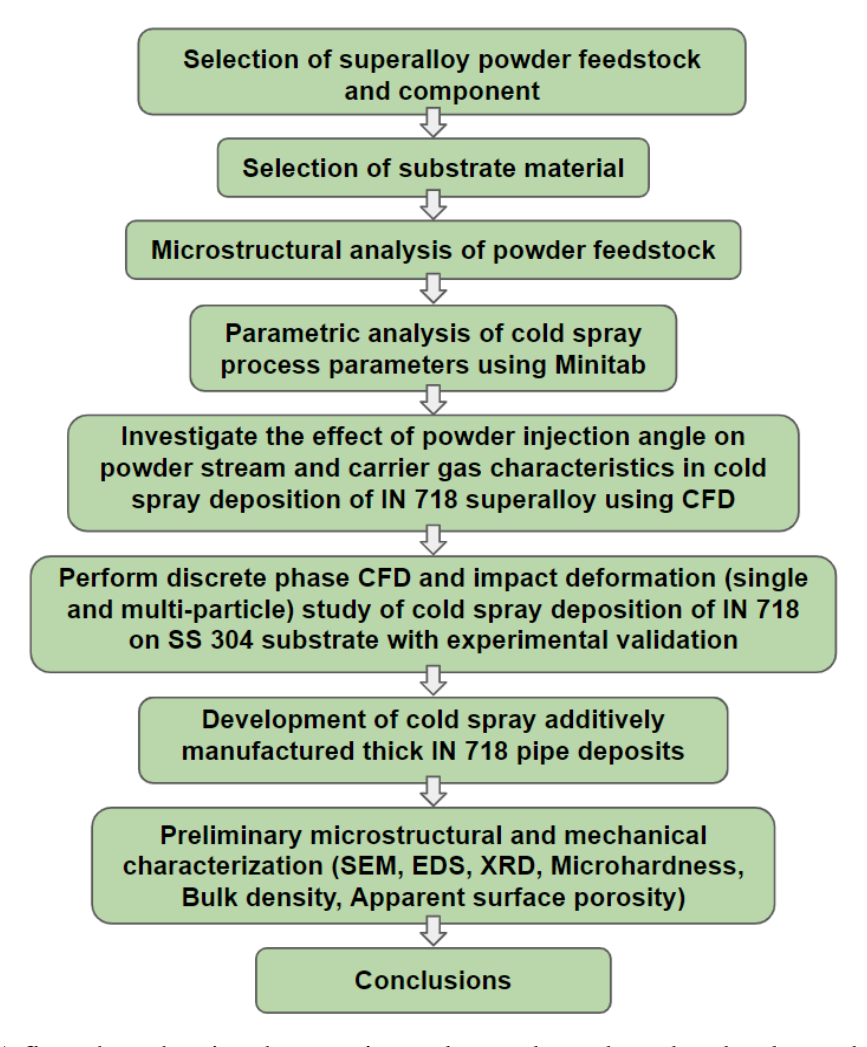


Figure 3.7 A flow chart showing the experimental procedure adopted to develop and characterize thick IN 718 pipe deposits using CSAM

The chemical composition of IN 718 powder is done through energy dispersive spectroscopy (EDS) results, as represented in Table 3.3. Particle size distribution, shown in Figure 3.9, was determined experimentally using a laser diffraction particle size analyzer (LS320, Beckman Coulter, Miami, FL, USA). IN 718 powder particles have a mean size of 22 µm.

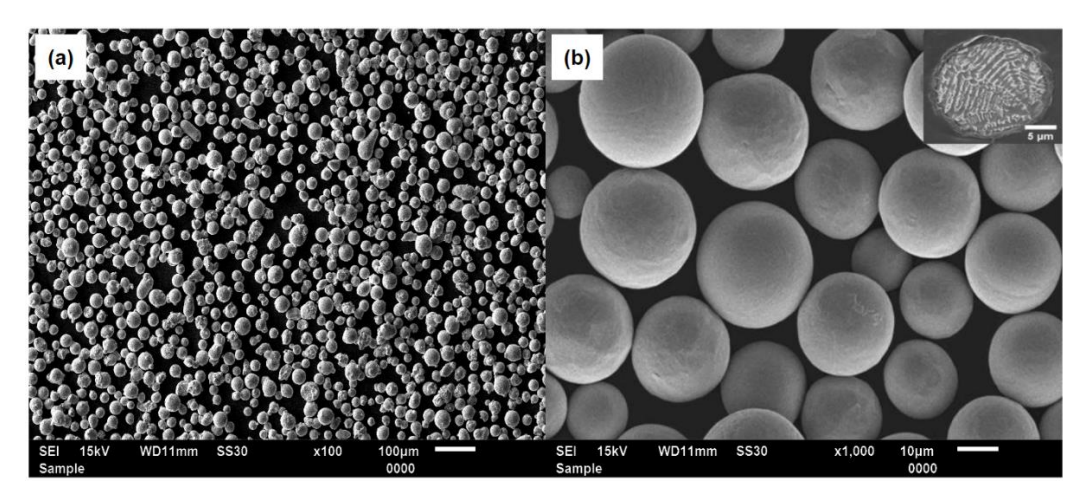


Figure 3.8 SEM images of as-received IN 718 powder feedstock used for cold spray additive manufacturing at (a) lower and (b) higher magnification

Table 3.3 Chemical composition of IN 718 powder feedstock

Elements	Ni	Cr	Nb	Mo	Ti	Al	Fe
Percentage (Wt%)	53.61	19.81	3.21	2.12	1.33	1.53	Balance

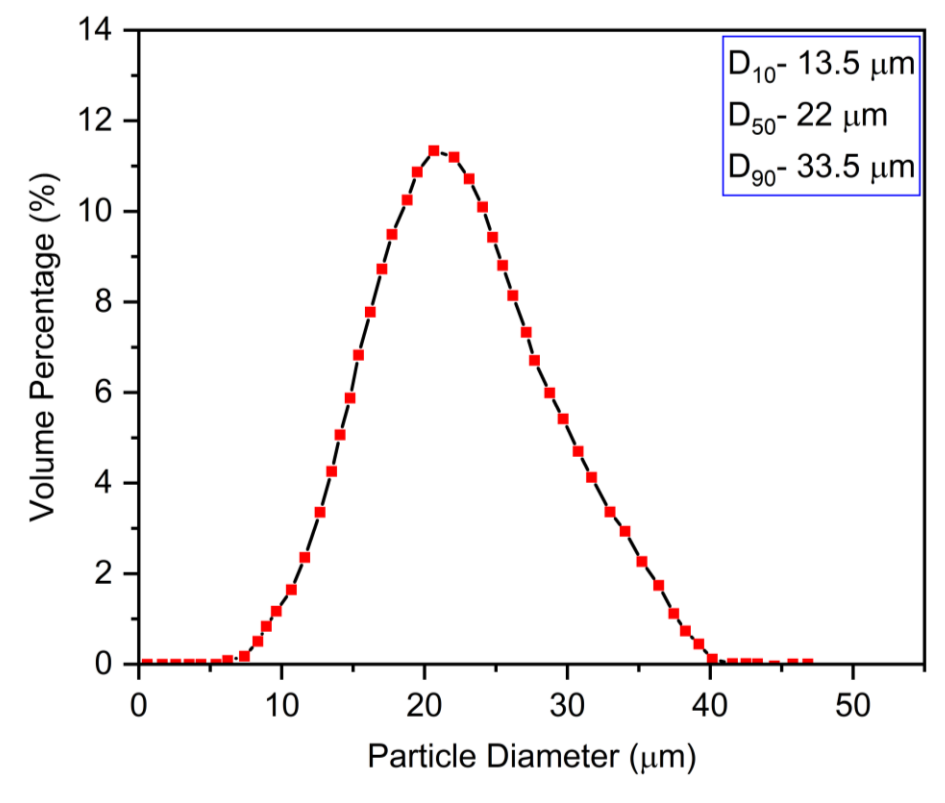


Figure 3.9 Particle size distribution of IN 718 powder feedstock

3.2 PROCESS PARAMETERS FOR CSAM

3.2.1 Proof-of-Concept

3.2.1.1 Thick Deposits

3.2.1.1.1 Pure Ti Deposits

A cold spray system (Impact Innovations GmbH) was used to manufacture the thick titanium deposits (designated as Ti-HIP) having thickness of 16 mm as seen in the macrographs given in the Figure 3.10. The system consists of a cold spray gun, cylinder pallets, a gas control unit, gas pressure regulators, a control console, a powder feeder and other associated peripherals. Two important components of the cold spray gun are a CD (convergent-divergent) nozzle and a gas preheating chamber. The nozzle has an exit diameter of 6 mm and a throat diameter of 2 mm. The barrel measures 100 mm in length from the throat to the exit. Nitrogen gas at 40 bar pressure was preheated at a temperature of 550 °C and supplied to the spray gun. Unheated nitrogen gas having more pressure (to prevent backflow of powder) is fed to the powder feeder for conveying the Ti powder particles to the spray gun. The distance between the nozzle exit and the substrate is called the standoff distance, which was kept at 30 mm. A robotic arm manipulated the cold spray gun to deposit multiple layers of titanium on IN 718 substrate material. Since titanium has a lower density and a hexagonal close-packed (HCP) crystal structure, it is exceedingly challenging to densify it during cold spraying; therefore, the manufactured deposits were processed under a hot isostatic press (HIP) at a temperature of 1650 °F (900 °C) and under a pressure of 15,000 psi (104 N/mm²) for 2 hrs to improve their properties. The cold sprayed samples were prepared at General Electric (Bengaluru), India.

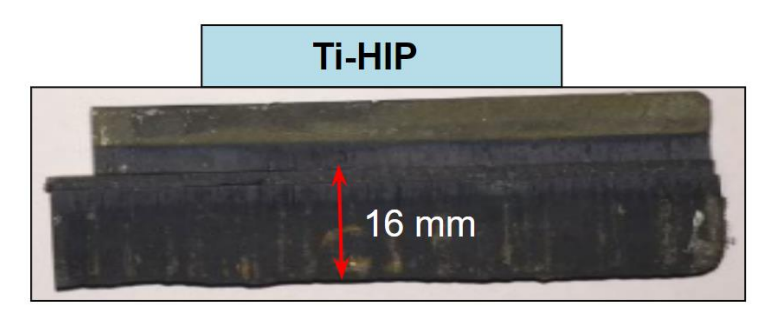


Figure 3.10 Macrographs of cold spray additively manufactured pure Ti thick deposits with IN 718 as a substrate

3.2.1.1.2 *Ni-20Cr Deposits*

A cold spray system (Sulzer Metco) was used to manufacture the Ni–20Cr deposits. The details of the cold spraying process parameters and pre-/post-heat treatments conducted on the CSAM deposits are given in Table 3.4. These cold-sprayed samples were prepared at General Electric (Bengaluru), India. The designation system for the sample is given in Table 3.5. The schematics of the pre-/post-heat treatment operations carried out on respective samples are also shown in Figure 3.11. Macrographs of the developed Ni–20Cr thick deposits along with thickness are shown in Figure 3.12. All of these deposits got detached from the substrate while sectioning the deposits using a w-EDM process. This may be due to poor adhesion, which is actually required to easily obtain standalone deposits. Standalone thick deposits were characterized to evaluate the effects of substrate heating (SH) and hot isostatic pressing (HIP) treatment on their properties.

Table 3.4 Detail of cold spraying process parameters and pre- and post-heat treatment

Cold Spraying Parameters								
Gas Used Gun Chamber Pressure Gun Chamber Temperature Standoff Distance	Nitrogen 40 bar 550 °C 30 mm							
Pre- and Post-Heat Treatment Details								
Substrate Heating (SH)								
Temperature of the substrate Medium Used	524 °C Oxy-fuel torch							
Hot Isostatic Pressing (HI	(P)							
Temperature Pressure Time Duration	900 °C 104 N/mm² 2 hrs							

Table 3.5 Details of cold spray additively manufactured Ni-20Cr samples

Powder Material	Substrate Material	Powder Size	Pre-/Post- Treatment	Layer Thickness	Sample ID
Ni-20Cr	IN 718	5-45 μm	As Sprayed	06 mm	Ni-20Cr-AS
Ni-20Cr	IN 718	5-45 μm	Hot Isostatic Pressing	10 mm	Ni-20Cr-HIP
Ni-20Cr	IN 718	5-45 μm	Substrate Heating	06 mm	Ni-20Cr-SH

Thermocouple Leads to Data Logger (a) SUBSTRATE HEATING (SH) Traverse Direction Robot Mounting Plate for Guns Cold Spray Gun Robot HVOF Gun Top Closure Pressure

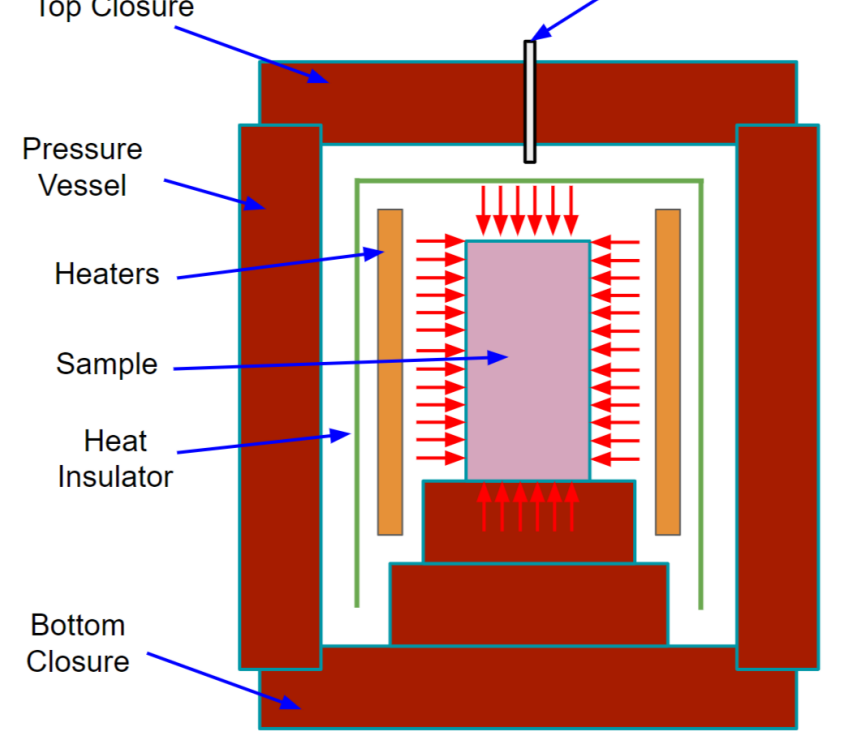


Figure 3.11 Schematics of the pre-/post-heat treatment operations: (a) substrate heating (SH) and (b) hot isostatic pressing (HIP)

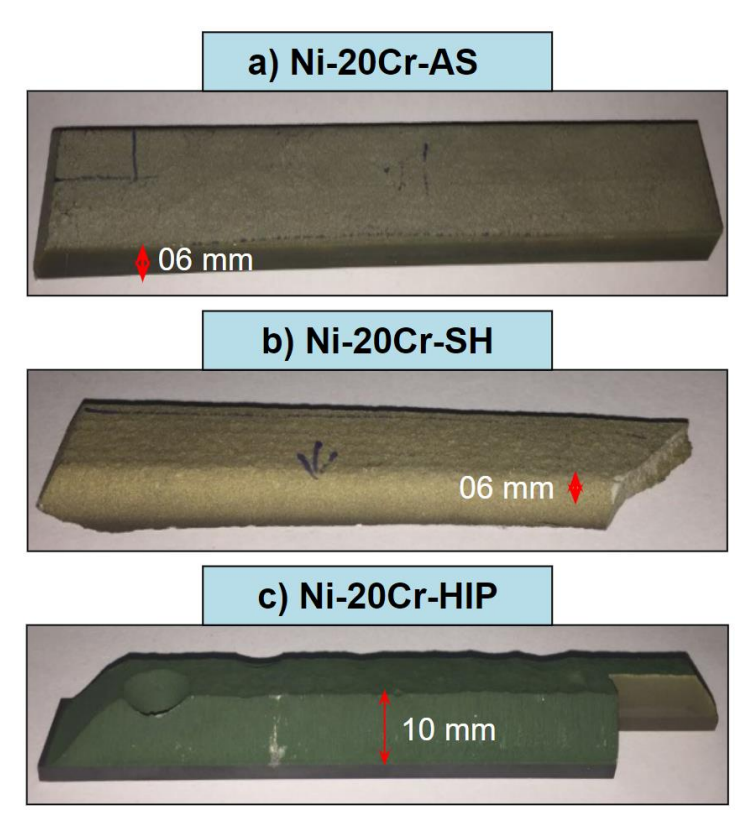


Figure 3.12 Macrographs of the cold spray additive manufactured Ni-20Cr thick deposits: (a) assprayed; (b) substrate heated; (c) hot-isostatic pressing treated

3.2.2 3D Standalone IN 718 Pipe Deposits

The optimized cold spray process parameters used in cold spray additive manufacturing of IN 718 thick pipe deposits are summarized in Table 3.6. A cold spray system (PCS-100, Plasma Giken, Japan) with maximum operating pressure and temperature of 50 bar and 1000 °C, was employed for fabrication of IN 718 thick pipe deposits. The cold spray gun affixed to the mounting plate of the robotic manipulator was held at a spray angle of 90 deg. The robot traversed at a speed of 1 mm/sec, while the substrate pipe was secured on the face-plate of the tilting turntable, rotating at 16 rpm. The robot moved longitudinally at the middle of the SS 304 substrate pipe. An overlap of 1 mm was kept between two consecutive passes. The cold spray footprint diameter was checked to be 5 mm. The schematic representation of the robot and tilting turntable parameters are displayed in Figure 3.13.

SS 304 substrate pipe used had a nominal bore of 50 mm and outside diameter of 60.3 mm. Cold spray additively manufactured (CSAMed) IN 718 pipe had a length of 6" (152.4 mm) and thickness of 5 mm. The spraying details are shown in Table 3.7 while the diagrammatic view as depicted in Figure 3.14 explains the setup for fabrication of IN 718 thick pipe deposits with a real-time image showing the fabrication in progress as given in Figure 3.15.

Table 3.6 Optimized cold spray process parameters for fabrication of IN 718 thick pipe deposits

Cold Spray Process Parameters							
Parameters	Abb.	Units	Value				
Main Gas Pressure Inlet	MGP	bar	50				
Carrier Gas Pressure Inlet	CGP	bar	51				
Difference between Carrier and Main Gas Pressure	Delta P	bar	1				
Main Gas Temperature Inlet	MGT	K	1273.15				
Carrier Gas Temperature Inlet	CGT	K	300				
Standoff Distance	SoD	mm	25				
Particle Flow Rate	PFR	kg/s	0.0005 (30 g/min)				

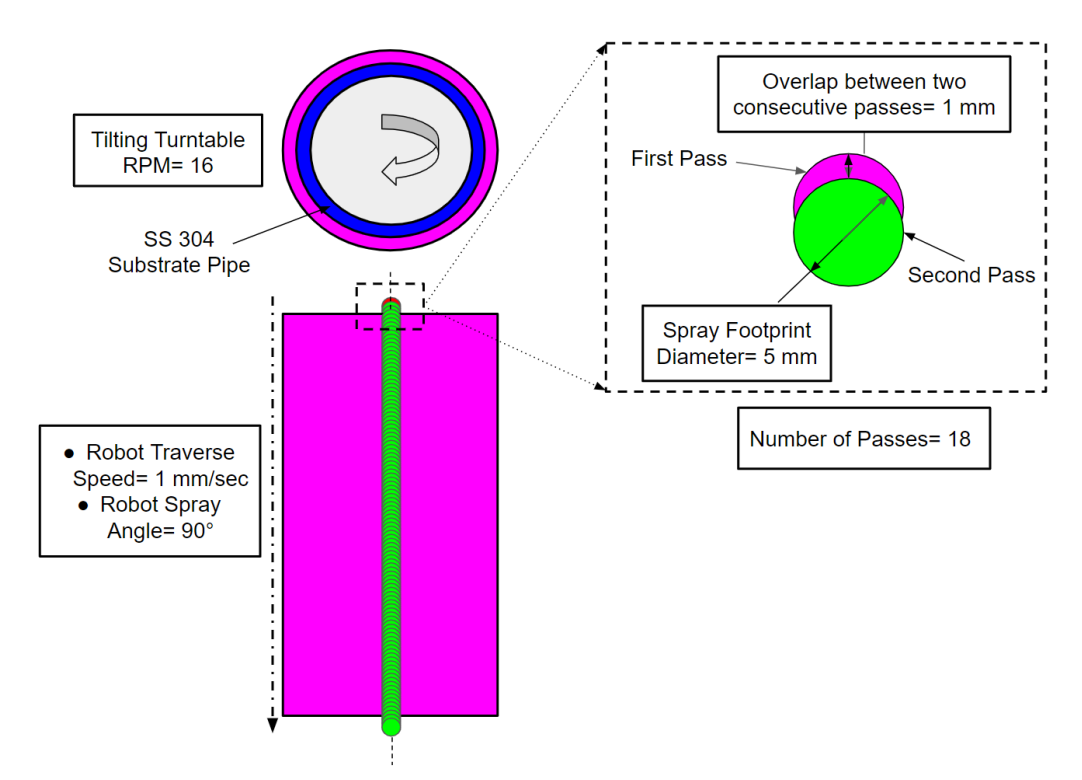


Figure 3.13 Detailed representation of optimized robot and tilting turntable parameters for cold spray based additive manufacturing of IN 718 thick pipe deposits

Table 3.7 Spraying details for fabricating IN 718 thick pipe deposits

Particle Flow Rate	30 g/min
Calculated Deposition Efficiency	96 %
Powder Deposited	28.8 g/min
Time for 1 Pass	2.54 min
Number of Passes	18
Total Printing Time	45.72 min
Mass of IN 718 Pipe	1316.74 g

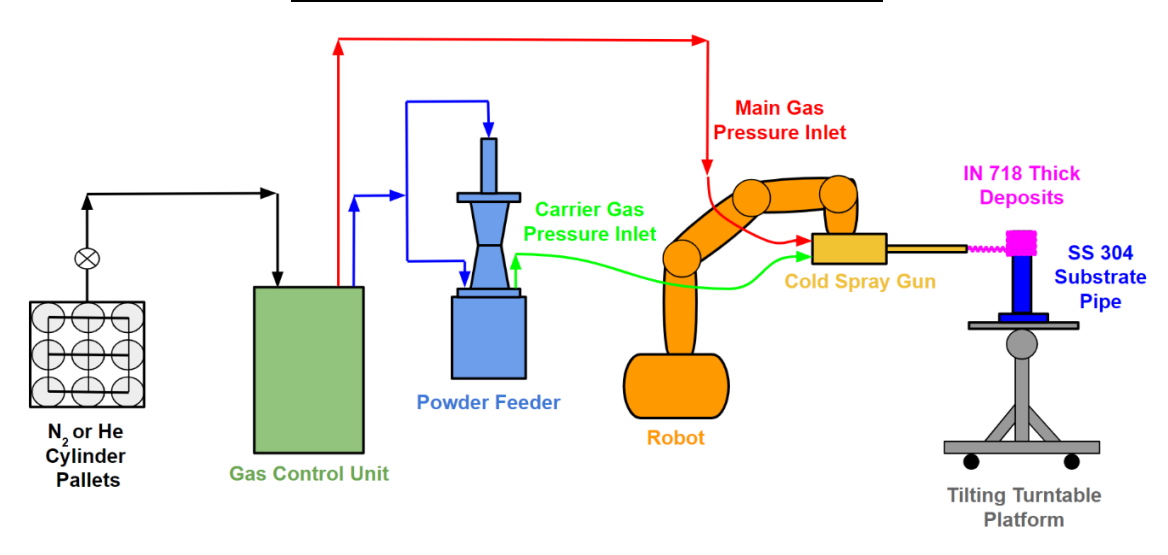


Figure 3.14 Cold spray setup for fabricating IN 718 thick pipe deposits



Figure 3.15 Real-time image showing the fabrication of IN 718 thick pipe deposits in progress

Macrographs of CSAMed IN 718 pipe is depicted in Figure 3.16. During the process of sectioning samples for microstructural characterization, the CSAMed IN 718 pipe deposits became detached from the SS 304 substrate pipe, as illustrated in Figure 3.17.

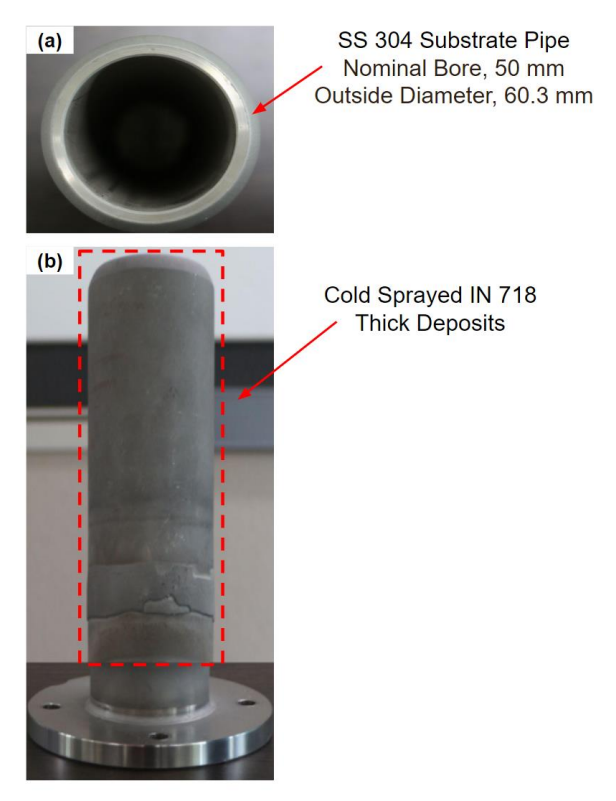


Figure 3.16 Macrographs of cold spray additively manufactured IN 718 seamless pipe
(a) top view (b) front view



Figure 3.17 Images showing sectioned cold spray additively manufactured IN 718 pipe during w-EDM (a) lower magnification (up) (b) higher magnification (down)

The detachment was attributed to poor adhesion caused by utilizing the as-received SS 304 substrate and the differential thermal expansion coefficients between the materials. Leveraging this phenomenon, we can effectively fabricate IN 718 seamless pipes on SS 304 substrates and easily remove the deposited 3D standalone structures. It is pertinent to mention that only the CSAMed IN 718 deposits has been characterized.

3.3 METALLURGICAL CHARACTERIZATION

3.3.1 SEM-EDS Analysis

For microstructural examination, both surface and sectioned samples were prepared from the cold spray additively manufactured deposits following standard metallurgical protocols. The cross-sectional surface of the deposits underwent mechanical polishing, beginning with SiC grinding paper until reaching a grit size of 4000. Subsequently, a series of polishing steps followed, involving the use of alpha alumina slurry (0.3µm size) and gamma alumina slurry (0.05µm size) to achieve the desired final polish. The cross-sectional and top-surface morphologies were analyzed using a scanning electron microscope (SEM) (JEOL JSM-6610LV, JEOL Ltd., Tokyo, Japan and CARL ZEISS ULTRA series, Munich) to study the microstructure of the deposits, focusing on oxide inclusions and pores. Energy dispersive spectroscopy (Oxford, 51-ADD0013) was utilized for spot checks and elemental mapping of the cold spray additively manufactured deposits.

Small samples were sectioned from the developed deposits for bulk density measurements in g/cc. For the purpose of calculating the volume, the dimensions of these dissected samples were measured using Vernier calipers, while the weights were recorded using an electronic balance with a sensitivity of 10⁻³ g. The apparent density was determined using an Archimedes principle-based density measuring kit (Mettler Toledo, MS-DNY-54, Zürich, Switzerland). The calculation of apparent surface porosity percentage and pore size distribution across all samples or deposits was carried out using Image-J, an open-source image analysis software. Ten random SEM images (greyscale) per sample were processed through Image-J, involving steps such as SEM image conversion to bmp or tiff formats, setting the scale in the software, threshold-based binarization, and subsequent analysis to determine pore size distribution and apparent surface porosity percentage.

3.3.2 X-Ray Diffraction Analysis

To identify the various phases, present in the deposits, X-ray diffraction (XRD) analysis was performed using an Analytical X-pert Pro instrument from Almelo, The Netherlands. The

diffraction patterns were generated with a diffractometer equipped with a nickel filter, operating at 35 kV and 20 mA using Cu-K α radiation. Intensity measurements were conducted with a goniometer at a scanning rate of 1°/min, and samples were scanned from 10 to 100° 2 θ angles at a speed of 1 kcps. The X-ray diffraction software integrated with the diffractometer provided "d" values for each diffraction peak, which were subsequently utilized to identify different phases within the deposits.

3.4 MECHANICAL CHARACTERIZATION

3.4.1 Microhardness Analysis

The cross-sectional microhardness of the deposit was examined using a standard Vickers indenter with the help of microhardness tester (Wilson, 402MVD, Chicago, IL, USA) applying a load of 300 g with a dwell time of 10 seconds. Five consecutive lines of indents with an inter-indent distance of 25 µm were taken all along the thickness of the deposits. At each specific location, an average of five indents were measured to determine the microhardness. Indents were applied to all potential locations (matrix, particles, splat boundaries, matrix-particle interfaces), ensuring a random distribution of values.

3.4.2 Nanoindentation Analysis

Quasistatic nanoindentation is the established method for nanomechanical material characterization. It was conducted using a Triboindenter (Hysitron, Inc., TI-950, Minneapolis, MN, USA). This instrument was utilized to determine nanohardness and Young's modulus across the surface and thickness of the cold spray additively manufactured deposits. Nanoindentation data were analyzed using the Oliver-Pharr method (Oliver and Pharr 1992). A matrix of twenty indentations, arranged in a 5 by 4 grid with 5 μ m spacing between indents, was performed on the surface. This experiment was repeated three times to ascertain average values and also to ensure repeatability. A Berkovich diamond tip indenter (three-sided) was employed with a constant load of 1000 μ N. The indenter's properties included a Poisson's ratio of 0.07 and an elastic modulus of 1140 GPa.

3.4.3 Tensile Testing

Tensile specimens were prepared from cold spray additively manufactured thick deposits using w-EDM and subsequently tested on a universal tensile testing machine (FIE, UTES 40, Kolhapur, Maharashtra, India). These specimens were dog-bone-shaped, following ASTM standard E8, with dimensions of 25 mm gauge length, 10 mm width, and 1 mm thickness. The testing procedure employed a load cell capable of handling up to 20 kN, applying a low strain rate of 0.02 mm/min.

Strain measurements were recorded via the machine's crosshead displacement, featuring digital indication with a resolution of 0.001 mm and a maximum displacement of 25 mm, interfaced with a PC. Additionally, a shear test was conducted on the same machine in accordance with ASTM C633 standards to evaluate the adhesion/shear strength of the cold spray additively manufactured pure Ti thick deposits on the IN 718 substrate. This standard employs a pull test to determine the tensile load required to debond the deposits from the substrate. Epoxy adhesive FM 300-4 (shear strength in the range of 30-45 MPa) was applied and subsequently cured at 300 °F to prepare the samples for testing. Micro-tensile tests were performed on SEM using a micro-tensile testing attachment (Kammrath Weiss GmBH, Schwerte, Germany). Dog-bone-shaped specimens, meeting ASTM standard E8 and measuring 25 mm gauge length, 3 mm width, and 1 mm thickness, were prepared using w-EDM. These specimens were subjected to straining at a crosshead speed of 0.5 mm/min with a 10 kN load cell. In situ microstructure changes were observed via SEM imaging, capturing micrographs at various stages including crack initiation, propagation, and fracture.

3.4.4 High Temperature Cyclic Oxidation Study

Cyclic oxidation tests were conducted in a silicon carbide tube furnace at an elevated temperature of 900 °C. The furnace temperature was calibrated to ±5 °C accuracy using a Platinum/Platinum-13 % Rhodium thermocouple connected to a temperature indicator. Following polishing, the cold spray additively manufactured deposits' physical dimensions were meticulously measured using a Vernier caliper to determine their total surface area. Subsequently, the specimens were cleaned with isopropyl alcohol and dried using hot air to remove any residual moisture. Alumina boats were used to hold the specimens during the experiments. The mass of the alumina boats remained constant throughout the cyclic oxidation tests, having been preheated to 1200 °C for 6 hours beforehand. The boat containing each specimen was then placed in the preheated zone of the furnace at 900 °C. After holding for one hour, the boat with the specimen was removed and allowed to cool to room temperature for 20 minutes. The next step involved measuring the combined mass of the boat and specimen, marking the completion of one cycle. Mass change measurements included accounting for any scales that may have detached from the boat. Mass measurements were conducted using an electronic balance sensitive to 10⁻³ g. Following each cycle, visual inspections were performed to observe any changes in color, luster, or other physical characteristics of the oxide scales. The oxidation results were quantified in terms of mass change per unit surface area (g/mm²) plotted against the number of cycles.

3.5 METHODOLOGY FOR PARAMETRIC OPTIMIZATION FOR COLD SPRAY DEPOSITION OF IN 718 USING MINITAB

3.5.1 Factorial Design Approach

Factorial design offers more accurate estimates of the main effects of factors and their interactions. In a full factorial design, every possible combination of factor setting is included, ensuring a comprehensive examination of all possible scenarios. The design helps in ascertaining how each factor influences the response and how these effects change when other factors are adjusted (Arenas *et al.* 2007; Elibol 2002). A typical experimental setup involves setting all input factors at two levels each, commonly referred to as 'high' and 'low' or denoted as '+1' and '-1' respectively. In a scenario where there are k factors, each with two levels, a full factorial design entails conducting 2^k experimental runs (Brasil *et al.* 2005). In the present study, a six-factor two-level factorial approach was followed for optimization of the process parameters in cold spray deposition of IN 718 by using VR as an indicator. The significance and effect of six different factors such as main gas pressure inlet, main gas temperature inlet, deltaP, powder particle flow rate, standoff distance and powder particle diameter on the VR has been checked. The values of the VR as per the design of the experiment are obtained from the CFD model. Table 3.8 displays all the factors along with high and low levels and units.

The values in parentheses (-1 or +1) indicate the coded representations for the factors being examined at their low (-1) and high (+1) levels, respectively. In the current study, a total of 64 CFD runs (as depicted in Table 3.9) with the help of ANSYS Fluent-19 were performed for optimizing the cold spray process parameters as per the VR response for the average size (D₅₀) for IN 718 powder. Subsequently, the assessment of VR values for alternative particle size distributions were also done to confirm that the optimized cold spray process parameters are also suitable for D₁₀ and D₉₀ sizes. The particle size distribution for IN 718 powder feedstock is provided in Figure 3.9 under Section 3.1.2.2.

Table 3.8 Levels of factors studied in cold spray deposition of IN 718

Factors	Abb.	Units	Low Level	High Level
Main Gas Pressure Inlet	MGP	bar	5 (-1)	50 (+1)
Difference between Carrier and Main Gas Pressure Inlet	DeltaP	bar	1 (-1)	5 (+1)
Main Gas Temperature Inlet	MGT	K	298.15 (-1)	1273.15 (+1)
Standoff Distance	SoD	mm	5 (-1)	100 (+1)
Particle Diameter	PD	μm	5 (-1)	100 (+1)
Powder Feed Rate	PFR	g/min	5 (-1)	100 (+1)

Table 3.9 Design of experiments with VR calculated using CFD analysis

MGP	DeltaP	MGT	SoD	PD	PFR	VR	StdOrder	RunOrder
5	5	298.15	5	5	5	0.5226911201	1	1
5	5	298.15	100	5	5	0.5465090183	2	2
50	1	1273.15	5	100	5	0.5367315931	3	3
50	1	1273.15	100	100	5	0.5568282539	4	4
50	5	1273.15	5	5	100	1.018143143	5	5
50	5	1273.15	100	5	100	1.039257546	6	6
50	1	298.15	5	100	5	0.4142255892	7	7
50	1	298.15	100	100	5	0.4303293435	8	8
5	1	298.15	5	5	100	0.5022119433	9	9
5	1	298.15	100	5	100	0.5156668499	10	10
50	5	1273.15	100	5	5	1.039221965	11	11
50	5	1273.15	5	5	5	1.017967294	12	12
5	1	298.15	100	5	5	0.515690242	13	13
5	1	298.15	5	5	5	0.5015240467	14	14
50	5	1273.15	100	100	100	0.4850107202	15	15
50	5	1273.15	5	100	100	0.4680712922	16	16
5	5	298.15	5	100	100	0.2334517779	17	17
5	5	298.15	100	100	100	0.2518600298	18	18
5	5	1273.15	5	5	100	0.5225165176	19	19
5	5	1273.15	100	5	100	0.5461854502	20	20
5	5	1273.15	100	100	100	0.2518600298	21	21
5	5	1273.15	5	100	100	0.2334517779	22	22
5	5	298.15	5	100	5	0.2334757869	23	23
5	5	298.15	100	100	5	0.2519080305	24	24
5	1	298.15	100	100	100	0.2203227046	25	25
5	1	298.15	5	100	100	0.2051343628	26	26
5	5	1273.15	5	100	5	0.2334757869	27	27
5	5	1273.15	100	100	5	0.2519080305	28	28
5	1	298.15	100	100	5	0.2203587207	29	29
5	1	298.15	5	100	5	0.2050863332	30	30

50	1	1273.15	100	5	5	1.458229096	31	31
50	1	1273.15	5	5	5	1.408915947	32	32
50	1	298.15	100	100	100	0.4303173499	33	33
50	1	298.15	5	100	100	0.4142135642	34	34
50	1	298.15	100	5	5	0.6315008775	35	35
50	1	298.15	5	5	5	0.5822358523	36	36
50	5	298.15	100	5	5	0.6263893299	37	37
50	5	298.15	5	5	5	0.5685871295	38	38
50	5	298.15	5	100	100	0.4069220874	39	39
50	5	298.15	100	100	100	0.4225853635	40	40
5	5	1273.15	5	5	5	0.5226911201	41	41
5	5	1273.15	100	5	5	0.5464961081	42	42
5	1	1273.15	100	5	5	0.6314043805	43	43
5	1	1273.15	5	5	5	0.6124064093	44	44
50	1	1273.15	5	100	100	0.544462099	45	45
50	1	1273.15	100	100	100	0.5672656762	46	46
50	1	1273.15	5	5	100	1.407751116	47	47
50	1	1273.15	100	5	100	1.456525426	48	48
5	1	1273.15	5	5	100	0.611809872	49	49
5	1	1273.15	100	5	100	0.6293100331	50	50
50	5	1273.15	5	100	5	0.4675174456	51	51
50	5	1273.15	100	100	5	0.4854014135	52	52
5	1	1273.15	5	100	5	0.2179403413	53	53
5	1	1273.15	100	100	5	0.2362513184	54	54
50	5	298.15	100	100	5	0.422609342	55	55
50	5	298.15	5	100	5	0.4068980441	56	56
5	1	1273.15	5	100	100	0.2174191442	57	57
5	1	1273.15	100	100	100	0.2357922469	58	58
5	5	298.15	100	5	100	0.5461854502	59	59
5	5	298.15	5	5	100	0.5225165176	60	60
50	1	298.15	5	5	100	0.5822695446	61	61
50	1	298.15	100	5	100	0.6315187479	62	62
50	5	298.15	5	5	100	0.5685821173	63	63
50	5	298.15	100	5	100	0.6263794844	64	64

3.5.2 Data Collection

At the heart of achieving high strain rate material deposition in the cold spray process stands the convergent-divergent (CD) nozzle, a critical component responsible for accelerating powder particles to supersonic velocities. The cold spray nozzle with 30 deg powder injection as shown in Figure 3.18 was employed in the CFD analysis. This pivotal nozzle was subjected to successful modeling and simulation using Ansys Fluent. The CFD study employs the eulerian-lagrangian approach as its fundamental methodology. This approach involves the utilization of discrete phase modeling to effectively simulate the interaction between powder particles and the gaseous flow, as well as the impact of particles on surfaces. The main gas pressure and temperature inlet were set as outlined in the design of experiments given in Table 3.9. While DeltaP decides the carrier gas pressure inlet as DeltaP is the difference between carrier gas and main gas pressure

inlet. Throughout the analysis, the carrier gas temperature remains constant at 300 K, reflecting its typical ambient temperature during the transport of powder particles. The particle diameter, powder feed rate, and standoff distance were also varied in accordance with the experimental design. The pressure outlet boundary condition was configured to match ambient temperature and pressure, while the wall was treated as adiabatic. Within the dispersed phase model, particle trajectories are meticulously calculated through the application of the equation of motion. The study also activates the energy equation, and turbulent modeling is accurately represented using the k- ω SST (shear stress transport) model (discussed in Section 3.6.1.1).

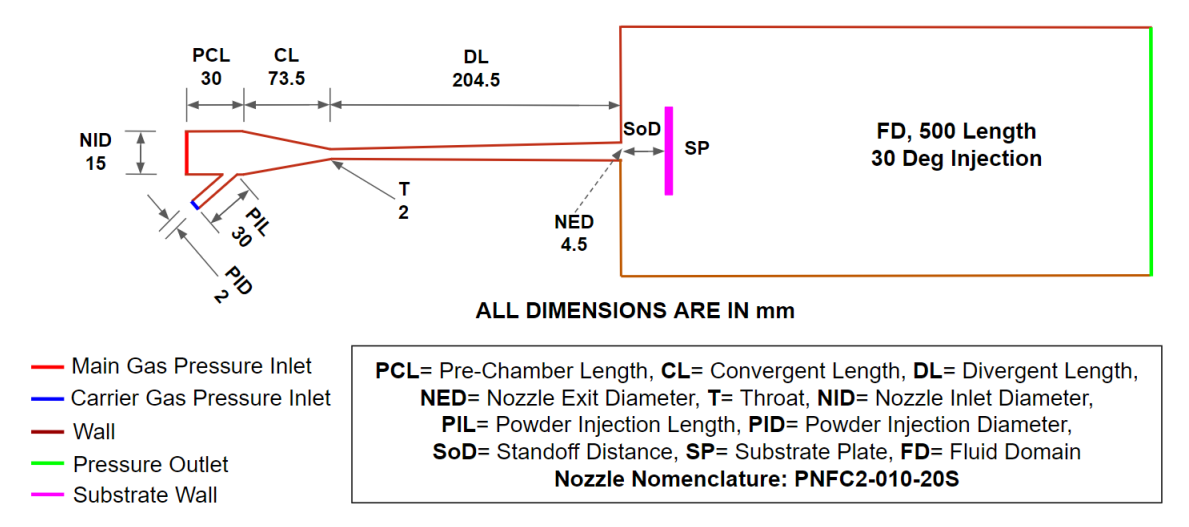


Figure 3.18 Schematic of the convergent-divergent (CD) nozzle used in the CFD analysis of the cold spray deposition of IN 718

The essence of our data collection method involved systematically adjusting cold spray process parameters, as designed through the two-level factorial analysis (TLFA), to precisely determine both particle impact temperature and velocity. ANSYS Fluent-19 software handle was employed in performing the CFD analysis of the cold spray process. A crucial metric, the VR, was calculated based on the critical velocity at the corresponding particle impact temperature and particle impact velocity at the designated SoD. This VR value was consistently calculated for all design points, ensuring a rigorous and uniform approach to the analysis.

3.6 METHODOLOGY FOR EFFECT OF INJECTION ANGLE ON POWDER STREAM AND CARRIER GAS CHARACTERISTICS IN COLD SPRAY DEPOSITION OF IN 718

3.6.1 Numerical Simulation Methodology

3.6.1.1 k-ω SST CFD Model

The k- ω SST (shear stress transport) model stands out as a prominent turbulence model within the realm of CFD. It is utilized to model the dynamics of turbulent flows, where the fluid motion is known for its disorderly and unpredictable nature, marked by chaos and irregularity. It is categorized within the family of Reynolds-averaged Navier-Stokes (RANS) turbulence models, wherein it encompasses the comprehensive modeling of all turbulence effects. Like the standard k- ω model, the k- ω SST model is also a two-equation model. The model addresses two transport equations, representing partial differential equations (PDEs), to consider historical effects such as the convection and diffusion of turbulent energy. These equations focus on two variables: turbulent kinetic energy (k), dictating the energy within turbulence, and specific turbulent dissipation rate (ω), governing the dissipation rate per unit of turbulent kinetic energy. Additionally, ω is commonly denoted as the turbulence scale (Moroni *et al.* 2022; Ranjan *et al.* 2020; Xiao *et al.* 2009).

The conventional k- ω model is designed for low Reynolds number scenarios, specifically suitable for flows characterized by thicker boundary layers, where the viscous sublayer can be effectively resolved. It relies on free stream values/inlet conditions for turbulence. Small variations in k can lead to significant changes in turbulent viscosity and skin friction coefficient, resulting in premature and excessive separations and inaccuracies in capturing body forces (Lew $et\ al.\ 2001$; Chen and Kim 1987). On the other hand, the k- ϵ model typically demonstrates excellent performance in the free stream region. The benefits of these two turbulence models can be amalgamated through the utilization of a blending function in k- ω SST model. The blending function (F_I) facilitates a transition from the k- ϵ model in the outer (free stream) region to the k- ω model in the near-wall region (Adanta $et\ al.\ 2020$; Hellsten $et\ al.\ 1997$).

The equation governing the transport of turbulent kinetic energy (k) is provided as follows:

$$\frac{\delta(\rho k)}{\delta t} + \frac{\delta(\rho U_i k)}{\delta x_i} = \frac{\delta}{\delta x_j} \{ (\mu + \frac{\mu_t}{\sigma_k}) \frac{\delta k}{\delta x_j} \} + P_k + P_b - \rho \epsilon + S_k \qquad \text{eq}(3.1)$$

In the prior equation, P_k signifies generation of turbulent kinetic energy (TKE) caused by mean velocity shear, P_b generation of TKE on account of buoyancy, S_k is user-defined source term, σ_k

denotes turbulent Prandtl number for TKE (k), μ_t states turbulent viscosity and ϵ is turbulent dissipation rate.

Another transport equation for turbulence variables is as under (Daly and Harlow 1970):

$$\frac{\delta(\rho\epsilon)}{\delta t} + \frac{\delta(\rho U_i \epsilon)}{\delta x_i} = \frac{\delta}{\delta x_j} \{ (\mu + \frac{\mu_t}{\sigma_{\varepsilon}}) \frac{\delta \epsilon}{\delta x_j} \} + \frac{\gamma}{\nu_t} P_k - \beta \rho \omega^2 + (I - F_I) \frac{2\rho \sigma_{\omega}^2}{\omega} \frac{\delta k}{\delta x_j} \frac{\delta \omega}{\delta x_j}$$
 eq(3.2)

In the above equations, σ_{ω} represents turbulent Prandtl number for specific turbulent dissipation rate (ω) , F_I states the blending function. The k- ω SST model is based on a hyperbolic function (F_I) , facilitating a seamless transition between the k- ω and k- ϵ models. The blending function, denoted as F_I , is equal to 0 away from the wall in the k- ϵ region and approaches a value of 1 near the wall in the k- ω region. Together with an additional viscosity limiter, this formulation serves as the foundation for the k- ω SST model. The model exhibits superior performance in predicting flow separation compared to most RANS models. Additionally, it demonstrates favorable behavior in adverse pressure gradients by effectively capturing the transport of the principal shear stress in boundary layers (Daly and Harlow 1970).

In this study, the Eulerian-Lagrangian approach was employed, utilizing the discrete phase model (DPM) to model the interaction between particles and the fluid, encompassing their impact on boundary walls. Within the framework of the dispersed phase model, particle trajectories were calculated through motion equations, activating the energy equation and employing the k- ω SST for turbulent modeling. The simulations incorporated high mach number rotational drag and the Magnus lift law. In order to account for particle dispersion resulting from turbulence, the stochastic-tracking model in Fluent was applied. Specifically, the discrete random walk (DRW) model was utilized to forecast the varying components of the overall particle velocity and their impact on trajectory, enabling an authentic portrayal of turbulence-induced random effects on particle dynamics following numerous path computations (Zahiri et al. 2014). A stable-state solution for gas flow was obtained utilizing the pressure-based solver. Both the main and carrier gas (nitrogen) were treated as ideal and compressible. The simulations involved the application of a coupled second-order spatial discretization scheme in all calculation instances.

Validating a CFD model stands as a pivotal step ensuring accuracy in replicating real-world fluid dynamics. In this study, the focus was on assessing the average powder particle impact velocity, using it as the output response to compare CFD-simulated results against actual experimental data (Seng et al. 2023). The comparison between the simulated findings and experimental results indicated that the CFD model is accurate as evident from Figure 3.19.

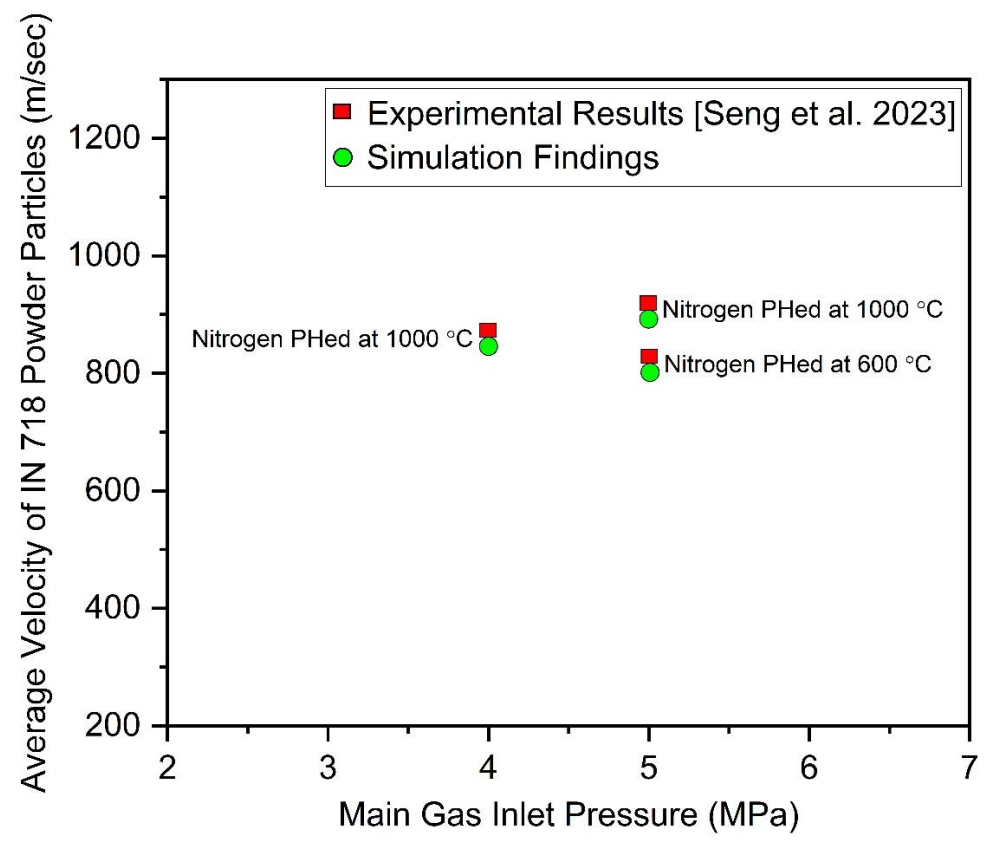


Figure 3.19 Validation of CFD model by comparing simulation findings and experimental results

The investigation encompassed three distinct sets of cold spray process parameters derived from experimentation: i) main gas inlet pressure at 4 MPa, pre-heated (PHed) to 1000 °C; ii) main gas inlet pressure at 5 MPa, PHed at 600 °C; and iii) main gas inlet pressure at 5 MPa, PHed at 1000 °C. For all the cases, powder particle flow rate was kept at 15 g/min while the standoff distance was 30 mm from the nozzle exit. Upon conducting CFD simulations, the average powder particle impact velocities were calculated as 865 m/sec (4 MPa and 1000°C), 805 m/sec (5 MPa and 600°C), and 904 m/sec (5 MPa and 1000 °C) respectively. Comparison with the corresponding experimental data [35] revealed slight variations of 1.39 %, 1.86 %, and 1.77 % lower in the CFD-simulated velocities. Importantly, these differences remained comfortably within acceptable limits, confirming the robustness of the simulations in replicating real-world observations. This validation bolsters confidence in the simulation process, providing a sturdy foundation to delve deeper into its potential implications. This validation not only underscores the accuracy of the CFD model but also solidifies its reliability in capturing complex fluid dynamics.

3.6.1.2 Geometry and Computational Domain

Figure 3.20 shows the detailed schematic of all three CS nozzles with different powder injection angles (90 deg, 0 deg and 30 deg). The fluid domain length in all the three cases is 500 mm only. In all three cases the convergent-divergent nozzle with conical convergent and divergent cross-section is the same, in order to check the effect of injection angle on the gas flow field and powder feedstock attributes. The dimensions of the convergent-divergent nozzle used are illustrated in Figure 3.20. The ratio of exit area and throat area (expansion ratio) is 5.06 while the length of the expansion section and throat diameter are 204.5 mm and 2 mm.

Figure 3.20 also illustrates the boundary limit conditions applied in all three cases. The optimized parameters of the cold spray process, determined through Minitab's optimization study, are utilized in this analysis to assess the impact of powder injection angle on the characteristics of the powder particle stream and gas flow attributes. The inlet pressure for the main gas was set at 5 MPa (50 bar) with a temperature of 1273.15 K, while the corresponding inlet pressure for the carrier gas was fixed at 5.1 MPa (51 bar) and a temperature of 300 K. IN 718 powder feedstock was used as a discrete phase with spherical morphology. The study adhered to the Rosin-Rammler distribution to characterize the particle size distribution of IN 718 powder. It is essential to specify the minimum, maximum, and mean diameters of the powder particles for precise tracking in the analysis. Table 3.13 provides detailed information regarding the particle size distribution, outlining the specific parameters essential for accurate simulation and analysis. This approach ensures that the computational modeling accurately reflects the real-world characteristics of the IN 718 powder particles used in the study. The flow rate and temperature of IN 718 powder feedstock were having a value of 0.0005 kg/s (30 g/min) and 300 K. Pressure outlet boundary was configured to correspond to ambient temperature and pressure while the wall was treated as adiabatic.

One way to determine an optimal mesh density is by conducting a grid independence test. The grid independence test in computational simulations involves running simulations at varying grid resolutions, comparing the results, and checking if the solution converges as the grid becomes finer. This process determines an optimal grid size that provides accurate results without excessive computational expense. Validation against experimental or analytical data ensures confidence in the simulation outcomes by verifying their accuracy independently of grid size. Table 3.10 displays the range of mesh variations tested across three specific injection angle scenarios, crucial for verifying grid independence.

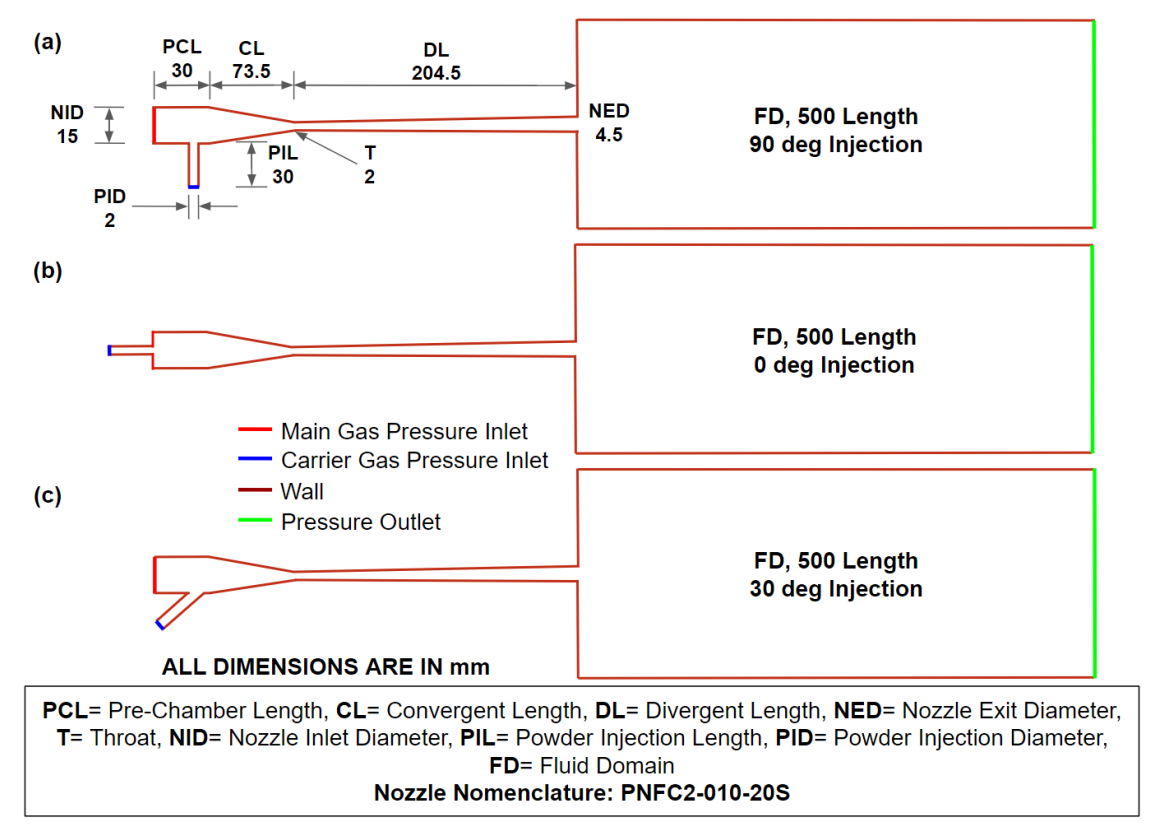


Figure 3.20 Detailed schematic of the three cold spray nozzles with different powder injection angle used in CFD simulation

Table 3.10 Detail of meshes used in the three cold spray nozzles with different powder injection angle for grid independence study

Angle of Injection	Mesh A	Mesh B	Mesh C	Mesh D
90 deg	110989	211850	308770	411651
0 deg	112074	212976	311057	412575
30 deg	111786	212117	309646	411986

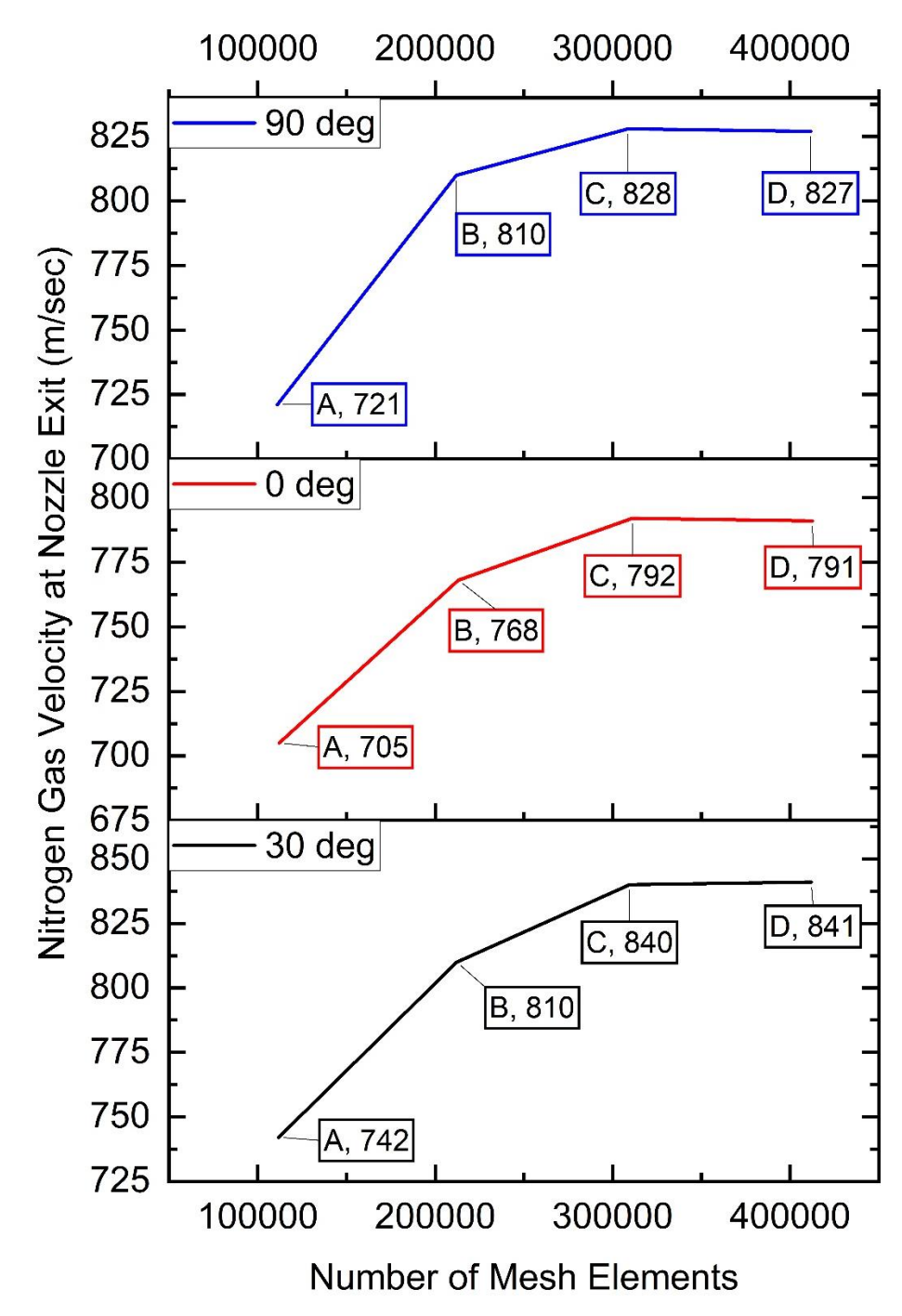


Figure 3.21 Grid independency results for all three cold spray nozzles with different powder injection angle [90 deg (top), 0 deg (middle) and 30 deg (bottom)]

In the grid independence test, nitrogen gas velocity at the nozzle exit was used as the output parameter to gauge its fluctuations in relation to alterations in mesh elements. Our analysis, prominently illustrated in Figure 3.21, notably favored Mesh C, highlighting its minimal deviation in nitrogen gas velocity when compared to Mesh D across all examined injection

angles. These findings underscore Mesh C's consistency in delivering superior accuracy while requiring fewer computational resources throughout the three distinct injection angle cases. The 2D computational domains for all three cases were meshed, with each exhibiting an orthogonal quality very close to 1 and very low skewness, as detailed in Table 3.11, signifying meshes of high quality. Figure 3.22 illustrates the mesh configurations employed in the CFD analysis for all three cases.

Table 3.11 Detail of mesh metrics in the three cold spray nozzles with different powder injection angle used in CFD simulation

S.no	Case	Orthogonal Quality	Skewness	Number of Elements
1.	90 deg	0.99854	0.026	308770
2.	0 deg	0.99868	0.028	311057
3.	30 deg	0.99613	0.030	309646

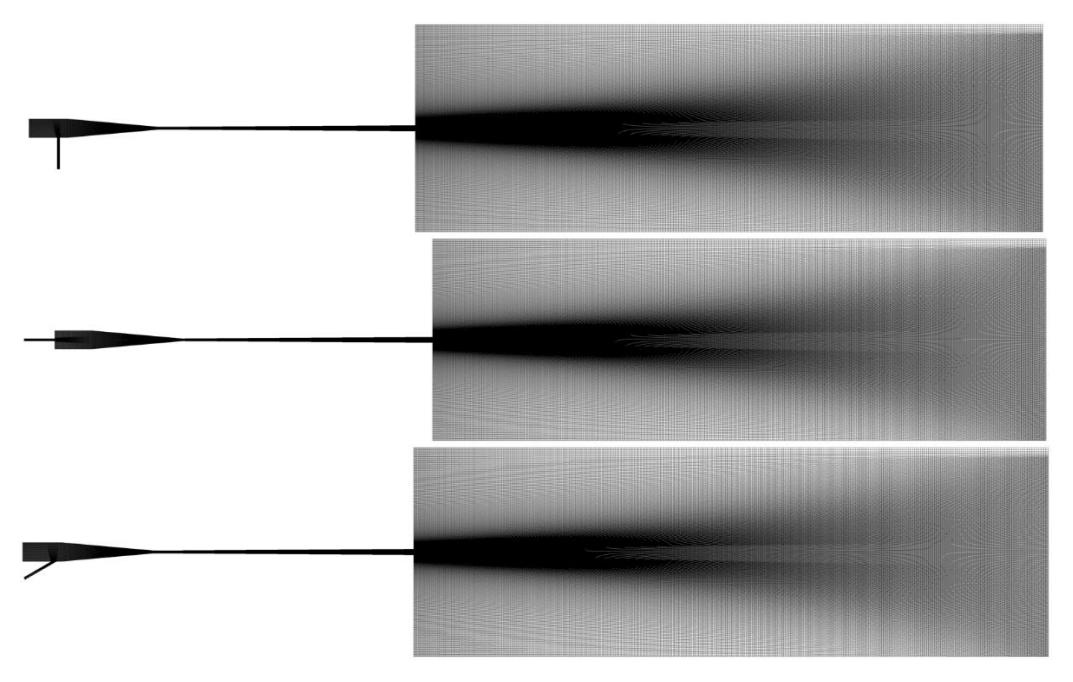


Figure 3.22 Meshed 2D computational domain of all three cold spray nozzles with different powder injection angle [90 deg (top), 0 deg (middle) & 30 deg (bottom)]

Nitrogen gas (continuous phase) was used as main and carrier gas as well. The behavior of the nitrogen gas was described by the ideal gas law, accounting for compressibility effects. The incorporation of the Sutherland coefficient was essential to account for variations in viscosity due

to temperature changes. The details of IN 718 powder used as discrete and nitrogen gas as continuous phases are given in Table 3.12 and 3.13.

Table 3.12 Detail of discrete phase injection properties

Discrete Phase Injection Properties				
Injection Type	Surface			
Injection Surface	Carrier Gas Pressure Inlet			
Injection Direction	Normal to Surface			
Particle Type	Inert			
Particle Material	Inconel 718			
Particle Material Density (kg/m³)	8190			
Particle Material Specific Heat (J/kg-K)	435			
Particle Material Thermal Conductivity (W/m-K)	11.4			
Particle Diameter (μm)	6 (min), 22 (mean) & 40 (max)			
Particle Temperature Inlet (K)	300			
Particle Velocity Inlet (m/sec)	0			
Particle Flow Rate (kg/s)	0.0005 (30 g/min)			

Table 3.13 Detail of nitrogen gas used as main and carrier gas

Gas Details			
Gas	Nitrogen		
Density (kg/m ³)	Ideal		
Specific Heat (J/kg-K)	1040.67		
Thermal Conductivity (W/m-K)	0.0242		
Viscosity (kg/m-s)	Sutherland		

3.7 METHODOLOGY FOR DISCRETE PHASE COMPUTATIONAL FLUID DYNAMICS AND IMPACT DEFORMATION (SINGLE- AND MULTI-PARTICLE) STUDY OF COLD SPRAY DEPOSITION OF IN 718 POWDER FEEDSTOCK ON SS 304 PIPE WITH EXPERIMENTAL VALIDATION

3.7.1 CFD Simulation Methodology

3.7.1.1 k-ω SST CFD Model

The selection of a convergent-divergent nozzle with a 30 deg powder injection angle was based on its superior performance for cold spray deposition of IN 718 powder feedstock onto an SS 304 substrate pipe. In our study, the k- ω SST turbulence model was employed for the CFD analysis, as detailed in Section 3.6.1.1. This model choice was pivotal due to its established capability in accurately capturing the complex flow dynamics inherent in cold spray processes.

To ensure the reliability of our simulations, rigorous validation of the k- ω SST model was conducted against experimental data, also discussed comprehensively in Section 3.6.1.1. This validation process was instrumental in confirming that the computational predictions align closely with the experimental findings, thereby enhancing the credibility and robustness of our study.

By leveraging the convergent-divergent nozzle and the k- ω SST model in our CFD simulations, we aimed to achieve a thorough understanding of the deposition process dynamics during cold spray of IN 718 on SS 304.

3.7.1.2 Geometry and Computational Domain

Figure 3.23 demonstrates the 2D computational domain of the 30 deg injection nozzle with a rotating SS 304 pipe with boundary limit conditions so applied. The standoff distance of the rotating SS 304 pipe is 25 mm respectively. The convergent-divergent nozzle resembles the geometry and dimensions of the commercial cold spray nozzle used in Plasma Giken system (PCS-100) as depicted in Figure 3.24.

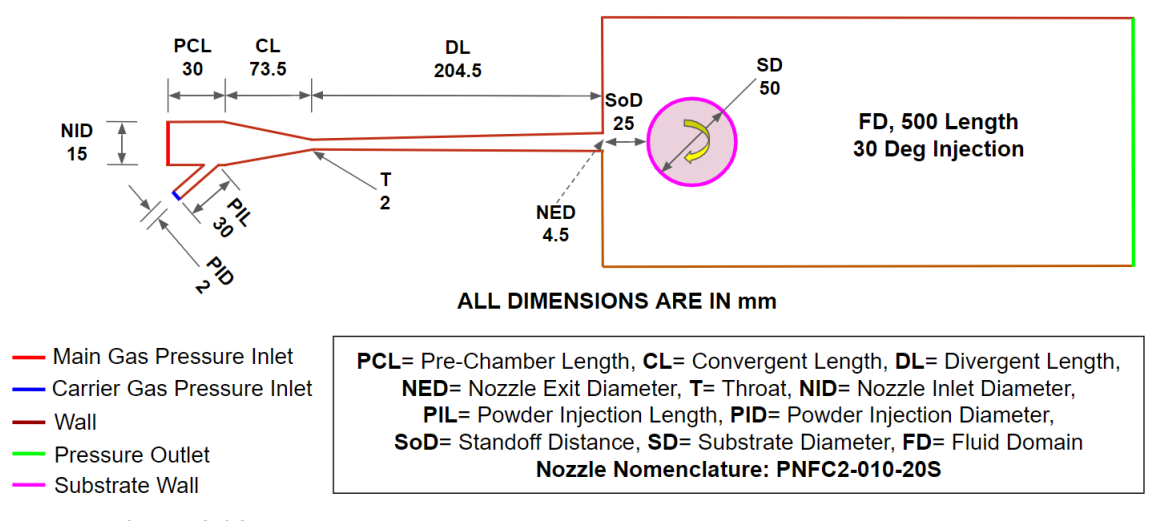


Figure 3.23 Detailed schematic showing the 30 deg powder injection cold spray nozzle with SS 304 substrate pipe used in CFD simulation

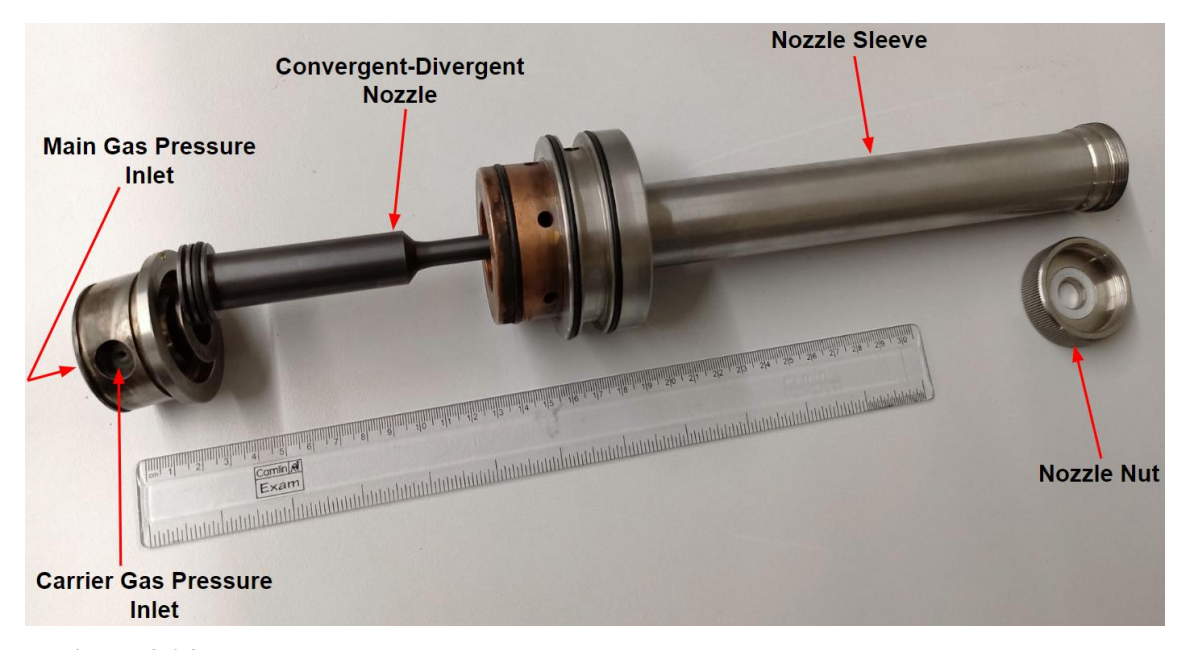


Figure 3.24 Commercial convergent-divergent nozzle with 30 deg powder injection used in Plasma Giken (PCS-100) cold spray system

In this analysis also, the same optimized cold spray parameters identified from the Minitab study as given in Section 3.6.1.2 are applied for performing the CFD analysis of cold spray deposition of IN 718 powder particles onto an SS 304 substrate pipe. The SS 304 substrate pipe is securely held by a fixture on the face-plate of a tilting turntable, as illustrated in Figure 3.14 under Section 3.2.2. During the process, the substrate pipe rotates at the lowest speed of 16 rpm to ensure uniform deposition along its longitudinal direction. The specifics of the discrete IN 718 phase and

the characteristics of the nitrogen gas are detailed in Tables 3.12 and 3.13, respectively, and remain consistent throughout the analysis.

Before conducting the CFD study, a grid independence test was performed using nitrogen gas velocity at SoD as the output parameter to assess variations with changes in mesh elements as displayed in Figure 3.25. Three different types of meshes were employed, detailed in Table 3.14. Mesh C was chosen for its superior accuracy and efficiency in computational requirements. Table 3.15 presents the mesh metrics for Mesh C, highlighting its orthogonal quality very close to 1 and minimal skewness, indicative of high-quality mesh characteristics. Figure 3.26 depicts the mesh configuration employed in the CFD analysis.

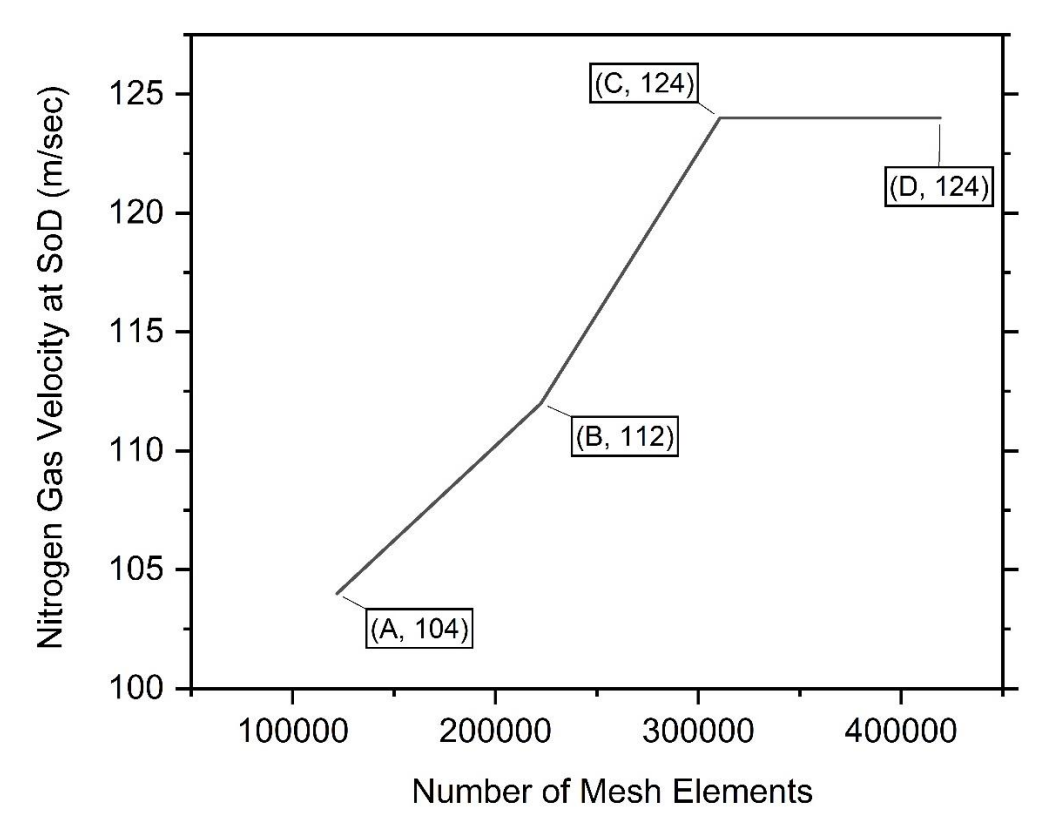


Figure 3.25 Grid independence testing for the 30 deg powder injection cold spray nozzle with SS 304 substrate pipe

Table 3.14 Detail of meshes used in the 30 deg powder injection cold spray nozzle with SS 304 substrate pipe for grid independence study

Case	Mesh A	Mesh B	Mesh C	Mesh D
30 deg Injection Nozzle with SS 304 Pipe	121812	222321	310605	418996

Table 3.15 Detail of mesh metrics for the 30 deg powder injection cold spray nozzle with SS 304 substrate pipe used in CFD simulation

Case	Orthogonal Quality	Skewness	Number of Elements
30 deg Injection Nozzle with SS 304 Pipe	0.99839	0.0219	310605



Figure 3.26 Meshed 2D computational domain of the 30 deg powder injection cold spray nozzle with SS 304 substrate pipe used in CFD simulation

3.7.2 Explicit Dynamics Simulation Methodology

The deformation of IN 718 powder feedstock, both single- and multi-particle impacts on an SS 304 substrate, was extensively analyzed using the commercially available finite element software ANSYS/Explicit version 2019 R3. The material response under conditions of high pressure and shock wave propagation was evaluated using the "Mie-Grüneisen" equation of state (EOS), integrated into the linear Hugoniot formulation. This approach accurately models particle deformation and deposition behavior during impact (Azarmi *et al.* 2021).

To depict the plastic behavior of particles and substrates during dynamic deformation under impact, the Johnson-Cook model was employed. This model incorporates considerations such as strain hardening, strain rate hardening, and thermal softening, thereby accounting for their respective influences within this theoretical framework. The Johnson-Cook model has been instrumental in precisely capturing and analyzing the plastic deformation characteristics of materials under high velocity conditions (Choi *et al.* 2024; Li *et al.* 2024).

In this impact analysis, single IN 718 powder particles with dimensions corresponding to D_{10} (13.5 μ m), D_{50} (22 μ m), and D_{90} (33.5 μ m) as detailed in Figure 3.9 (Section 3.1.2.2), were subjected to impact onto an SS 304 substrate. The particle impact velocity and temperature were derived from the CFD analysis as specified in Section 3.7.1. These were used as input parameters for the powder particles for the impact deformation analysis with SS 304 substrate remaining at room temperature of 300 K. Figure 3.27 depicts the boundary conditions corresponding to the D_{50} particle size, and similar conditions apply to both D_{10} and D_{90} particles as well. In the multi-

particle analysis, particles (D_{10} , D_{50} and D_{90}) were randomly distributed above the SS 304 substrate for impact deformation. Each particle shared identical impact velocity and temperature conditions as seen in Figure 3.28 respectively. The explicit modeling parameters for simulating the impact between the SS 304 substrate and IN 718 powder feedstock were selected based on the temperatures of both the powder feedstock and substrate, as outlined in Table 3.16.

In order to select the mesh element size for the single- and multi-particle impact deformation analysis, the temporal development of maximum effective plastic strain for different meshing sizes for IN 718 powder particles modeled by Lagrangian method was done. Different meshing sizes tried for both single- and multi-particle were 2 μ m, 1.5 μ m, 1 μ m and 0.5 μ m respectively. In both the scenarios, a steep increment of maximum effective plastic strain for meshing sizes of 0.5 and 1 μ m was observed as displayed in Figure 3.29 for single particles and Figure 3.30 for multi-particle.

Assadi *et al.* (2003) pointed out that this steep increase is because of adiabatic shear instability (as detailed in Chapter 2 under Section 2.4.5.1) which is absent in other cases. Therefore, mesh sizes of 0.5 μ m were selected for both single-particle and multi-particle analyses. The meshed 2D computational domain for single-particle corresponding to D₅₀ has only been shown in Figure 3.31 while for multi-particle is depicted in Figure 3.32 respectively.

Table 3.16 Detail of explicit impact modeling parameters for impact deformation analysis for single-particles and multi-particle of IN 718 powder feedstock onto an SS 304 substrate

Explicit Impact Modeling Parameters					
Property	Symbol	Unit	IN 718 (673 K)	SS 304 (300 K)	
Heat Conductivity	k	W/(mK)	11.4	16.2	
Density	ρο	kg/m3	8220	7920	
Elastic shear modulus	Ge	GPa	69.521	86	
Speed of sound	со	m/sec	4530	4570	
Gruüneisen's constant	χο	-	1.83	1.93	
Hugoniot slope	S	-	1.53	1.49	
Specific heat	Ср	J/(kg-K)	520	450	
Melting temp	Tm	K	1593	1800	
	A B	MPa MPa	1108 699	260 1350	
Johnson Cook	n C	-	0.5189 0.0085	0.62 0.02	
	m	-	1.2861	1	

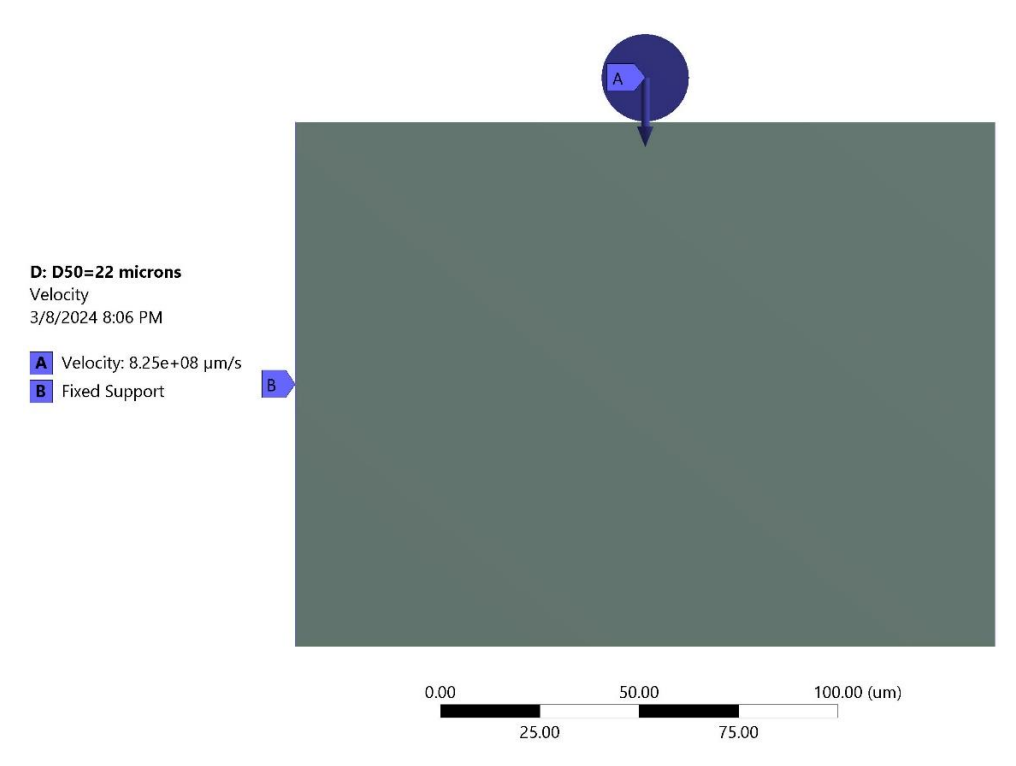


Figure 3.27 Illustration of boundary conditions implemented for impact deformation analysis for single-particles of IN 718 powder feedstock onto an SS 304 substrate

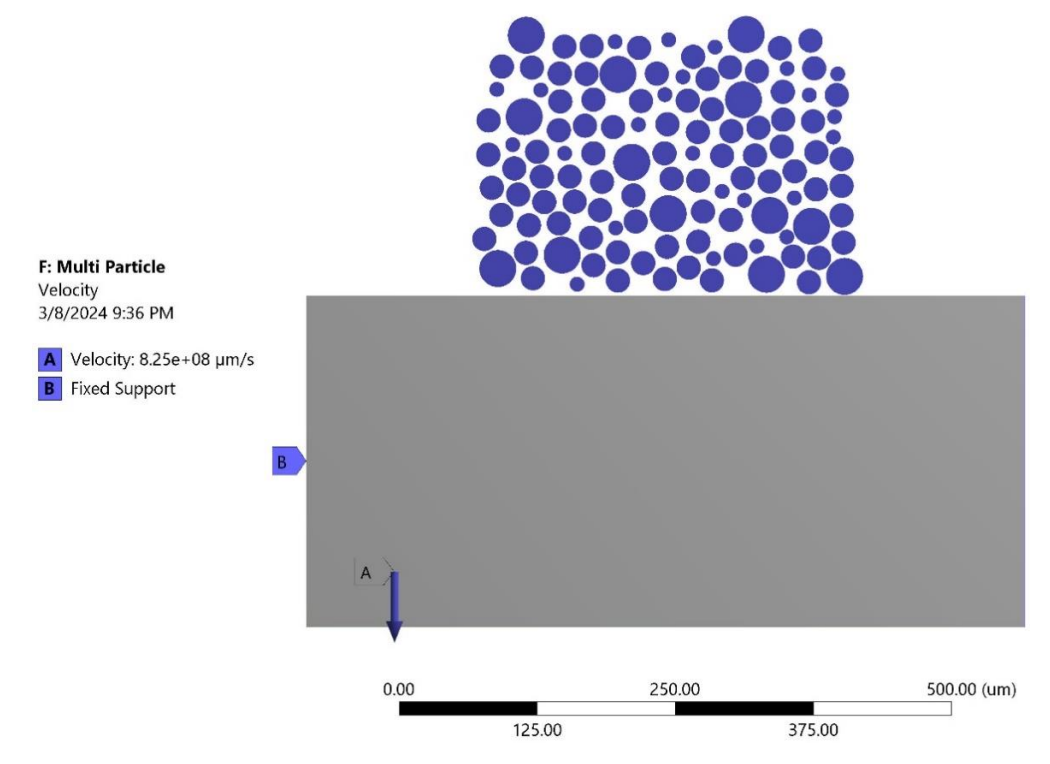


Figure 3.28 Representation of boundary conditions implemented for impact deformation analysis for multi-particle of IN 718 powder feedstock onto an SS 304 substrate

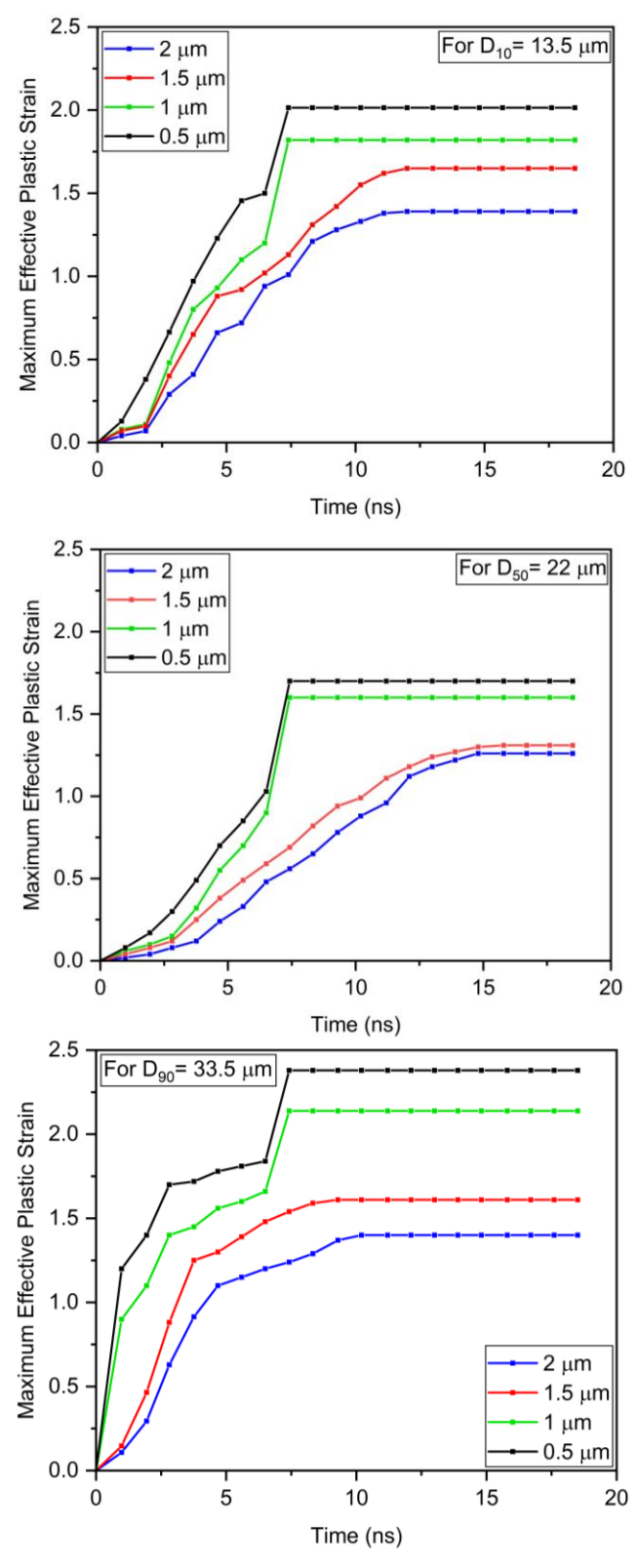


Figure 3.29 Temporal development of maximum effective plastic strain for different particle sizes [D_{10} (top), D_{50} (middle) and D_{90} (bottom)] for impact deformation analysis for single-particles of IN 718 powder feedstock onto an SS 304 substrate

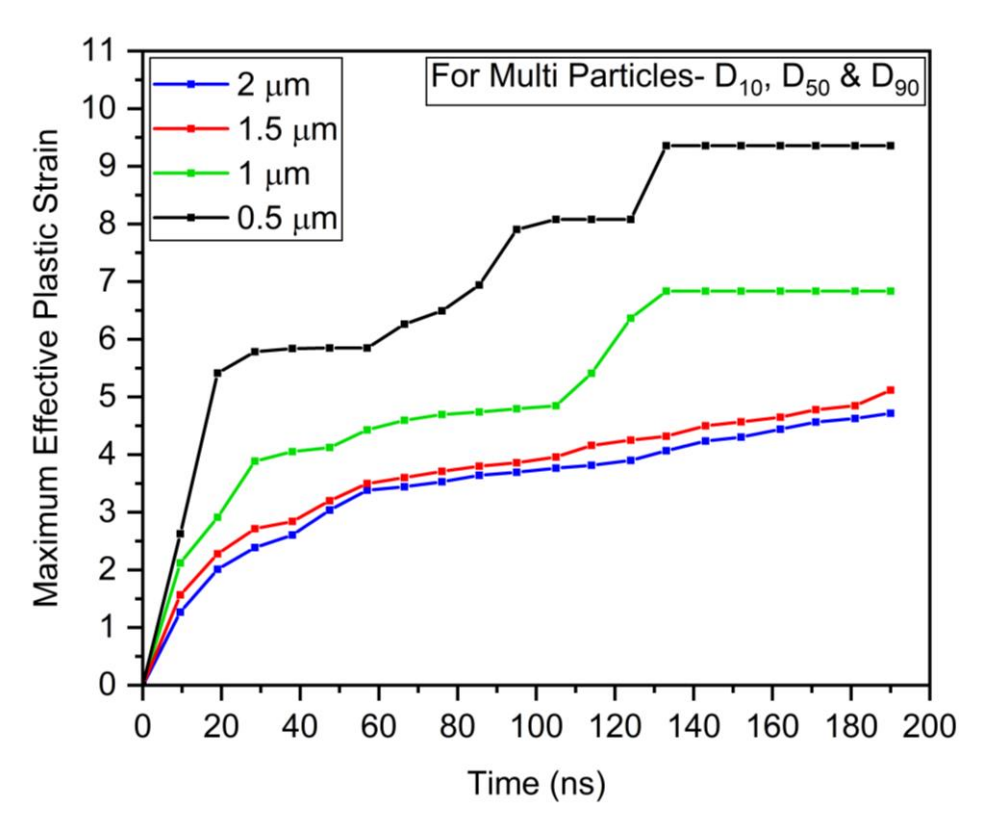


Figure 3.30 Temporal development of maximum effective plastic strain for impact deformation analysis for multi-particle of IN 718 powder feedstock onto an SS 304 substrate

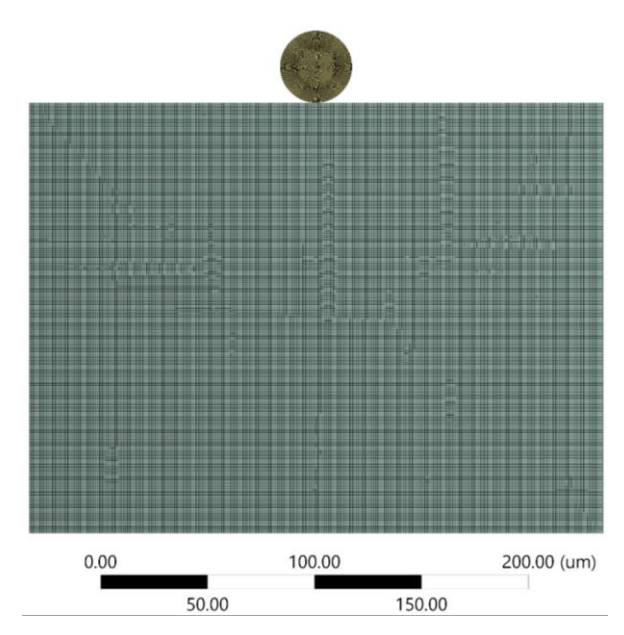


Figure 3.31 Meshed 2D computational domain for impact deformation of single-particle (D_{50}) of IN 718 powder feedstock onto an SS 304 substrate

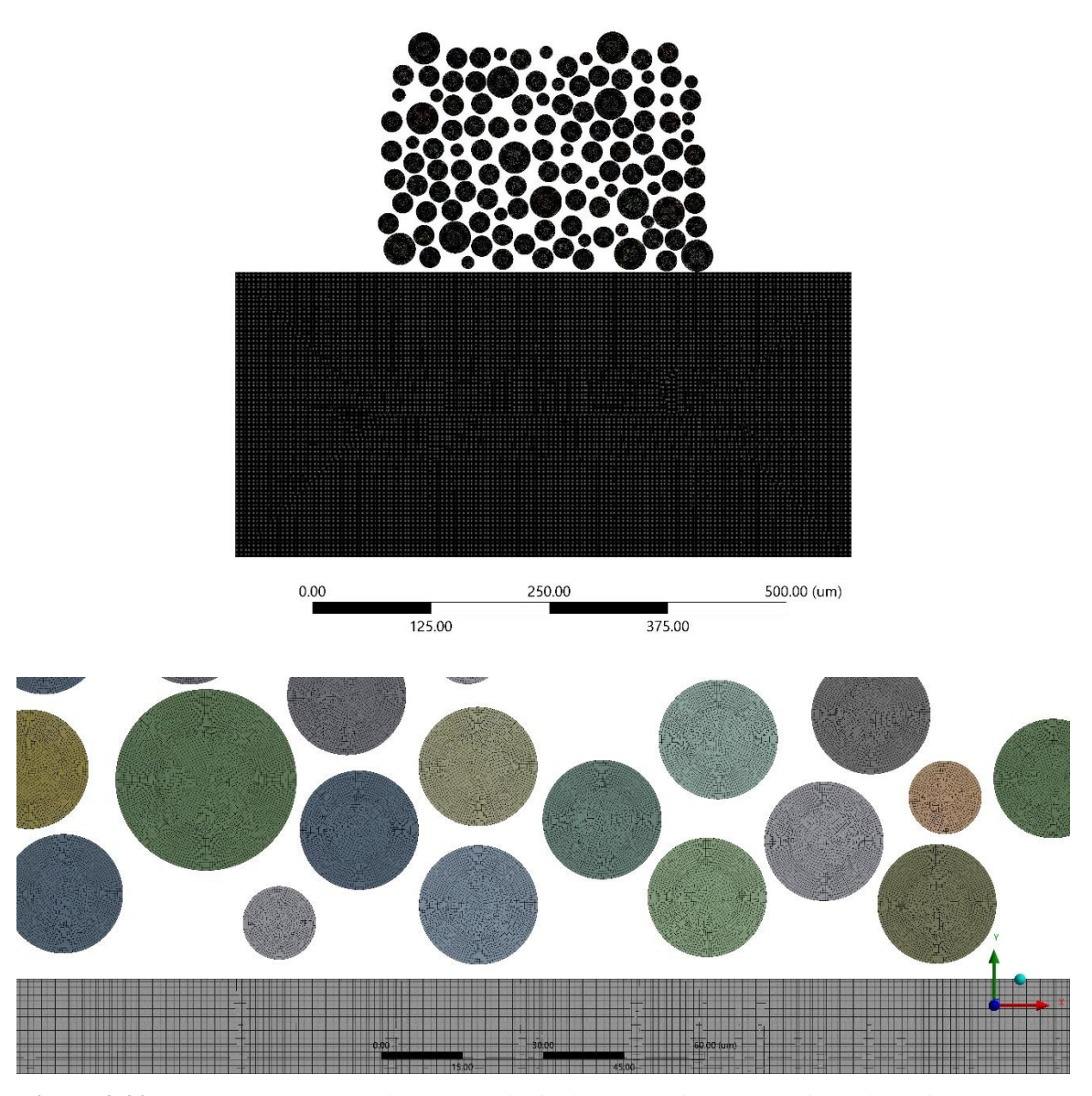


Figure 3.32 Meshed 2D computational domain for impact deformation of multi-particle (D_{10} , D_{50} and D_{90} randomly distributed) of IN 718 powder feedstock onto an SS 304 substrate along with closer view

CHAPTER 4

PROOF-OF-CONCEPT

This chapter evaluates thick plates developed as a proof-of-concept using cold spray based additive manufacturing (CSAM). It investigates the impact of pre- and post-heat treatment techniques, such as hot-isostatic pressing (HIP) and substrate heating (SH). This proof-of-concept demonstrates CSAM's potential for fabricating thick, standalone deposits from materials that are challenging to weld, form, and fabricate. The chapter is divided into two sections, each focusing on a different material fabricated using CSAM.

The first section discusses the characterization and high-temperature oxidation behavior of HIP-treated titanium deposits. These pure titanium deposits, approximately 16 mm thick, were created using high-pressure cold spraying. The HIP-treated titanium was analyzed for metallurgical and mechanical properties to assess the feasibility of CSAM for titanium components. Additionally, high-temperature cyclic oxidation tests were conducted to evaluate the stability of the HIP-treated titanium deposits at elevated temperatures. This work has been published previously (Singh et al., 2013a).

The second section highlights the investigation of Ni-20Cr plates with thicknesses between 6 and 10 mm, focusing on microstructural and mechanical characterization. The study applied pre-heat treatment SH and post-heat treatment HIP to assess their impact on the deposits' properties. Successful deposition without oxide formation was achieved, and HIP treatment notably reduced porosity. Additionally, Ni-20Cr-SH deposits exhibited excellent oxidation resistance at 900°C (Singh et al., 2013b).

4.1 PURE Ti DEPOSITS

4.1.1 Results and Discussion

4.1.1.1 Microstructural Analysis

The optical micrographs of the HIP-treated CSAMed pure titanium deposit are represented in Figure 4.1. The deposit is found to have two different types of microstructures. A granular structure with spherical grains of ($\alpha + \beta$ phase of titanium) has been observed near the center of the deposit. However, a bunch of bush-like structures (Widmanstatten) has been observed near the interface, which was further identified (via XRD, SEM, and microhardness) as α -titanium.

SEM images of the developed Ti deposit are presented in Figure 4.2. It can be seen from Figure 4.2 (a) that there is no gap at the interface, which indicates appropriate adhesion between the substrate and the first layer of the deposit. This information can be useful if one is interested in developing Ti deposits on IN718. There were no cracks found in the Ti deposit. However, micron-sized inter-particulate pores, as well as weakly bonded inter-particulate boundaries, were found as displayed in Figure 4.2 (b). These imperfections, cavities, and pores could be the result of inadequate plastic deformation of powder particles during deposition. It is worth mentioning as a side note that these features are very important in medical prostheses, such as orthopedic or dental implants, to act as nucleation sites for the cells to proliferate, aiding in osseointegration. Osseointegration helps in improving prosthetics for amputees.

A white layer was observed at the interface, as depicted in Figure 4.2 (c). A high-magnification SEM image, shown in Figure 4.2 (d), reveals the presence of bush-like structures (Widmanstatten) near the interface. These structures were further identified as α -titanium through XRD (Figure 4.4) and microhardness analysis, which is discussed in subsequent sections. The EDS mappings (Figure 4.3) showed pure titanium on the deposit side and nickel, chromium, and iron on the substrate side. There was no oxide formation in the deposit during cold spraying and HIP processing, highlighting the capability of the used approach for the development of standalone pure titanium products.

Moreover, no inter-diffusion across the Ti-layer and substrate material was observed. A microstructure comprising a variety of irregularly shaped particles and voids has been observed at the inter-particle boundaries. These voids were not noticeable in the un-etched sample/deposit (Figure 4.2 (a), (b)), while the mass loss due to attack by the etchant (Figure 4.2 (c), (d)) exposed the hidden pores. Therefore, it can be concluded that the un-etched surface can lead to the underestimation of porosity (Hussain *et al.* 2011).

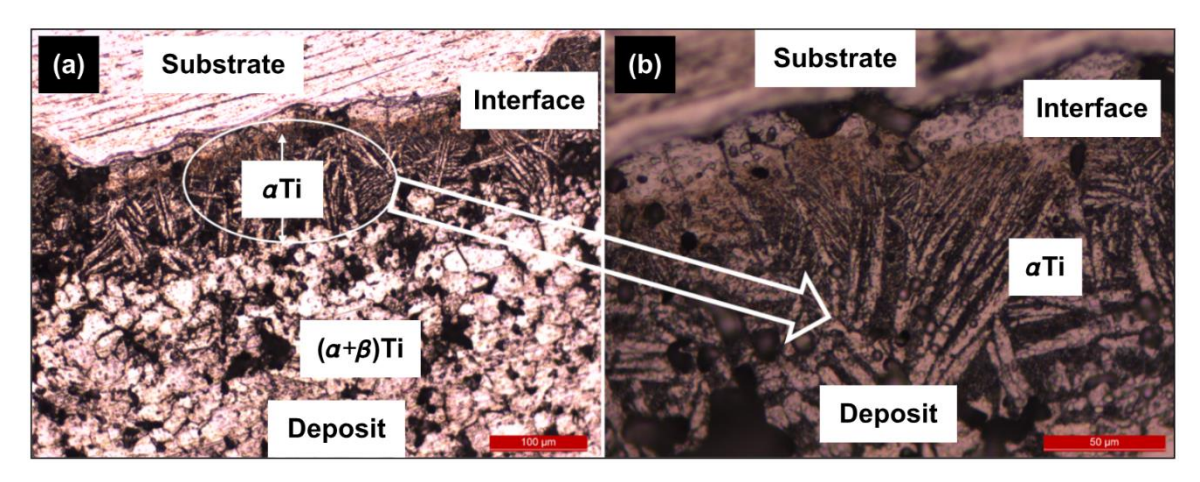


Figure 4.1 Optical images of HIP-treated CSAMed pure titanium deposit around the interface at (a) low magnification; (b) high magnification

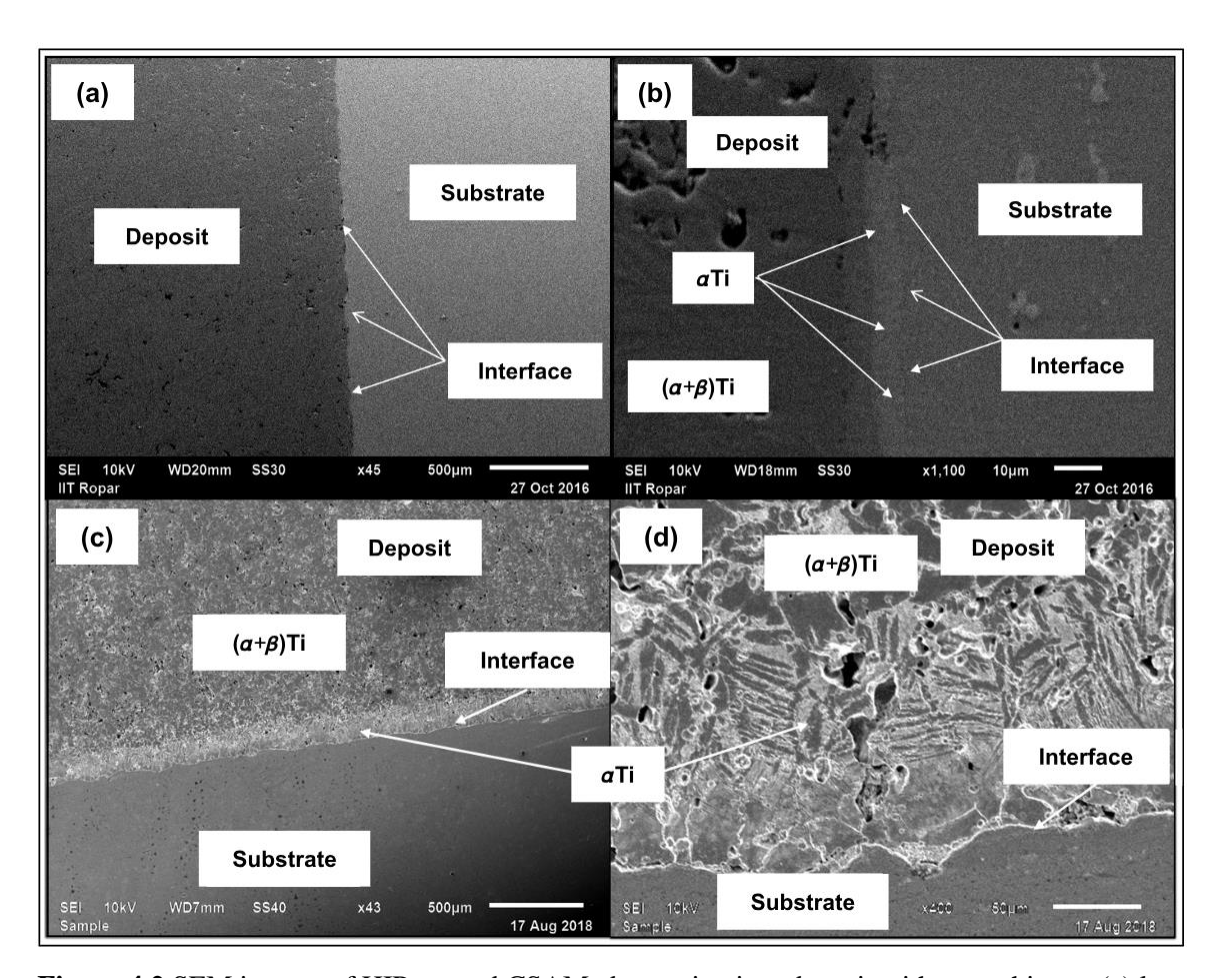


Figure 4.2 SEM images of HIP-treated CSAMed pure titanium deposit without etching at (a) low and (b) high magnification and with etching at (c) low and (d) high magnification

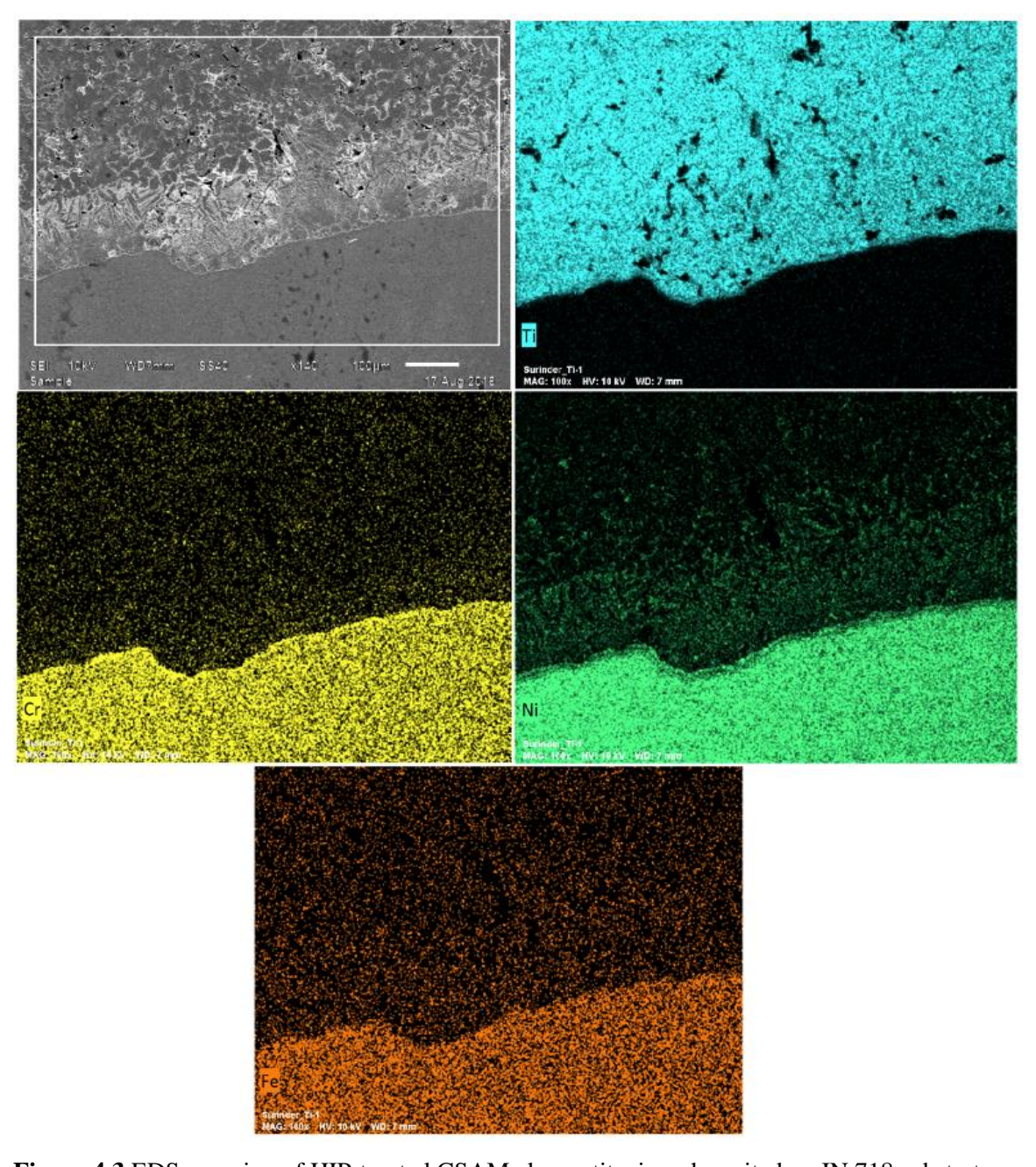


Figure 4.3 EDS mapping of HIP-treated CSAMed pure titanium deposited on IN 718 substrate

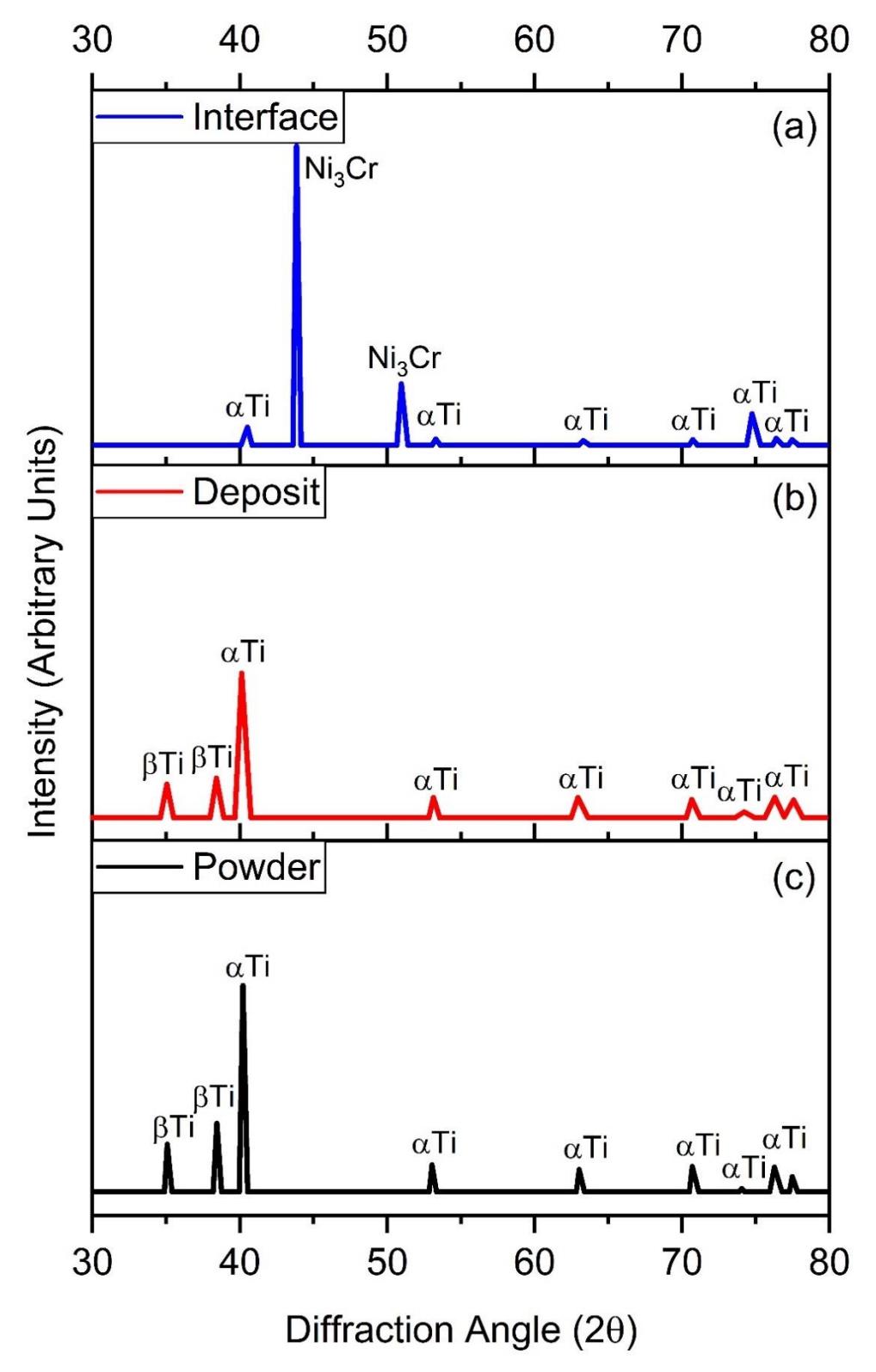


Figure 4.4 XRD data of (a) feedstock titanium powder; (b) central region of HIP-treated CSAMed pure titanium deposit and (c) at interface of the deposited titanium layer and IN 718 substrate

Figure 4.4 shows the XRD analysis of the developed HIP-treated Ti deposit near the interfacial area and inside the deposit performed by placing the sample in line with the mark of the XRD fixture, which indicates the sight of the XRD scan. XRD analysis of both areas indicates that no oxide phases were formed. This observation was also supported by the EDS analysis. This is a positive attribute regarding the development of pure-Ti products using the cold spraying process. Additionally, the absence of intermetallic phases at the interface proved that cold spraying is superior to conventional high-temperature additive manufacturing technologies in inhibiting the synthesis of brittle intermetallic phases at the multi-materials interface. The XRD analysis revealed that the deposit exhibited a more pronounced peak broadening compared to the powder and interface regions, as depicted in Figure 4.4. This phenomenon could be attributed to the combined influence of strain and size effects in HIP-treated CSAMed pure titanium deposits. The strain and dislocation movements might vary the lattice spacing, resulting in peak broadening. The crystallite size decreased due to grain subdivision, dynamic recrystallization, and grain refinement. Smaller crystallites had a limited number of lattice planes contributing to the diffraction, resulting in broader diffraction peaks (Zitting et al. 2023).

The XRD analysis of the HIP-treated CSAMed pure titanium deposits and the used powder showed the presence of both α - and β -titanium, while at the interface, only α -titanium peaks were observed. The reduced α-Ti peak height in the deposit and at the interface was indeed due to the severe plastic deformation in the cold spray process, which refined the grains and changed the crystallographic texture of the α-Ti phase. This effect led to peak broadening or a lower peak height in the XRD pattern, reflecting altered grain orientation and reduced crystalline order. The presence of both the phases (α and β) in the titanium powder, as illustrated in Figure 4.4, was a result of the material's unique phase diagram and the specific manufacturing processes used to produce the powder. At high temperatures (above the β transus temperature, typically around 882 °C or 1620°F), titanium exists in the β phase, which has a body-centered cubic (BCC) crystal structure. As the temperature decreases below the β transus, titanium undergoes a phase transformation to the α phase, which has a hexagonal close-packed (HCP) crystal structure. It is important to mention that the method used for making the feedstock titanium powder was atomization in this case. In this method, molten titanium is sprayed or atomized into fine droplets using high-pressure gas or other means. These droplets are rapidly cooled and solidified into powder particles. During the rapid cooling process, the material could become "frozen" in a metastable state, preserving both the α and β phases in the powder. This was because the cooling rate is so fast that the phase transformation from β to α may not have had time to complete before the particles solidified. The presence of only α-Ti peaks at the interface suggests that a transformation of β to α occurred in the titanium deposits. This transformation is often influenced by two main factors: rapid cooling from the β phase or $\alpha + \beta$ regions, which might have taken place after HIP, especially the interfacial region, which was closer to the substrate than the other part of the deposit, and plastic deformation during cold spraying, which induced this transformation. The fast cooling at the interface led to the formation of Widmanstatten- α laths. Moreover, the HIP treatment applied to the CSAMed Ti deposits resulted in the spheroidization of the colony microstructure within each β grain. This process produced a micro-duplex structure comprising primary α particles in a matrix of β grains/sub-grains. These β grains/sub-grains developed during the slow cooling of the deposit after HIP in contrast to the interfacial region. This is the reason for the α and β peaks in the case of the deposit, as depicted in Figure 4.4 (Semiatin 2020; Motyka *et al.* 2020).

The density for the HIP-treated CSAMed pure titanium sample/deposit was observed at 4.14 g/cc when determined using the Archimedes method, respectively. However, the density of the pure bulk Ti (manufactured through special casting machines) was measured as being 4.50 g/cc when determined using the aforesaid method. It is very challenging to produce a pore-free deposit of titanium powder using cold spraying (solid-state deposition) alone due to the irregularly shaped morphology of powder particles. Furthermore, owing to its low density and hexagonal close-packed (HCP) crystal structure, it is very difficult to densify Ti (Hussain *et al.* 2011). Therefore, the HIP treatment of the CSAMed thick Ti deposits has been performed to achieve a comparatively denser microstructure with a density approaching that of bulk Ti. An apparent surface porosity having a value of less than 1 % has been achieved in HIP-treated CSAMed pure titanium Ti deposit. However, pores with size variation from 3 to 10 μ m have been observed in the deposit when measured using the Image-J analyzer. Relatively higher amounts of smaller pores (having a pore size ranging between 3 and 6 μ m) have been observed as compared to that of larger pores (having a pore size range of 6–10 μ m).

4.1.1.2 Mechanical Properties Evaluation

The microhardness plot (hardness v/s thickness) of the HIP-treated CSAMed pure titanium deposits is shown in Figure 4.5. The average microhardness of the Ti-layers is 214 HV, which is slightly higher than that of the commercially available bulk titanium (202 HV) (Rocha *et al.* 2006). The average microhardness value at the interface was observed as being 519 HV (at the white line observed in SEM images). This jump was observed because of the strain hardening of the substrate at the interfacial region due to the extremely high-velocity bombardment of the Ti particles. Additionally, it may be due to the presence of α phase, which has hexagonal close

packing (HCP) compared to the β phase possessing a body-centered cubic (BCC) crystal structure, leading to the greater hardness of the α phase compared to the β phase (Rocha *et al.* 2006). The transition elements in the substrate might have stabilized the α phase of titanium by lowering the β - α phase transition temperature during HIP treatment at 900 °C (Henriques et al. 2005). The XRD data (Figure 4.4) also established the stabilization of the α phase because β phase peaks were not seen in the XRD analysis at the interface (Leyens and Peters 2006).

Localized mechanical properties of the deposited titanium without the substrate were measured via nanoindentation. The load-displacement curve is depicted in Figure 4.6. The nanohardness was found to be 5.2 GPa. Young's modulus of the sample was found to be 148 GPa in comparison to 105-115 GPa of the bulk titanium (Hussain 2013). The magnitude of Young's modulus was found to be higher because the applied stress needs to first overcome the residual compressive stresses owing to cold spraying and HIP treatment before straining the material. It may also be due to individual particle sampling in nanoindentation, which offers less in terms of contribution from pores/oxides (Rocha *et al.* 2006).

The ultimate tensile strength (UTS) was found to be 384 MPa, with a total elongation of 6 %, as represented in Figure 4.7. The UTS achieved in the present study is more than that achieved by Hussain (2013), which was 247 ± 15 MPa for titanium deposit sprayed with a commercially available CGT system using nitrogen at 800 °C at 4.0 MPa. Additionally, the achieved UTS was near to the UTS of bulk titanium (434 MPa) (Hussain 2013). This may be due to the HIP treatment of as-sprayed titanium, which led to lesser porosity and higher UTS. It is well known that the elongation can be augmented via the post-heat treatment routes available in the literature. The slight drop in stress observed in HIP-treated CSAMed pure titanium deposits containing both α and β phases during stress-strain testing could be attributed to several factors. The interaction between these phases may have caused a temporary redistribution of stress during deformation, leading to a short-lived reduction in load-bearing capacity. Moreover, the limited slip systems present in the α -phase could have impeded dislocation movement, resulting in localized deformation that contributed to this stress drop. In total, two samples were tested for ensuring repeatability of the results.

The shear strength between the first layer of the deposit and the substrate was found to be 26 MPa. This poor adhesion may be due to the formation of a hard face (α -titanium) near the interface. Additionally, the diffusion coefficient of HCP α -titanium is lower than the diffusion coefficient of BCC β -titanium due to the dense packing of atoms in HCP α -titanium (Hussain 2013). This decreased diffusion and formation of the hard phase of HCP α -titanium at the interface might have led to poor metallurgical bonding at the interface. It is pertinent to mention

that this lower shear strength is beneficial with regard to the AM aspect of cold spraying, as one has to remove the substrate in the case that a standalone structure of Ti is required to be manufactured.

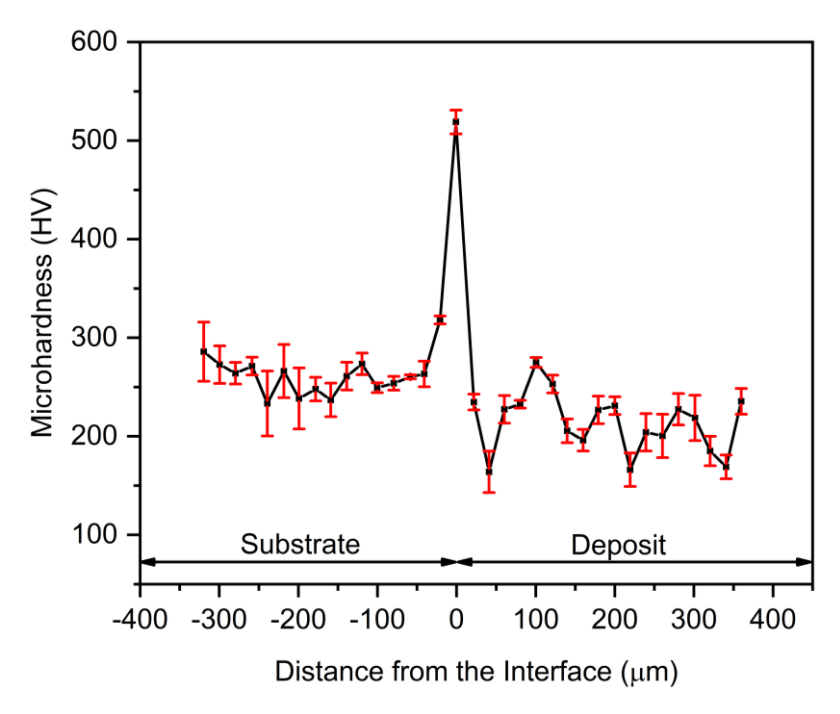


Figure 4.5 Cross-sectional microhardness analysis of the HIP-treated CSAMed pure titanium on IN 718 substrate

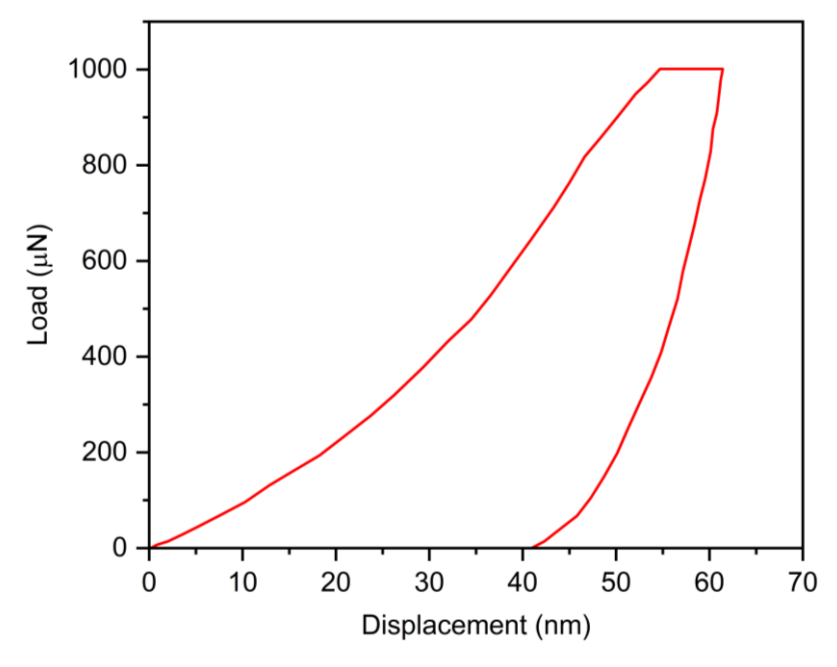


Figure 4.6 Load-displacement curve of the HIP-treated CSAMed pure titanium deposit obtained through nanoindentation

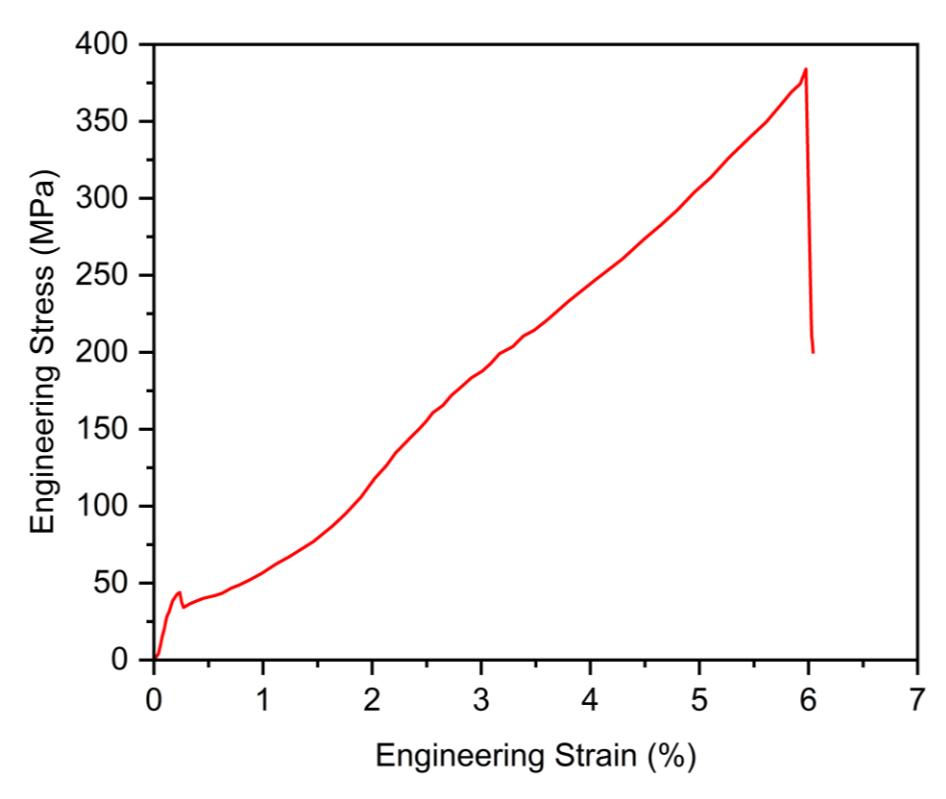


Figure 4.7 Macro-tensile plot showing engineering stress versus engineering strain for the HIP-treated CSAMed pure titanium deposit

Micro-tensile plot showing engineering stress versus engineering strain, along with the corresponding SEM images at various stages, is shown in Figure 4.8. A complete brittle nature of the fracture can be observed from the tensile curve. The ultimate tensile strength was found to be 462 MPa, with an elongation of 1.6 % only. Moreover, micro-UTS was found to be higher than macro-UTS. It may be due to the polishing performed on the micro-tensile sample. A finely polished surface might have delayed the crack initiation, which led to higher yield strength and UTS. Young's modulus achieved by micro-tensile (53.5 GPa) is higher than that achieved from a macro-tensile sample (22.5 GPa); however, it is very less than that observed during nanoindentation (143 GPa). The lower modulus in macro-tensile compared to micro-tensile analysis could be attributed to the polishing of samples required for micro-tensile for in-situ analysis in SEM. It has been reported that the sprayed deposits have a significantly lower modulus often as compared to bulk material because of less compliance between the splats (Torrance and Stefanescu 2004). Moreover, higher values achieved through nanoindentation may be due to individual particle sampling, which offers less contribution from pores/oxides.

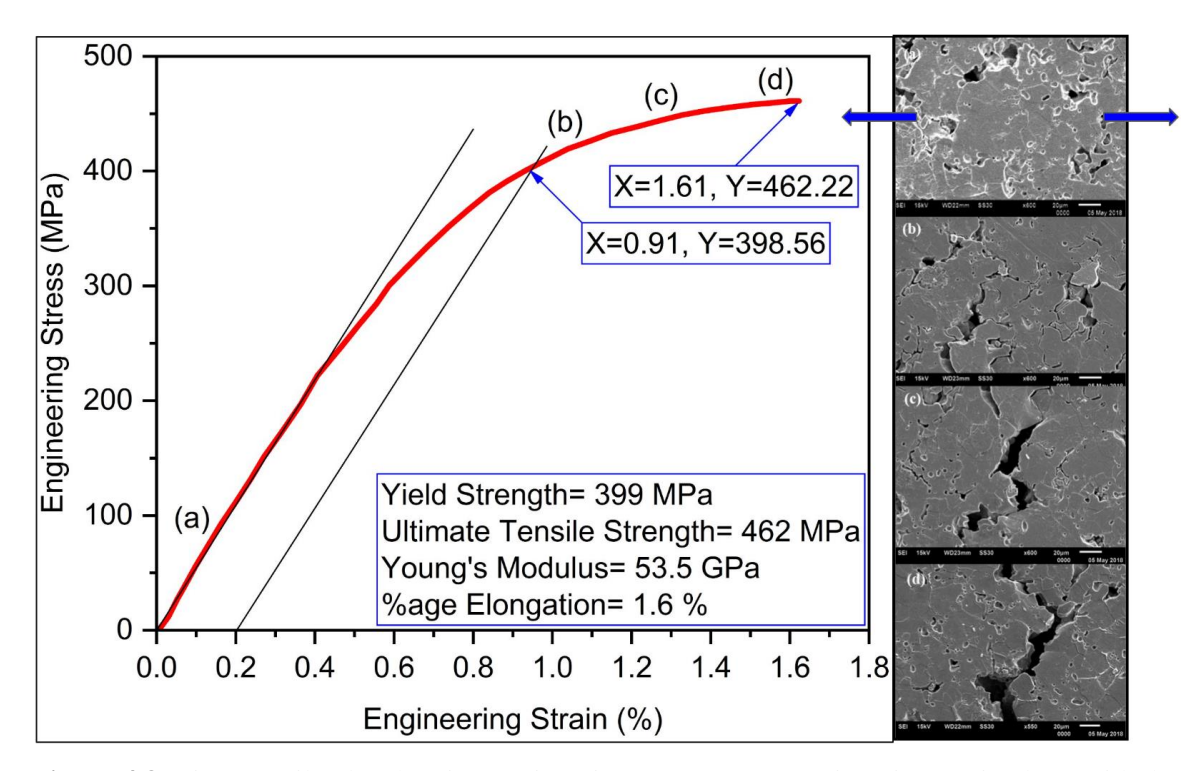


Figure 4.8 Micro-tensile plot showing engineering stress versus engineering strain along with the in-situ SEM-micrographs at various crack stages for the HIP-treated CSAMed pure titanium deposit

It was also observed during the in situ tensile testing that no cracks were nucleated (Figure 4.8 (a)) till 399 MPa (Yield strength). The cracks started nucleating from the pore boundaries above the yield point, as represented in Figure 4.8 (b). Further, straining of the material led to the propagation of cracks through the splat boundaries. The cracks passed from pore to pore through the splat and grain boundaries (Figure 4.8 (c)). The final fracture of the material showed a brittle nature (Figure 4.8 (d)). An examination of the fractured surfaces of the deposited Ti sample was performed using SEM, which is shown in Figure 4.9. Despite the fact that some localized dimples were also visible, the fractography study does not provide any indications of distinctive features like cup and cone. These fractured surfaces are significantly similar to those found in powder metallurgy (MacDonald et al. 2017).

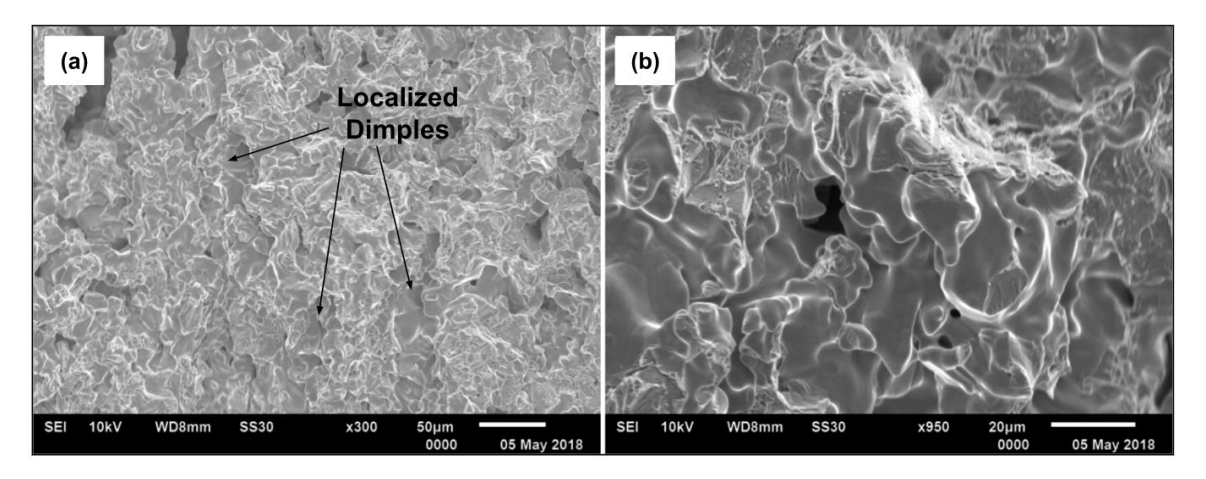


Figure 4.9 Fractography analysis of the HIP-treated CSAMed pure titanium deposit after microtensile test at (a) lower and (b) higher magnification

4.1.1.3 High Temperature Cyclic Oxidation Study

Cyclic oxidation was performed to evaluate the deposit's sustainability under high-temperature conditions. The plot of the mass gain vs. number of cycles is represented in Figure 4.10. To ascertain the rate law for high-temperature cyclic oxidation of the sample, the square of mass gain vs. number of cycles plot is drawn as displayed in Figure 4.11. A parabolic relationship was observed to approximate the data. The parabolic rate constant of deposited Ti can be calculated as follows (Kaur *et al.* 2015):

$$(\Delta W)^2 = K_p.t \qquad \text{eq}(4.1)$$

where ΔW is the mass change per total surface area, K_p is the parabolic rate constant, and t is the oxidation time. The value of K_p for the HIP-treated CSAMed pure titanium sample is found to be $1.17 \times 10^{-11} \text{ g}^2 \text{ mm}^{-4} \text{ s}^{-1}$, which describes the cyclic oxidation rate quantitatively. The magnitude of K_p was observed to be less than that of titanium specimens prepared via the powder metallurgy process assisted with inductive sintering $(1.43 \times 10^{-11} \text{ g}^2 \text{ mm}^{-4} \text{ s}^{-1})$ (Latief *et al.* 2020). The mass of the HIP-treated CSAMed pure titanium sample was found to increase during the first 67^{th} cycles. However, the mass of the sample stabilized after the 68^{th} cycle. This mass stabilization effect is evident from the parabolic nature of the curve, as shown in Figure 4.10 (Kang *et al.* 2019). No spallation was observed during the whole oxidation study. The mass change trend shows that the material could have good oxidation resistance during longer usage. That may be due to the forming of a protective layer of titanium oxide. However, no stabilization in mass gain was observed in the studies available in the literature, even after 1500 cycles of oxidation in air at

a 700 °C temperature for pure bulk titanium (Latief *et al.* 2020). This concretes that HIP-treated CSAMed pure titanium deposit is more advantageous for high-temperature applications.

The macrographs of one of the samples subjected to cyclic oxidation at high temperatures are presented in Figure 4.12. Overall, the scale was smooth and continuous without cracks, with no trend of scale spalling during the entire study. The sample at its initial stage was metallic in color with a shining surface due to fine polishing. After the first oxidation cycle, the whole surface became creamish in color, and gray spots started appearing after the 4th cycle with a cream color in the backdrop. These gray spots started increasing in size, and almost 80 % of the surface became gray after the 27th cycle. Further, the gray shade became creamish, and the creamish color began changing to a light-yellow tone. Almost the whole surface of the sample turned light yellow towards the end of the high-temperature cyclic oxidation study carried out for 85 cycles. These color variations may be due to changes in the mineral form of titanium dioxide from anatase to rutile or vice versa during heating (Kanjer *et al.* 2018; Kavei *et al.* 2011).

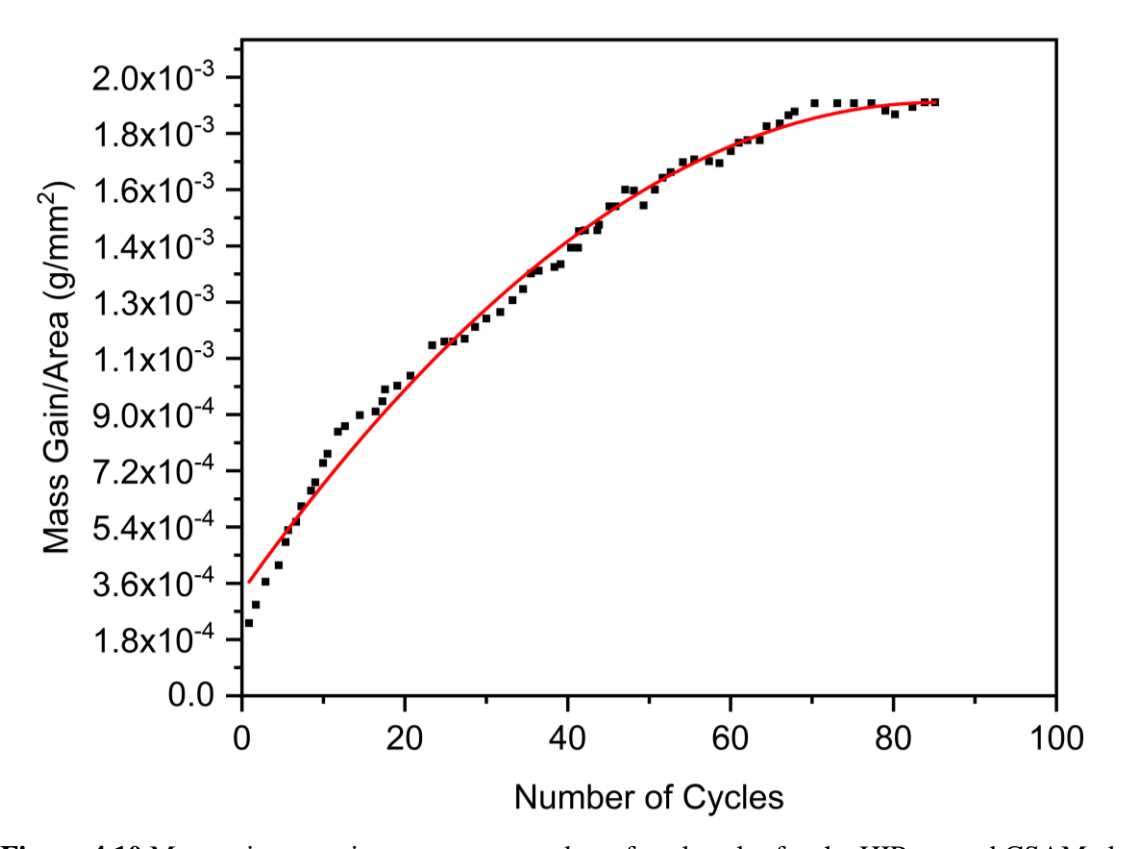


Figure 4.10 Mass gain per unit area versus number of cycles plot for the HIP-treated CSAMed pure titanium deposit subjected to cyclic oxidation in air at 900 °C

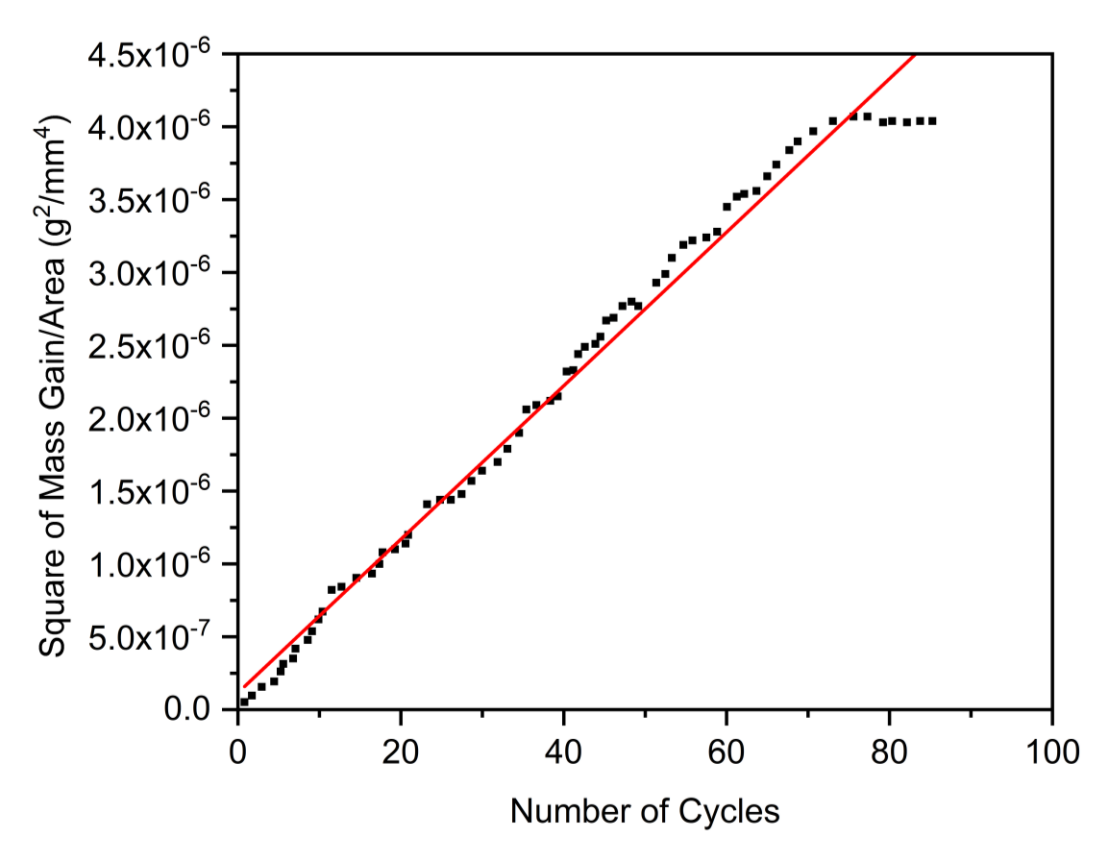


Figure 4.11 Square of mass gain per unit area versus number of cycles plot for the HIP-treated CSAMed pure titanium deposit subjected to cyclic oxidation in air at 900 °C

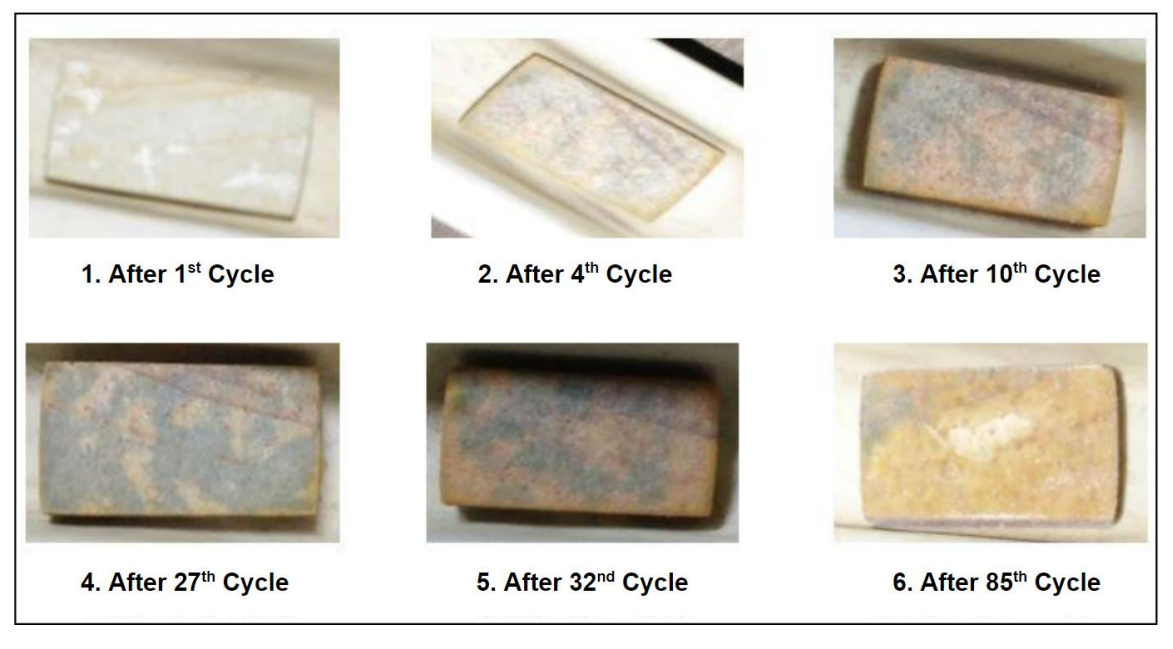


Figure 4.12 Macrographs of the HIP-treated CSAMed pure titanium deposit subjected to high-temperature cyclic oxidation in air at 900 °C

Cross-sectional optical images and microhardness analysis of the HIP-treated CSAMed pure titanium deposit subjected to high-temperature cyclic oxidation are represented in Figure 4.13 (a) and (b), respectively. High-temperature cyclic oxidation induced the development of a layered oxide structure through a complex interplay of oxidation and reduction cycles. This cyclic process led to the continuous growth of the oxide scale with each cycle, resulting in distinct layers. Moreover, diffusion and segregation of elements at the oxide-metal interface significantly influenced the composition and structure of the layers. Additionally, phase changes of the oxide layers in response to varying conditions and the intricate influence of microstructural features, such as grain boundaries, precipitates, and defects, were pivotal factors shaping the layered oxide structure. Understanding these phenomena was crucial for improving the performance and durability of materials in high-temperature environments, particularly in gas turbine components, heat exchangers, and other applications subjected to repeated thermal cycling in oxidizing atmospheres (Xu et al. 2021). A cracked oxide scale of 400 µm thickness and an average microhardness of 818 HV was observed, which implies the critical scale thickness for spallation. The tremendous rise in the oxide scale microhardness is because of the mineral forms of titanium dioxide present in the oxide scale. Rutile and anatase phases were the mineral forms of titanium dioxide investigated through XRD analysis. These two mineral forms have body-centered tetragonal (BCT) crystalline structures, which have fewer active slip systems and hence high hardness and brittleness. The microhardness of the HIP-treated CSAMed pure titanium deposit was observed to be higher (775 HV) at the deposit-oxide scale interface (0 μm), which starts to decrease up to 500 µm deeper inside the deposit, attaining a microhardness of 202 HV. The microhardness value stabilized to an average value of 175 HV after 500 µm distance from the deposit-oxide scale interface. The variation in hardness may be due to comparatively higher oxygen concentration (enrichment of titanium with oxygen) in the outer layers than in the inner layers of the deposit. Therefore, from the obtained microhardness values and optical micrographs, it can be concluded that oxidation of titanium comprises both oxidation dissolution of the titanium near the interface and oxide scale formation.

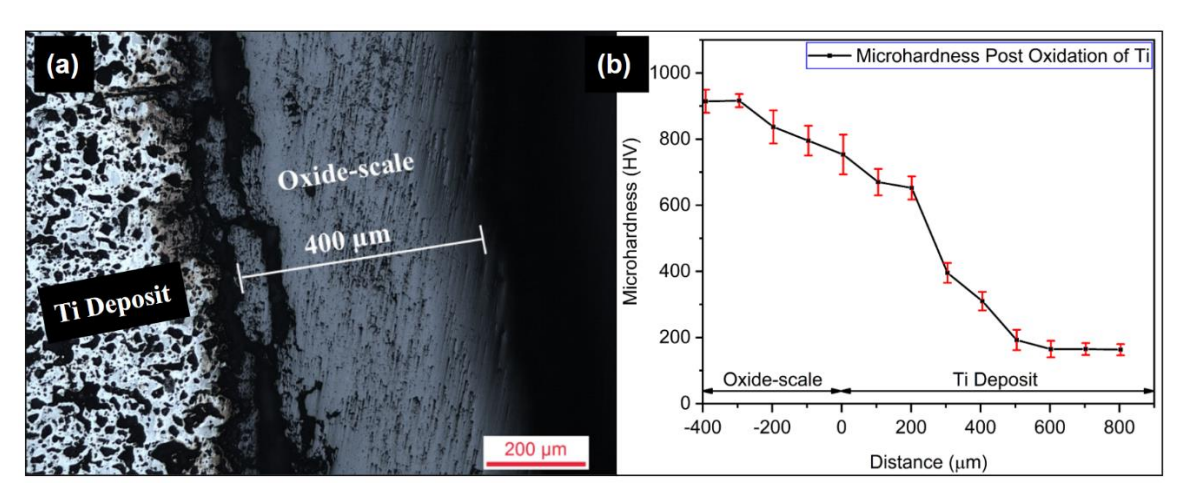


Figure 4.13 (a) Cross-sectional optical micrograph; (b) cross-sectional microhardness analysis of the HIP-treated CSAMed pure titanium deposit subjected to high-temperature cyclic oxidation in air at 900 °C

Surface SEM analysis of the oxidized deposit is provided in Figure 4.14 (a). A crystalline structure can be seen, like a bunch of rods with variations in length. The development of a crystalline rod-like structure with varying lengths during high-temperature cyclic oxidation of titanium arose from the influence of Ti's hexagonal close-packed (HCP) crystal structure. The repeated oxidation-reduction cycles in an oxidizing environment facilitated the preferential growth of rutile titanium oxide (TiO₂) along specific crystallographic directions, resulting in the formation of rod-like morphologies. This phenomenon was affected by crucial parameters such as temperature, oxygen concentration, and the number of oxidation cycles, which contributed to the observed variations in rod lengths. Additionally, microstructural features, including grain boundaries and defects, played a significant role by serving as preferential sites for oxide growth, thereby enhancing the diversity in rod lengths. A comprehensive understanding of these factors was essential for tailoring and optimizing the performance of titanium-based materials under high-temperature conditions, thus enabling advancements in various industrial applications (Liu et al. 2021). EDS analysis with point spectrum and mapping showed the presence of titanium and oxides on the whole surface (Figure 4.14 (b) and Figure 4.15, respectively). EDS square spectrum analysis (shown in Figure 4.14 (b)) showed an 80 % concentration of oxide and a 20 % concentration of titanium on the surface. The presence of platinum in the EDS spectrum is due to the sputtering performed before the SEM/EDS analysis to make the oxide layer conductive for obtaining better results in SEM/EDS.

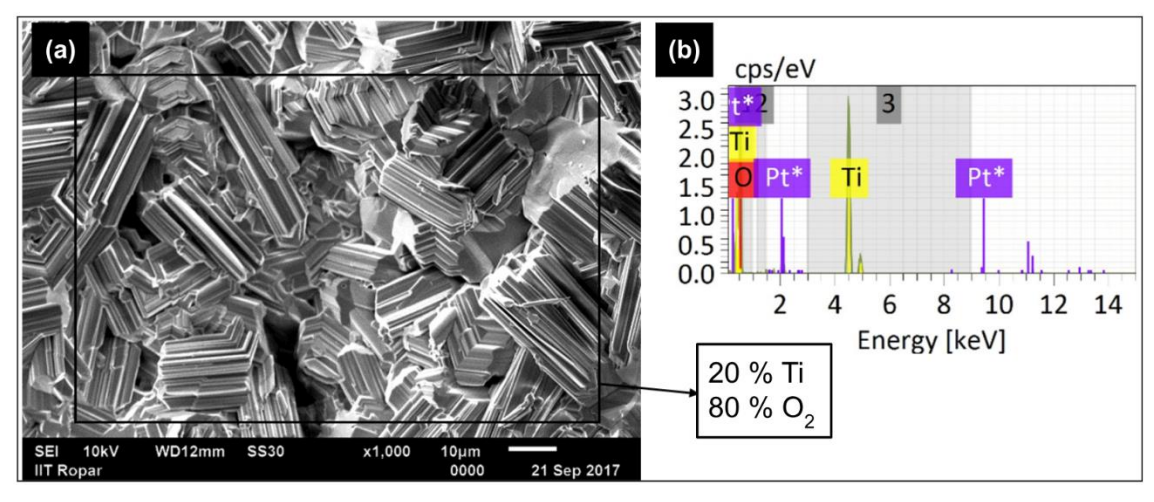


Figure 4.14 (a) Surface SEM micrographs; (b) EDS spectrum of the HIP-treated CSAMed pure titanium deposit subjected to high-temperature cyclic oxidation in air at 900 °C

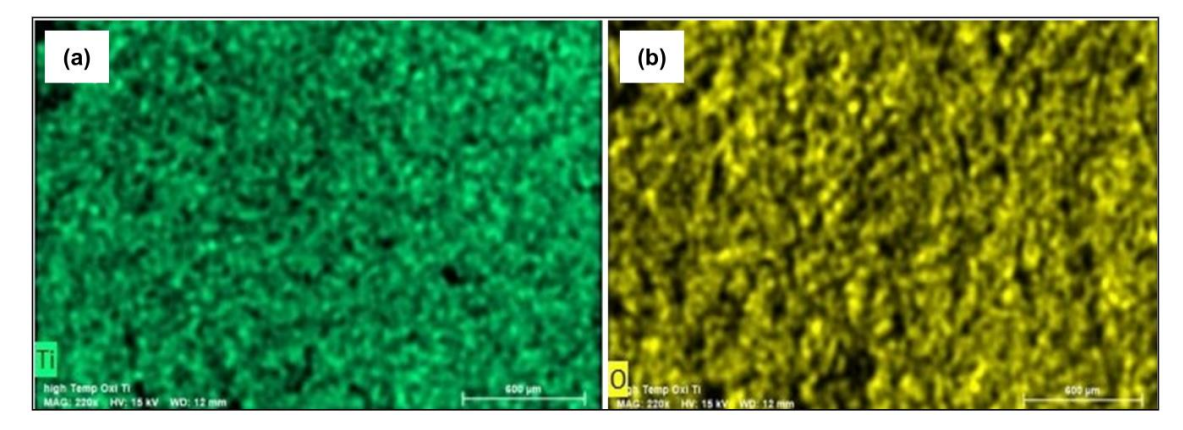


Figure 4.15 EDS mapping of the HIP-treated CSAMed pure titanium deposit subjected to high-temperature cyclic oxidation in air at 900 °C: (a) titanium; (b) oxygen

The X-ray diffractogram for the HIP-treated CSAMed pure titanium deposit subjected to high-temperature cyclic oxidation is displayed in Figure 4.16. It is evident from the XRD analysis that the HIP-treated CSAMed pure titanium sample developed a layer of titanium oxide TiO₂ after high-temperature cyclic oxidation. Diffraction peaks observed were of TiO₂ having a crystalline structure in the form of rutile and anatase, which are the two mineral forms of the crystalline structure of titanium dioxide (Kavei *et al.* 2011). Most of the peaks are rutile, and very few have an anatase structure. The formation and transformation of rutile and anatase phases during high-temperature cyclic oxidation were governed by a complex interplay of temperature-dependent thermodynamics, phase transition kinetics, and microstructural influences. Initially, rapid oxidation resulted in the thermodynamically favored rutile phase formation. Subsequent heating and cooling cycles induced fluctuations in temperature and oxygen concentration, impacting

microstructure and stability. Lower temperatures promoted the kinetics-favorable transformation to metastable anatase, while higher temperatures reverted anatase to rutile due to equilibrium thermodynamics.

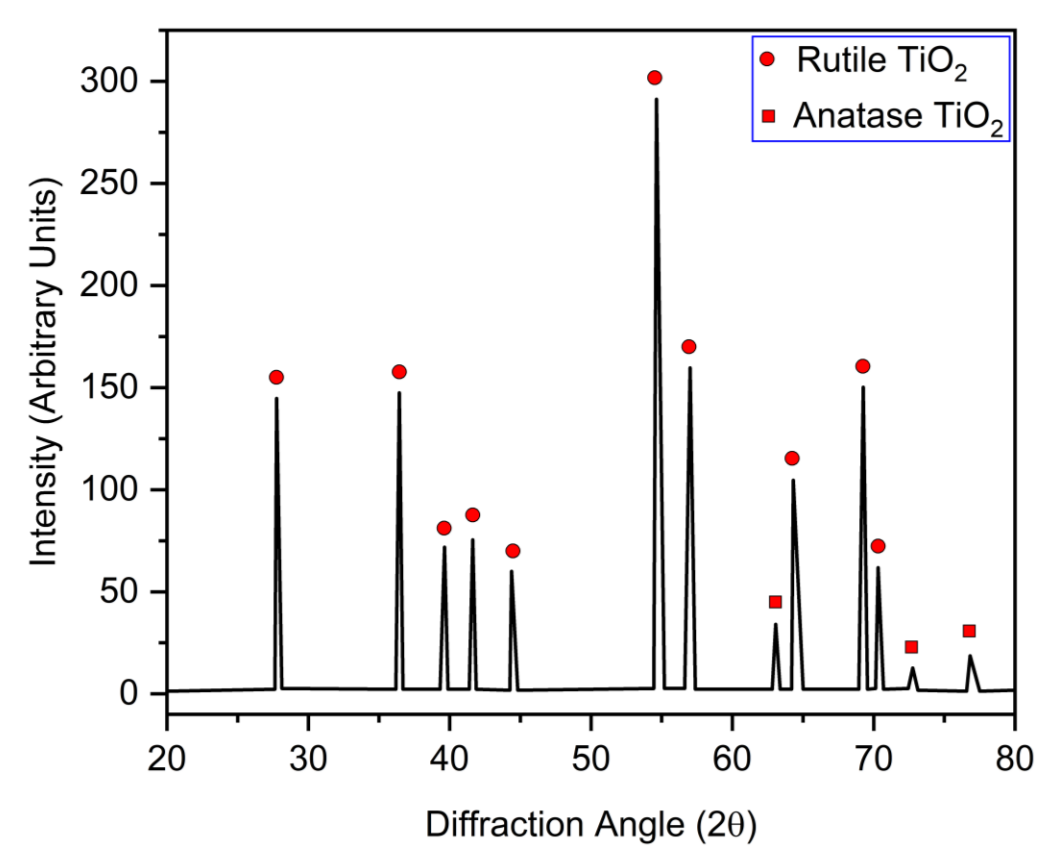


Figure 4.16 XRD analysis of the HIP-treated CSAMed pure titanium deposit subjected to high-temperature cyclic oxidation in air at 900 °C

Microstructural features, such as grain boundaries and defects, influenced phase nucleation and growth. Additionally, oxygen diffusion into the oxide scale during oxidation-reduction cycles significantly affected phase transformation kinetics, contributing to the observed phase changes (Hanaor and Sorrell 2011). Therefore, it may be concluded that initially (after 1st cycle) rutile structure of titanium dioxide was formed, which probably appeared creamish in color. After further heating cycles, it converted into anatase and appeared blackish after the 27th cycle. Further heating cycles may lead to the conversion of anatase to a rutile crystal structure of titanium dioxide. The rutile crystal is the most stable polymorph of TiO₂ at all temperatures compared to metastable anatase. The color variation is due to a change in crystal structure having a difference in refractive index. Rutile has a higher refractive index (RI) when compared to anatase. Therefore, the scattering of light is relatively higher by the rutile phase, leading to

creamish/yellow color, whereas anatase has comparatively lesser RI, scatters less light, and appears grayish. The rutile type of pigments is generally preferred over anatase because they scatter light more efficiently, are more stable, and are less likely to catalyze photodegradation (Luttrell *et al.* 2014). Additionally, rutile can be converted into a titanium sponge through the Kroll process. Summarizing the above discussion on oxidation behavior, it is concluded that the manufactured titanium deposit has a high oxidation resistance.

4.2 Ni-20Cr DEPOSITS

4.2.1 Results and Discussion

4.2.1.1 Microstructural Analysis

Cross-sectional SEM images of cold spray additively manufactured (CSAMed) Ni-20Cr-AS, Ni-20Cr-SH, and Ni-20Cr-HIP have been represented in Figure 4.17 (a), 4.17 (b) and 4.17 (c), respectively. Moreover, the comparison of density, apparent surface porosity, and pore size distribution has been represented in Figure 4.18. The pores/voids were large in numbers, and size was of the order of 2-10 µm in the Ni-20Cr-AS (Figure 4.17 (a)), which resulted in 9.54 % apparent surface porosity (calculated from Image-J analysis) and lesser density of the magnitude of 6.43 g/cc (calculated by Archimedes principle using density measuring kit) as compared to the density of bulk Ni-20Cr alloy (8.3 g/cc). Comparatively smaller pores of the order of 1-3 µm have been observed in Ni-20Cr-SH (Figure 4.17 (b)) with 6.36 % apparent surface porosity. The density of the sample (7.36 g/cc) was observed better than Ni-20Cr-AS but lesser than the bulk material. However, a surface with the least defects (porosity and voids) was observed for Ni-20Cr-HIP samples (as represented in Figure 4.17 (c)). The least apparent surface porosity having a value of 2.43 % and the best density of the order of 8.14 g/cc were achieved with HIP treatment. A pore size in the range of 1-4 µm was observed as comparatively bigger than Ni-20Cr-SH. It can be perceived from Figure 4.17 and Figure 4.18 that HIP treatment improved the microstructure by reducing the porosity and improving the density by 75 % and 27 %, respectively. EDS spectra of Ni-20Cr-AS, Ni-20Cr-SH, and Ni-20Cr-HIP deposits are represented in Figure 4.19 (a), 4.19 (b) and 4.19 (c), respectively. There is a small difference in the elemental compositions of all three samples that might be due to some measurement error. The elemental composition showed the absence of oxygen and the presence of a mixture of nickel and chromium in all the deposited specimens. The same has also been supported by XRD analysis as represented in Figure 4.20.

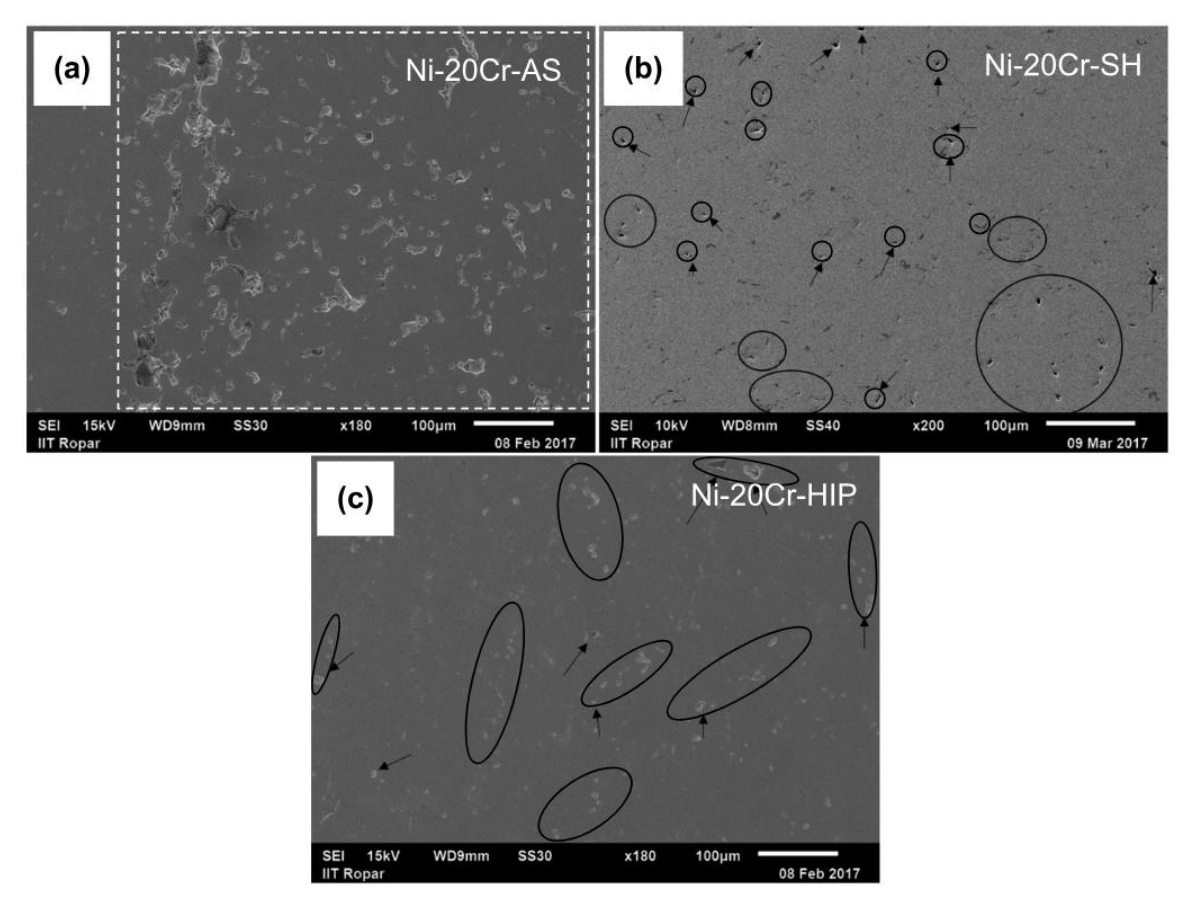


Figure 4.17 Cross-sectional SEM analysis of the CSAMed Ni-20Cr thick plates: (a) as-sprayed; (b) substrate heated; (c) hot-isostatic pressing treated, pores in the microstructures are encircled

XRD analysis of all the specimens showed no-oxide formation. Only the Ni₃Cr phase was observed in the specimens and powder feedstock. However, the shifting of peaks towards a lower diffraction angle for Ni-20Cr-AS was observed. Peak shifts can be caused by changes in chemical composition or by strain (Mazhdi and Tafreshi 2018). Since the chemical composition remained unchanged, the only other possibility for peak shifting is strain. This might have been caused by residual stress from high-velocity particle impact deformation in the cold-sprayed deposits (Marzbanrad *et al.* 2018). The shifting observed was towards a lower diffraction angle, suggesting that the stresses/strains might be compressive in nature (Marzbanrad *et al.* 2018).

Moreover, peak broadening of the Ni-20Cr-SH deposit was observed, which depicted the grain refinement or recrystallization of the deposited material. As the high-velocity particles strike the heated substrate, they become deformed, resulting in dynamic recrystallization and a refined grain structure leading to peak broadening in the XRD analysis (Li *et al.* 2021).

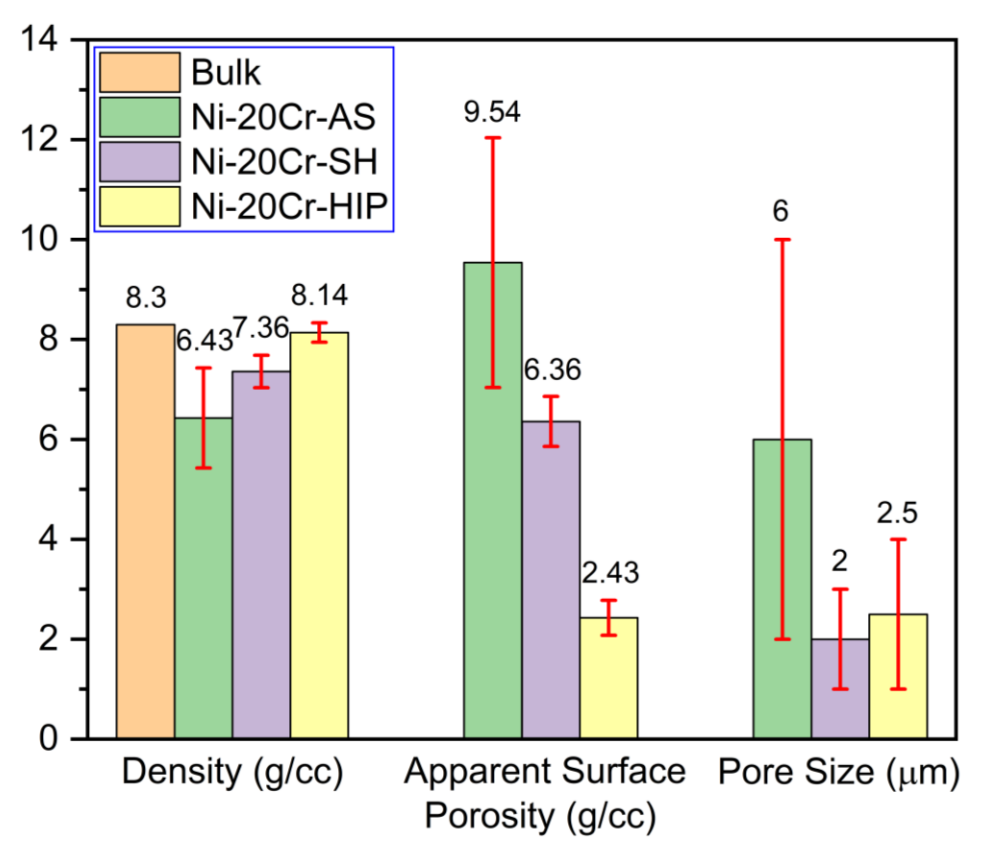


Figure 4.18 Density, apparent surface porosity, and pore size data of the CSAMed Ni-20Cr thick plates in as-sprayed, substrate heated, and hot-isostatic pressing treated conditions

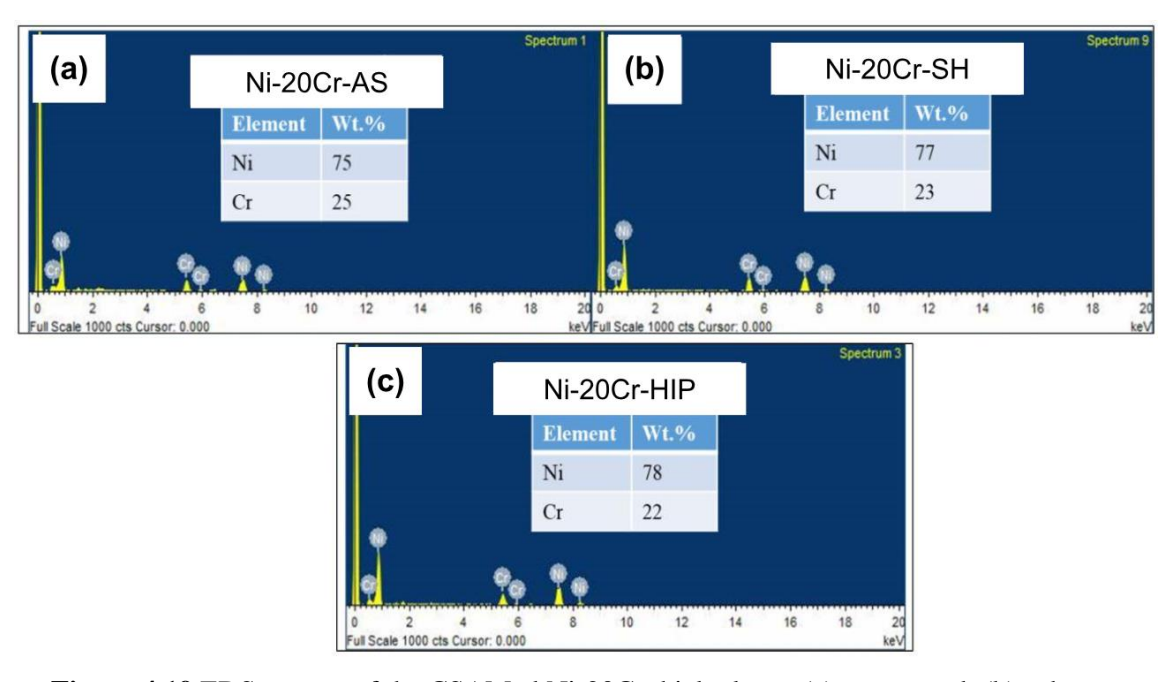


Figure 4.19 EDS spectra of the CSAMed Ni-20Cr thick plates: (a) as-sprayed; (b) substrate heated; (c) hot-isostatic pressing treated

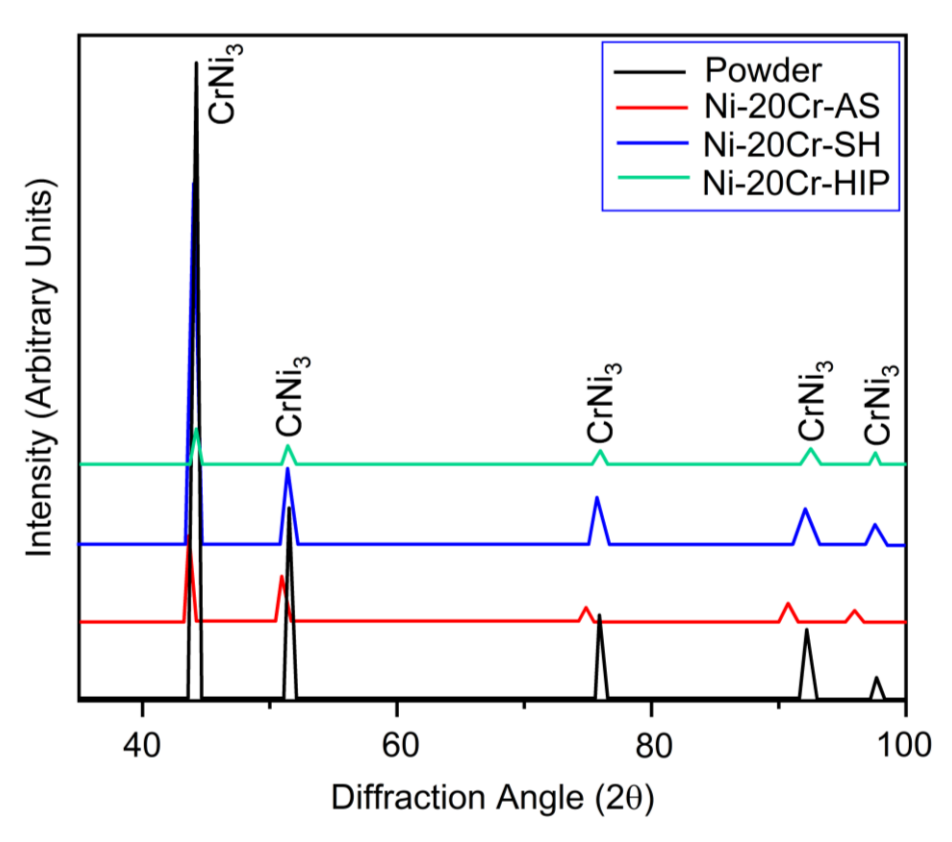


Figure 4.20 XRD data of as-received Ni-20Cr powder feedstock and CSAMed Ni-20Cr thick plates

4.2.1.2 Mechanical Behaviour

The microhardness, nanohardness, and elastic modulus of Ni-20Cr-AS, Ni-20Cr-SH, and Ni-20Cr-HIP deposits are displayed in Table 4.1.

Table 4.1 Microhardness, nanohardness, and elastic modulus data of the CSAMed Ni-20Cr thick plates in as-sprayed, substrate heated, and hot-isostatic pressing treated conditions

Name of Sample	Microhardness (HV)	Nanohardness (GPa)	Modulus of Elasticity (GPa)
Ni-20Cr-AS	389 ± 50	6.8 ± 0.7	229 ± 11
Ni-20Cr-SH	422 ± 10	6.3 ± 0.4	210 ± 7
Ni-20Cr-HIP	185 ± 15	4.8 ± 0.5	227 ± 9

The average microhardness of Ni-20Cr-SH was observed to be the highest among the investigated cases, with the least variations (highest= 432 HV, lowest= 412 HV). Moreover, Ni-20Cr-AS deposits showed higher variations in hardness (highest= 439 HV, lowest= 339 HV). Ni-

20Cr-HIP deposits showed the lowest hardness among the investigated cases with moderate variations. These variations in microhardness can be related to the porosity observed. Ni-20Cr-AS has the highest apparent surface porosity, hence resulting in higher hardness variations as compared to the other two deposits. The Ni-20Cr-HIP sample has the least apparent surface porosity compared to the other two deposits, hence resulting in the least variations in hardness values. Moreover, the nanohardness of Ni-20Cr-HIP was observed to be the lowest, whereas it was the highest for Ni-20Cr-AS deposits. It is worth mentioning that the elastic modulus of all the Ni-20Cr deposits was found to be closer to that of the Ni-20Cr bulk material (214 GPa) (Bobbio et al. 2021), which is a desirable attribute for the cold spray process to qualify as an additive manufacturing approach. The load-displacement curves were plotted for all the cases using the data obtained from the nanoindentation testing and represented in Figure 4.21. Ni-20Cr-SH was found to be harder and stiffer while Ni-20Cr-HIP was observed to be softer and more plastic of all the three Ni-20Cr cold sprayed deposits. The Ni-20Cr-AS deposit showed moderate characteristics. Therefore, the results obtained from the microhardness (Table 4.1) were validated through load-displacement curves. The decrease in hardness due to HIP treatment was observed as residual compressive stresses are released. Moreover, the HIP time period of 2 hrs at 900 °C might have resulted in recovery, recrystallization, and grain growth of the Ni-20Cr deposits (Chen et al. 2019). Therefore, the lowest values of microhardness and nanohardness were observed. On the other hand, it is believed that the grain was refined in Ni-20Cr-SH deposits on account of dynamic recrystallization, which might have resulted in increased hardness, as per the well-known Hall-Petch effect. It is worth mentioning that for Ni-20Cr-SH cases, the substrate temperature is higher during cold spraying as HVOF (high velocity oxy-fuel) gun is also being traversed alongside the cold spray gun for the purpose of substrate heating. This heating ensures enhanced deformation of already deposited powder particles. It is reported that such additional deformation would lead to more nucleation sites for recrystallization which further induces grain refinement (Annasamy et al. 2019). Moreover, elongated and distorted grains in Ni-20Cr-AS showed high hardness compared to Ni-20Cr-HIP on account of mechanically induced grain refinement (Cinca et al. 2019).

The engineering stress vs engineering strain curves of Ni-20Cr-AS, Ni-20Cr-SH, and Ni-20Cr-HIP deposits are represented in Figure 4.22. The comparison of macro-tensile results of all cold-sprayed Ni-20Cr deposits with bulk material properties of Ni-20Cr is represented in Table 4.2. The UTS (ultimate tensile strength) was observed highest (nearest to bulk) for the Ni-20Cr-SH deposit with a moderate percentage of elongation. However, the highest percentage of elongation with the lowest UTS was observed for Ni-20Cr-HIP. The percentage elongation of the Ni-20Cr-

HIP is equal to the percentage elongation of the bulk Ni-20Cr (Bobbio et al. 2021; Zheng et al. 2012). Ni-20Cr-AS showed moderate UTS with the least percentage of elongation. It is worth mentioning that the elastic modulus and yield strength of Ni-20Cr-SH deposits are nearest to that of the bulk Ni-20Cr alloy. The lesser yield strength of Ni-20Cr-AS may be due to the porosity, owing to which the crack initiation might have started at a lesser stress leading to lower UTS and percentage of elongation. However, the effect of grain refinement and recrystallization in Ni-20Cr-SH dominated over the porosity effect, hence resulting in better UTS and percentage of elongation as compared to Ni-20Cr-AS. Similarly, the higher modulus in Ni-20Cr-SH deposit may be due to the recrystallization (grain refinement), whereas the lowest elastic modulus of Ni-20Cr-HIP may be due to grain growth after recrystallization during HIP treatment (Chen et al. 2019; Annasamy et al. 2019). Therefore, Ni-20Cr-SH may have a greater number of grain boundaries to pile up the dislocations and lesser volume for their movement (gliding) as compared to the lesser number of grain boundaries of Ni-20Cr-HIP and more volume for their movements (Samaee et al. 2020). Hence, it resulted in more ductility, lesser elastic modulus, and yield strength for Ni-20Cr-HIP and vice-versa for the Ni-20Cr-SH case. Moreover, the elastic modulus values obtained with nanoindentation analysis were observed as comparatively higher than the values obtained from macro-tensile testing. This mismatch may be primarily explained by the application of Oliver and Pharr's technique, which is based on Sneddon's analysis of elastic contact (Oliver and Pharr 1992; Hay and Pharr 1998). The lateral stresses produced by the indentation process are not taken into consideration by the effective elastic modulus (E_{eff}) , which is solely influenced by the elastic modulus of the material in the indentation direction. Through the parameter, which is shown in the following equation, this stress mechanism results in an overestimation of the elastic modulus.

$$E_{eff} = \frac{1}{\beta} \frac{\sqrt{\pi}}{2} \frac{S}{\sqrt{A(h_c)}} \qquad \text{eq}(5.1)$$

where β is equal to 1.034 for a Berkovich indenter, S is the contact stiffness, and $A(h_c)$ is the contact area (Hay *et al.* 1999; King 1987).

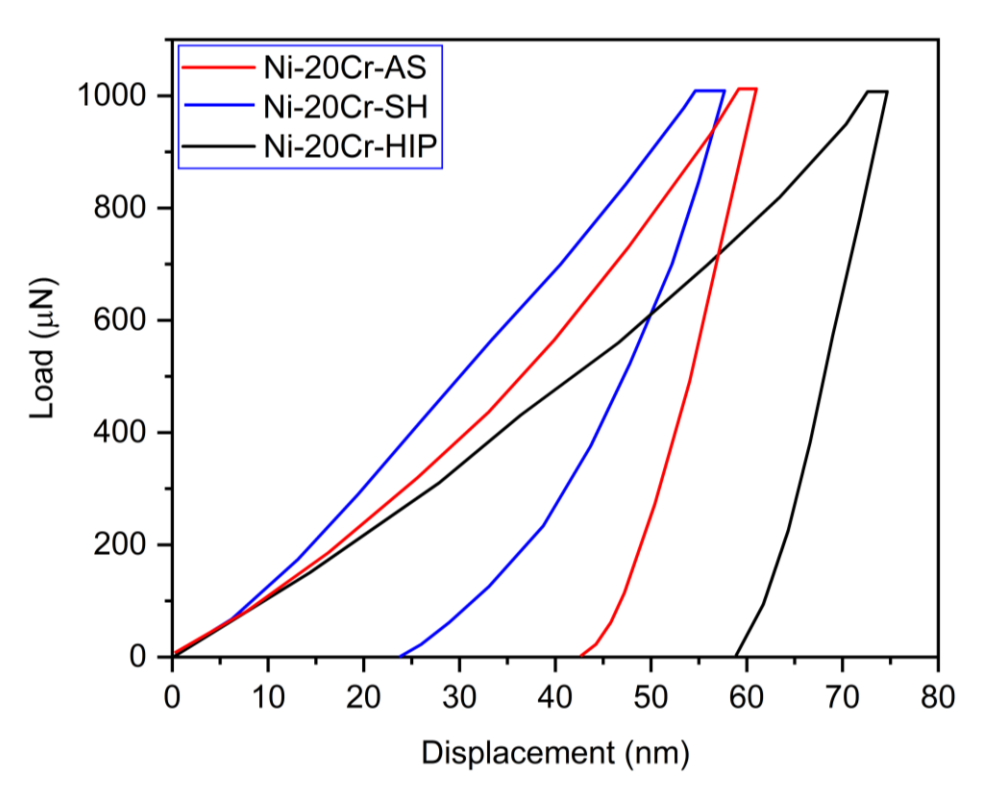


Figure 4.21 Combined load-displacement nanoindentation curves for the CSAMed Ni-20Cr thick plates in as-sprayed, substrate heated, and hot-isostatic pressing treated conditions

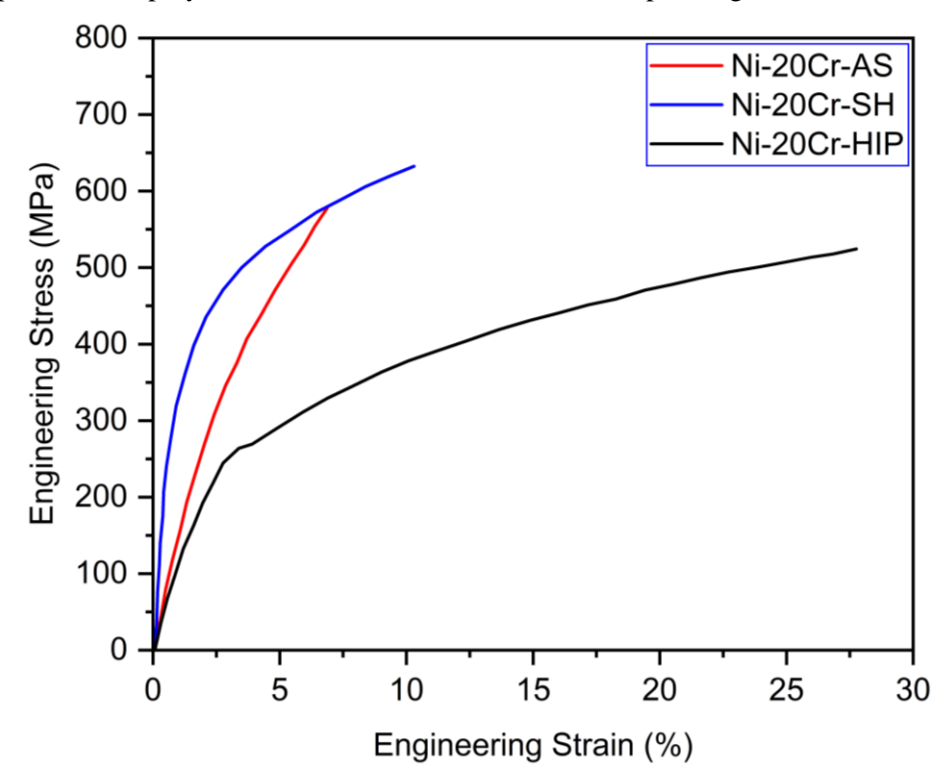


Figure 4.22 Engineering stress vs engineering strain curves for the CSAMed Ni-20Cr thick plates in as-sprayed, substrate heated, and hot-isostatic pressing treated conditions

Table 4.2 Comparison of macro-tensile data of the CSAMed Ni-20Cr thick plates in as-sprayed, substrate heated, and hot-isostatic pressing treated conditions with that of bulk Ni-20Cr alloy

Mechanical Property	Bulk Material	Ni-20Cr-AS	Ni-20Cr-SH	Ni-20Cr-HIP
Modulus of Elasticity, GPa	214	111 ± 19	200 ± 15	142 ± 17
Ultimate Tensile Strength, MPa	730	590 ± 29	635 ± 20	512 ± 23
Yield Strength, MPa	350	270 ± 19	301 ± 13	260 ± 14
% age Elongation (%)	28	7.1 ± 1.5	10.5 ± 1.1	28 ± 1.0

4.2.1.3 High Temperature Cyclic Oxidation

It was observed from the initial characterization results that Ni-20Cr-SH has the best properties approaching the bulk material among all the investigated cases. Therefore, to study its sustainability at high temperatures, a cyclic oxidation study for the Ni-20Cr-SH deposit was performed. The mass change data for the deposit are depicted in Figure 4.23 and Figure 4.24, which establish that the mass loss has shown a tendency to become stabilized with minor deviations. However, the overall mass loss by the sample at the end of the 50th cycle has been observed as marginal (3.684 mg/cm²), which demonstrates its stability at high-temperature applications.

After each oxidation cycle, visual inspections were performed, and variations in color, luster, adherence spalling tendency, and crack propagation were documented. The exposed samples were thoroughly examined after the end of the 1st, 4th, 27th, 38th, 46th, and 50th cycles. Their macrographs were then obtained and are shown in Figure 4.25. The samples at the start were slightly green and as the cycles progressed, they turned bluish-green.

It can be observed from the macrographs that after the 50th cycle, a blister has formed on the sample surface. The observed color changes and minor mass gains and losses (deviations) indicate the formation and evaporation of phases during oxidation.

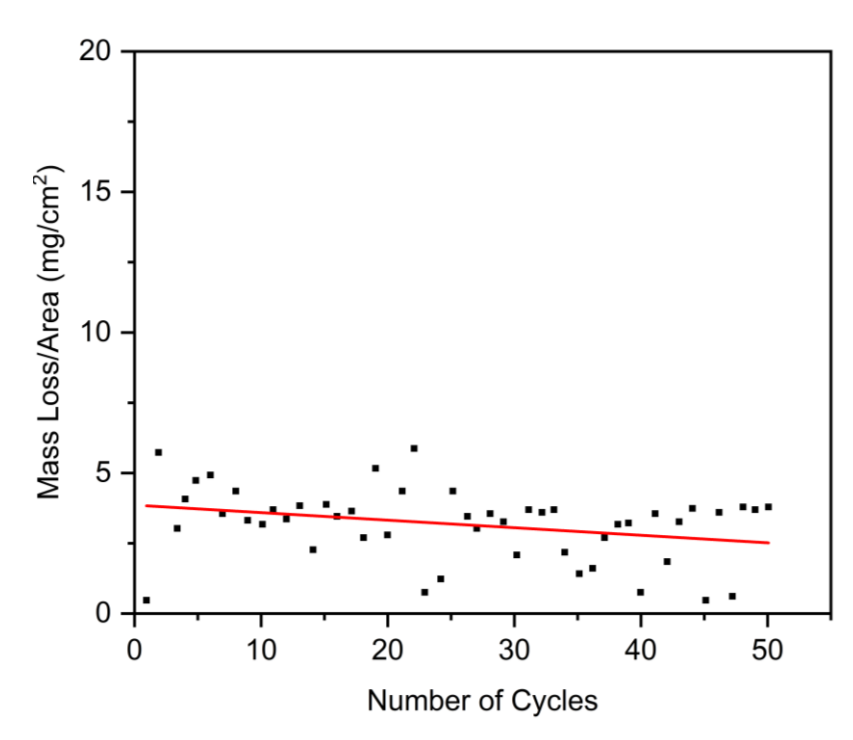


Figure 4.23 Plot of mass loss/area vs. number of cycles for the CSAMed Ni-20Cr thick plate in substrate heated condition (Ni-20Cr-SH) exposed to 50 cycles of high-temperature cyclic oxidation in air at 900 °C

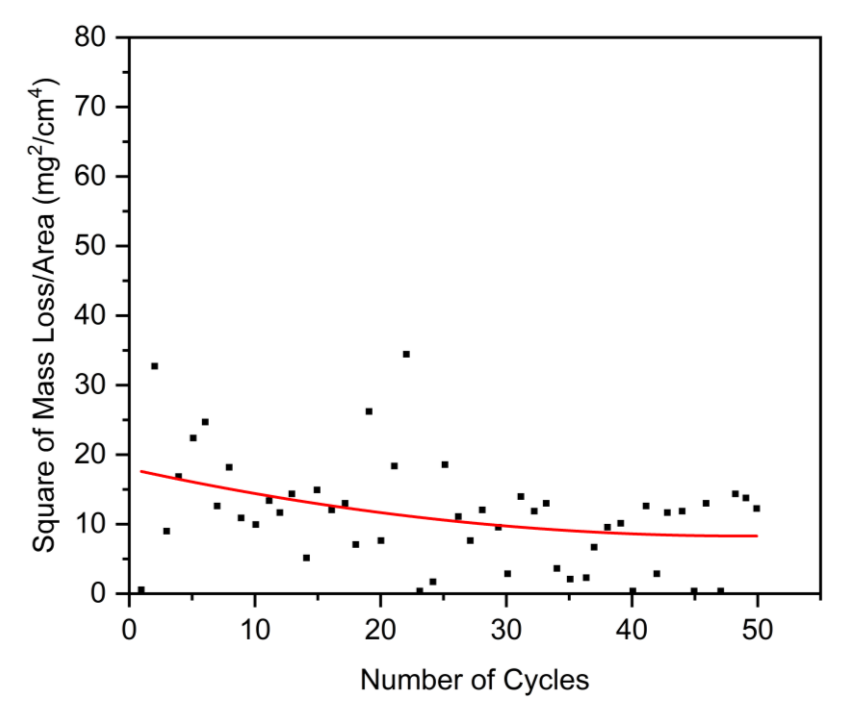


Figure 4.24 Plot of square of mass loss/area vs. number of cycles for the CSAMed Ni-20Cr thick plate in substrate heated condition (Ni-20Cr-SH) exposed to 50 cycles of high-temperature cyclic oxidation in air at 900 °C

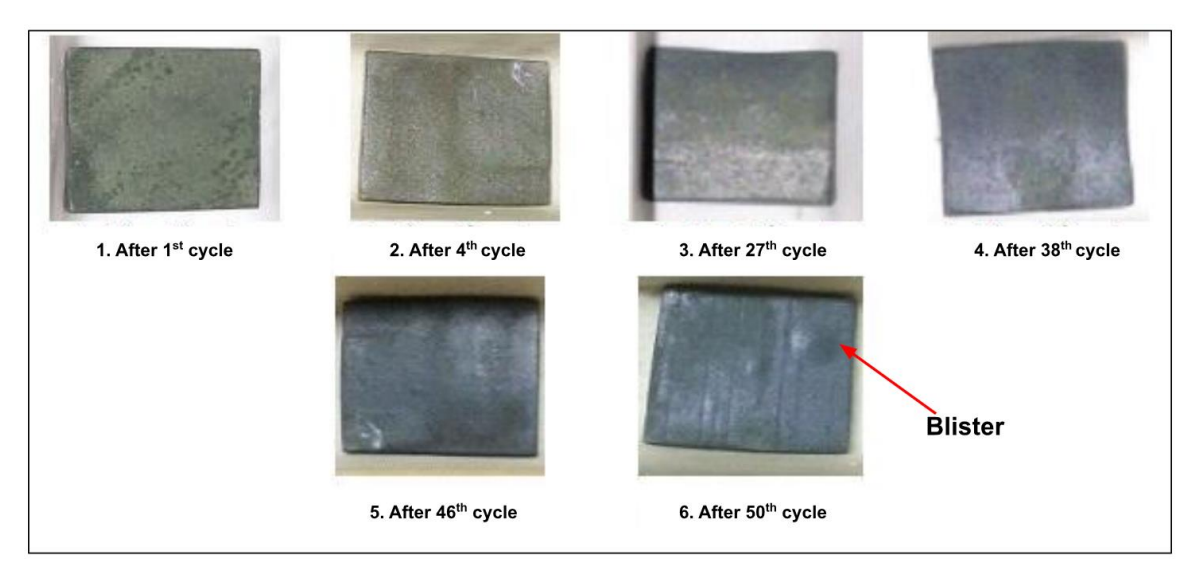


Figure 4.25 Macrographs of the CSAMed Ni-20Cr thick plate in substrate heated condition (Ni-20Cr-SH) exposed to 50 cycles of high-temperature cyclic oxidation in air at 900 °C

Further, the SEM, EDS, and XRD analyses of Ni-20Cr-SH deposits subjected to high-temperature cyclic oxidation in air at 900 °C for 50 cycles, are displayed in Figure 4.26, Figure 4.27, and Figure 4.28, respectively. The SEM image shows an irregular and rough surface with a disintegrated oxide scale morphology. The EDS mapping showed the existence of Ni, Cr, and O on the entire surface scale. Further, the XRD data showed a mixture of CrNi₃ and CrO₃ phases in the oxide scales. The phase of chromium with oxygen (CrO₃) is volatile in nature. The outer layer of chromia (Cr₂O₃) formed during the cyclic oxidation of the Ni-20Cr-SH sample evaporates owing to its conversion leading to deviations in mass. According to the differential equation that quantifies the oxidation kinetics and the analysis of the mass gain curves obtained using thermogravimetry after 50 cycles, the formation of Cr₂O₃ results in a small mass gain, whereas the converted phase's evaporation (due to its volatile nature) results in a small mass loss (Berthod 2005; Watanabe *et al.* 2016). The mass change has been observed as marginal; therefore, the Ni-20Cr-SH deposits can be sustained in high-temperature environments for a longer time.

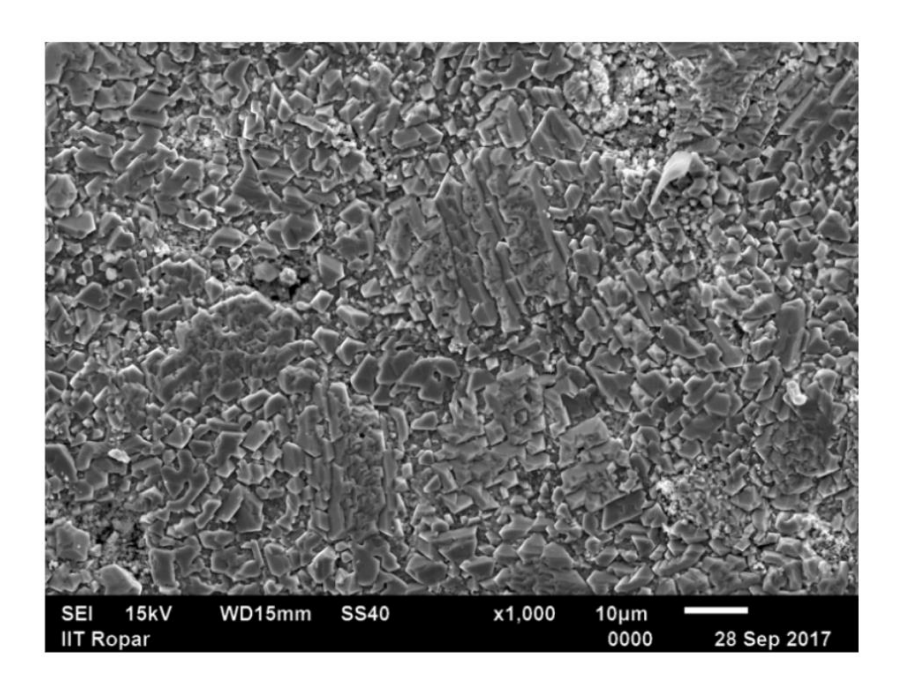


Figure 4.26 Surface SEM image of oxide scale for the CSAMed Ni-20Cr thick plate in substrate heated condition (Ni-20Cr-SH) subjected to 50 cycles of high-temperature cyclic oxidation in air at 900 °C

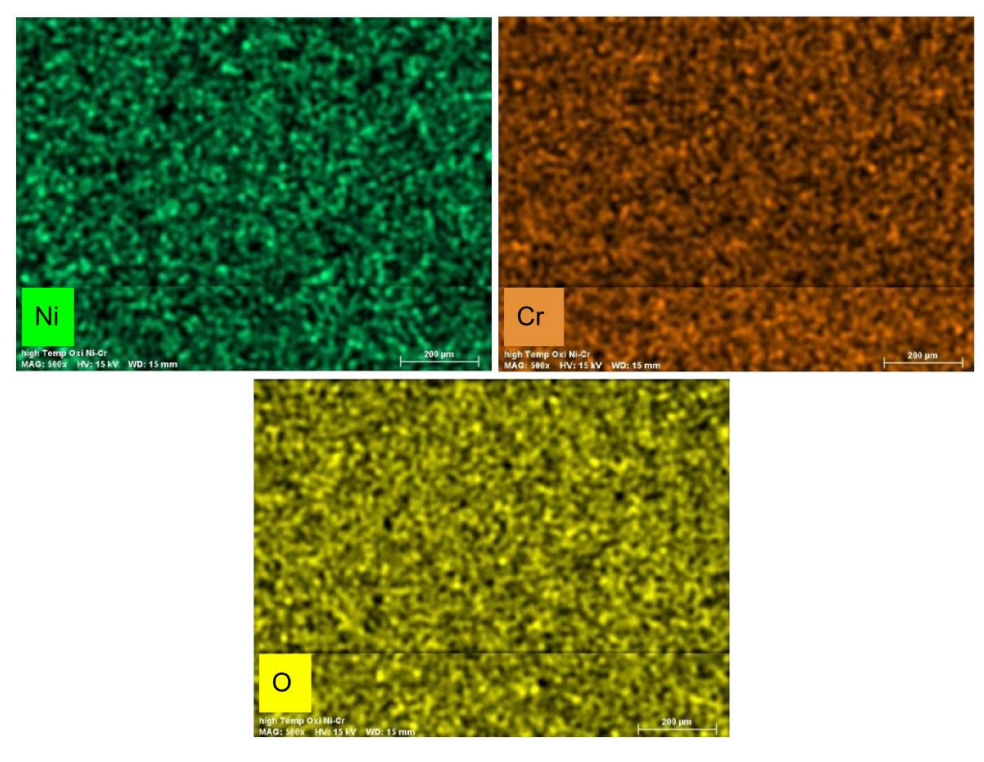


Figure 4.27 EDS analysis of oxide scale for the CSAMed Ni-20Cr thick plate in substrate heated condition (Ni-20Cr-SH) subjected to 50 cycles of high-temperature cyclic oxidation in air at 900 °C

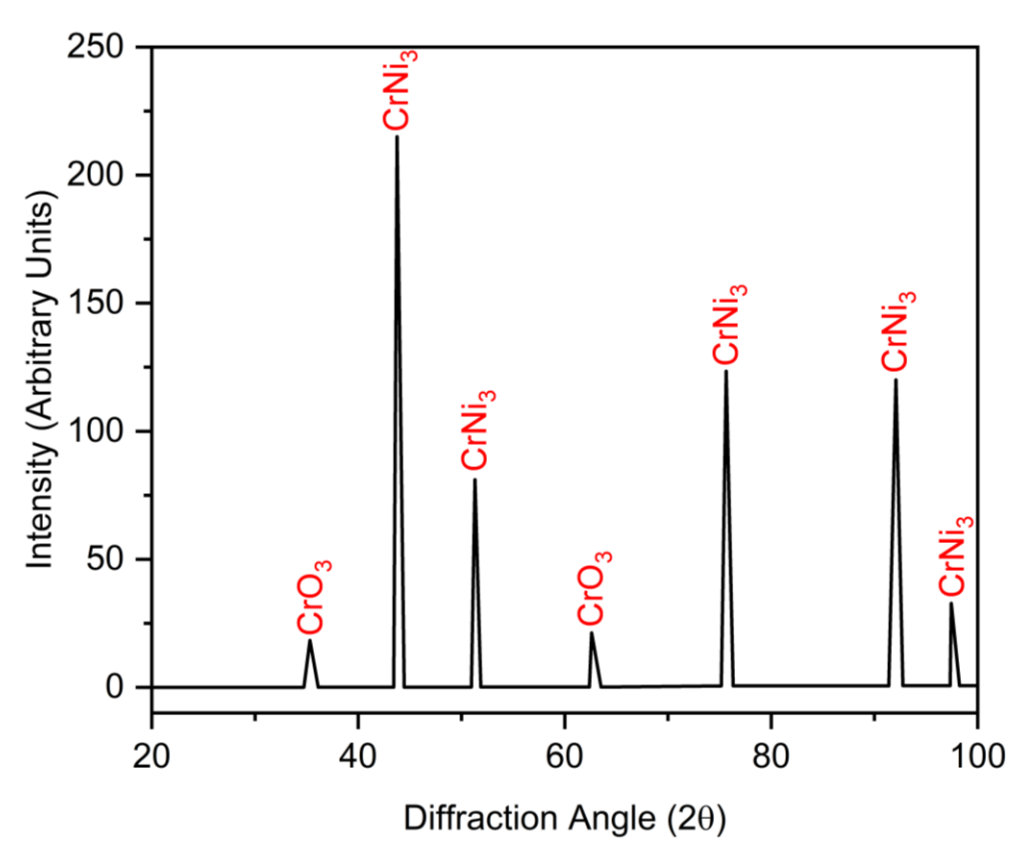


Figure 4.28 XRD analysis of oxide scale for the CSAMed Ni-20Cr thick plate in substrate heated condition (Ni-20Cr-SH) subjected to 50 cycles of high-temperature cyclic oxidation in air at 900 °C

CHAPTER 5

PARAMETRIC ANALYSIS OF COLD SPRAY PROCESS

This chapter is divided into two interconnected sections. The first section focuses on optimizing cold spray process parameters, while the second examines the effect of powder injection angle on powder stream and process gas characteristics, utilizing the optimized parameters derived from the first section.

In the first section, a full factorial two-level approach was used to optimize parameters for effective cold spray deposition of IN 718. Cold spraying high-strength materials like IN 718 is challenging due to their limited deformability, impacting coating quality. Adjusting process parameters to achieve high particle impact velocities and temperatures is crucial for forming well-bonded interfaces between particles and particle-substrate. Achieving properties similar to bulk counterparts requires maintaining a particle impact velocity at the standoff distance (SoD) exceeding the critical velocity and a velocity ratio (particle impact velocity at SoD divided by critical velocity) within the 1.1-2 range to ensure deposition efficiency between 80-100 %. The velocity ratio (VR), an indicator of deposition efficiency, was chosen as the output response for optimization. Parameters were optimized based on the average particle size (D_{50}) of IN 718 powder, with efficacy verified across other size distributions (D_{10} and D_{90}). The study explored various cold spray process parameters at both low and high levels, focusing on identifying critical parameters and analyzing their main and interaction effects.

In the next section, a cold spray nozzle featuring diverse injection angles (90 deg, 30 deg and 0 deg injection) was numerically modeled, employing IN 718 as the powder feedstock and nitrogen as the process gas. Gas flow field simulations and particle trajectory analyses were carried out for varied injection angles using the k- ω SST (shear stress transport) model. This turbulence model, a prevalent choice in computational fluid dynamics (CFD) simulations, utilizes a dual-equation approach to comprehensively describe turbulent flows encountered in diverse engineering applications. Injection angle was found to have an effect on the attributes of the process gas and powder stream characteristics. This variation in injection angle notably influences the cold spray footprint, a crucial factor in generating precise and well-defined tracks for intricate geometries.

5.1 OPTIMIZING COLD SPRAY PROCESS PARAMETERS

5.1.1 Results and Discussion

5.1.1.1 Analysis of Variance

The analysis of the interactions among independent factors utilizes analysis of variance (ANOVA), and the determination of main effects in the successful cold spray deposition of IN 718 is based on assessing significance with a confidence level exceeding 95 %. Factors that exhibited P values < 0.05 for both main and interaction effects were deemed potentially significant, as presented in Table 5.1.

Table 5.1 presents ANOVA for interactions involving up to three factors. ANOVA with interactions of four or more variables was not pursued because it led to an inadequate model, considering the principle of sparsity of effect.

When a factor has a negative impact, it led to a decrease in VR as the factor moved from a low to a high level (as illustrated by changes in DeltaP and PD). Conversely, if the factor has a positive impact, VR increases at higher levels of that factor (as observed in MGP and MGT). Importantly, the PFR parameter was not considered statistically significant, as its P value exceeded 0.05. Additionally, the well-fitted models, which had a squared correlation coefficient (R-squared) of 0.9977 (as detailed in the model summary in Table 5.2), aligned closely with the statistical model. The following regression equation in uncoded units is used to explain the 2^6 full factorial design of VR:

$$VR = 0.4385 - 0.002114 \text{ MGP} + 0.02692 \text{ DeltaP} + 0.000115 \text{ MGT} + 0.000090 \text{ SoD} - 0.002152 \text{ PD}$$

0.000001 MGP*DeltaP*MGT

- 0.000001 MGP*DeltaP*SoD + 0.000007 MGP*DeltaP*PD + 0.000001 DeltaP*MGT*PD

Where *VR* is the predicted response, MGP refers to main gas pressure, MGT denotes main gas temperature, SoD is standoff distance, PFR indicates powder feed rate, PD is particle diameter while DeltaP represents the difference between the main gas and carrier gas pressure.

 Table 5.1 Analysis of variance

Term	Effect	Coef	SE Coef	T-Value	P-Value	VIF
Constant		0.54091	0.00310	174.44	0.000	
MGP	0.30085	0.15043	0.00310	48.51	0.000	1.00
DeltaP	-0.06390	-0.03195	0.00310	-10.30	0.000	1.00
MGT	0.19681	0.09841	0.00310	31.74	0.000	1.00
SoD	0.02487	0.01243	0.00310	4.01	0.001	1.00
PD	-0.38438	-0.19219	0.00310	-61.98	0.000	1.00
PFR	0.00036	0.00018	0.00310	0.06	0.954	1.00
		2-Way Inte	I.			
MGP*DeltaP	-0.06008	-0.03004	0.00310	-9.69	0.000	1.00
MGP*MGT	0.16517	0.08258	0.00310	26.63	0.000	1.00
MGP*SoD	0.00612	0.00306	0.00310	0.99	0.334	1.00
MGP*PD	-0.06587	-0.03294	0.00310	-10.62	0.000	1.00
MGP*PFR	0.00062	0.00031	0.00310	0.10	0.921	1.00
DeltaP*MGT	-0.07359	-0.03679	0.00310	-11.87	0.000	1.00
DeltaP*SoD	-0.00032	-0.00016	0.00310	-0.05	0.960	1.00
DeltaP*PD	0.05476	0.02738	0.00310	8.83	0.000	1.00
DeltaP*PFR	-0.00041	-0.00020	0.00310	-0.07	0.948	1.00
MGT*SoD	-0.00139	-0.00069	0.00310	-0.22	0.825	1.00
MGT*PD	-0.14558	-0.07279	0.00310	-23.48	0.000	1.00
MGT*PFR	0.00035	0.00018	0.00310	0.06	0.955	1.00
SoD*PD	-0.00723	-0.00362	0.00310	-1.17	0.256	1.00
SoD*PFR	-0.00005	-0.00002	0.00310	-0.01	0.994	1.00
PD*PFR	0.00071	0.00036	0.00310	0.12	0.909	1.00
		3-Way Inte	eractions			
MGP*DeltaP*MGT	-0.04194	-0.02097	0.00310	-6.76	0.000	1.00
MGP*DeltaP*SoD	-0.00265	-0.00133	0.00310	-0.43	0.673	1.00
MGP*DeltaP*PD	0.02805	0.01403	0.00310	4.52	0.000	1.00
MGP*DeltaP*PFR	-0.00053	-0.00026	0.00310	-0.08	0.933	1.00
MGP*MGT*SoD	-0.00233	-0.00117	0.00310	-0.38	0.711	1.00
MGP*MGT*PD	-0.12100	-0.06050	0.00310	-19.51	0.000	1.00
MGP*MGT*PFR	0.00062	0.00031	0.00310	0.10	0.921	1.00
MGP*SoD*PD	-0.00609	-0.00305	0.00310	-0.98	0.336	1.00
MGP*SoD*PFR	0.00011	0.00006	0.00310	0.02	0.986	1.00
MGP*PD*PFR	0.00059	0.00030	0.00310	0.10	0.924	1.00
DeltaP*MGT*SoD	-0.00297	-0.00149	0.00310	-0.48	0.636	1.00
DeltaP*MGT*PD	0.05323	0.02662	0.00310	8.58	0.000	1.00
DeltaP*MGT*PFR	-0.00033	-0.00016	0.00310	-0.05	0.958	1.00
DeltaP*SoD*PD	0.00017	0.00008	0.00310	0.03	0.978	1.00
DeltaP*SoD*PFR	-0.00004	-0.00002	0.00310	-0.01	0.994	1.00
DeltaP*PD*PFR	-0.00066	-0.00033	0.00310	-0.11	0.916	1.00
MGT*SoD*PD	0.00266	0.00133	0.00310	0.43	0.672	1.00
MGT*SoD*PFR	0.00002	0.00001	0.00310	0.00	0.998	1.00
MGT*PD*PFR	0.00073	0.00037	0.00310	0.12	0.907	1.00
SoD*PD*PFR	0.00015	0.00008	0.00310	0.02	0.981	1.00

Table 5.2 Model summary

S	R-sq	R-sq(adj)	R-sq(pred)
0.0248064	99.77%	99.34%	98.05%

5.1.1.2 Main and Interaction Effects

The main effects of factors like MGP, MGT, PD, DeltaP, SoD and PFR on VR are shown in Figure 5.1. The impact of a factor is the shift in response caused by altering the level of that factor. This is commonly known as a main effect, as it pertains to the primary factor under scrutiny in the experiment (Rathinam $et\ al.\ 2011$). It was observed that the greater the height of the vertical line, the more substantial the alteration in VR when transitioning from level -1 to level +1. Importantly, the significance of a factor is directly linked to the length of the vertical line (Bingol $et\ al.\ 2010$). The most significant factor identified was PD (Particle Diameter), as also evident in the Pareto chart (Figure 5.3). The negative slope indicated a negative impact on VR. Specifically, when the powder feedstock had a larger average diameter, VR tended to be lower compared to feedstock with a smaller average diameter. It's crucial to note that extremely small average diameter powder feedstock encounters flowability challenges due to increased surface forces. Therefore, maintaining an appropriate particle size distribution is essential. This ensures not only the absence of flowability issues but also contributes to achieving a satisfactory VR for successful cold spray deposition.

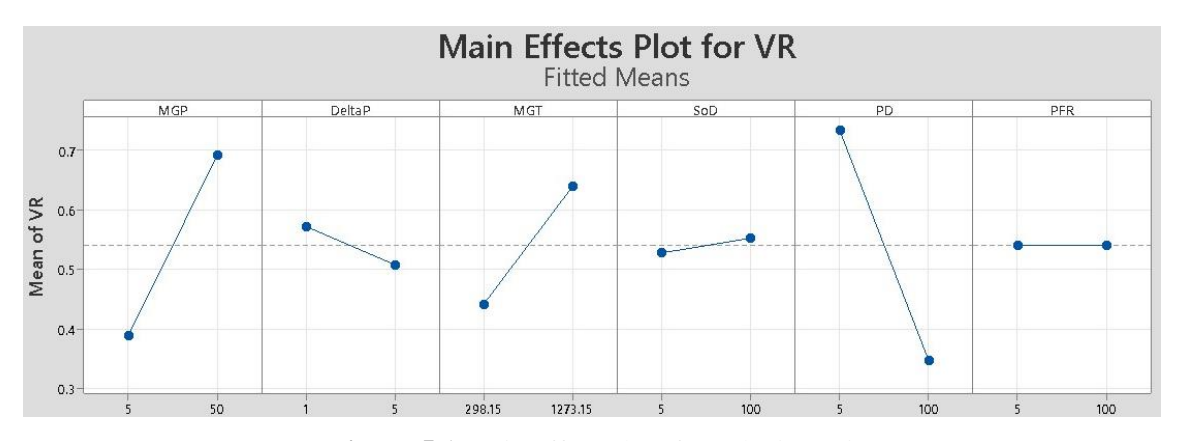


Figure 5.1 Main effect plots for velocity ratio

MGP and MGT emerged as the second and third most influential factors, exerting a positive impact on VR. Conversely, DeltaP, representing the difference between carrier and main gas pressure, had a negative effect on VR. SoD positively influenced VR, while PFR showed no discernible effect as it transitioned from low to high levels.

Interaction arises when a specific factor fails to elicit a consistent response across various levels of another factor. The occurrence of interaction between two factors is marked by the observation that a modification in the values of one variable brings about a change in the impact on another factor. This suggests that negligible interactions among factors result in consistent patterns of response across various levels of another factor (Sezgin and Berkalp 2018).

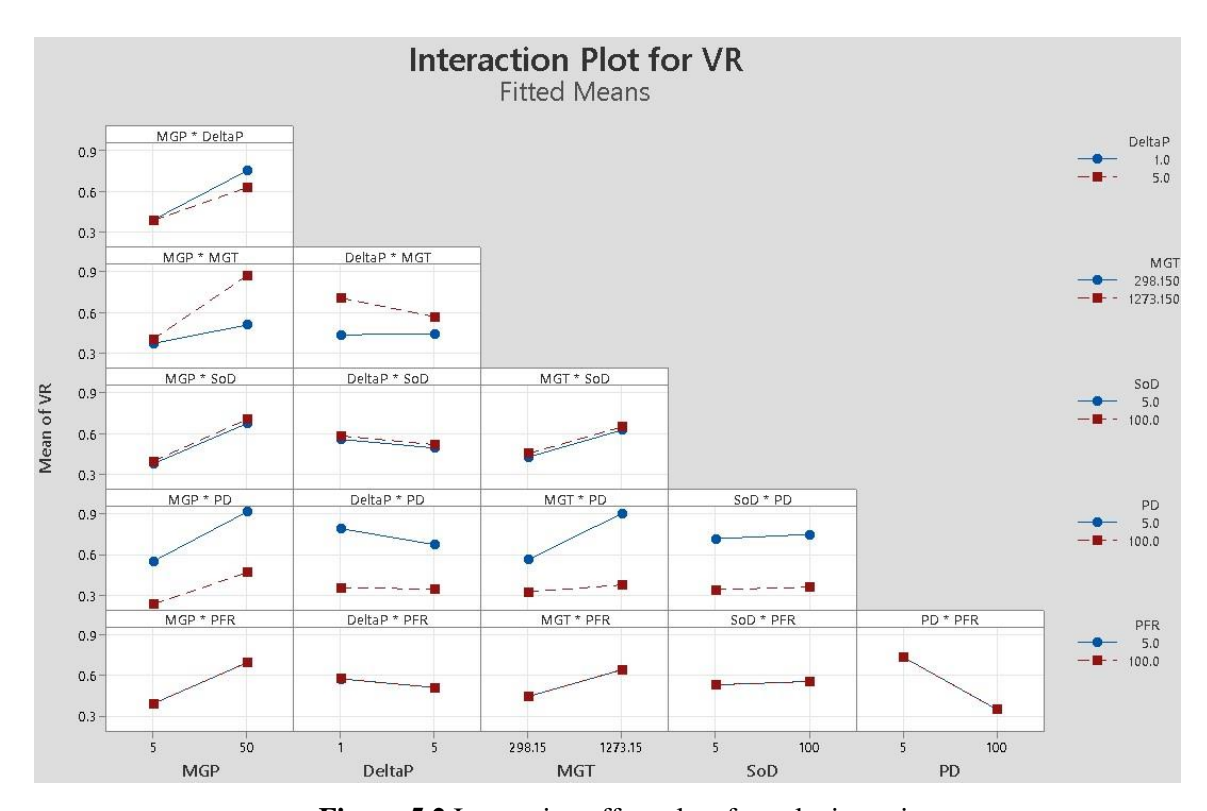


Figure 5.2 Interaction effect plots for velocity ratio

In interaction plots as displayed above in Figure 5.2, the absence of interaction between factors is indicated when the lines run parallel to each other. Additionally, the extent of interaction grows as the difference in slope between the lines increases. The interaction effects of the six combinations were statistically significant namely MGP-DeltaP, MGP-MGT, MGP-PD, DeltaP-MGT, DeltaP-PD and MGT-PD. These interaction effects played an important role in varying *VR*.

The pareto chart as depicted in Figure 5.3 clearly shows the ordering in which the main and interaction factors influenced *VR* for the successful cold spray deposition of IN 718 powder feedstock. Main factors such as PD, MGP and MGT were the three most important factors among all other factors and their interactions.

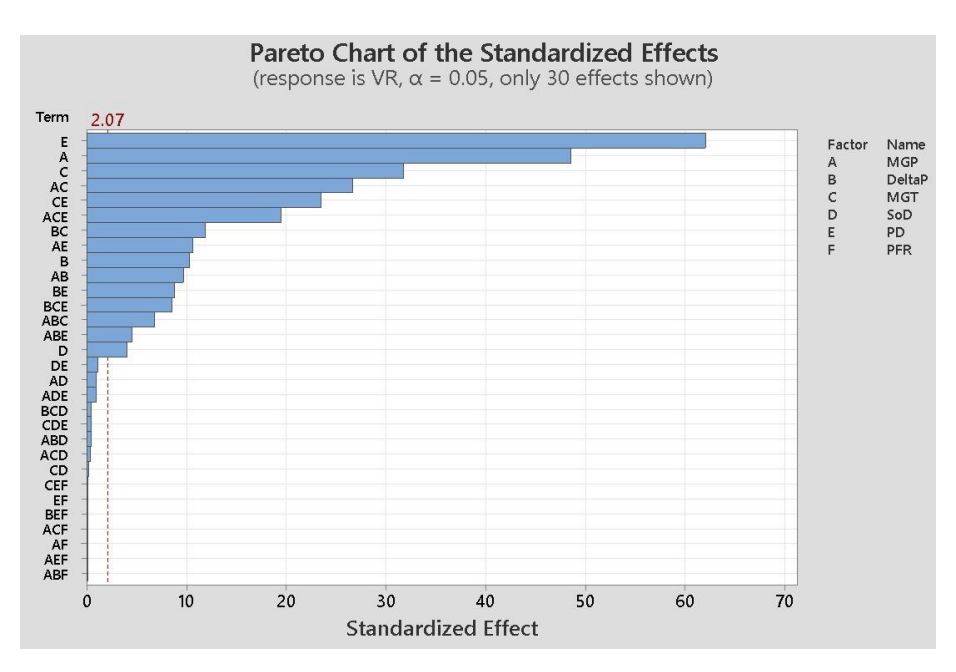


Figure 5.3 Pareto chart of standardized effects on the velocity ratio (VR)

5.1.1.3 Normal Probability Plot of Residuals

To assess the normality of the data, one can examine a normal probability plot of the residuals. If the data points on the plot closely align with the straight line, it suggests that the data follows a normal distribution (Anthony and Antony 2016). The normal distribution plot has been illustrated in Figure 5.4. Upon observation, it is evident that the data points closely approximated the straight line, indicating that the experiments were derived from a population with a normal distribution.

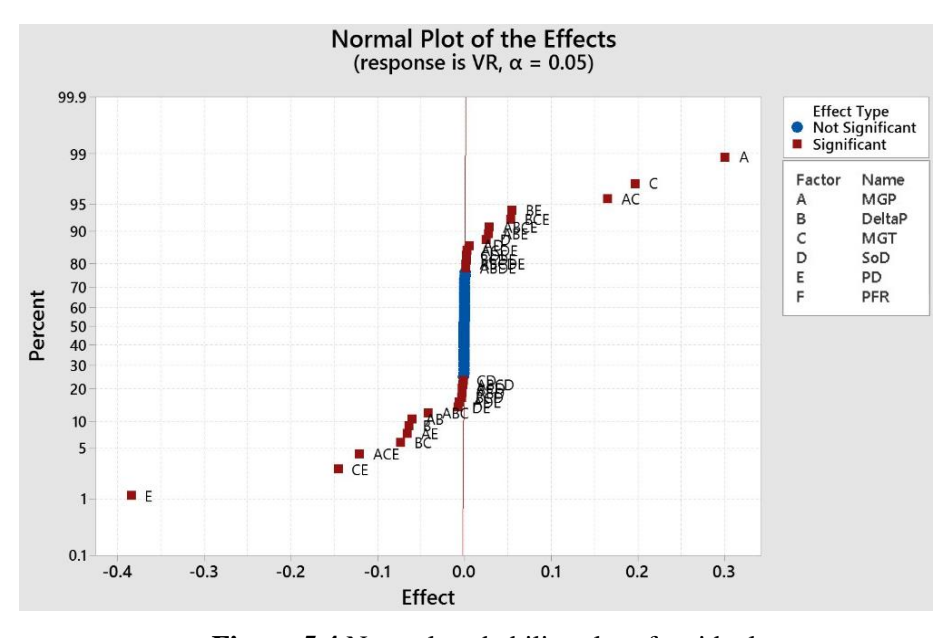


Figure 5.4 Normal probability plot of residuals

5.1.1.4 Optimization

The optimization of VR response in the context of cold spray deposition involved meticulous adjustments to key process parameters. As IN 718 powder was procured with particle size distribution as discussed in the Section 3.1.2.2 of Chapter 3, the average particle diameter (D_{50}) of the powder feedstock was held constant during response optimization using a full factorial analysis. As part of this optimization, certain cold spray process parameters, namely PFR and SoD, were intentionally set at fixed values of 30 g/min and 25 mm, respectively. Through statistical analysis, it was revealed that PFR is a non-significant parameter in influencing VR during the successful cold spray deposition of IN 718. However, in multi-pass cold spray deposition, a higher PFR contributes to a Gaussian-shaped cross-section with sloped sides on either end, which adversely affects the deposition quality. Experimentally, it was observed that at feed rates exceeding typical ranges, strong gas-particle interactions reduce particle impact velocity, leading to increased porosity, lower deposition efficiency, and compromised mechanical properties, such as reduced hardness and tensile strength. Additionally, high feed rates induce localized residual stresses, which can cause delamination failure. Typical cold spray additive manufacturing (CSAM) feed rates of 10–30 g/min have minimal impact on particle velocity, as supported by Ozdemir et al. (2017). Experimental results further revealed that a feed rate of 30 g/min produced a significantly smoother and flatter deposition surface. Consequently, the requisite PFR selection was optimized to balance surface quality, mechanical properties, and deposition efficiency effectively.

Conversely, SoD exhibited a minimal positive effect on *VR* compared to other process parameters. The strategic freezing of SoD is justified by the observation that variations in SoD could impact the cold spray footprint diameter. A higher SoD resulted in an increased footprint diameter, leading to reduced deposition accuracy due to deviations in the trajectory of powder particles. Conversely, a lower SoD, such as 25 mm, contributed to a narrow and well-defined spray footprint, ensuring greater deposition accuracy.

Response optimization efforts yielded a solution set, as presented in Table 5.3, where the first solution emerged as the most optimized, offering a higher *VR* value. Subsequent assessments of *VR* values for alternative particle size distributions, as outlined in Table 5.4, affirmed that the optimized cold spray process parameters, including a main gas pressure (MGP) of 50 bar, pressure difference (DeltaP) of 1 bar, main gas temperature (MGT) of 1273.15 K, standoff distance (SoD) of 25 mm, and powder feed rate (PFR) of 30 g/min, facilitated the successful cold spray deposition of IN 718 powder feedstock across various particle size distributions.

Table 5.3 Optimized solution sets for effective cold spray deposition of IN 718 powder feedstock

Solution	MGP (bar)	DeltaP (bar)	MGT (K)	SoD (mm)	PD (μm)	PFR (g/min)	VR Fit
1	50	1	1273.15	25	22	30	1.26224
2	50	1.73571	1273.15	25	22	30	1.2
3	50	1.73571	1273.15	25	22	30	1.2
4	50	1	1186.58	25	22	30	1.2
5	46.09	1	1273.15	25	22	30	1.2

 Table 5.4 Velocity ratio for Inconel 718 particle size distribution

Diameter Distribution	PD (µm)	VR Fit	
\mathbf{D}_{10}	13.5	1.5406	
D ₅₀	22	1.26224	
D ₉₀	33.5	1.1562	

5.2 EFFECT OF POWDER INJECTION ANGLE

5.2.1 Results and Discussion

5.2.1.1 Gas Flow Field Analysis

Figure 5.5 illustrates velocity contour maps for three different powder injection angles, revealing the complex underexpanded flow structures characterized by Mach diamonds and shock waves.

When high-pressure gas exits a nozzle into a lower ambient pressure environment, expansion fans (Prandtl-Meyer expansion waves) are formed (Menon and Skews 2010; Li *et al.* 2012). The nitrogen gas pressure on exiting the nozzle was observed greater in all cold spray nozzles with values of 6.5, 6.2 and 6.6 bar for 90 deg, 0 deg and 30 deg powder injection angles in comparison with ambient pressure of 1.01325 bar as seen in Figure 5.6. The nitrogen gas temperature was highest for 30 deg powder injection angle having magnitude of 1030 K at the exit of the nozzle. On the other hand, gas temperature at the exit of 90 deg and 0 deg was 991 K and 890 K as depicted in Figure 5.7. Upon passing through the expansion fans immediately after nozzle exit, the gas undergoes a rapid reduction in both pressure and temperature, as indicated by the arrows in Figures 5.6 and 5.7. This reduction led to a significant increase in Mach number, as depicted by the arrows in Figure 5.8. Consequently, the flow transitions from a lower Mach number at the nozzle exit to a higher Mach number in the expanding jet, achieving supersonic speeds or accelerating further if already supersonic.

In contrast, when the flow encounters oblique shock waves, it experiences an increase in pressure and temperature due to compression (Délery and Dussauge 2009). This phenomenon is evidenced by the dashed boxes in Figures 5.6 and 5.7 respectively. The pressure variation after encountering shock waves is shown in the inset graphs for all the cold spray nozzles with different powder injection angles. Across the shock wave, the Mach number decreased, causing the flow to decelerate while still remaining supersonic, as shown by the dashed box in Figure 5.8. This alternating pattern of expansion and compression forms Mach diamonds, which are characterized by regions where the flow periodically expands and compresses.

Within each Mach diamond, the flow experienced a decrease in pressure and temperature, accompanied by an increase in Mach number through the expansion waves. This is followed by an increase in pressure and temperature, along with a decrease in Mach number, through the shock waves. These oscillations in flow properties diminished further downstream as the flow stabilized and equilibrated with the ambient pressure on account of viscous damping, as described by Ekanayake *et al.* (2009).

The 30 deg injection convergent-divergent cold spray nozzle showcased a higher velocity of nitrogen gas at its exit having a value of 840 m/sec in comparison with 90 deg (828 m/sec) and 0 deg (792 m/sec) as illustrated in Figure 5.9. This disparity could be attributed to the temperature contour maps displayed in Figure 5.10. Specifically, the 30 deg injection nozzle demonstrated the ability to generate a more uniform temperature profile on account of better mixing of the carrier gas and heated main gas. In contrast, the 0 deg injection nozzle failed to facilitate optimal heat transfer from the heated main gas originating from the heater. Consequently, the more uniform

temperature profile created by the 30 deg injection nozzle contributed to the heightened velocity of nitrogen gas observed at its exit. The nitrogen gas with comparatively high thermal energy in a 30 deg injection nozzle would increase the gas velocity at the exit due to its conversion into kinetic head.

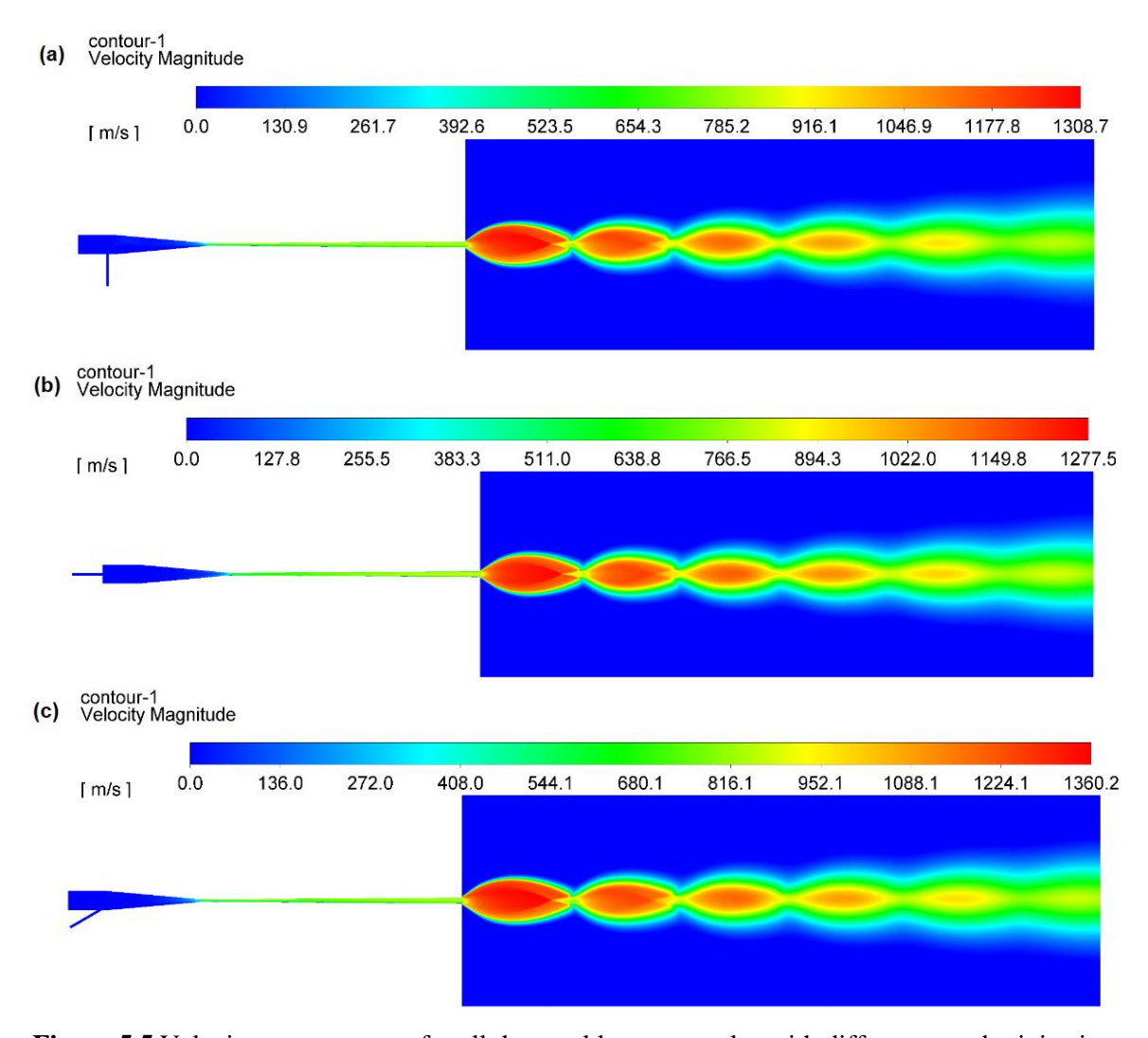


Figure 5.5 Velocity contour maps for all three cold spray nozzles with different powder injection angle (a) 90 deg; (b) 0 deg and (c) 30 deg

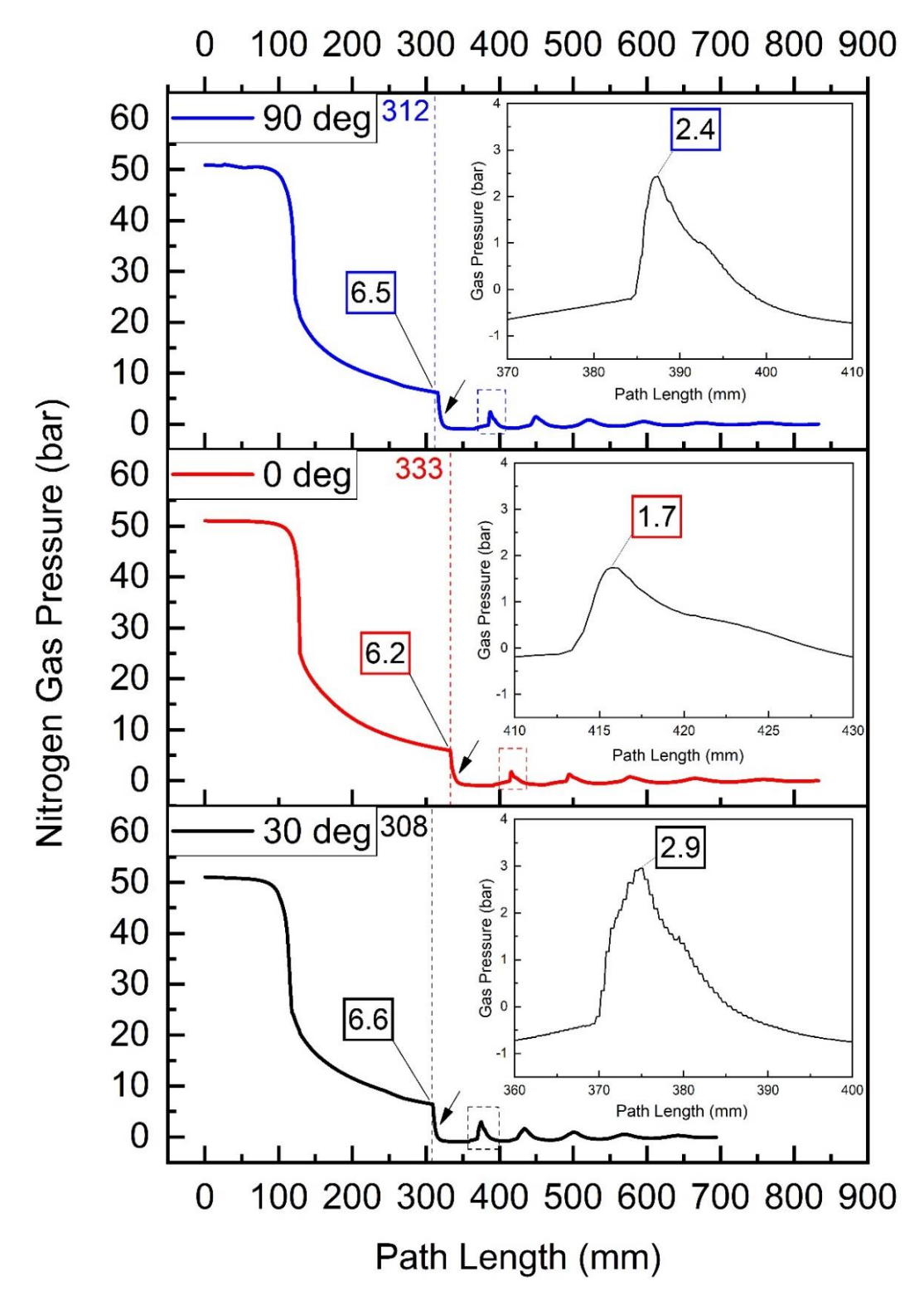


Figure 5.6 Variation of nitrogen gas pressure versus path length for all three cold spray nozzles with different powder injection angle [90 deg (top); 0 deg (middle) and 30 deg (bottom)] with arrows showing gas flow through expansion fan along with inset graphs showing pressure increase as the gas flow encounters oblique shock waves as depicted through dashed boxes

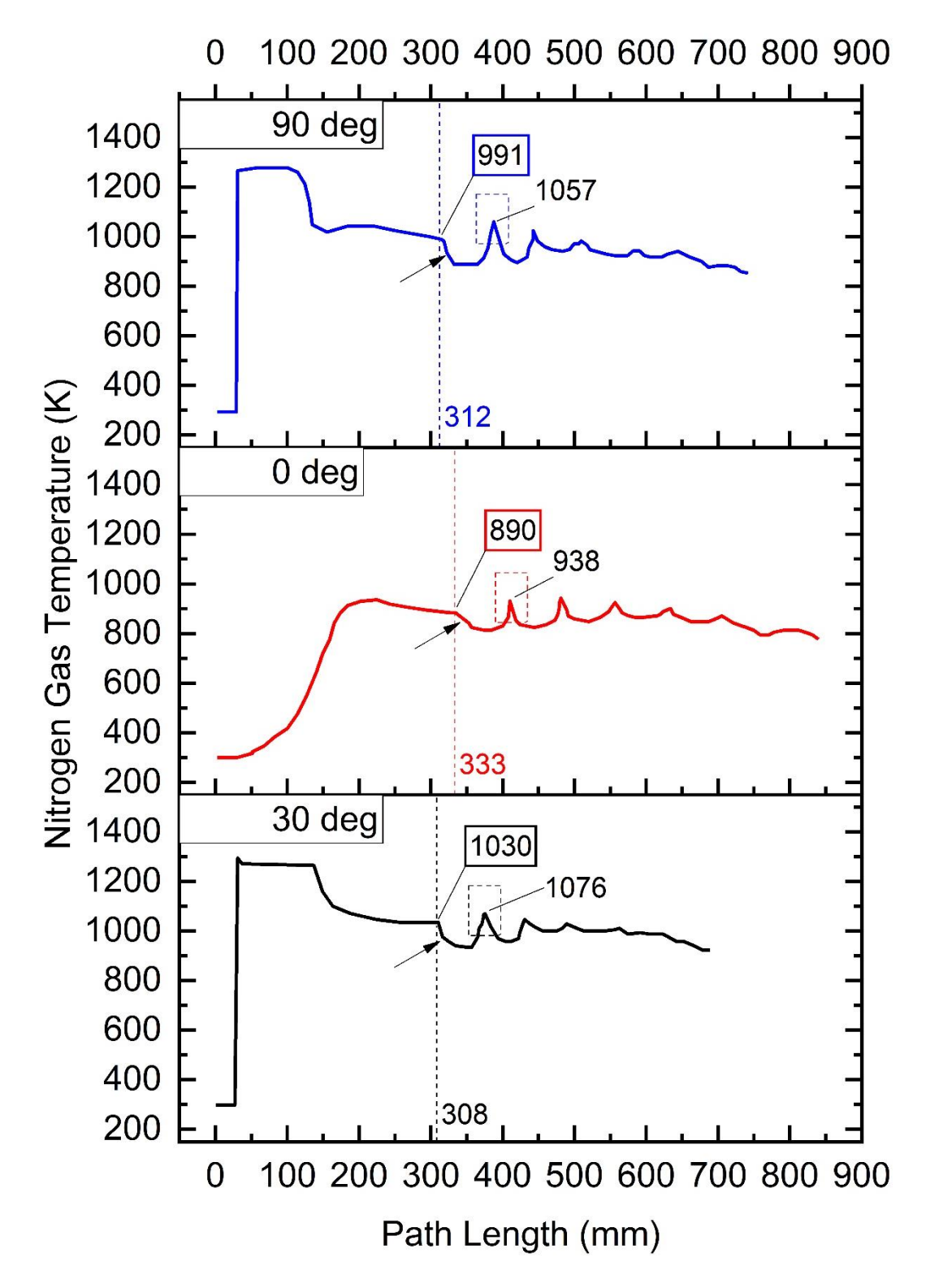


Figure 5.7 Variation of nitrogen gas temperature versus path length for all three cold spray nozzles with different powder injection angle [90 deg (top); 0 deg (middle) and 30 deg (bottom)] with arrows showing gas flow through expansion fan along with dashed boxes depicting the gas flow encountering oblique shock waves

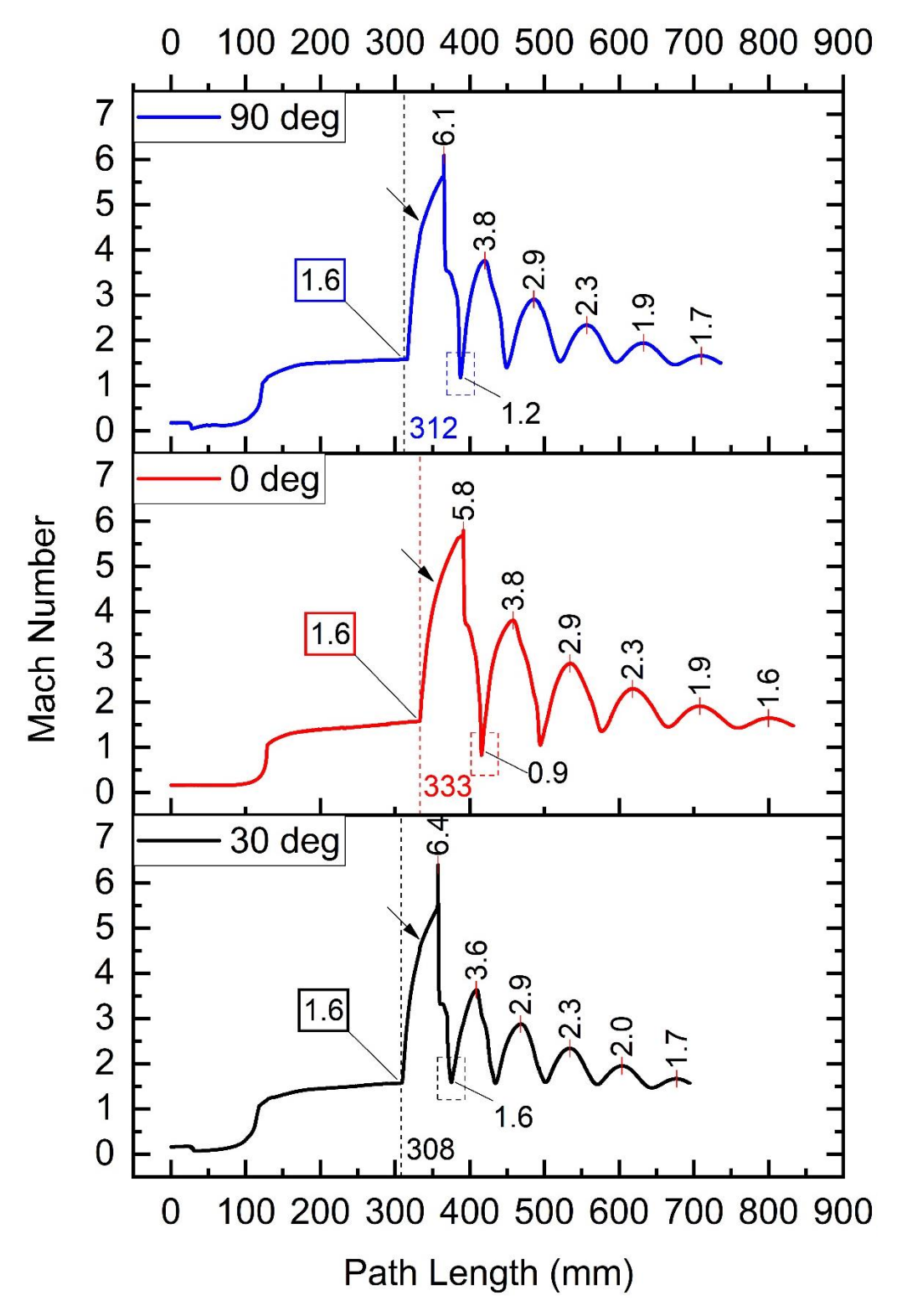


Figure 5.8 Variation of Mach number versus path length for all three cold spray nozzles with different powder injection angle [90 deg (top); 0 deg (middle) and 30 deg (bottom)] with arrows showing gas flow through expansion fan along with dashed boxes depicting the gas flow encountering oblique shock waves

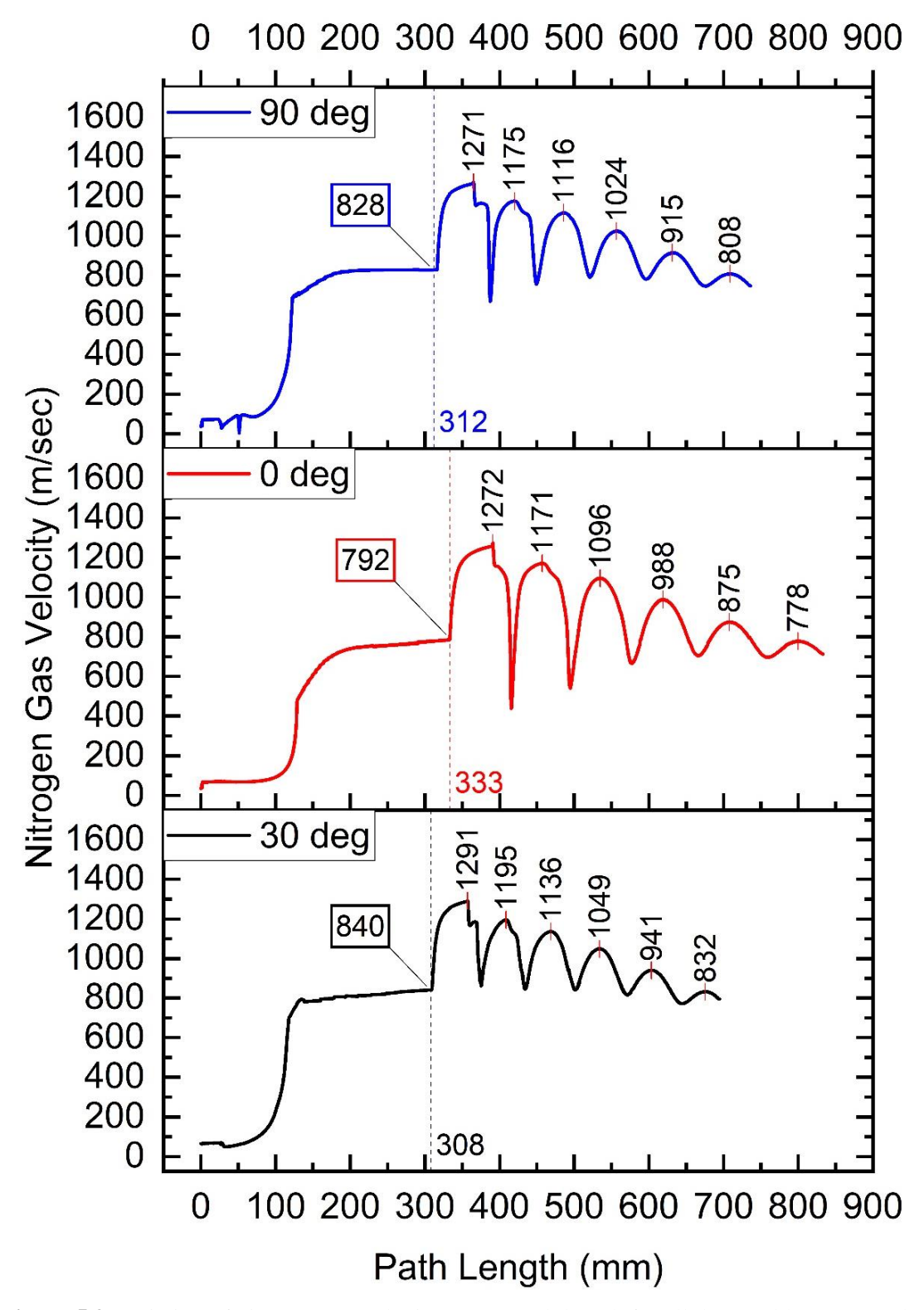


Figure 5.9 Variation of nitrogen gas velocity versus path length for all three cold spray nozzles with different powder injection angle [90 deg (top); 0 deg (middle) and 30 deg (bottom)]

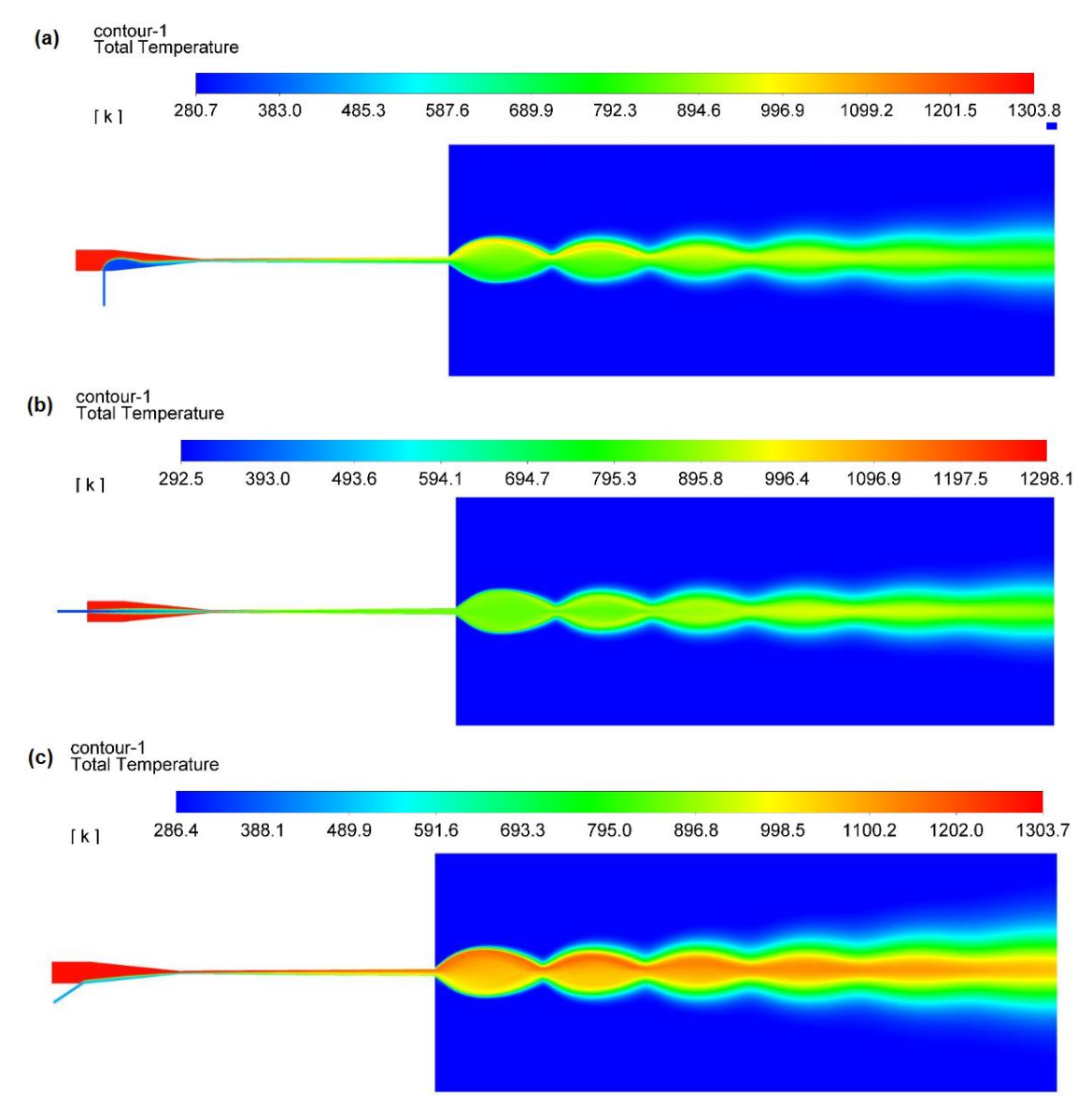


Figure 5.10 Temperature contour maps for all three cold spray nozzles with different powder injection angle (a) 90 deg; (b) 0 deg and (c) 30 deg

Figure 5.11 presents contour maps of turbulent kinetic energy (TKE) for cold spray nozzles with different powder injection angles. These maps clearly indicate that immediately after the nozzle exit, TKE was considerably higher at the outer edges of the cold spray plume. This increase in TKE was primarily due to several factors (Meyer and Lupoi 2018). Firstly, shear layers formed at the interface between the high-velocity gas jet and the slower-moving surrounding air, creating turbulent eddies that raise TKE. Additionally, the interaction between the high-speed jet and the ambient air led to vortex shedding, where vortices periodically detach and contribute to

turbulence in the plume's periphery. The jet itself experienced various instabilities as it moved through the surrounding medium, amplifying turbulent fluctuations and increasing TKE, especially at the plume's edges. Furthermore, the cold spray jet's mixing with the surrounding air added to the turbulence, enhancing the energy within the turbulent eddies and elevating TKE. As the spray plume traveled further, TKE started to increase with distance because of the amplification of these effects downstream.

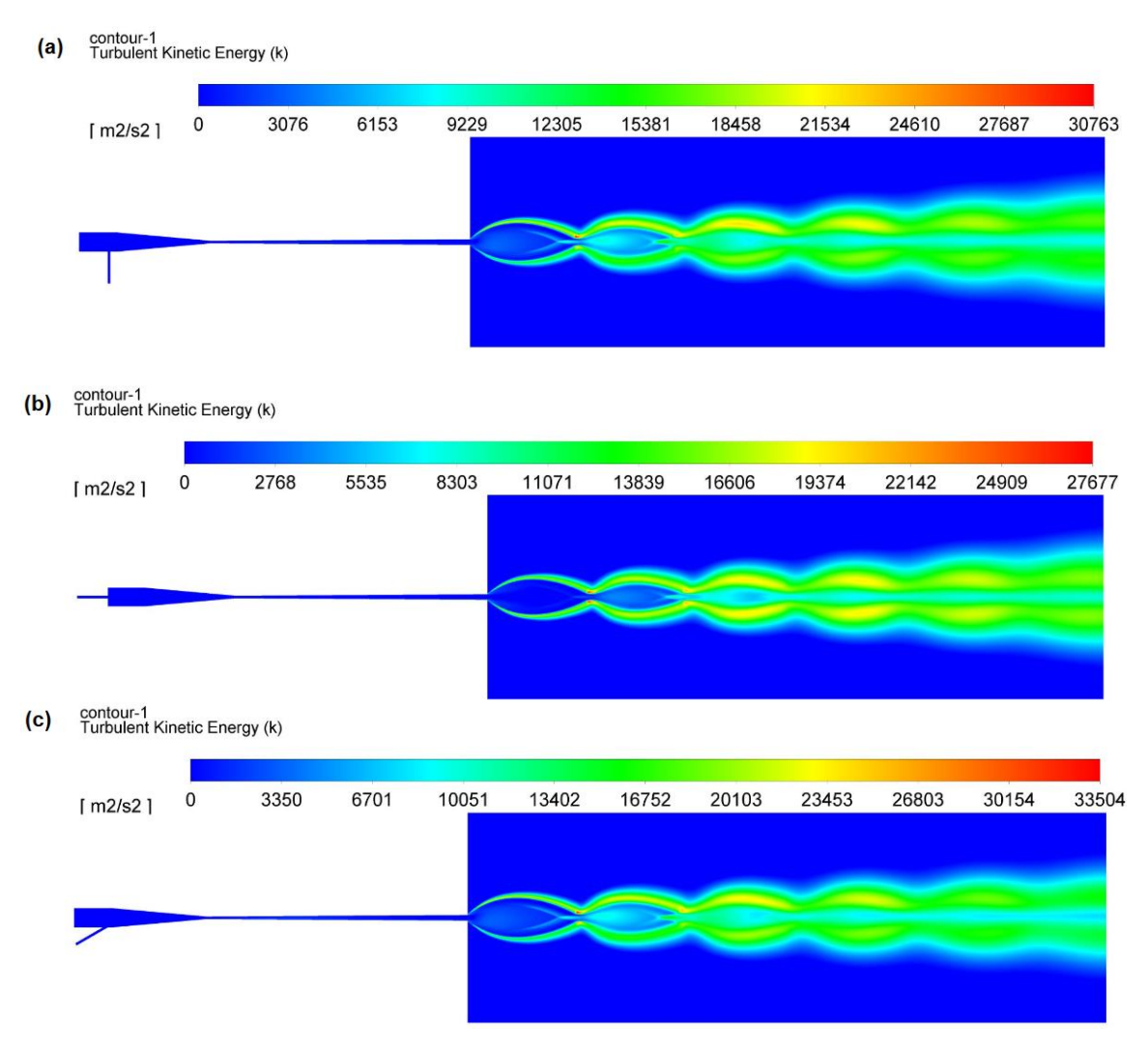


Figure 5.11 Turbulent kinetic energy contour maps for all three cold spray nozzles with different powder injection angle (a) 90 deg; (b) 0 deg and (c) 30 deg

In cases where powder injection angles were 90 deg and 30 deg, TKE was higher compared to a 0 deg injection angle. Elevated TKE enhanced the mixing of particles with the process gas, promoting a more uniform particle distribution within the spray plume. This uniformity is crucial for achieving consistent layer formation. Enhanced mixing prevented particle clumping, which

could cause uneven layer thickness and defects. The turbulent gas flow transfers more energy to the particles, resulting in higher impact energies. The increased kinetic energy leads to significant plastic deformation upon impact, improving particle adherence to the substrate and to each other, thus forming a denser and more cohesive coating. Higher impact velocities activate the substrate surface more effectively, enhancing mechanical interlocking and metallurgical bonding between particles and substrate (Reddy *et al.* 2021). Turbulent flows also improve convective heat transfer between the gas and particles, causing particle heating which enhances particle deformation (Kuerten *et al.* 2011). Even minimal increases in particle temperature can induce thermal softening, making particles more malleable upon impact and improving continuous coating formation. Increased TKE also leads to a faster deposition rate, reducing particle exposure time to the environment. This rapid coverage minimizes the risk of oxidation and contamination, preserving the coating's material properties. Understanding these flow dynamics is crucial for optimizing the cold spray process to achieve desired coating properties and deposition efficiency.

5.2.1.2 Powder Particle Stream Analysis

Figure 5.12 depicts the trajectories of IN 718 powder particles, highlighting velocity magnitudes at different powder injection angles. With a 30 deg injection nozzle, the particles formed a concentrated stream within the supersonic core, resulting in a narrower, more uniform distribution that enhances deposition accuracy. In contrast, a 90 deg injection nozzle led to a sparse particle distribution due to the initial divergence caused by the injection angle. This divergence resulted in centrifugal forces pushing the particles outward, creating a more dispersed plume. The varying velocity profile at the nozzle exit further contributed to this spread, with particles exiting at different speeds and angles.

In the case of a 0 deg injection nozzle, particles were notably absent from the central core of the spray jet. This absence is attributed to the boundary layer effects. Lower TKE in comparison with 90 deg and 30 deg cases as specified earlier, increased the boundary layer thickness in the 0 deg injection nozzle. Consequently, particles were pushed away from the core towards the periphery of the jet, as shown in Figure 5.12.

Conversely, the 30 deg injection nozzle achieved a more concentrated particle distribution. This design optimally balanced particle introduction and alignment with the gas flow, reducing centrifugal forces and controlling mixing. As a result, it maintained a focused spray plume, providing a more concentrated particle distribution compared to both 0 deg and 90 deg powder injection cold spray nozzles.

Figure 5.13 outlines the average velocity of IN 718 powder particles upon exiting the nozzle, considering various powder injection angles. Notably, the velocity was measured higher at a 30 deg injection angle (787 m/sec) compared to both 0 deg (723 m/sec) and 90 deg (783 m/sec). This outcome aligned with expectations due to the increased nitrogen gas velocity observed at the 90 deg and 30 deg injection angles. The elevated gas velocity generated a more pronounced drag effect, which consequently contributed to the accelerated motion of the powder particles when contrasted with the 0 deg injection angle. This phenomenon occurred due to the mechanics of gas-particle interactions within the nozzle. At 0 deg, the injection angle allowed for relatively straightforward particle ejection, encountering less resistance from the gas flow. In contrast, both 90 deg and 30 deg angles introduced powder particles into gas streams facing more significant gas flow, resulting in heightened drag forces (Bhattiprolu *et al.* 2018). Consequently, the higher gas velocity in these angles led to increased momentum transfer to the particles, propelling them at a higher average velocity upon exit.

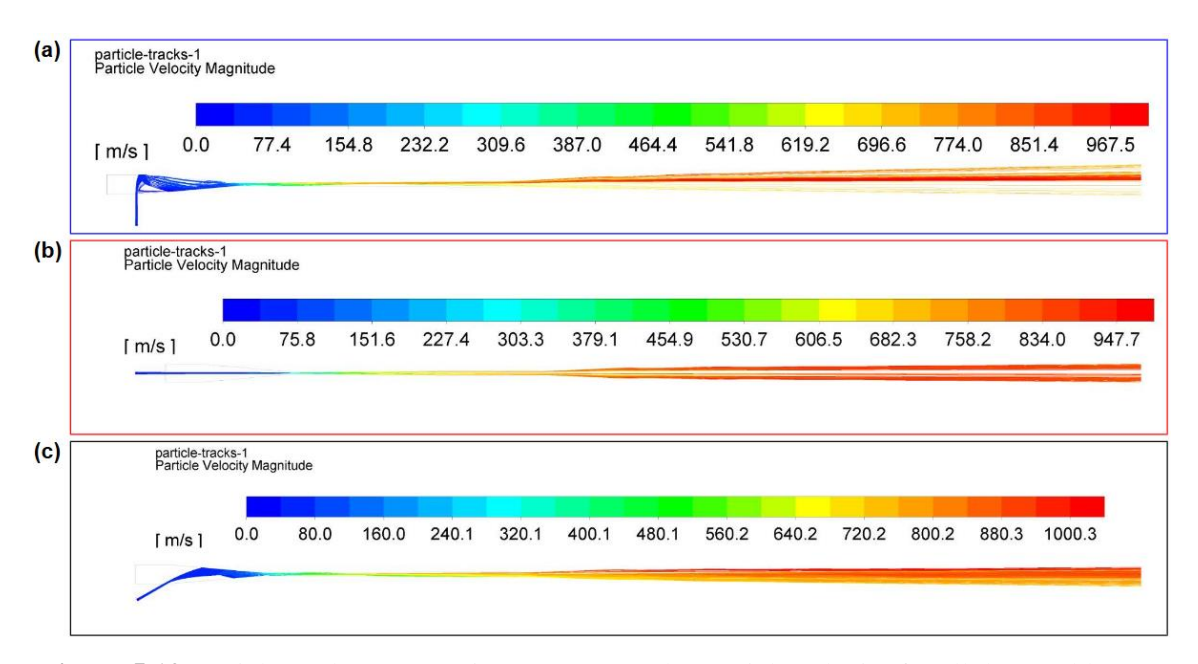


Figure 5.12 Particle tracks representing IN 718 powder particle velocity for all three cold spray nozzles with different powder injection angle (a) 90 deg; (b) 0 deg and (c) 30 deg

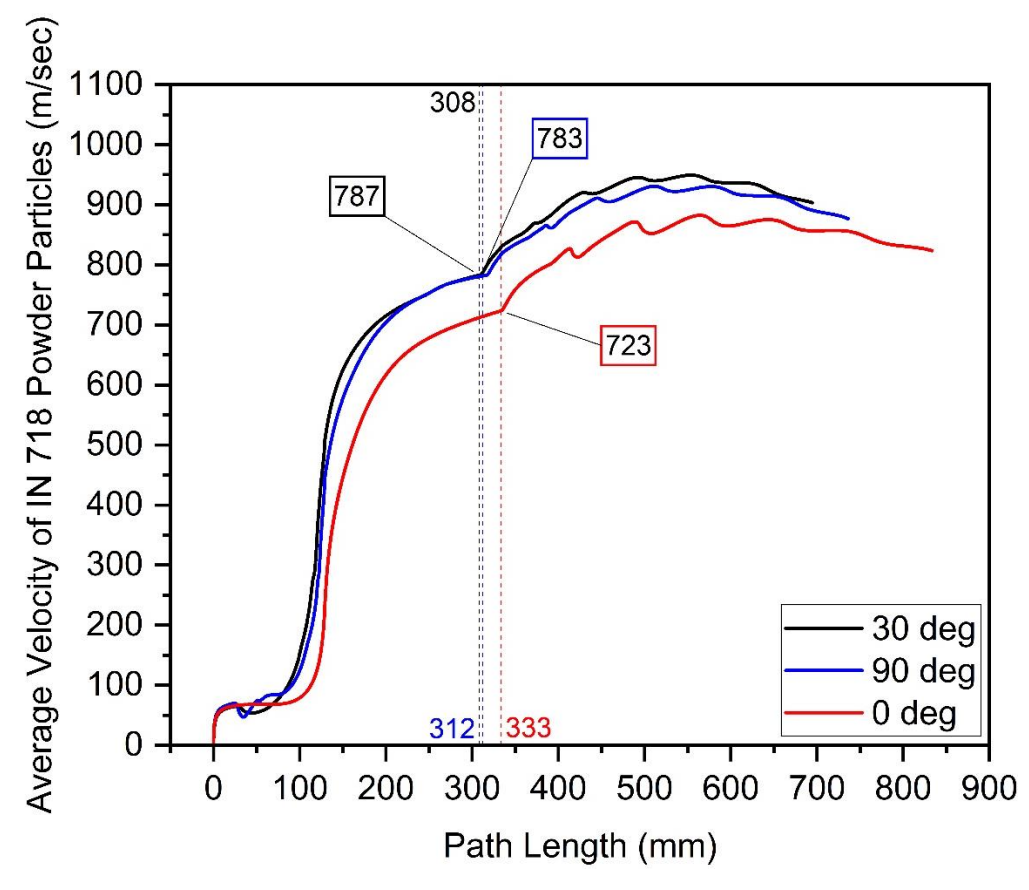


Figure 5.13 Variation of average velocity of IN 718 powder particles with path length for all three cold spray nozzles with different powder injection angle [90 deg; 0 deg and 30 deg]

Figure 5.14 represents the particle trajectories of IN 718 powder showing particle temperature for different powder injection angle cold spray nozzles. The elevated temperature of the powder particles in the case of 30 deg and 90 deg could be traced back to better heat transfer from the heated main gas to the carrier gas conveying the powder particles as shown in closer view of the convergent sections of different powder injection angle cold spray nozzles in Figure 5.15. The temperature of IN 718 powder particles upon exiting a convergent-divergent nozzle at a 30 deg injection angle averaged at 780 K. This temperature surpassed the average temperatures observed at exit points with 0 deg (625 K) and 90 deg (735 K) injection angles, as indicated in Figure 5.16. On the contrary, the heat transfer was not that much effective in case of 0 deg injection angle which ultimately led to lower average temperature of IN 718 powder particles. This disparity in heat transfer efficacy between different injection angles distinctly influenced the final temperatures experienced by the particles upon exiting the nozzle.

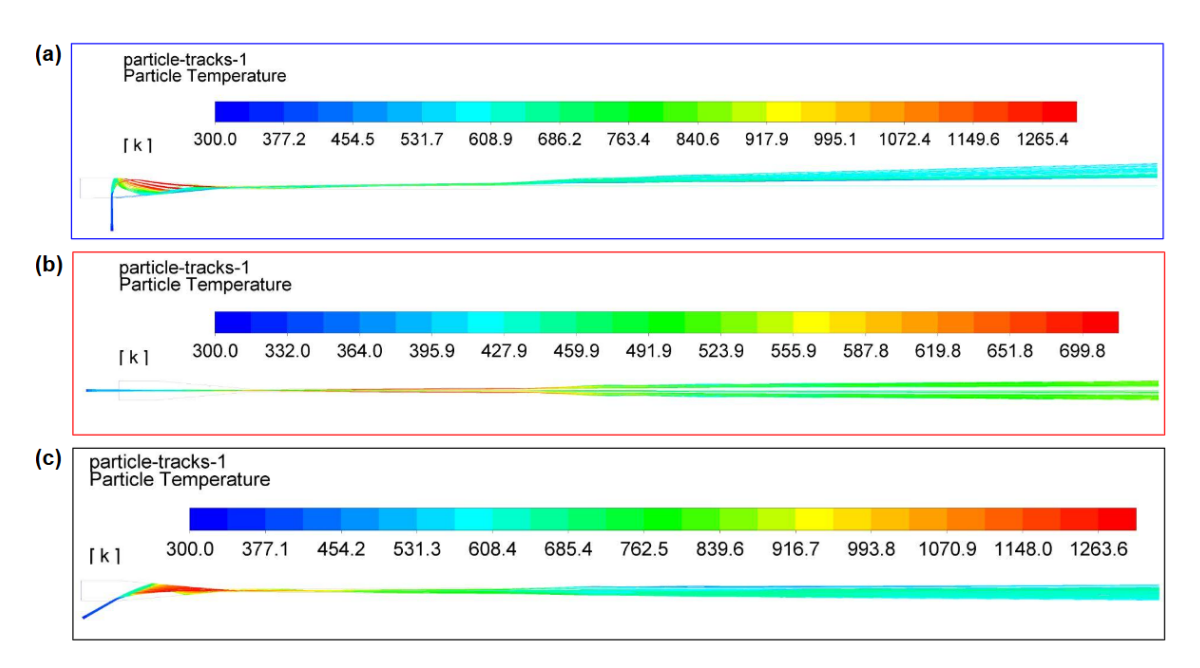


Figure 5.14 Particle tracks representing IN 718 powder particle temperature for all three cold spray nozzles with different powder injection angle (a) 90 deg; (b) 0 deg and (c) 30 deg

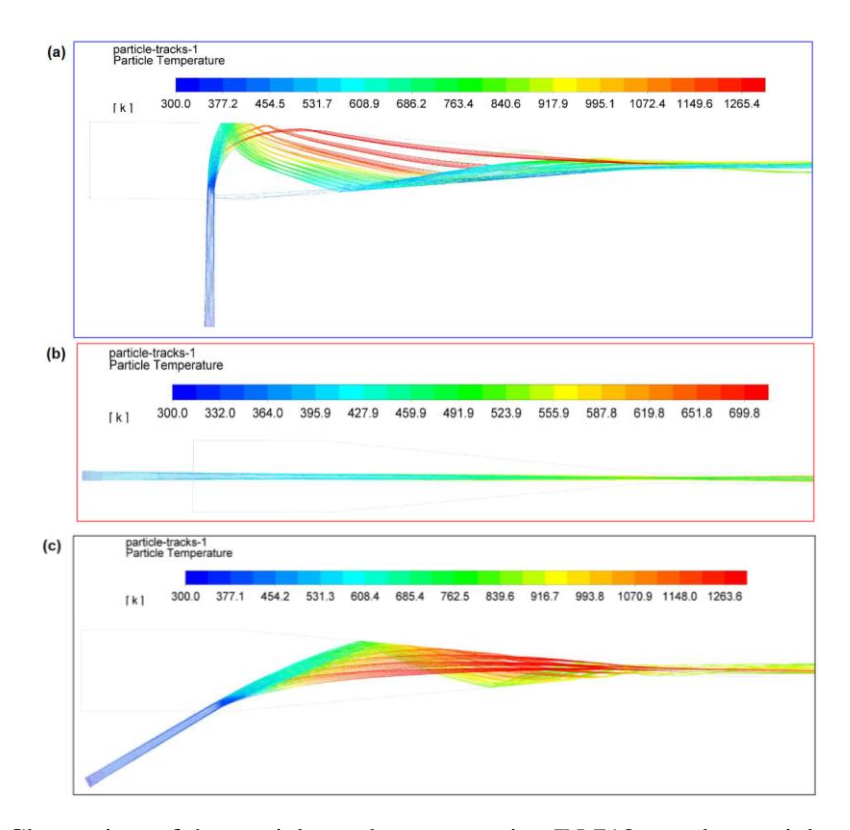


Figure 5.15 Closer view of the particle tracks representing IN 718 powder particle temperature in convergent sections for all three cold spray nozzles with different powder injection angle (a) 90 deg; (b) 0 deg and (c) 30 deg

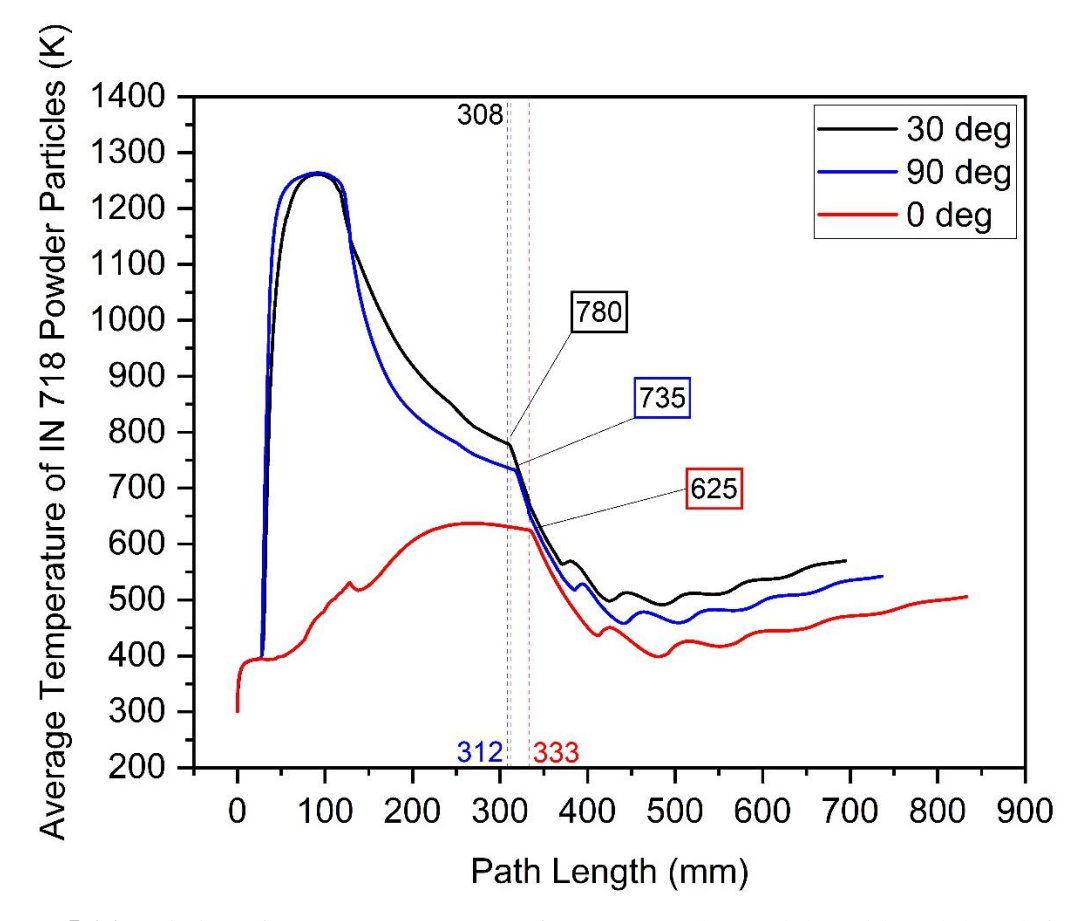


Figure 5.16 Variation of average temperature of IN 718 powder particles with path length for all three cold spray nozzles with different powder injection angle [90 deg; 0 deg and 30 deg]

CHAPTER 6

SIMULATION AND CHARACTERIZATION OF IN 718 PIPE

This chapter is divided into two interconnected sections. The first section focuses on discrete phase computational fluid dynamics study using the optimized set of cold spray process parameters and impact deformation (single- and multi-particle) analysis of cold spray deposition of IN 718 powder feedstock onto an SS 304 substrate pipe along with experimental validation. Another section covers the preliminary microstructural and mechanical characterization of the developed 3D standalone IN 718 pipe deposits.

In the first section, discrete phase computational fluid dynamics analysis of cold spray deposition of IN 718 powder feedstock onto an SS 304 substrate pipe was performed in order to understand the gas flow dynamics while impacting the SS 304 substrate pipe and particle tracks to obtain information regarding the average velocity and temperature of the IN 718 powder feedstock at the standoff distance (SoD). These parameters were then used as inputs for an explicit impact deformation study. Initially, a single-particle analysis was performed, focusing on particle sizes corresponding to the D₁₀, D₅₀, and D₉₀ distributions. The impact deformation results from this analysis were compared to the microstructure of a single-pass coating. Subsequently, a multiparticle analysis was conducted using 120 particles of varying sizes corresponding to the aforementioned distributions with random arrangement. The multi-particle impact deformation results revealed morphology similar to that of a five-pass coating microstructure.

In the subsequent section, preliminary microstructural and mechanical characterization of the cold spray additively manufactured seamless 3D standalone IN 718 pipe deposits was performed. Preliminary characterization revealed a dense microstructure with minimal porosity and absence of oxides in the CSAMed IN 718 deposits. XRD analysis confirmed the presence of desired phases, including the primary strengthening phase γ'' and δ phase precipitates. Preliminary microstructural and mechanical characterization confirmed that CSAM could swap the conventional process of fabricating IN 718 pipes as a sustainable alternative.

6.1 DISCRETE PHASE CFD AND EXPLICIT IMPACT DEFORMATION STUDY

6.1.1 Results and Discussion

6.1.1.1 Gas Flow Field and Powder Particle Stream Analysis

Figure 6.1 depicts the contour maps representing Mach number during the cold spray deposition of IN 718 powder feedstock onto an SS 304 substrate pipe. Flow perturbations were caused due to the presence of SS 304 substrate pipe acting as a mandrel for the fabrication of seamless 3D standalone IN 718 pipe deposits. This resulted in the formation of bow shock at the impingement zone (Pattison *et al.* 2008) as indicated in the Figure 6.1 respectively. This phenomenon is crucial in understanding how the deposition process is affected by the interaction between high-velocity gas jets and the substrate.

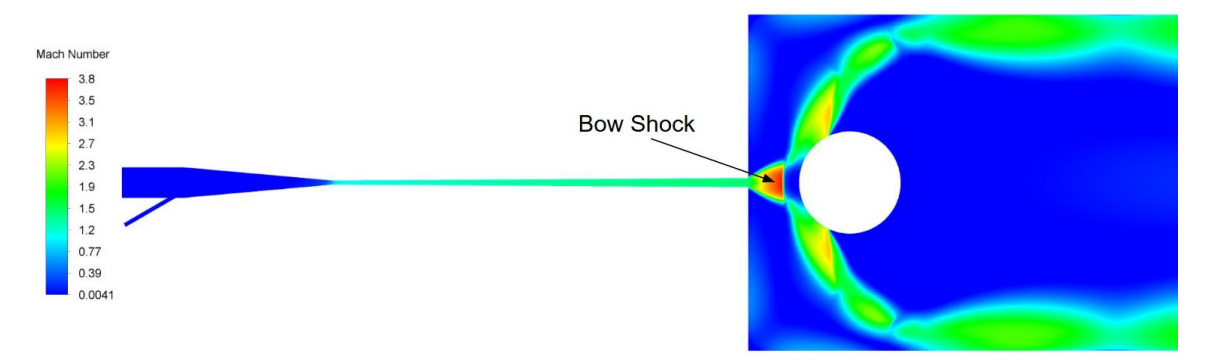


Figure 6.1 Contour maps representing Mach number during cold spray deposition of IN 718 powder feedstock onto an SS 304 substrate pipe

In the earlier analysis presented under Section 5.2.1.1 in Chapter 5, cold spray nozzles with varying powder injection angles were modeled without the substrate. It was noted that as the gas jet traversed multiple Mach diamonds, consisting of Prandtl-Meyer expansion waves and oblique shock waves due to compression, its kinetic energy gradually dissipated (Belbaki and Mebdoua 2017). This dissipation is prevalent till the nitrogen process gas pressure is equilibrated with the surrounding up to ambient pressure.

Introducing a substrate in the path of a cold spray jet will result in increase in the nitrogen gas pressure and density in a localized region due to the bow shock phenomenon. In case there is generation of strong bow shock at the substrate that will lead to the formation of a high stagnation pressure zone near the substrate. This high-pressure region will cause the particles to decelerate and may result in off-normal impacts. As a consequence, particle trajectories may deviate from the centerline significantly, with some particles potentially missing the substrate entirely and being carried away by the gas flow. Particles that do impact the substrate with low normal

velocities may fail to bond effectively; leading to poor adhesion and potentially sliding off the substrate. These issues directly reduce the efficiency of the deposition process (Samareh and Dolatabadi 2007).

In our case, it was a cylindrical substrate with SS 304 as pipe material. Figure 6.2 shows sharp gradients in nitrogen gas pressure as marked by blue arrows in the figure. The nitrogen gas pressure at the location of the bow shock was found to be 3.4 bar which remained constant on the SS 304 substrate's surface as well. The value of this stagnation pressure will determine the magnitude of the impact on gas flow dynamics and particle trajectories as shown in the upcoming results.

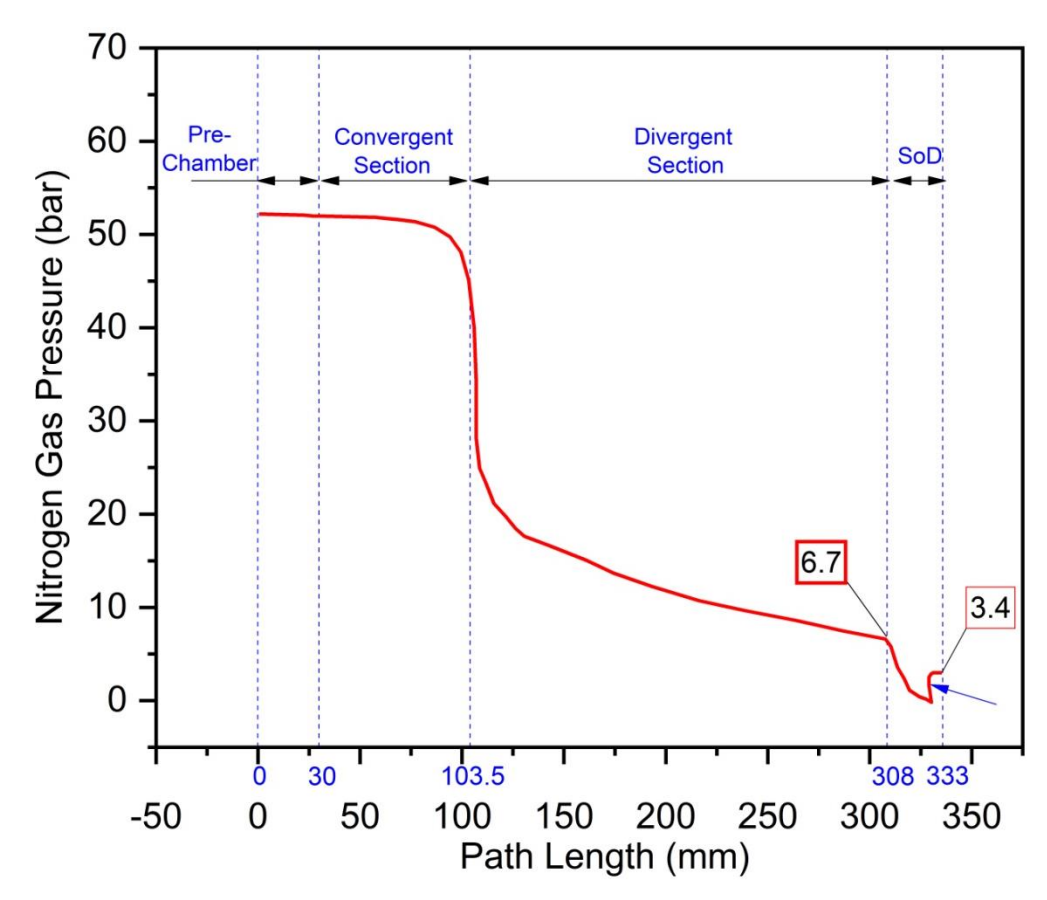


Figure 6.2 Variation of nitrogen gas pressure versus path length in cold spray deposition of IN 718 powder feedstock onto an SS 304 substrate pipe with blue arrow showing increase in pressure due to bow shock phenomenon

Figure 6.3 shows the slight increase in the density of the nitrogen gas owing to bow shock phenomenon. The gas density at the nozzle exit was reported to be 3.8 kg/m³, which dropped down because of the nitrogen gas flow through the expansion waves. There was an increase in the

density of the gas to a value of 2.2 kg/m³ at standoff distance as shown by blue arrows in the figure.

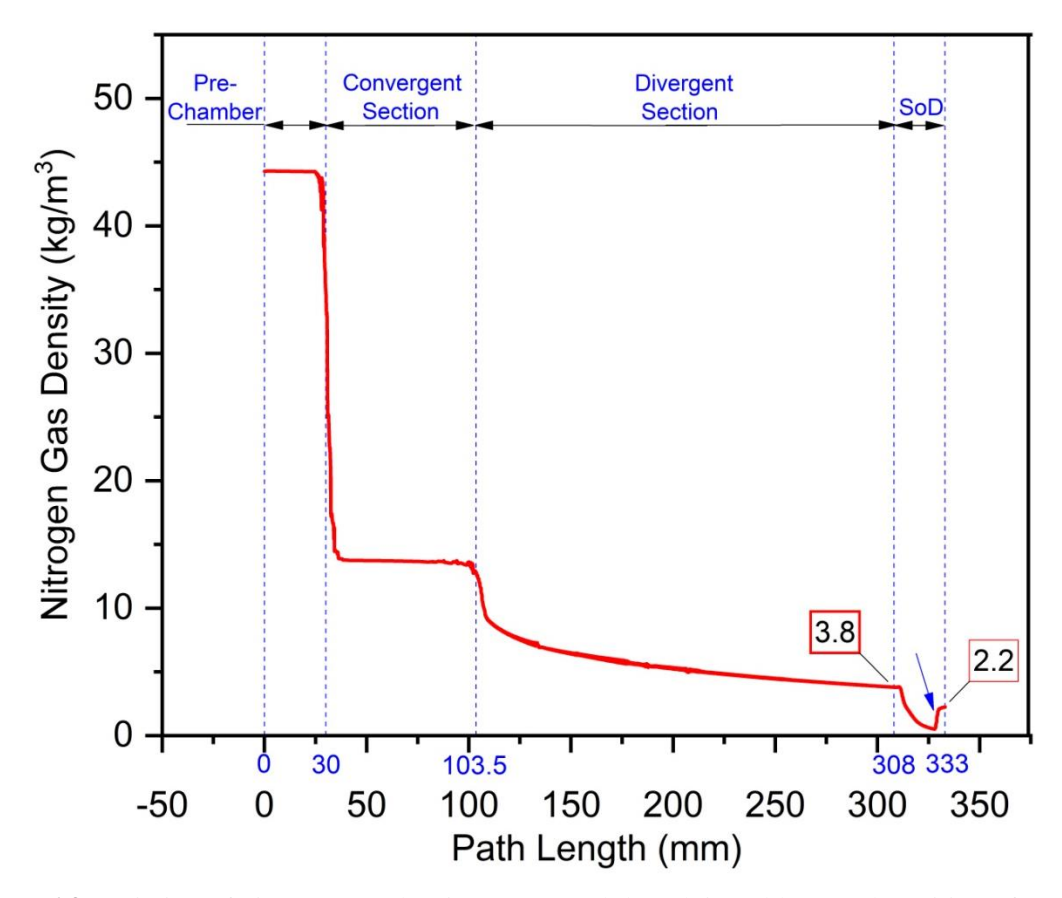


Figure 6.3 Variation of nitrogen gas density versus path length in cold spray deposition of IN 718 powder feedstock onto an SS 304 substrate pipe with blue arrow showing increase in density due to bow shock phenomenon

In subsonic flow conditions, increasing the gap between the substrate and nozzle exit generally leads to a reduction in the peak pressure rise. In contrast, within supersonic flows, the complex interaction between Prandtl-Meyer expansion waves and oblique shock waves causes the peak pressure to vary as the substrate's position is adjusted. When the substrate is cylindrical rather than flat, the strength of the bow shock diminishes due to the flow encountering less resistance and partially bypassing the cylinder. However, the cylindrical geometry as such in this case, alters flow patterns and reduces normal impact velocities, which in turn decreases the likelihood of particles striking the substrate, adversely affecting coating deposition efficiency and quality. Thus, selecting an optimal standoff distance is critical, as it significantly influences the behavior of the particles as they approach the substrate. A high stagnation pressure on the substrate slows particles before impact, reducing deposition efficiency. Conversely, a low-pressure region near

the substrate enhances particle impact velocity, minimizes dispersion, and improves deposition efficiency. One way to mitigate the impact of bow shock phenomenon on gas flow dynamics and particle trajectories is by increasing the standoff distance between the nozzle exit and the substrate (Pattison *et al.* 2008; Dykhuizen and Neiser 2003). However, this approach comes with its own set of challenges. Increasing the standoff distance reduces the temperature of the powder particles, which subsequently raises the critical velocity required for the powder feedstock, regardless of the material (Li *et al.* 2008; Li *et al.* 2006). Additionally, as the particles travel downstream, they tend to diverge, which negatively impacts deposition accuracy and efficiency, particularly when particles strike a cylindrical substrate at off-normal angles (Samareh and Dolatabadi 2007). Therefore, it is essential to carefully balance these factors when determining the optimal standoff distance. This study concludes that positioning the substrate 25 mm from the nozzle exit results in the lowest peak pressure of 3.4 bars as discussed earlier, offering a potential solution to these challenges.

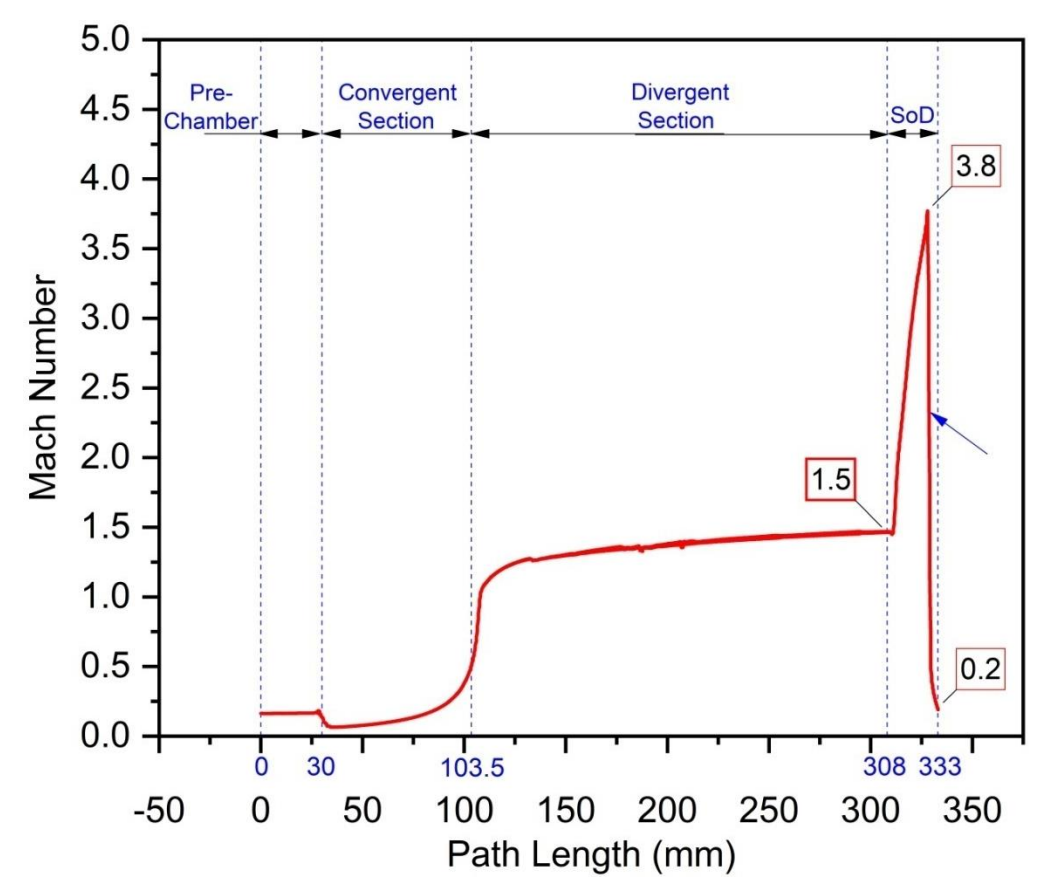


Figure 6.4 Variation of Mach number versus path length in cold spray deposition of IN 718 powder feedstock onto an SS 304 substrate pipe with blue arrow showing drop in Mach number due to bow shock phenomenon

Figure 6.4 shows the variation of Mach number with path length in cold spray deposition of IN 718 powder feedstock onto an SS 304 substrate pipe. The Mach number dropped from 3.8 at the location of bow shock to 0.2 value at the substrate's surface. This drop is caused by the dissipative nature of bow shock which results in conversion of kinetic energy into thermal energy (Fauchais *et al.* 2014; Samareh *et al.* 2009) which increases the nitrogen gas temperature as indicated by blue arrows in Figure 6.5 respectively. Initially at the nozzle exit, the gas temperature was 1040 K which dropped due to gas flow through expansion waves and then it rose to a temperature of 960 K at the standoff distance. The average temperature of IN 718 powder particles at the nozzle exit was 781 K which decreased to a value of 673 K at the standoff distance as can be clearly seen from Figure 6.5. The temperature value of IN 718 powder particles was used for performing the explicit impact analysis.

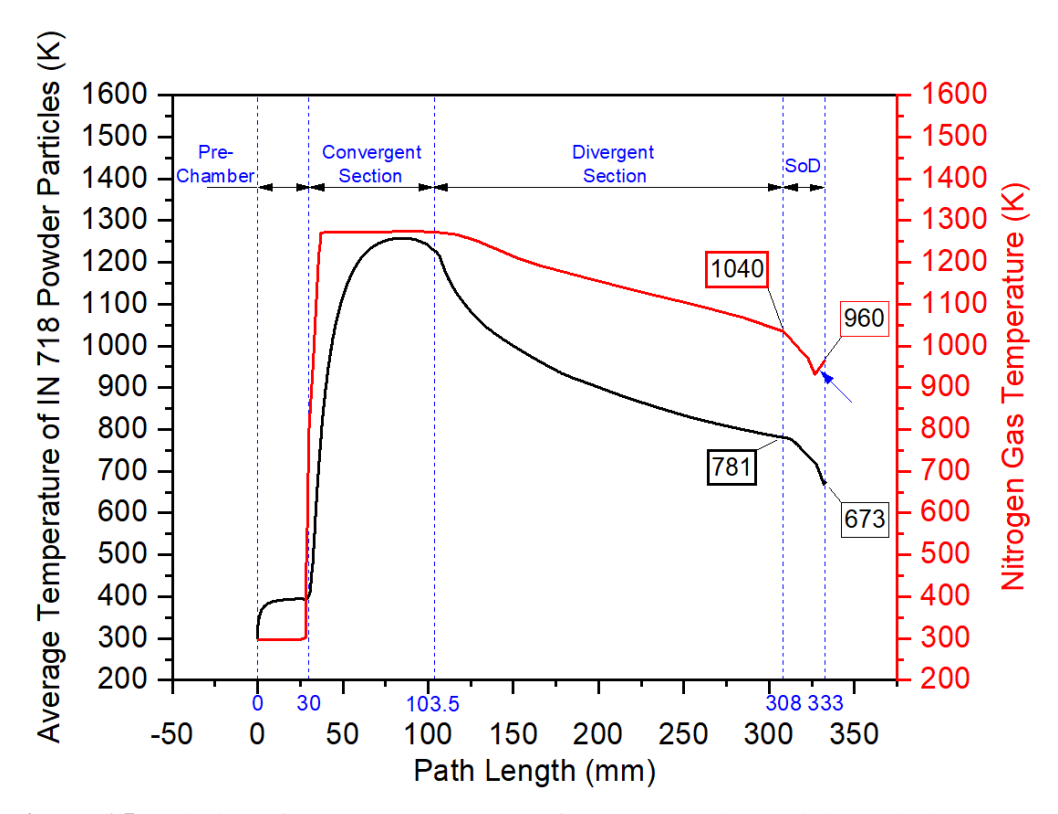


Figure 6.5 Variation of average temperature of IN 718 powder particles and nitrogen gas temperature versus path length in cold spray deposition of IN 718 powder feedstock onto an SS 304 substrate pipe with blue arrow showing increase in nitrogen gas temperature due to bow shock phenomenon

Figures 6.6, 6.7 and 6.8 show contour maps representing nitrogen gas velocity, nitrogen gas temperature and turbulent kinetic energy in cold spray deposition of IN 718 powder feedstock

onto an SS 304 substrate pipe when kept at a standoff distance of 25 mm from the nozzle exit. Here, it is important to mention that the SS 304 substrate pipe was rotating at a rpm of 16.

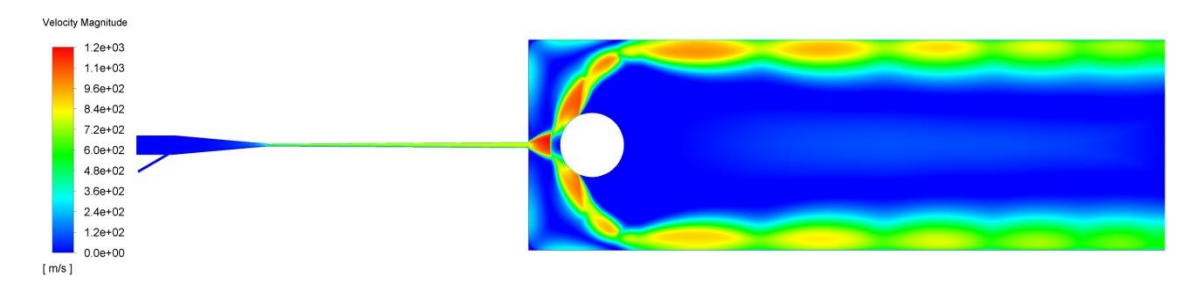


Figure 6.6 Contour maps representing nitrogen gas velocity during cold spray deposition of IN 718 powder feedstock onto an SS 304 substrate pipe

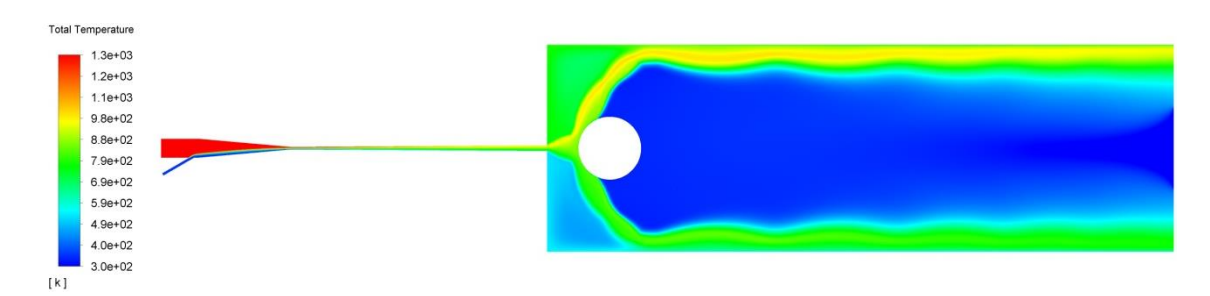


Figure 6.7 Contour maps representing nitrogen gas temperature during cold spray deposition of IN 718 powder feedstock onto an SS 304 substrate pipe

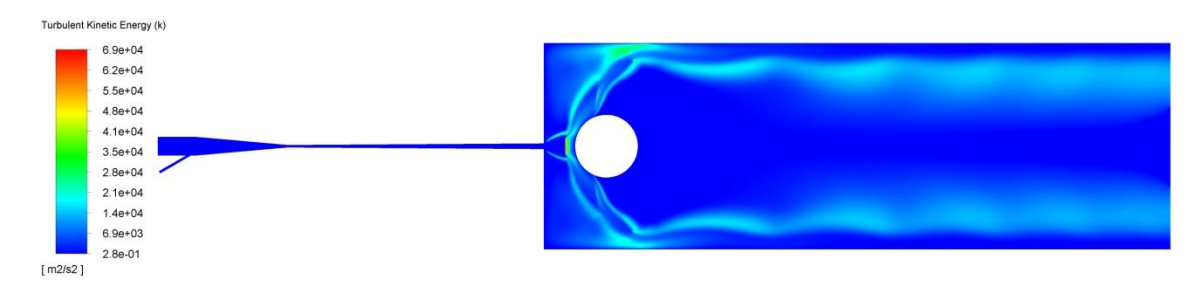


Figure 6.8 Contour maps representing turbulent kinetic energy during cold spray deposition of IN 718 powder feedstock onto an SS 304 substrate pipe

It is crucial to analyze the trajectories of IN 718 powder feedstock as it impacts an SS 304 substrate pipe positioned 25 mm from the nozzle exit. At this location, the lower peak pressure of 3.4 bar on the substrate ensured that the powder particles experienced minimal deviation from their intended paths. This reduced deviation is vital for achieving accurate and consistent coating deposition. Figures 6.9 and 6.10 illustrate the particle trajectories, highlighting the velocity and temperature profiles of the IN 718 powder feedstock as it approaches the substrate. These visual representations provide valuable insight into how the particles behave under the given conditions,

reinforcing the importance of optimizing the standoff distance and stagnation pressure for achieving the desired coating results.

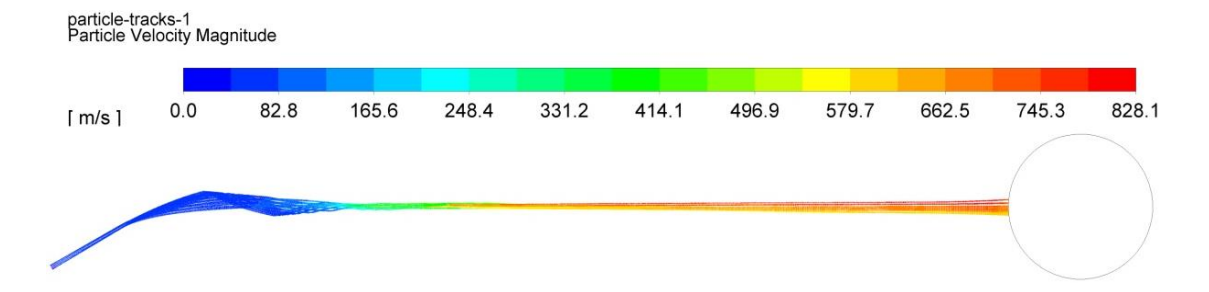


Figure 6.9 Particle tracks representing powder particle velocity during cold spray deposition of IN 718 powder feedstock onto an SS 304 substrate pipe

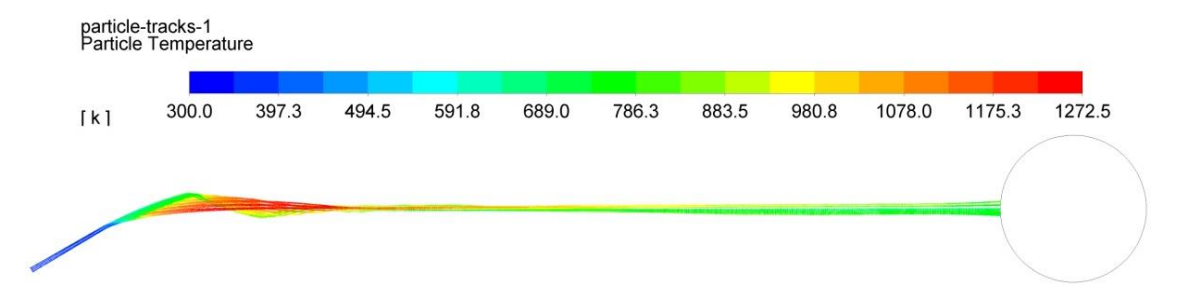


Figure 6.10 Particle tracks representing powder particle temperature during cold spray deposition of IN 718 powder feedstock onto an SS 304 substrate pipe

These figures clearly demonstrate that the powder particle tracks were narrow and well-defined, resulting in a highly concentrated cold spray footprint with a diameter of approximately 5 mm. The ability to achieve such precise deposition not only improves the quality of the final product but also enhances the overall efficiency of the manufacturing process by reducing material waste and machining time.

Figure 6.11 illustrates the variation in nitrogen gas velocity and the average velocity of IN 718 powder particles along the path length during the cold spray deposition process onto an SS 304 substrate pipe. A significant observation was the sharp decline in nitrogen gas velocity compared to the minimal drop in the average velocity of the IN 718 powder particles, which is attributed to the bow shock phenomenon. This disparity was primarily due to the high density of the IN 718 powder feedstock, which gave the particles substantial inertia, allowing them to maintain their motion despite the sudden drop in gas velocity. Additionally, the lower peak pressure at a standoff distance of 25 mm from the nozzle exit played a crucial role in sustaining the particle velocity.

Initially, the nitrogen gas exited the nozzle at a velocity of 778 m/sec, which then increased to 1184 m/sec as the gas flowed through expansion waves. However, upon encountering the bow shock, the gas velocity experienced a sharp reduction, dropping to 124 m/sec. In contrast, the IN 718 powder particles exited the nozzle at an average velocity of 756 m/sec and, despite the effects of the bow shock, their velocity increased through the expansion waves. Remarkably, the powder particles experienced only a minimal decrease in velocity, reaching 825 m/sec at the standoff distance. This average velocity and temperature of IN 718 powder particles at standoff distance as seen earlier were used for performing the explicit impact analysis.

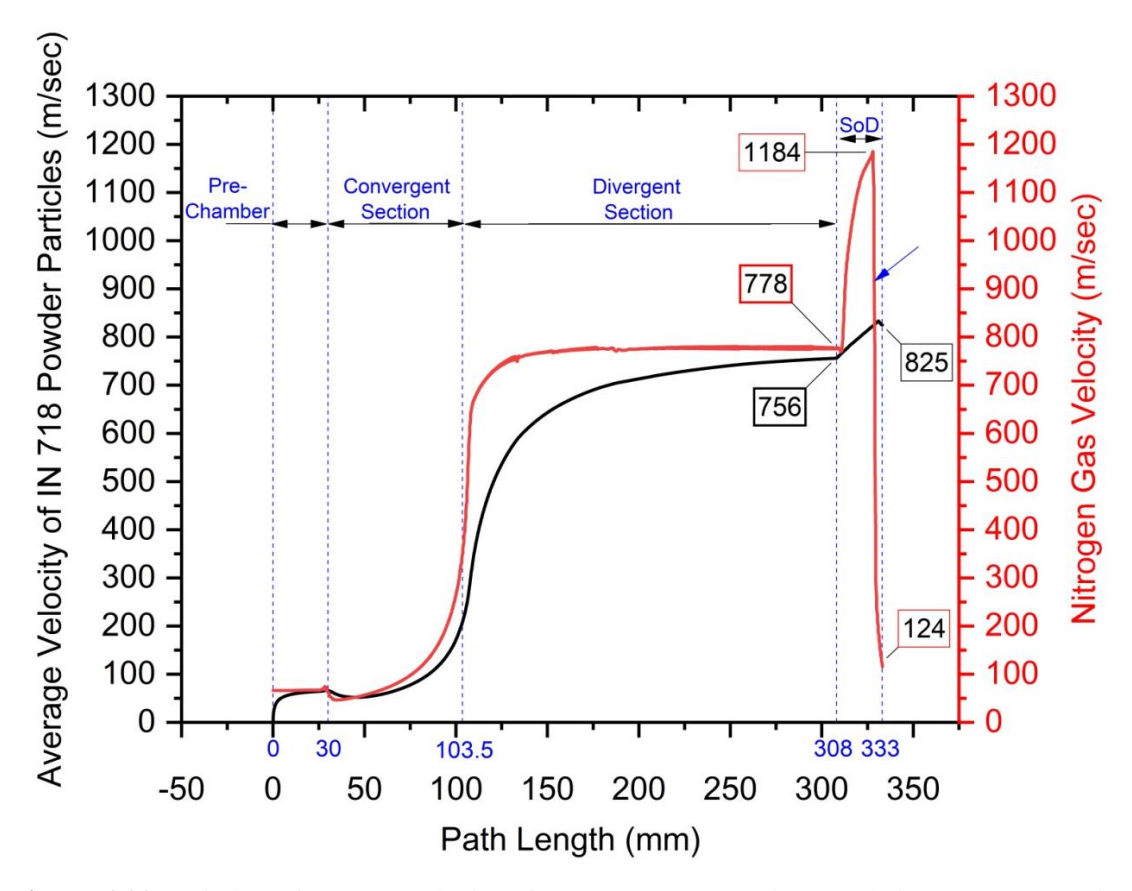


Figure 6.11 Variation of average velocity of IN 718 powder particles and nitrogen gas velocity versus path length in cold spray deposition of IN 718 powder feedstock onto an SS 304 substrate pipe with blue arrow showing drop in nitrogen gas velocity due to bow shock phenomenon

6.1.1.2 Impact Deformation Analysis and Experimental Validation

6.1.1.2.1 Single-Particle Impact Analysis

In this subsection, we will conduct an explicit impact analysis to assess the deformation of IN 718 powder particles upon impacting an SS 304 substrate. The average velocity and temperature of the powder particles used in this analysis were derived from the discrete phase computational

fluid dynamics study described in Section 6.1.1.1. For the single-particle impact analysis, IN 718 powder particles with dimensions corresponding to D_{10} (13.5 μ m), D_{50} (22 μ m), and D_{90} (33.5 μ m), as detailed in Figure 3.9 (Section 3.1.2.2), were subjected to impacts onto an SS 304 substrate at room temperature. The explicit impact modeling parameters for IN 718 powder feedstock and SS 304 substrate are specified in Table 3.16 (Section 3.7.2). All three particle sizes were impacted onto the SS 304 substrate at a velocity of 825 m/s. Figure 6.12 shows PEEQ for different diameter distribution of IN 718 powder feedstock and SS 304 substrate.

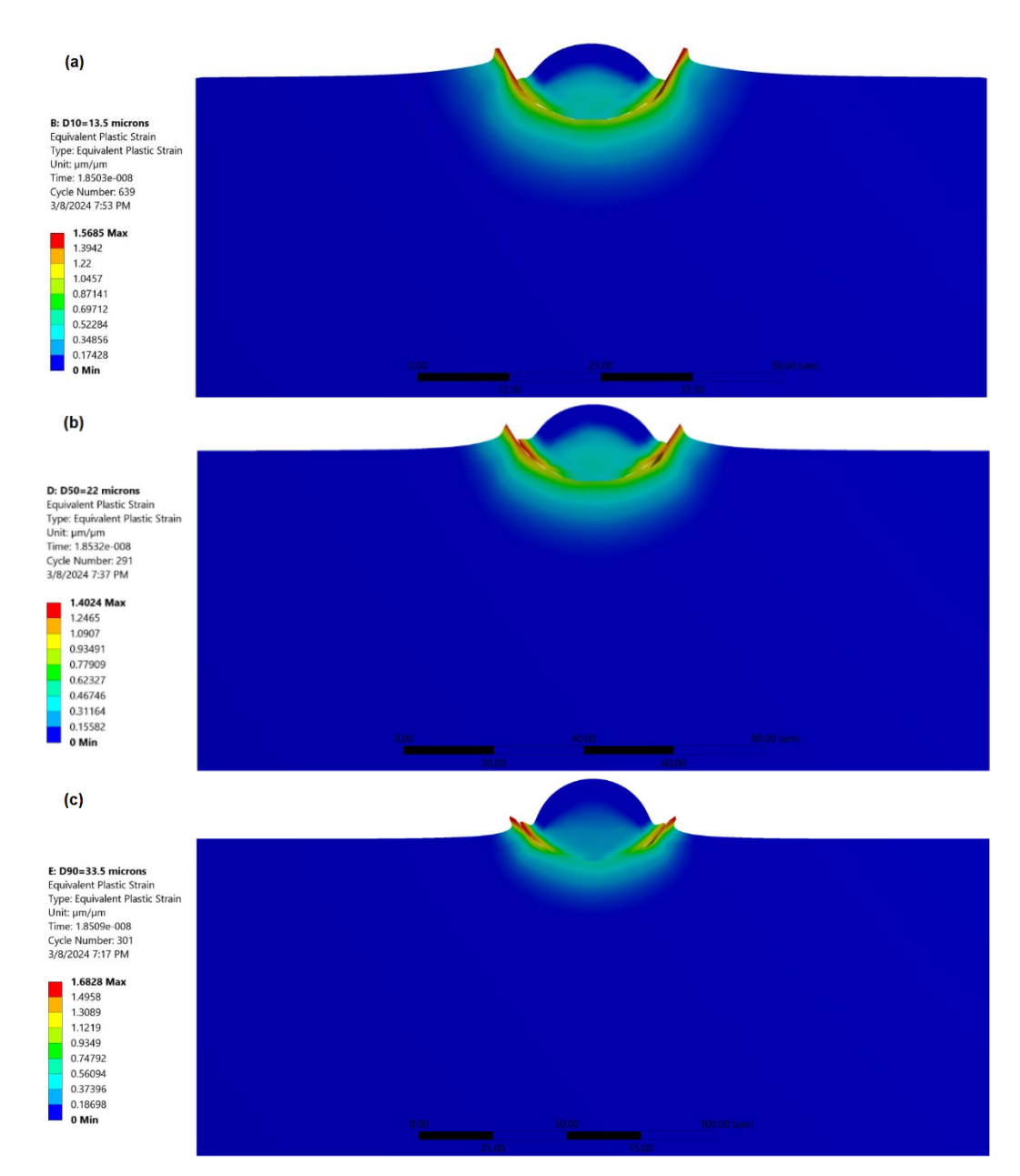


Figure 6.12 Simulated contours of PEEQ for different diameters of IN 718 powder feedstock impacting onto an SS 304 substrate (a) D_{10} (13.5 μ m); (b) D_{50} (22 μ m); and (c) D_{90} (33.5 μ m)

Above figures clearly illustrate that all the powder particles exhibited a characteristic jetting formation, which strongly suggests that the particle impact velocity and temperature at the standoff distance was sufficient to trigger adiabatic shear instability. This phenomenon is crucial in the cold spray process, as it indicates that the particles have achieved the necessary velocity and temperature to deform plastically upon impact, ensuring a strong bond with the substrate or among them (Grujicic *et al.* 2004).

The depth of penetration is largely governed by the particle size and impact velocity. As a result, the D_{10} case, as depicted in Figure 6.12 (a), shows a greater penetration depth compared to the cases illustrated in Figures 6.12 (b) and (c). The critical diameter for the IN 718 powder feedstock, calculated using the equations provided in Section 2.4.5.2, Chapter 2 (equations 2.3 and 2.4), was determined to be 12.5 μ m. Particles smaller than this critical diameter are unable to induce adiabatic shear instability, a necessary condition for effective bonding. Instead of plastically deforming, these smaller particles penetrated the substrate, embedding them within it (Palodhi *et al.* 2021).

During the cold spray process, these sub-critical particles created craters upon impact with the substrate, and it was within these craters that the particles became trapped. This trapping mechanism occurred without the typical plastic deformation and bonding that would otherwise have been expected. Moreover, particles whose diameters are close to the critical value experience a reduction in the jetting effect. This diminished jetting is primarily due to the substantial absorption of impact energy by the substrate, which deforms to accommodate the penetrating particles. Hence, we could say that the relationship between particle shape, impact velocity, and critical diameter is crucial in determining the outcome of the cold spray process (Hassani-Gangaraj *et al.* 2016; Hassani-Gangaraj *et al.* 2018).

Figure 6.13 depicts contour maps showing von-Mises stresses for IN 718 powder particles with dimensions corresponding to D_{10} (13.5 μ m), D_{50} (22 μ m), and D_{90} (33.5 μ m) respectively. It can be seen that D_{50} and D_{90} sizes (Figures 6.13 (b) and (c)) have higher von-Mises stresses and more uniform distribution at the contact area and within the lower part of the splat, as compared to D_{10} size (Figure 6.13 (a)). Larger particles tend to have higher von-Mises stresses because of their increased surface area, strain localization, and greater force absorption, which leads to more complex and intense stress distribution compared to smaller particles.

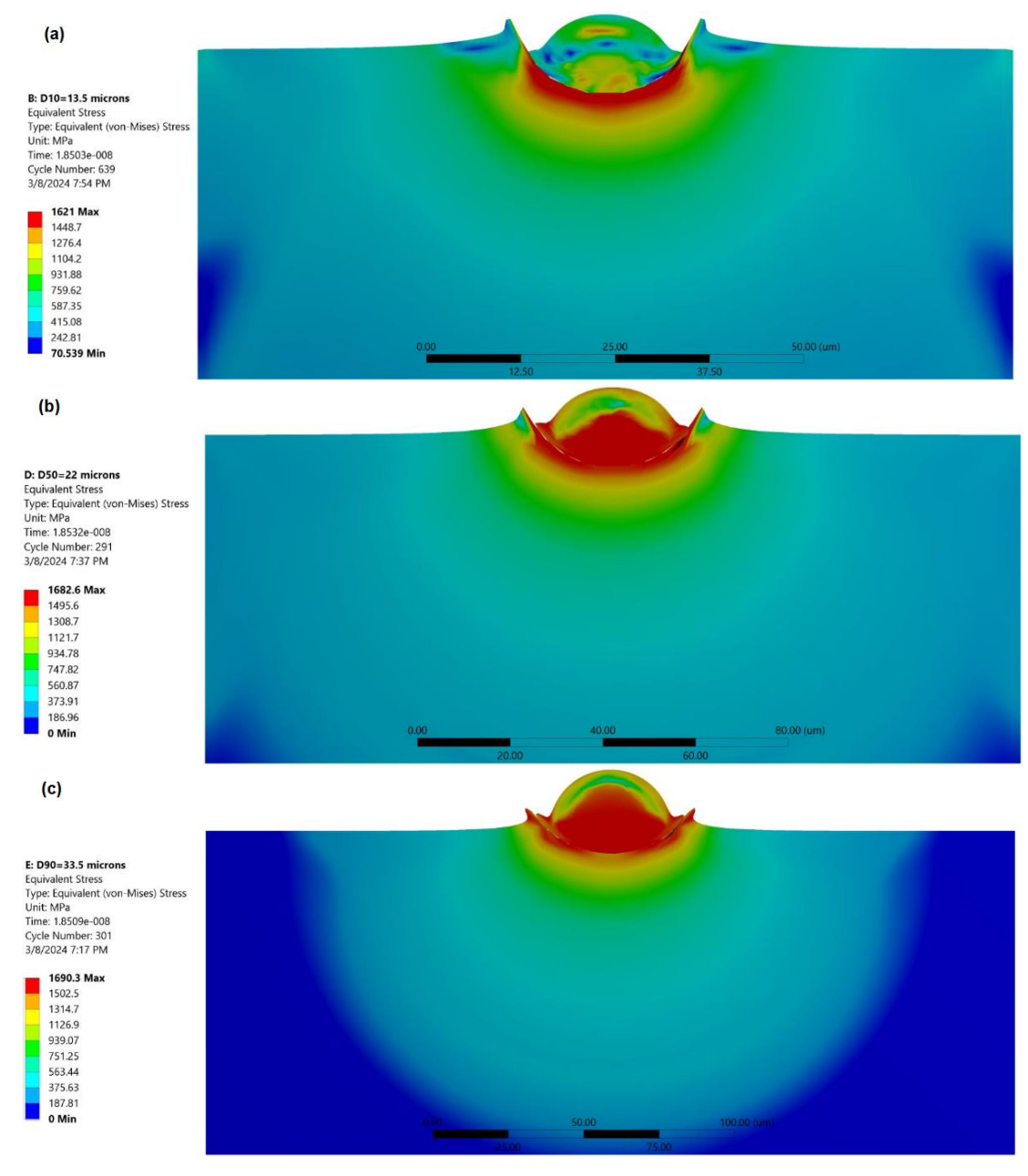


Figure 6.13 Simulated contours of von-Mises stresses for different diameters of IN 718 powder feedstock impacting onto an SS 304 substrate (a) D_{10} (13.5 μ m); (b) D_{50} (22 μ m); and (c) D_{90} (33.5 μ m)

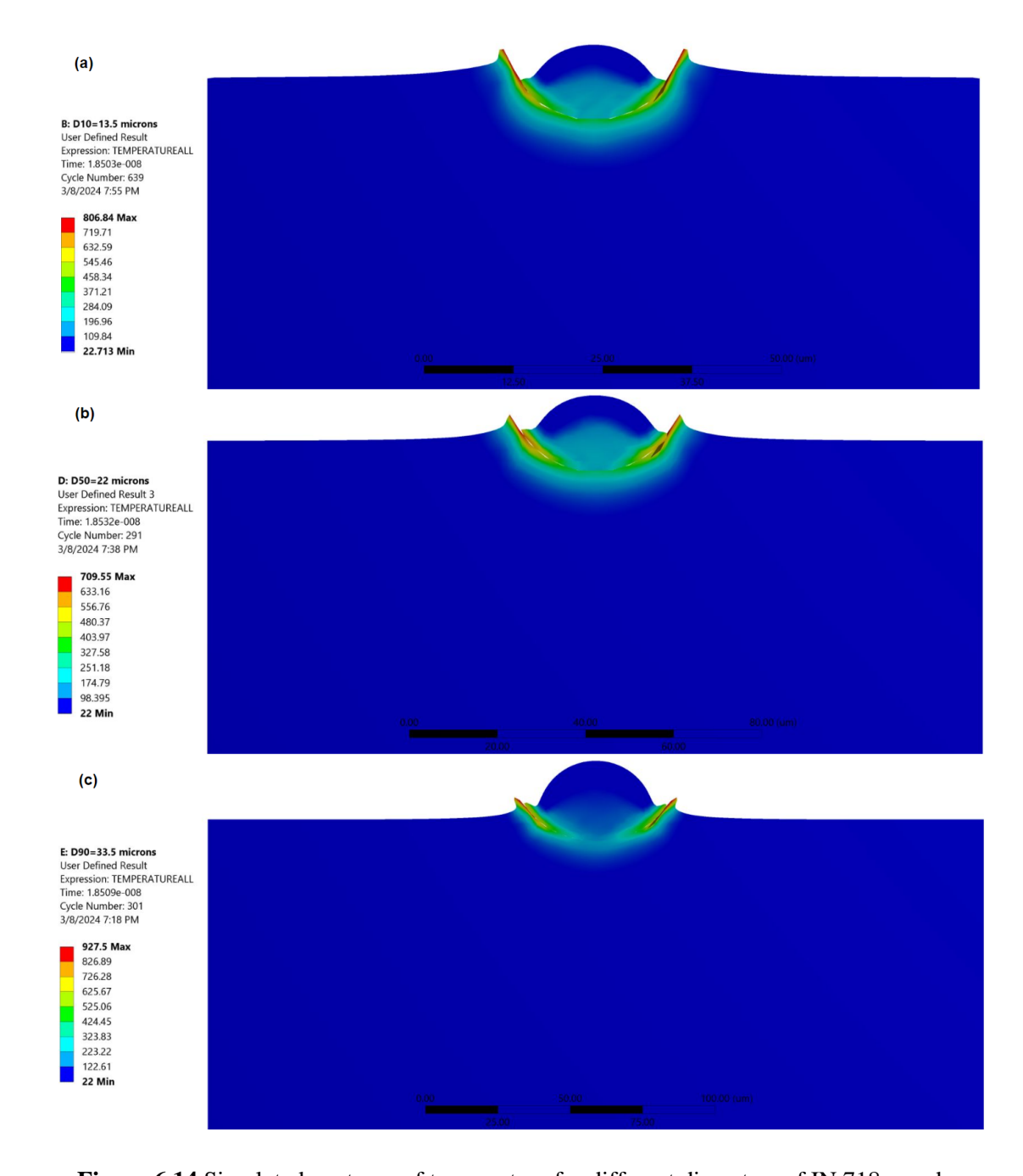


Figure 6.14 Simulated contours of temperature for different diameters of IN 718 powder feedstock impacting onto an SS 304 substrate (a) D_{10} (13.5 μ m); (b) D_{50} (22 μ m); and (c) D_{90} (33.5 μ m)

Figure 6.14 depicts contour maps of temperature for different diameters of IN 718 powder feedstock.

The results of the explicit impact analysis for single particles across various particle size distributions as shown in Figure 6.12, were experimentally validated by examining the

microstructure of single-pass coatings as displayed in Figure 6.15 respectively. This validation focused on identifying jetting formation in particles larger than the critical diameter and observing the penetration effects in particles smaller than the critical diameter. The single-pass coating microstructure was meticulously developed using an optimized set of cold spray process parameters, including finely tuned robotic configurations and precise tilting turntable settings. By comparing these experimental findings with the computational predictions, the study confirmed the accuracy and reliability of the discrete phase computational fluid dynamics (CFD) simulations and explicit impact analysis. This thorough validation process was crucial in demonstrating the effectiveness of the computational models in predicting particle behavior during the cold spray process, ensuring that the simulations accurately represented the real-world interactions between particles and the substrate.

Figure 6.15 clearly illustrates that the larger particles, highlighted by the dashed yellow rectangles, exhibit proper jetting formation. This occurred because the thermal diffusion within these particles was sufficiently slow, allowing them to retain the necessary energy to undergo plastic deformation and initiate jetting upon impact. This jetting formation is a key indicator of effective bonding, as it suggests that the particles have achieved the conditions necessary for adiabatic shear instability, which is crucial for creating a strong bond with the substrate or between particles themselves (Assadi et al. 2003). In contrast, smaller particles with diameters below the critical threshold did not exhibit any significant shape changes. This lack was due to the absence of plastic deformation, which is essential for initiating the bonding process. These smaller particles have a high surface area to volume ratio, which significantly affects their thermal and mechanical behavior during impact. Due to their higher surface area, these particles rapidly dissipated heat, which, coupled with their smaller mass, prevented them from reaching the energy levels required to catalyze adiabatic shear instability at the interface (King and Jahedi 2010). As a result, instead of deforming and bonding with the substrate, these sub-critical particles merely penetrate the substrate without undergoing the necessary plastic deformation. This penetration occurred without the jetting effect seen in larger particles, as the energy dissipation and high shear strength inhibited the onset of the adiabatic shear instability. Consequently, these smaller particles do not contribute effectively to the bonding process, highlighting the importance of particle size in determining the success of the cold spray process.

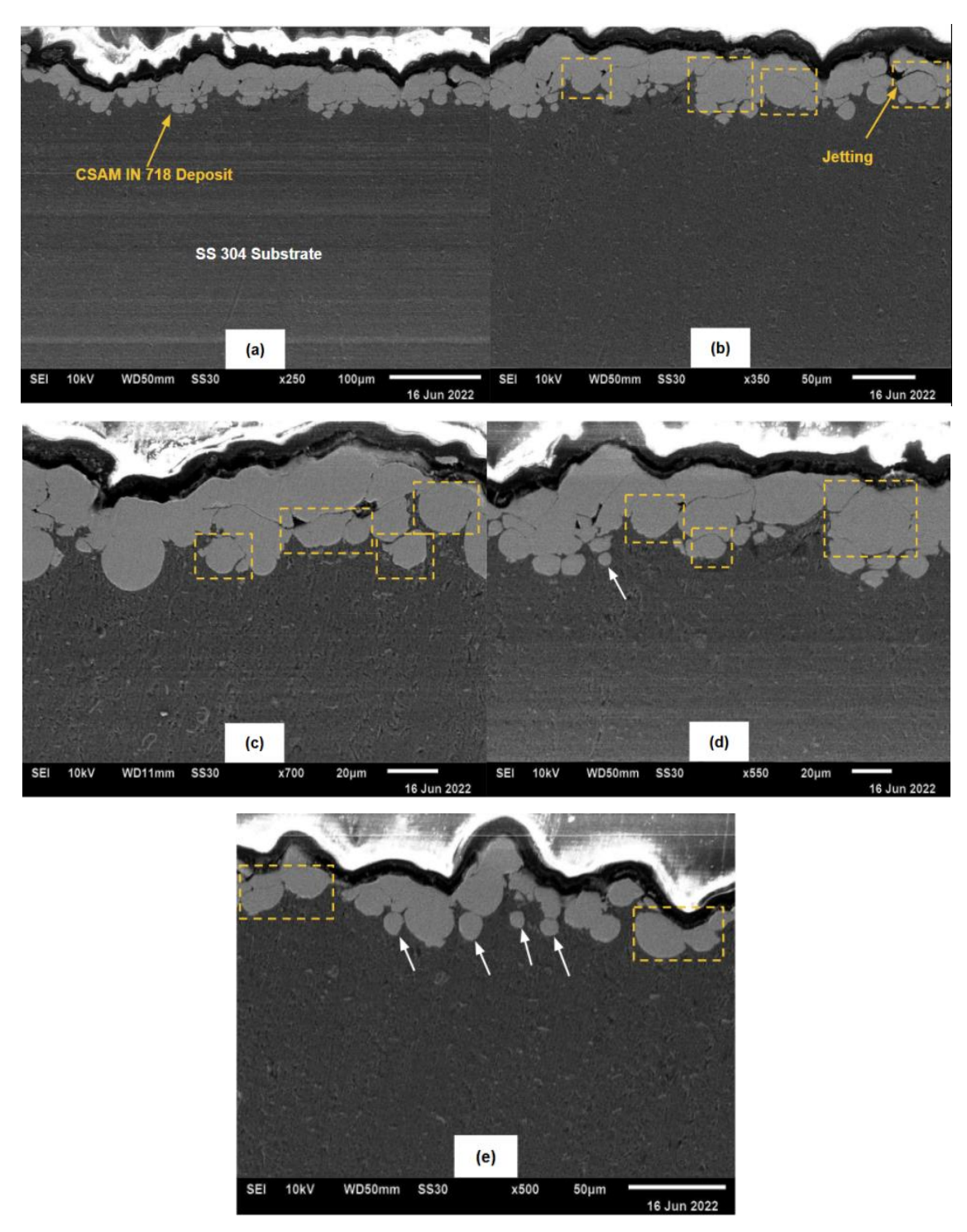


Figure 6.15 Single-pass coating cross SEM micrographs showing microstructure of IN 718 powder splats in (a); (b); (c); (d); and (e) with bigger particles in dashed yellow rectangles showing jetting formation and white arrows depicting smaller particle penetrating deeper inside comparatively softer SS 304 substrate

6.1.1.2.2 Multi-Particle Impact Analysis

This section delves into the analysis of multi-particle impacts involving IN 718 powder feedstock, characterized by a random distribution of particle diameters. The purpose of this analysis was to understand and establish a correlation between the deformation behavior of multiple particles and the resulting microstructure in a five-pass coating process. The interaction of multiple particles during impact leads to more extensive deformation due to various effects such as tamping, interlocking, and extrusion (Zhou *et al.* 2010).

The tamping effect plays a crucial role in cold spray processes, particularly when multiple particles impact and accumulate on the initial deposit layer. Each incoming particle exerts pressure on the previously deposited layer, enhancing compression and causing further deformation and flattening of particles. This compaction increases the coating's density and cohesion, both of which are vital for its mechanical performance. By compressing the particles more tightly, the tamping effect reduces porosity and eliminates voids, resulting in a more uniform microstructure. This uniformity directly improves hardness, strength, and resistance to mechanical wear, which are essential qualities for coatings subjected to high-stress conditions. Additionally, the tamping effect influences the coating's deformation behaviour, affecting residual stress distribution and its response to operational loads. The controlled deformation strengthens interparticle bonding and refines the internal stress distribution, thereby enhancing fatigue resistance, toughness, and durability. This even stress distribution helps prevent crack initiation and propagation, contributing to the coating's overall resilience and long-term stability (Gao et al. 2023).

Similarly, the interlocking effect in cold spray coatings occurs when high-velocity particle impacts cause material from a previously deposited particle to form a jet that embeds within an incoming particle, creating a mechanical interlock. This interlocking significantly enhances the cohesion and bond strength between particles, improving the coating's stability under stress by resisting particle pull-out. It also leads to a dense, well-bonded microstructure with minimal voids, which directly enhances hardness, wear resistance, and durability. This dense arrangement improves resistance to cracking and delamination, particularly under mechanical or thermal stresses. Furthermore, the interlocking effect refines internal stress distribution, reducing the likelihood of stress concentrations that could lead to coating failure. This behavior makes the coating more resistant to fatigue and better suited for high-stress or cyclic environments, thus improving its long-term durability (Hussain *et al.* 2009).

The extrusion effect, another important phenomenon in cold spray, occurs when incoming particles cause lateral material flow around previously deposited particles, consolidating and

engulfing them. This process fills gaps and voids between particles, which not only improves the coating's density but also enhances its surface finish, a key requirement for applications requiring smooth, uniform coatings. The extrusion effect reduces internal porosity, creating a denser microstructure with fewer pathways for crack propagation, thus improving resistance to wear, corrosion, and impact. The controlled deformation during extrusion also helps distribute internal stresses more evenly, minimizing localized stress concentrations that could weaken the coating. This cohesive, densely packed structure enhances fatigue resistance and extends the coating's lifespan under operational stresses (Zhou *et al.* 2010).

These phenomena such as tamping, interlocking, and extrusion are essential to the cold spray process when multiple particles impact the substrate. They work together to ensure that the coating not only adheres well to the substrate but also develops the desired mechanical properties, such as high density, strength, and durability. Understanding these effects is crucial for optimizing the cold spray process and achieving the best possible coating performance. Figure 6.16 shows these effects in the developed microstructure from single-pass and five-pass cold spraying of IN 718 powder feedstock onto an SS 304 substrate. Figures 6.16 (a), (b) and (c) shows single-pass coating microstructure with the interlocking (white arrows) and extrusion (yellow arrows) while Figure 6.16 (d) shows multi-pass coating microstructure with the tamping effect which helps in closing the pores and densification of the deposits.

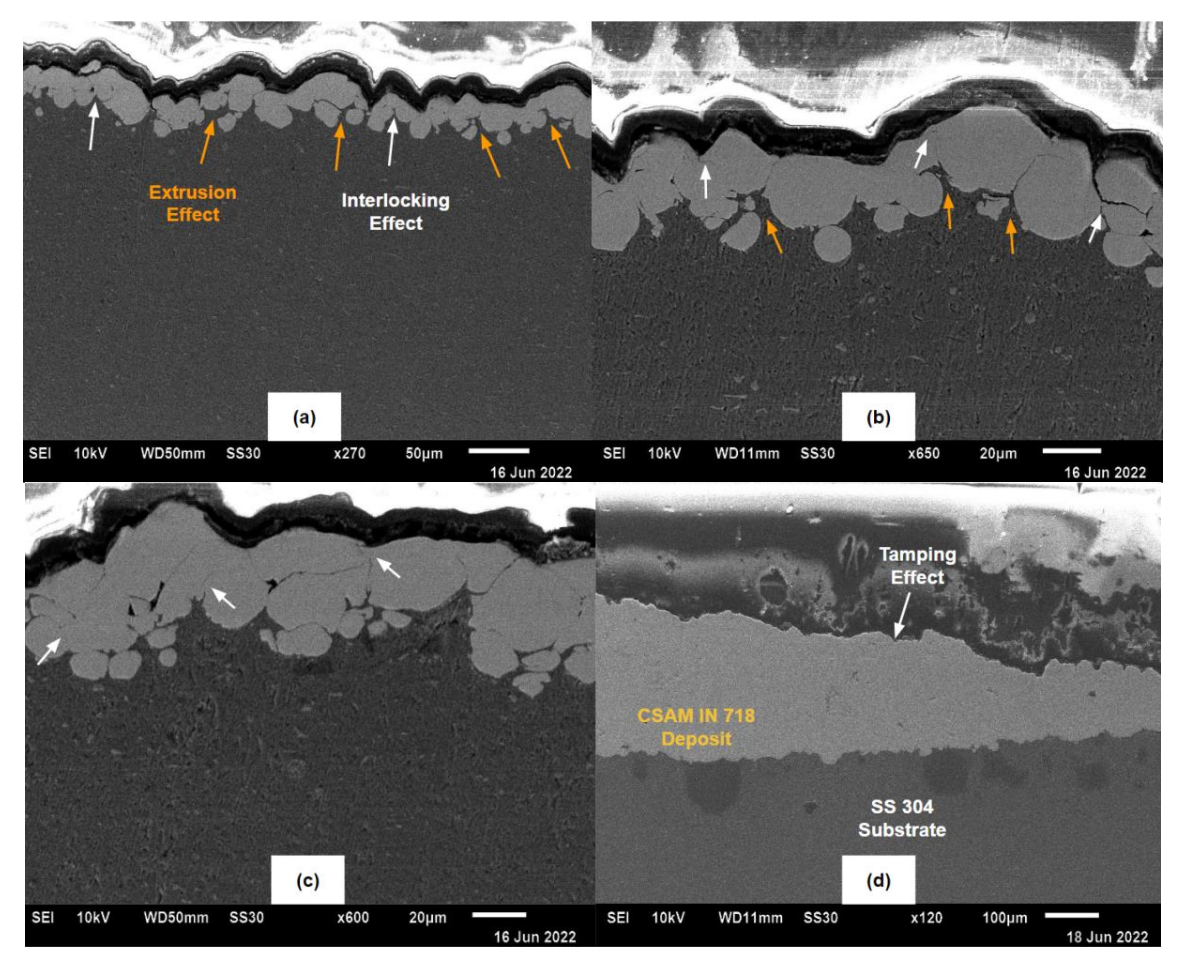


Figure 6.16 Cross SEM micrographs showing microstructure of IN 718 powder splats in (a); (b) and (c) with yellow and white arrows showing extrusion and interlocking effects and (d) showing tamping effect

The simulation in Figure 6.17 demonstrates the contours of equivalent plastic strain (PEEQ) and von-Mises stresses for multiple IN 718 powder particles of various sizes (D_{10} : 13.5 μ m, D_{50} : 22 μ m, and D_{90} : 33.5 μ m) in a random distribution impacting onto an SS 304 substrate. These simulated results are then compared with the microstructure produced from a five-pass coating process as shown in Figure 6.18. Specific regions within both the impact simulation (Figure 6.18 (a) and the coating microstructure (Figures 6.18 (b); (c); (d) and (e)) that exhibit similar deformation patterns are highlighted with the same colors, indicating strong correlation.

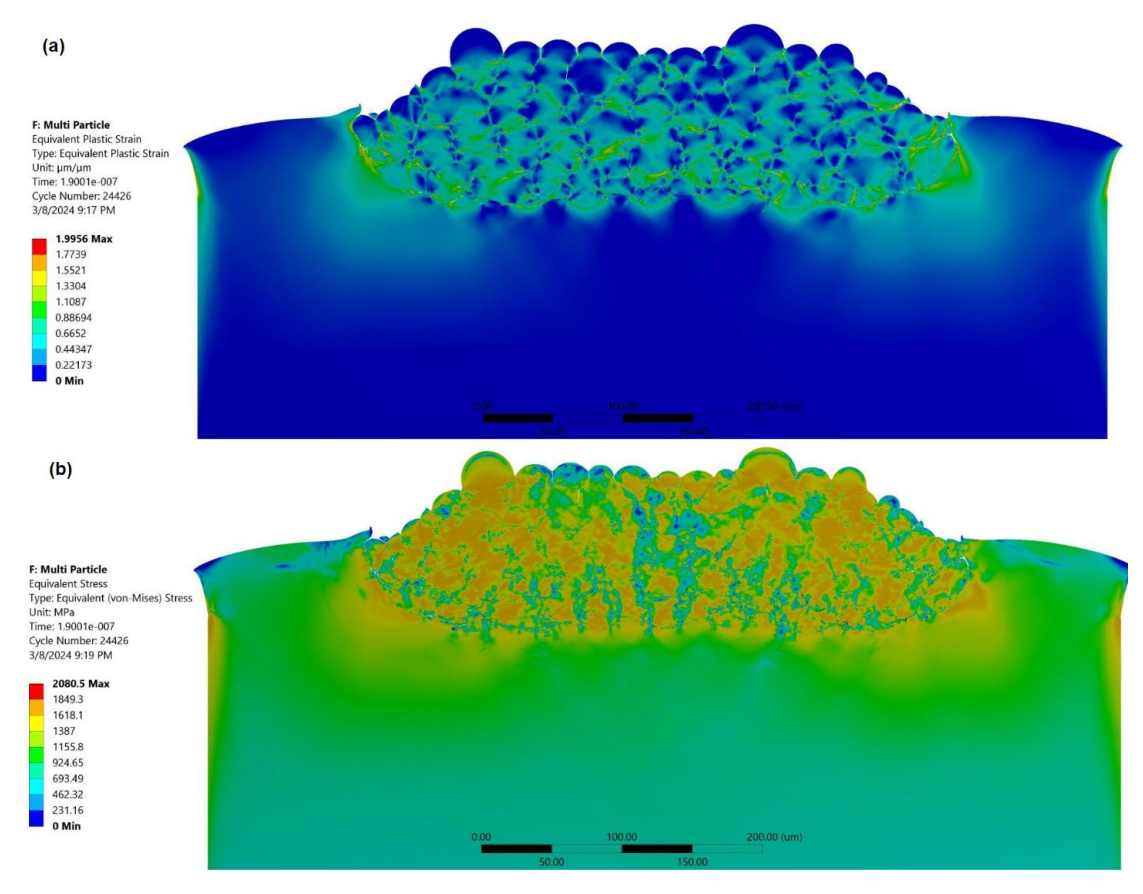
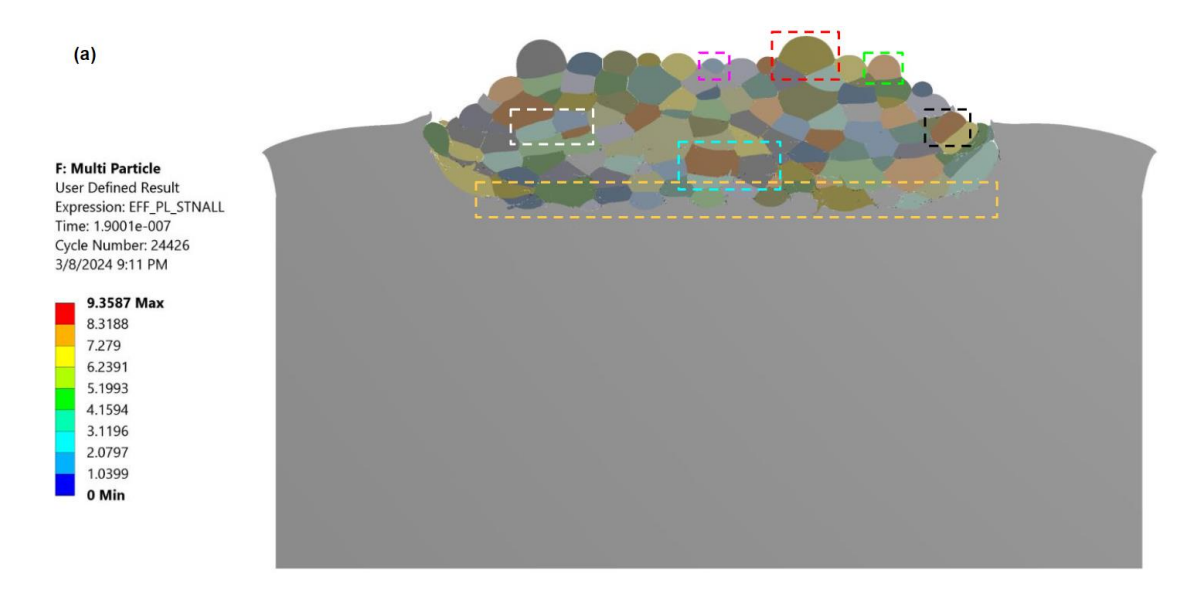


Figure 6.17 Simulated contours of (a) PEEQ and (b) von-Mises stresses for multi-particle impact simulation of IN 718 powder feedstock onto an SS 304 substrate with different diameters D_{10} (13.5 μ m); D_{50} (22 μ m); and D_{90} (33.5 μ m) in random distribution



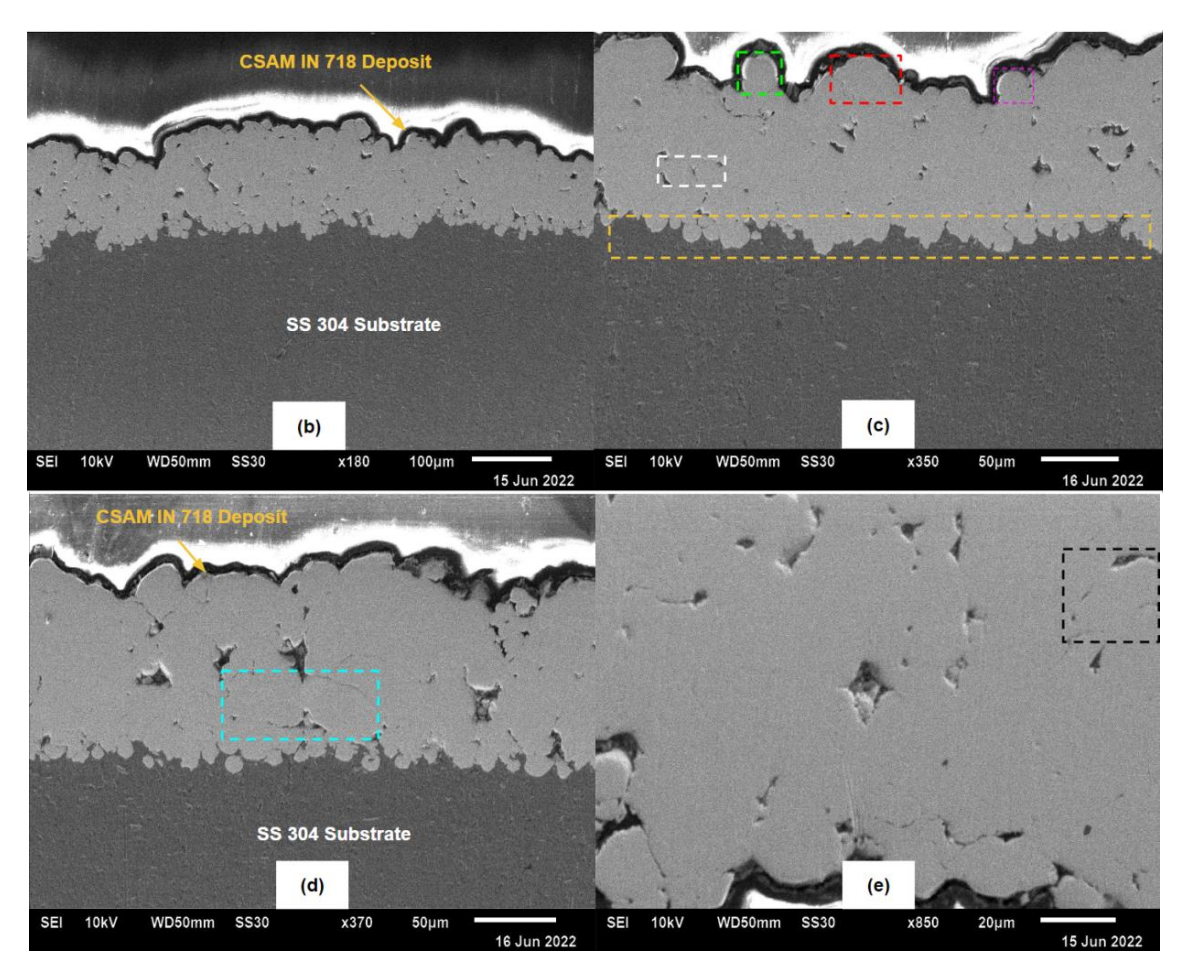


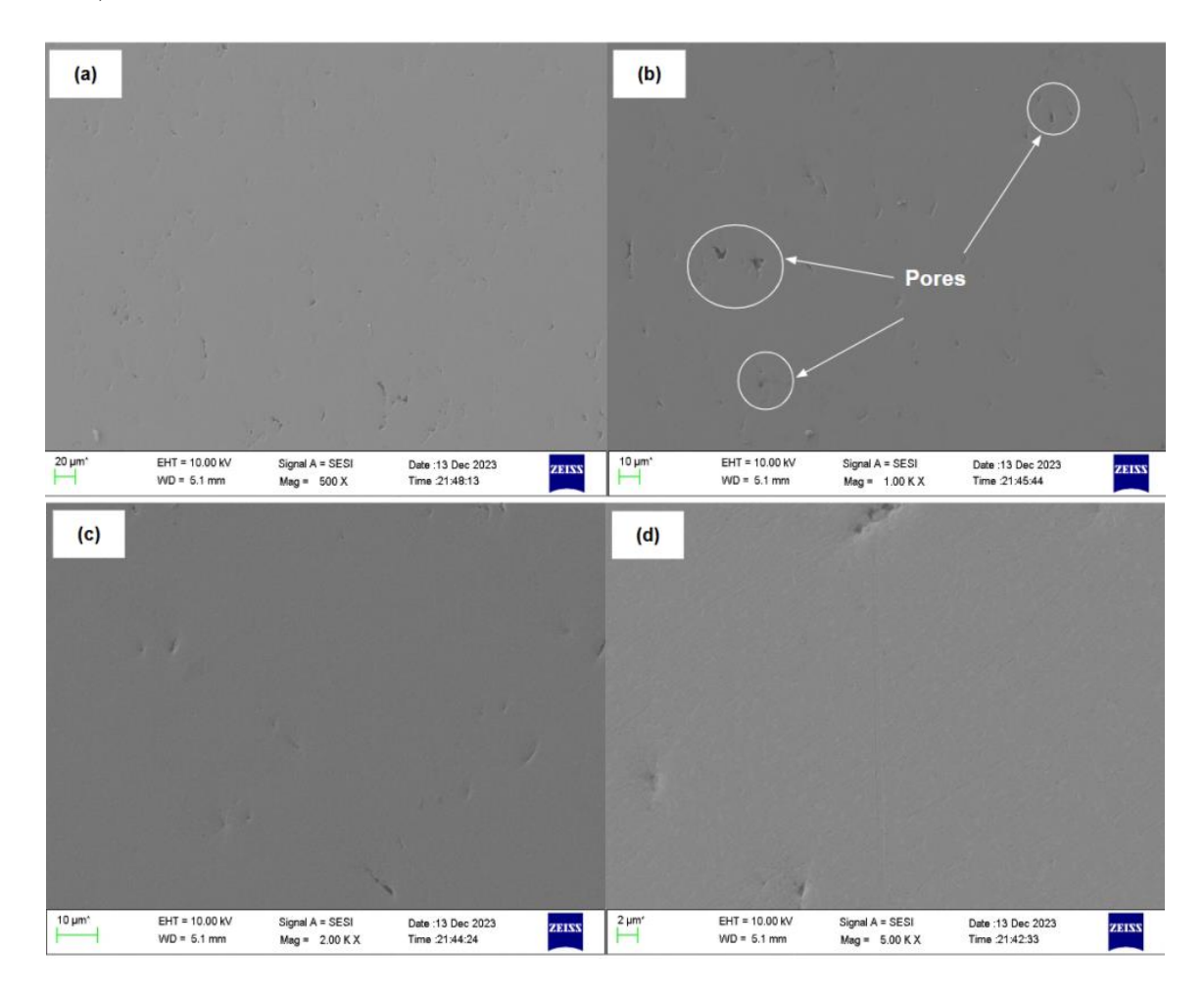
Figure 6.18 Five-pass coating cross SEM micrographs showing microstructure of IN 718 powder splats in (b); (c); (d); and (e) in comparison with simulation results given in (a) with similar plastic deformation in same colors during multi-particle impact onto an SS 304 substrate

6.2 CHARACTERIZATION OF CSAMed 3D STANDALONE IN 718 PIPE DEPOSITS

6.2.1 Results and Discussion

6.2.1.1 Microstructural Characterization

The SEM micrographs as presented in Figure 6.19 reveal a dense microstructure with minimal porosity, highlighting the effectiveness of the optimized cold spray process. This result is a direct outcome of carefully calibrated robot configurations and precise control of tilting turntable parameters, which together ensured a uniform and high-quality deposition. Upon closer examination at higher magnification, particularly in micrographs (e) and (f), the presence of δ phase particles became evident. These δ phase particles, which typically precipitate at grain boundaries, are associated with the high concentration of Nb in the alloy. During solidification, niobium tends to get segregated, leading to the formation of δ phase particles at the interfaces between grains, which could influence the mechanical properties of the material (Azadian *et al.* 2004).



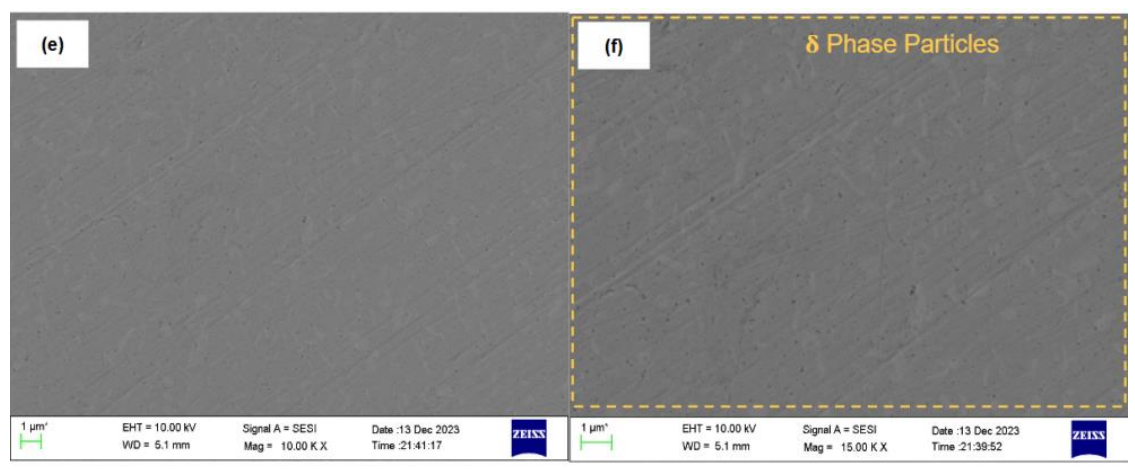


Figure 6.19 Cross SEM micrographs of CSAMed IN 718 thick pipe deposits (a) 500 X; (b) 1 KX; (c) 2 KX; (d) 5 KX; (e) 10 KX; and (f) 15 KX image showing δ phase particles

Furthermore, EDS mapping, as shown in Figure 6.20, confirms the presence of all major and minor alloying elements in the CSAMed IN 718 pipe deposits. Importantly, the analysis revealed no signs of oxide formation. The lack of oxides was a clear testament to the superior quality of the cold spray deposition process, ensuring that the material's properties remained intact.

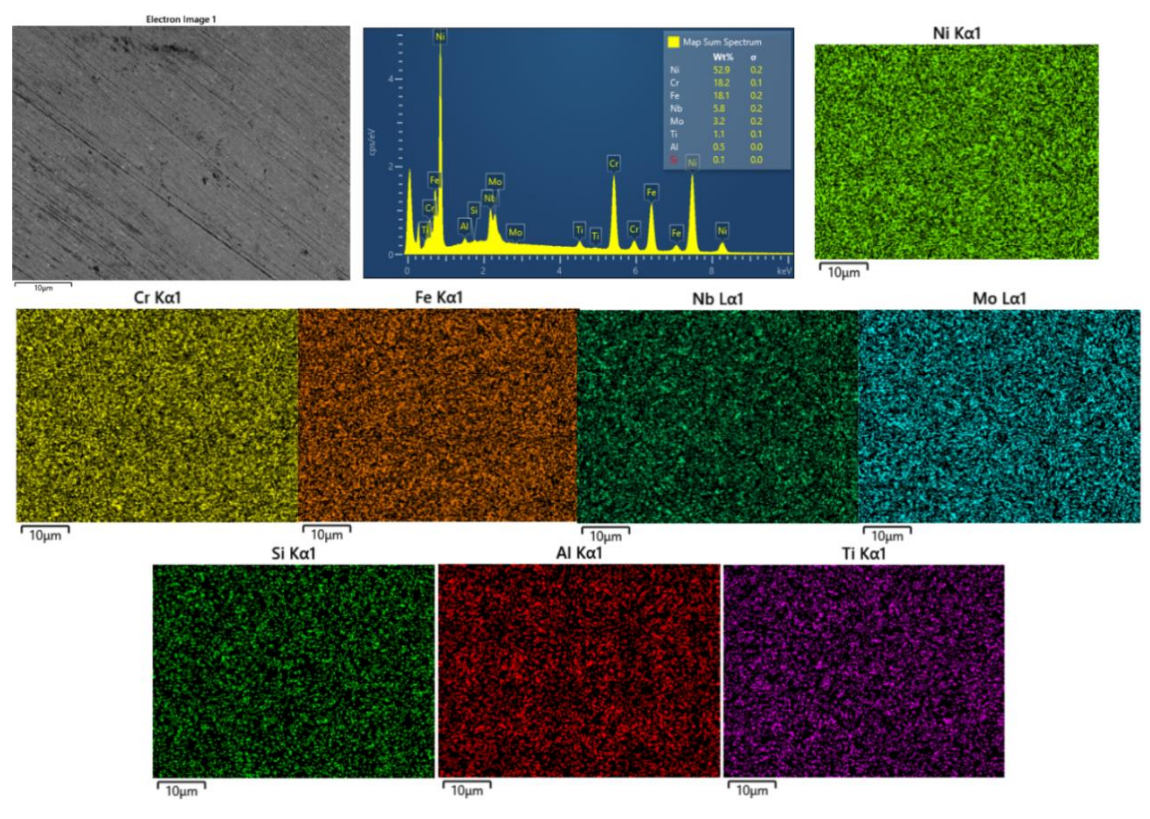


Figure 6.20 EDS mapping of CSAMed IN 718 thick pipe deposits

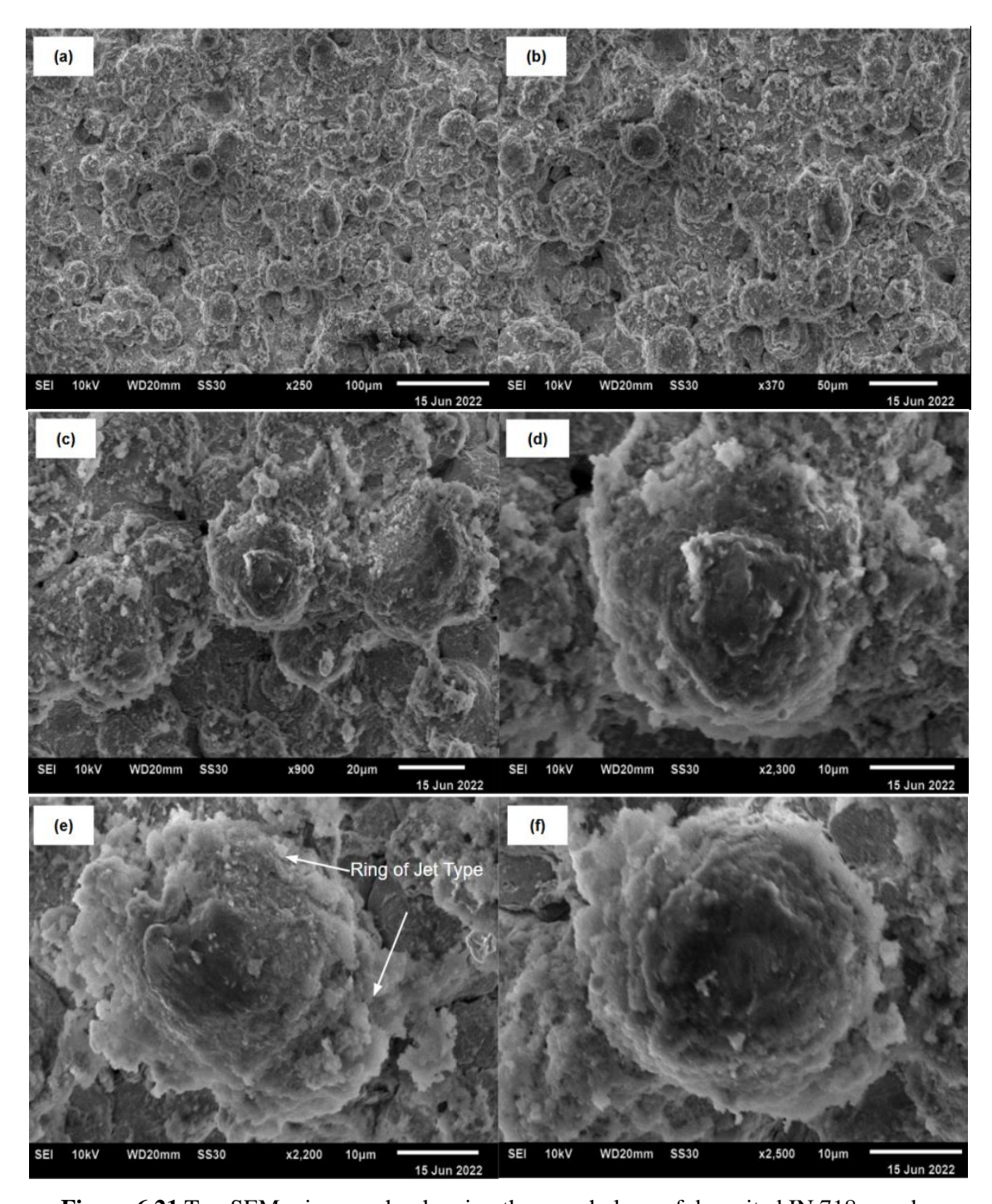


Figure 6.21 Top SEM micrographs showing the morphology of deposited IN 718 powder particles (a); (b); (c) lower magnification and (d); (e); (f) higher magnification showing ring of jet type morphology

The top SEM micrographs displayed in Figure 6.21 reveal the formation of rings with jet-type morphology around the impacted IN 718 powder particles. This observation suggested excellent cohesion with the already deposited IN 718 particles. This phenomenon could be elaborated by

considering adiabatic shear instability (ASI), a mechanical process that occurs during high strain rate deformation. ASI typically resulted in the formation of localized zones of intense deformation, leading to the creation of jet-like structures, or "rings," around the impacted particles. In the context of cold spray deposition, ASI occurs due to the high-velocity impact of powder particles onto the substrate or already deposited IN 718 powder particles, resulting in localized heating, plastic deformation, and material flow, ultimately contributing to the formation of the observed morphology (Wu *et al.* 2012; Liu *et al.* 2024).

Point EDS mapping of the CSAMed IN 718 thick pipe deposits was conducted to confirm whether the particles observed in the cross SEM micrographs are indeed δ phase. δ phase particles in IN 718 typically form during heat treatment processes as a result of δ phase precipitation. This precipitation is facilitated by the presence of certain alloying elements, particularly Nb (Liu *et al.* 1999). During solidification and subsequent heat treatment, niobium segregates to grain boundaries, initiating the nucleation and growth of δ phase particles. These particles tend to precipitate preferentially at grain boundaries due to the elevated Nb concentration in these regions as confirmed by the EDS composition of δ phase particles in Figure 6.22 respectively. The formation of δ phase particles in an adequate amount is critical in shaping the microstructure and mechanical properties of IN 718, influencing factors such as strength, ductility, and creep resistance (Ran *et al.* 2020).

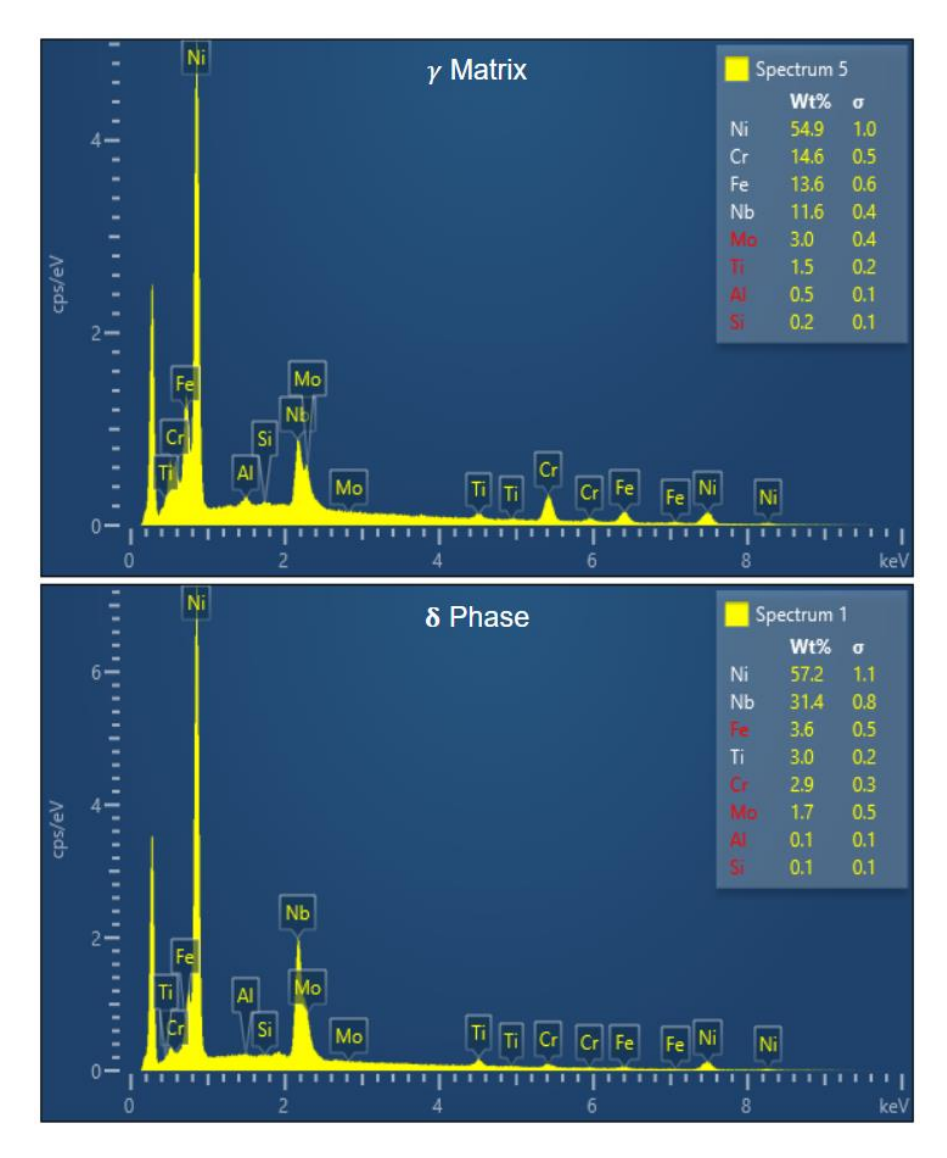


Figure 6.22 EDS spectra of γ matrix and δ phase in CSAMed IN 718 thick pipe deposits

Comparison of the point EDS data of the γ matrix and δ phase confirmed that the particles are indeed δ phase, discernible by their higher Nb concentration. These δ phase particles exhibited a plate-like and needle-like structure (Gan *et al.* 2020) as illustrated in Figure 6.23. The average length of δ phase precipitates is measured 625 nm, with a standard deviation of 265 nm. The average area of these precipitates is 0.092 μ m² having a standard deviation of 0.062 μ m².

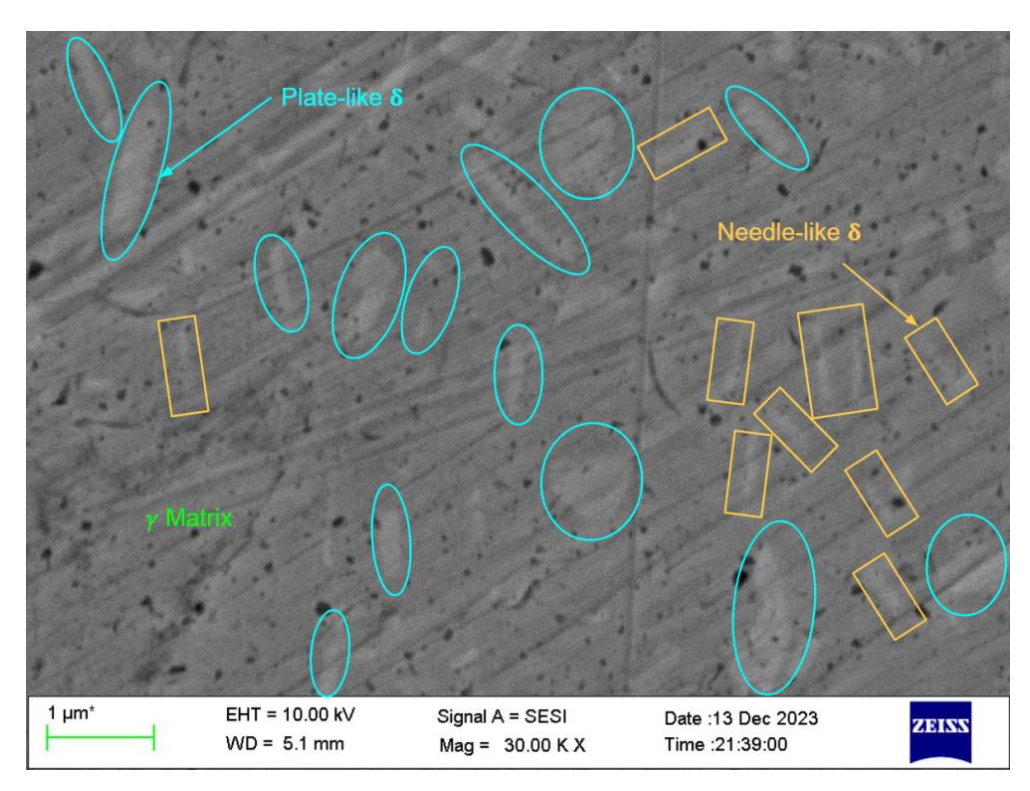


Figure 6.23 SEM micrograph depicting morphology of δ phase in CSAMed IN 718 thick pipe deposits

The XRD study, as depicted in Figure 6.24, corroborated the absence of oxides and provided additional support for the findings of the EDS analysis. The phases present in the CSAMed IN 718 thick pipe deposits align with those found in the powder feedstock, suggesting that no phase transformation occurs during the CSAM process. This distinct advantage of cold spray technology lies in its ability to facilitate solid-state deposition (with temperature much lower than the point of fusion) without inducing any phase transformations, a feature not commonly found in other conventional and additive manufacturing processes. Furthermore, the presence of the primary strengthening phase, identified as γ'' , with its tetragonal structure, significantly augments mechanical properties. Additionally, the detection of the δ phase, characterized by its orthorhombic structure and discernible peak, strongly indicates a beneficial impact on material performance (Slama and Abdellaoui 2000). The XRD analysis confirms that the as-received IN 718 powder feedstock has undergone heat treatment with aging, rather than solution annealing alone, as indicated by the presence of gamma double prime (γ'') and delta (δ) precipitates. Solution annealing is intended to dissolve these strengthening phases into a single γ -phase matrix, while the subsequent aging process promotes controlled precipitation of γ'' and δ phases, which are essential for enhancing the mechanical strength of IN 718 through precipitation hardening.

SEM morphological studies and EDS analysis provided further confirmation of the δ phase precipitates.

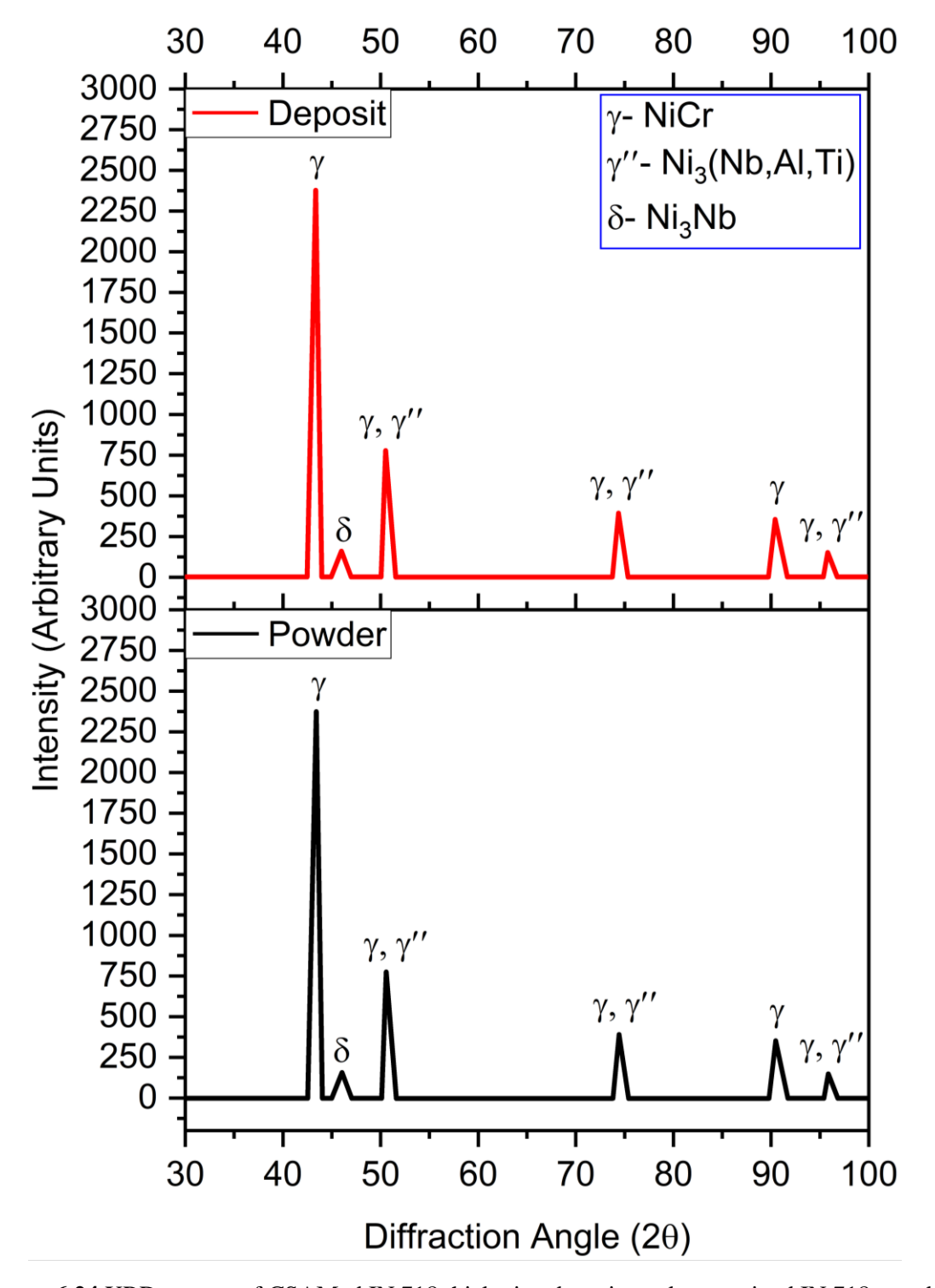


Figure 6.24 XRD spectra of CSAMed IN 718 thick pipe deposits and as-received IN 718 powder feedstock

The CSAMed IN 718 thick pipe deposits exhibited a density of 7.98 g/cc, as measured by the Archimedes method. In contrast, the density of pure bulk IN 718 produced via specialized casting techniques was found to be 8.19 g/cc (Kurdi *et al.* 2023) using the same method, as illustrated in Figure 6.25. Remarkably, the CSAMed IN 718 thick pipe deposits exhibited minimal surface porosity, with a value of just 0.23 %, underscoring the deposit's exceptional quality and structural integrity.

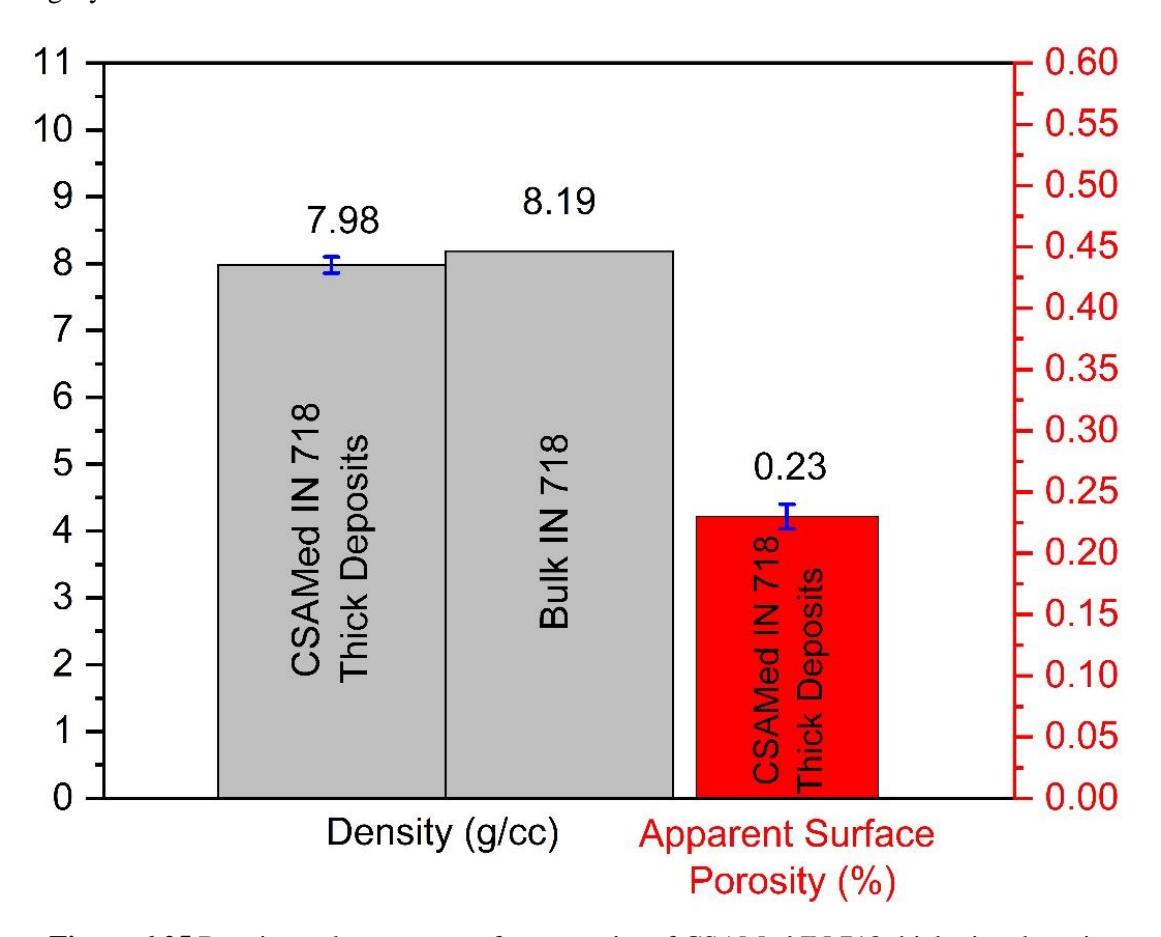
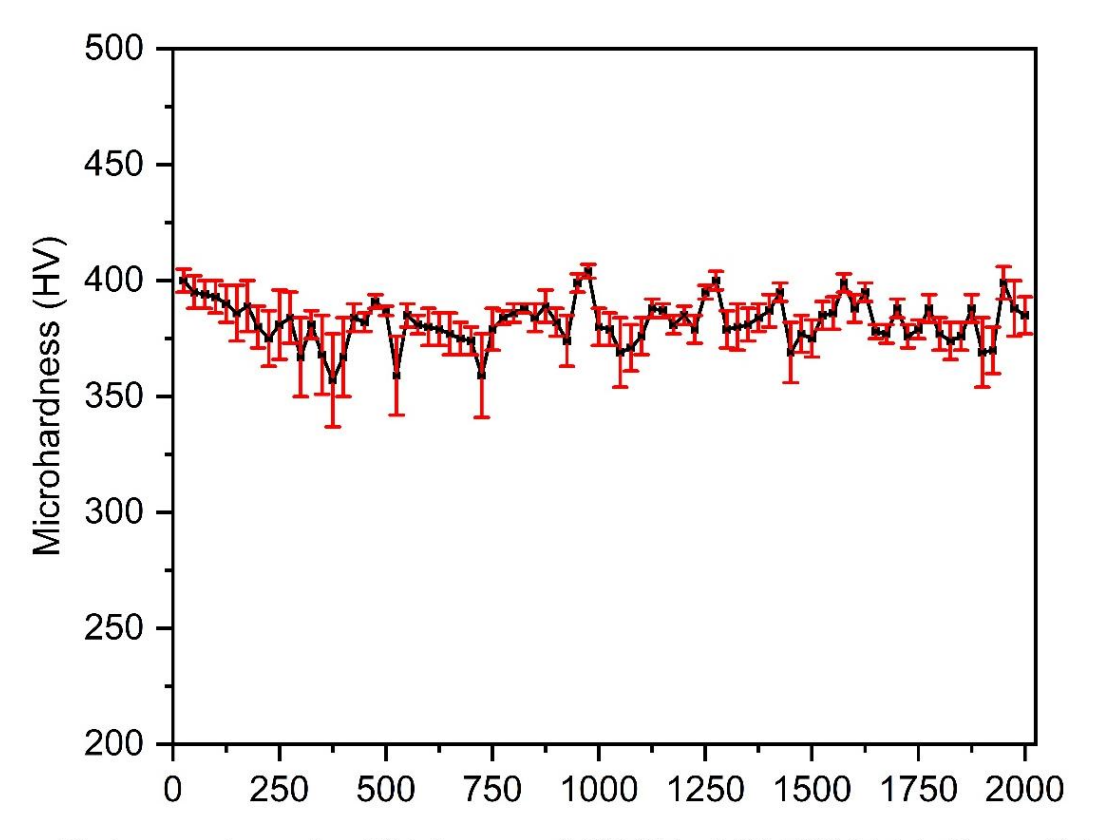


Figure 6.25 Density and apparent surface porosity of CSAMed IN 718 thick pipe deposits

6.2.1.2 Mechanical Properties Evaluation

The CSAMed IN 718 thick pipe deposits had an average microhardness of 390 HV, which is almost identical to the microhardness of bulk IN 718, measured at 388 HV (Hasani *et al.* 2021) as shown in Figure 6.26 respectively. This similarity was achieved by carefully adjusting the cold spray process, robot traverse, and tilting turntable parameters. These adjustments ensured that the average temperature of the IN 718 powder particles at the point of deposition (SoD) is 673 K. At this temperature, thermal softening plays a bigger role than work hardening, resulting in similar microhardness values for both CSAMed IN 718 thick pipe deposits and bulk IN 718.



Distance along the Thickness of CSAMed IN 718 Thick Deposit (μm)

Figure 6.26 Microhardness plot of CSAMed IN 718 thick pipe deposits

This indicates that the CSAM process effectively maintained the material's hardness, which is crucial for preserving its mechanical properties. It is worth noting that the microhardness remained consistently uniform throughout the thickness of CSAMed IN 718 thick pipe deposits, with only minor variations.

Micro-tensile plot showing engineering stress versus engineering strain is shown in Figure 6.27. A total of 3 micro-tensile samples were tested to ensure the repeatability of the results. The micro-UTS of the CSAMed IN 718 deposits was found to be 1124 MPa, which is comparable to the UTS of bulk IN 718, typically reported as 1375 MPa. However, the percentage elongation of the CSAMed IN 718 deposits was measured at 7.2 %, which is significantly lower compared to the 25 % elongation observed for bulk IN 718, indicating reduced ductility in the deposits. It is pertinent to mention that the micro-tensile results of CSAMed IN 718 deposits were compared with macro-tensile results of bulk IN 718 as available in the literature. The lower percentage elongation in micro-tensile tests is primarily due to size effects, sensitivity to defects, and strain distribution limitations, which exacerbate premature failure compared to macro-scale tensile tests. The micro-yield strength of the deposits was determined to be 1054 MPa, which is close to the

1100 MPa yield strength of bulk IN 718 (www.specialmetals.com). However, the Young's modulus of the CSAMed IN 718 deposits was found to be 38.5 GPa, significantly lower than the 200 GPa reported for bulk IN 718, suggesting some degree of reduced stiffness in the material (www.hightempmetals.com). The reduced Young's modulus of CSAMed IN 718 deposits, despite comparable yield strength and UTS to bulk IN 718, arises from many factors. Residual porosity and weak inter-splat boundaries in the deposits, if any might disrupt stress transfer during elastic deformation, lowering stiffness. Microstructural anisotropy and heterogeneity, including grain size variation and compressive residual stresses, might reduce uniform stress distribution. Additionally, the absence of thermal treatments like second solution annealing and aging, which optimize grain structure in IN 718, contributes to the lower modulus. Fractographic analysis as seen in Figure 6.28, revealed the presence of weak inter-splat boundaries within the deposits. These weak interfaces contributed to a brittle fracture mechanism, as evidenced by the fractographic features.

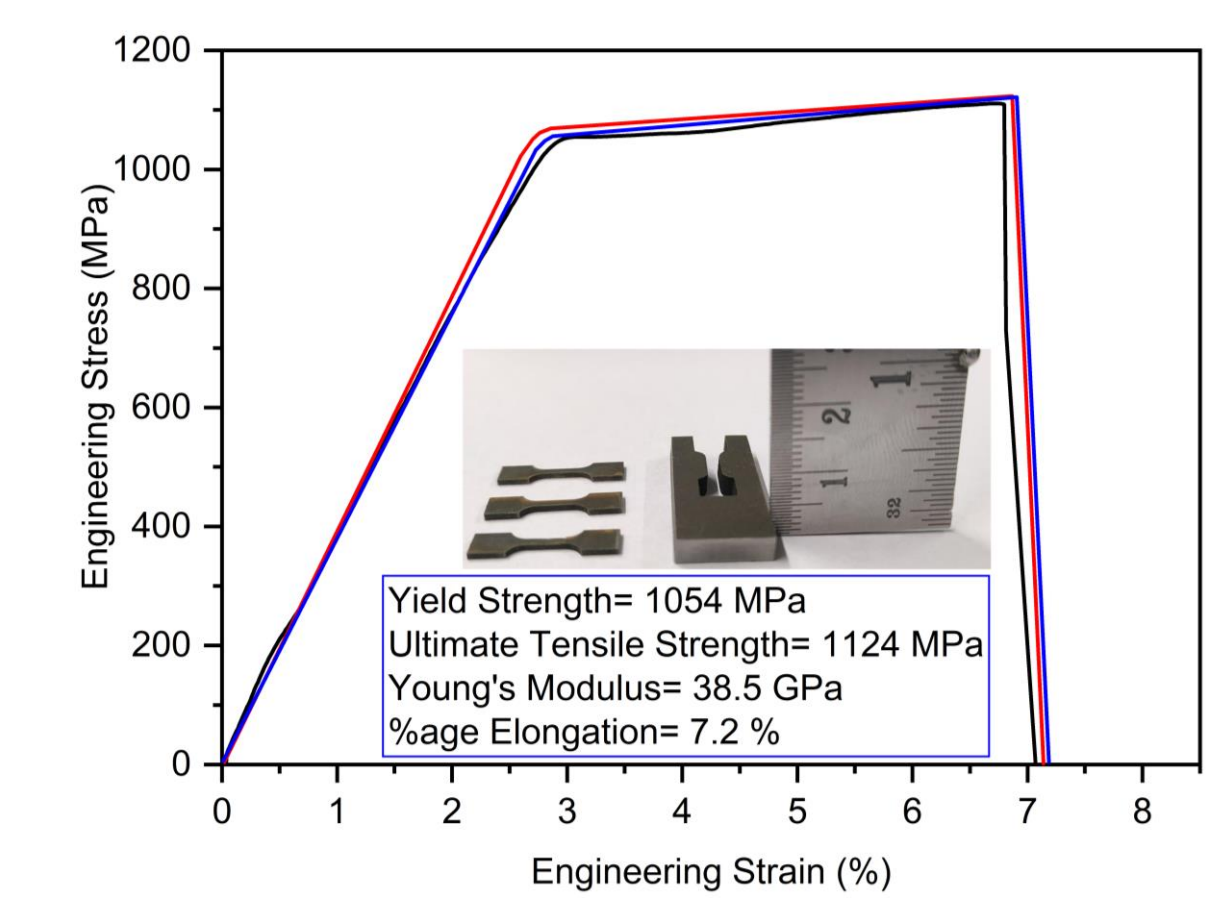


Figure 6.27 Micro-tensile plot showing engineering stress versus engineering strain along with the in-situ SEM micrographs at various crack stages of the CSAMed IN 718 deposits

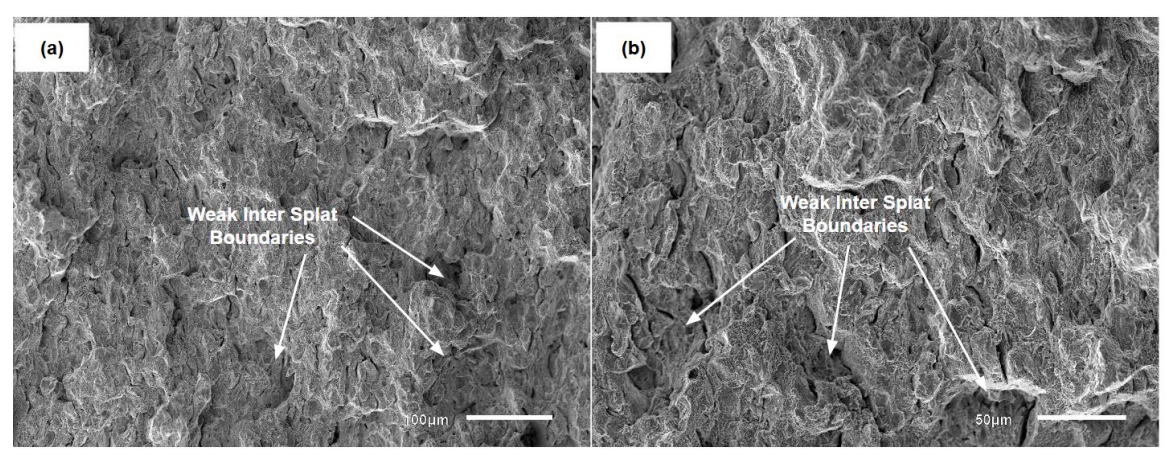


Figure 6.28 Fractography analysis of the CSAMed IN 718 deposits after micro-tensile test at (a) lower and (b) higher magnification

CHAPTER 7

CONCLUSIONS

This work investigates the CSAM of IN 718 superalloy. Cold spraying was first employed to demonstrate the fabrication of thick plates from challenging materials like pure titanium and Ni-20Cr alloys. A thorough characterization of the fabricated plates was conducted to assess the impact of pre- and post-heat treatment procedures. Subsequently, IN 718 superalloy was selected for the development of thick pipe deposits through CSAM. To optimize the cold spray process parameters for effective deposition of IN 718, a two-level full factorial analysis was performed, focusing on the velocity ratio (VR). Additionally, computational modeling using the k-ω SST (shear stress transport) turbulence model was done to investigate the effects of various powder injection angles on the nitrogen gas flow field dynamics and the particle trajectory analyses of IN 718 powder during deposition. A discrete phase CFD analysis was also conducted with an SS 304 substrate pipe to study how the positioning of the substrate pipe influenced the nitrogen gas flow and IN 718 powder particles. Further analysis determined the average particle impact temperature and velocity at the specified standoff distance, enabling explicit impact simulations for both single- and multi-particle. Experimental validation confirmed the accuracy of the CFD and impact simulations. Following this, thick pipe deposits of IN 718 were successfully fabricated using optimized cold spray process parameters, precise robot configurations, and finely tuned tilting turntable settings. Finally, preliminary microstructural and mechanical characterization of the IN 718 thick pipe deposits was carried out which confirmed the effectiveness of the cold spray process. The deposits demonstrated high material efficiency with minimal waste, maintaining the desired microstructure without unwanted phase transformations. Additionally, the developed 3D standalone IN 718 thick pipe deposits exhibited strong mechanical integrity, indicating a robust and cohesive structure. These results suggest that the cold spray method was successful in producing high-quality, industrial-grade IN 718 deposits, meeting key criteria for structural stability and performance. This validates cold spray as a promising technique for the efficient and reliable fabrication of IN 718 components. This chapter summarizes the key findings of the study, with relevant descriptions of the results provided for clarity and completeness.

7.1 CONCLUSIONS

7.1.1 Proof-of-Concept

The cold spray developed thick plates of pure Ti and Ni-20Cr with different pre- and post-heat treatments were examined using various characterization techniques to understand the effects of employing different heat treatment procedures. Some important conclusions from this work module are listed below:

- CSAM was successfully used to develop thick Ti deposits having 16 mm thickness via the solid-state deposition of Ti-powder feedstock. Due to the low density and HCP crystal lattice structure of Ti, densification was performed on as-sprayed deposits through hot isostatic pressing (HIP). Macro-tensile testing was performed on HIP-treated Ti deposits, showing a UTS (ultimate tensile strength) of 384 MPa, with a total elongation of 6 % (comparable UTS to that of bulk Ti). HIP treatment led to lesser porosity and higher UTS. The micro-tensile test revealed brittle fractures, having some localized dimples with the nucleation of cracks initiating from pores and traveling through pores, splat, and grain boundaries. The formation of hard-phase α-titanium (HCP) was augmented via the presence of transition elements in the IN 718 substrate by lowering the β - α phase transition temperature during HIP treatment. This not only increased the hardness at the deposit-substrate interface but also helped in removing the thick standalone deposits from the substrate. It can be concluded that the application of HIP treatment after cold spraying is helpful in fabricating industry-relevant standalone components, which have a requirement for a hardened surface with a softer core. Furthermore, the formation of a hard, protective oxide scale of titanium dioxide (rutile crystal structure) on the developed HIP-treated Ti deposits helped in achieving very good hightemperature oxidation resistance. Therefore, the developed approach could be used to additively manufacture Ti standalone components for high-temperature applications such as nuclear, automobile, and aerospace.
- The CSAM process was successfully employed to fabricate plates of Ni-20Cr with thicknesses ranging from 6 to 10 mm, achieving properties comparable to those of bulk Ni-20Cr alloy. The study demonstrated the feasibility of utilizing the CSAM process to create standalone Ni-20Cr products, contingent upon the ability to manipulate the cold spray gun using a robotic arm that could follow the precise paths required for the deposition of such geometries. Given the advancements in robotic manipulators, this was shown to be a practical and achievable method with current technology. The research further identified two key

interventions to enhance the properties of the deposited material: substrate heating (SH) pretreatment and hot isostatic pressing (HIP) post-treatment. Both treatments were found to improve distinct aspects of the deposits. Substrate heating was particularly effective in enhancing tensile strength, making it an ideal supplement for applications requiring higher strength. On the other hand, hot isostatic pressing was observed to increase ductility while reducing porosity, making it a valuable post-treatment option for applications where flexibility and minimal porosity were more critical. The appropriate treatment could be selected based on the specific requirements of the intended application. Overall, this study confirmed that products fabricated through CSAM have the potential to serve as viable replacements for their counterparts produced by conventional manufacturing processes. This underscores the versatility and effectiveness of the CSAM process in generating high-quality components with tailored properties, depending on the desired application and treatment method.

7.1.2 Parametric Analysis of Cold Spray Process

In this, first a full factorial two-level approach was used to optimize the cold spray process parameters for effective cold spray deposition of IN 718 on the basis of *VR*. The study explored the cold spray process parameters at both high and low levels, focusing on identifying critical parameters. Adjusting process parameters so as to achieve high particle impact velocities and temperatures is crucial for forming well-bonded interfaces between particles and particle-substrate. Subsequently, the optimized set of process parameters were chosen to examine the effect of powder injection angle on the gas flow dynamics and particle trajectories. Some important conclusions are given below:

The study identified key cold spray process parameters influencing the *VR* during the cold spray deposition of IN 718, including particle diameter (PD), main gas pressure (MGP), main gas temperature (MGT), pressure difference (DeltaP), and standoff distance (SoD). While SoD exhibited a minimal positive effect on *VR*, it was found to influence the spray footprint diameter and deposition accuracy. A lower SoD of 25 mm ensured a narrow and well-defined footprint, enhancing accuracy. Powder feed rate (PFR) was determined to be statistically non-significant in affecting *VR*. However, higher PFR values in multi-pass deposition led to Gaussian-shaped cross-sections with sloped sides, compromising deposition quality. Experimentally, a PFR of 30 g/min was found to produce a smoother and flatter deposition surface, supporting its selection as an optimized parameter. Statistical

analysis revealed significant interaction effects between parameters such as MGP-DeltaP, MGP-MGT, MGP-PD, DeltaP-MGT, DeltaP-PD, and MGT-PD, emphasizing the interdependencies of gas pressures, temperatures, and particle characteristics. *VR* values for particle size distributions (D₁₀, D₅₀, and D₉₀) remained within the acceptable range of 1.1 to 2, indicating effective calibration of process parameters. The response optimization determined that an MGP of 50 bar, DeltaP of 1 bar, MGT of 1273.15 K, SoD of 25 mm, and PFR of 30 g/min provided the most effective deposition conditions for IN 718 powder feedstock, ensuring consistent performance across various particle size distributions.

The study revealed the influence of powder injection angles (90 deg, 0 deg, and 30 deg) on the cold spray process, highlighting the complex underexpanded flow structures characterized by Mach diamonds and shock waves. Within each Mach diamond, flow properties oscillated, with a decrease in pressure and temperature and an increase in Mach number through expansion waves, followed by the opposite changes through shock waves. These oscillations diminished further downstream as the flow stabilized with the ambient pressure due to viscous damping. The 30 deg and 90 deg injection angles demonstrated higher turbulent kinetic energy (TKE) compared to the 0 deg angle, which significantly enhanced particle mixing with the process gas. Elevated TKE improved particle distribution within the spray plume, preventing clumping and ensuring uniform coating formation. The turbulent gas flow transferred more energy to the particles, resulting in higher impact velocities and significant plastic deformation, thereby improving particle adherence and forming a denser, more cohesive coating. The 30 deg injection angle outperformed the others, exhibiting the highest gas temperature (1030 K) and velocity (840 m/s) at the nozzle exit. Better mixing of carrier and main gases contributed to a uniform temperature profile. Additionally, the 30 deg angle achieved the most focused particle stream, leading to superior deposition accuracy. In contrast, the 90 deg angle caused more dispersed particle streams due to centrifugal forces, and the 0 deg angle suffered from lower TKE and thicker boundary layers, resulting in less concentrated particle distribution. Elevated gas velocities in the 30 deg and 90 deg cases on account of increased drag forces, enhancing particle impact velocities and heat transfer from the gas to the particles. This resulted in particle heating, thermal softening, and improved deformation upon impact, enabling continuous and uniform coating formation. The 30 deg injection angle emerged as the optimal configuration, providing the best combination of particle concentration, uniformity, and deposition quality. Improved mechanical interlocking and metallurgical bonding at higher impact velocities lead

to enhanced coating performance. Moreover, increased TKE enabled faster deposition rates, reducing particle exposure to the environment and enhancing overall process efficiency.

7.1.3 Simulation and Characterization of IN 718 Pipe

First, a discrete phase computational fluid dynamics study was conducted using the optimized cold spray process parameters, followed by an impact deformation analysis (both single- and multi-particle) of IN 718 powder feedstock deposition onto an SS 304 substrate pipe. This was accompanied by experimental validation. Subsequently, the preliminary microstructural and mechanical characterization of the developed 3D standalone IN 718 thick pipe deposits was performed. The key conclusions from the study are summarized as follows:

The first study investigated the impact of flow perturbations, caused by a cylindrical SS 304 substrate pipe, on the cold spray deposition of IN 718 powder feedstock. The presence of the substrate induced a bow shock effect, increasing nitrogen gas pressure and causing localized density variations. This phenomenon when happening with large effect leads to a highpressure zone near the substrate, which slows down the particles and causes deviations from their intended trajectories, potentially resulting in poor adhesion/cohesion and reduced deposition efficiency. A standoff distance of 25 mm from the nozzle exit was identified as optimal, minimizing peak pressure (3.4 bar) and particle deviation. The powder particle tracks were narrow and well-defined, resulting in a highly concentrated cold spray footprint with a diameter of approximately 5 mm which results in increasing the deposition accuracies and quality of the final product. The Mach number dropped significantly from 3.8 to 0.2 due to the dissipative nature of the bow shock, and the gas temperature initially decreased from 1040 K and then increased to 960 K, while particle temperatures dropped from 781 K to 673 K. Despite a sharp decline in nitrogen gas velocity from 1184 m/s to 124 m/s, the highdensity IN 718 particles maintained relatively high velocities, reaching 825 m/s at SoD. The powder particles of sizes corresponding to D_{10} (13.5 μ m), D_{50} (22 μ m), and D_{90} (33.5 μ m) exhibited characteristic jetting formation, indicating that their impact velocities and temperature at SoD were sufficient to trigger adiabatic shear instability. The depth of penetration was largely influenced by particle size and impact velocity. Among these, D₁₀ particles showed greater penetration depth compared to larger particles. However, particles smaller than the critical diameter (12.5 µm in this case) were unable to induce adiabatic shear instability, which is essential for effective bonding. These smaller particles, instead of plastically deforming, penetrated and became embedded within the substrate. Sub-critical

particles, due to their higher surface area-to-volume ratios, generated insufficient temperature upon impact, and their high shear strength further contributed to their deeper penetration without effective deformation. Conversely, particles larger than the critical diameter retained sufficient energy to undergo plastic deformation, initiating significant jetting upon impact. This behavior was attributed to their slower thermal diffusion, allowing them to retain the energy necessary for adiabatic shear instability. Single-pass coating microstructure analysis validated these findings by identifying jetting formation in particles larger than the critical diameter and observing the penetration effects of particles smaller than this threshold. Multi-pass coating microstructures revealed phenomena such as tamping, interlocking, and extrusion, which collectively ensured strong adhesion to the substrate while enhancing mechanical properties. A comparison of multi-particle impact simulation results with a five-pass coating microstructure showed a strong correlation. Specific regions in both the simulation and coating microstructure exhibited similar deformation patterns, confirming the consistency between simulated predictions and experimental observations.

Subsequently, the CSAM process was successful in producing dense IN 718 thick pipe deposits with minimal porosity (0.23 %) and a uniform microhardness of 390 HV, closely matching the bulk IN 718 (388 HV). The dense microstructure, as revealed by cross SEM micrographs and rings of jet-type morphology around all deposited IN 718 particles from top SEM analysis, resulted from optimized cold spray process parameters, precise calibration of robot configurations and tilting turntable settings, ensuring uniform deposition. SEM analysis identified δ phase precipitates with plate- and needle-like morphology, with an average length of 625 nm and a standard deviation of 265 nm, forming at grain boundaries due to Nb segregation. These findings were confirmed by EDS and XRD, which also demonstrated the absence of oxides and the retention of phase consistency between the powder feedstock and CSAMed deposits. The presence of both the primary strengthening phase (γ') and δ phase contributed significantly to the mechanical properties of the deposits. The CSAMed IN 718 thick pipe deposits exhibited a density of 7.98 g/cc, slightly lower than the bulk IN 718 density of 8.19 g/cc. The micro-UTS and micro-yield strength of the CSAMed IN 718 deposits were found to be 1124 MPa and 1054 MPa which was comparable to the bulk IN 718 (macro-tensile results) while reduced percentage elongation and lower Young's modulus were due to size effects and some weak inter-splat boundaries. Preliminary microstructural and mechanical characterization strongly supports the potential of the CSAM process to replace traditional methods for IN 718 pipe fabrication as a sustainable alternative.

- In-depth characterizations of the 3D standalone IN 718 thick pipe deposits could be conducted to examine the nanoscale precipitates and matrix, focusing on their composition and chemical identification.
- Various techniques, such as laser re-melting and vacuum heat treatment, could be
 employed for post-treatment of the thick pipe deposits. The resulting changes in
 microstructure and their impact on mechanical and tribological properties would be
 particularly noteworthy.
- A comparison of in-situ and ex-situ oxidation of cold spray additively manufactured IN
 718 deposits could be conducted to investigate microstructural changes before and after
 heating. Additionally, a sequence for the formation of potential oxides at various
 temperatures could be proposed.
- Alternative coating techniques could also be explored and investigated for the additive manufacturing of the IN 718 superalloy.
- More complex geometries could be attempted and studied using cold spray based additive manufacturing of the IN 718 superalloy.
- Automation of process control would improve consistency, while enhanced quality assurance methods, such as in-situ monitoring and advanced inspection techniques, could ensure component integrity. Post-processing steps, including heat treatment and surface finishing, would need to be adapted for larger components. Additionally, improving material efficiency and managing costs would be crucial for industrial viability. Prototyping and rigorous testing would be necessary to validate performance for industrial applications.

- 1. Hall, A. C., Cook, D. J., Neiser, R. A., Roemer, T. J., & Hirschfeld, D. A. (2006). The effect of a simple annealing heat treatment on the mechanical properties of cold-sprayed aluminum. *Journal of Thermal Spray Technology*, *15*, 233-238.
- 2. Abe, F., Osakada, K., Shiomi, M., Uematsu, K., & Matsumoto, M. (2001). The manufacturing of hard tools from metallic powders by selective laser melting. *Journal of materials processing technology*, 111(1-3), 210-213.
- 3. Adaan-Nyiak, M. A., & Tiamiyu, A. A. (2023). Recent advances on bonding mechanism in cold spray process: A review of single-particle impact methods. *Journal of Materials Research*, 38(1), 69-95.
- 4. Adanta, D., Fattah, I. R., & Muhammad, N. M. (2020). Comparison of standard k-epsilon and sst k-omega turbulence model for breastshot waterwheel simulation. *Journal of Mechanical Science and Engineering*.
- 5. Additive, G. E. (2018). New manufacturing milestone: 30,000 additive fuel nozzles. *General Electric, Detroit*.
- 6. Agarwala, M., Bourell, D., Beaman, J., Marcus, H., & Barlow, J. (1995). Direct selective laser sintering of metals. *Rapid Prototyping Journal*, *1*(1), 26-36.
- 7. Akisin, C. J., Bennett, C. J., Venturi, F., Assadi, H., & Hussain, T. (2022). Numerical and experimental analysis of the deformation behavior of CoCrFeNiMn high entropy alloy particles onto various substrates during cold spraying. *Journal of Thermal Spray Technology*, 31(4), 1085-1111.
- 8. Alagha, A. N., Hussain, S., & Zaki, W. (2021). Additive manufacturing of shape memory alloys: A review with emphasis on powder bed systems. *Materials & Design*, 204, 109654.
- 9. Alkhimov, A. P., Kosarev, V. F., & Klinkov, S. V. (2001). The features of cold spray nozzle design. *Journal of thermal spray technology*, *10*, 375-381.
- 10. Alkhimov, A. P., Papyrin, A. N., Kosarev, V. F., Nesterovich, N. I., & Shushpanov, M. M. (1994). *U.S. Patent No.* 5,302,414. Washington, DC: U.S. Patent and Trademark Office.
- 11. Alojaly, H. M., Hammouda, A., & Benyounis, K. Y. (2023). Review of recent developments on metal matrix composites with particulate reinforcement.
- 12. Amato, K. N., Gaytan, S. M., Murr, L. E., Martinez, E., Shindo, P. W., Hernandez, J., ... & Medina, F. J. A. M. (2012). Microstructures and mechanical behavior of Inconel 718 fabricated by selective laser melting. *Acta Materialia*, 60(5), 2229-2239.

- 13. Amon, C., Beuth, J., Kirchner, H., Merz, R., Prinz, F., Schmaltz, K., & Weiss, L. (1993). Material issues in layered forming.
- 14. Amsterdam, E., & Kool, G. A. (2009, May). High cycle fatigue of laser beam deposited Ti-6Al-4V and Inconel 718. In *ICAF 2009, Bridging the Gap between Theory and Operational Practice: Proceedings of the 25th Symposium of the International Committee on Aeronautical Fatigue, Rotterdam, The Netherlands, 27–29 May 2009* (pp. 1261-1274). Dordrecht: Springer Netherlands.
- 15. Ang, A. S. M., & Berndt, C. C. (2014). A review of testing methods for thermal spray coatings. *International Materials Reviews*, *59*(4), 179-223.
- 16. Ang, A. S. M., Sanpo, N., Sesso, M. L., Kim, S. Y., & Berndt, C. C. (2013). Thermal spray maps: Material genomics of processing technologies. *Journal of thermal spray technology*, 22, 1170-1183.
- 17. Angrish, A. (2014, March). A critical analysis of additive manufacturing technologies for aerospace applications. In *2014 IEEE Aerospace Conference* (pp. 1-6). IEEE.
- 18. Anish Mathews, P., Bhardwaj, S., Gadhe, P., & R Dameracharla, S. (2016). Patent trends of detonation spray coating technology. *Recent Patents on Mechanical Engineering*, *9*(1), 9-19.
- 19. Annasamy, M., Haghdadi, N., Taylor, A., Hodgson, P., & Fabijanic, D. (2019). Static recrystallization and grain growth behaviour of AlO. 3CoCrFeNi high entropy alloy. *Materials Science and Engineering: A*, 754, 282-294.
- 20. Anthony, S., & Antony, J. (2016). Academic leadership and Lean Six Sigma: A novel approach to systematic literature review using design of experiments. *International Journal of Quality & Reliability Management*, 33(7), 1002-1018.
- 21. Anusha, K., Routara, B. C., & Guha, S. (2023). A Review on High-Velocity Oxy-Fuel (HVOF) Coating Technique. *Journal of The Institution of Engineers (India): Series D*, 104(2), 831-848.
- 22. Anzalone, G. C., Zhang, C., Wijnen, B., Sanders, P. G., & Pearce, J. M. (2013). A low-cost open-source metal 3-D printer. *IEEE Access*, *1*, 803-810.
- 23. Arenas, L. T., Lima, E. C., dos Santos Jr, A. A., Vaghetti, J. C., Costa, T. M., & Benvenutti, E. V. (2007). Use of statistical design of experiments to evaluate the sorption capacity of 1, 4-diazoniabicycle [2.2. 2] octane/silica chloride for Cr (VI) adsorption. *Colloids and Surfaces A: Physicochemical and Engineering Aspects*, 297(1-3), 240-248.
- 24. Ashokkumar, M., Thirumalaikumarasamy, D., Sonar, T., Deepak, S., Vignesh, P., & Anbarasu, M. (2022). An overview of cold spray coating in additive manufacturing, component

- repairing and other engineering applications. *Journal of the Mechanical Behavior of Materials*, 31(1), 514-534.
- 25. Assadi, H., Gärtner, F., Stoltenhoff, T., & Kreye, H. (2003). Bonding mechanism in cold gas spraying. *Acta materialia*, *51*(15), 4379-4394.
- 26. Assadi, H., Kreye, H., Gärtner, F., & Klassen, T. J. A. M. (2016). Cold spraying–A materials perspective. *Acta Materialia*, *116*, 382-407.
- 27. Astm, I. (2015). ASTM52900-15 standard terminology for additive manufacturing—general principles—terminology. *ASTM International, West Conshohocken, PA, 3*(4), 5.
- 28. Aydinöz, M. E., Brenne, F., Schaper, M., Schaak, C., Tillmann, W., Nellesen, J., & Niendorf, T. (2016). On the microstructural and mechanical properties of post-treated additively manufactured Inconel 718 superalloy under quasi-static and cyclic loading. *Materials Science and Engineering:* A, 669, 246-258.
- 29. Azadian, S., Wei, L. Y., & Warren, R. (2004). Delta phase precipitation in Inconel 718. *Materials characterization*, *53*(1), 7-16.
- 30. Azarmi, F., Chen, X., Cizek, J., Cojocaru, C., Jodoin, B., Koivuluoto, H., ... & Toma, F. (2021). Numerical Simulation of Solid Ti6AI4V Particles Impinging on a Stainless-Steel Substrate at High Speed: Influence of the Particle Temperature.
- 31. Bae, G., Kumar, S., Yoon, S., Kang, K., Na, H., Kim, H. J., & Lee, C. (2009). Bonding features and associated mechanisms in kinetic sprayed titanium coatings. *Acta Materialia*, *57*(19), 5654-5666.
- 32. Bagherifard, S., & Guagliano, M. (2020). Fatigue performance of cold spray deposits: Coating, repair and additive manufacturing cases. *International Journal of Fatigue*, *139*, 105744.
- 33. Bagherifard, S., Roscioli, G., Zuccoli, M. V., Hadi, M., D'Elia, G., Demir, A. G., ... & Guagliano, M. (2017). Cold spray deposition of freestanding Inconel samples and comparative analysis with selective laser melting. *Journal of Thermal Spray Technology*, 26, 1517-1526.
- 34. Bakan, E., Mauer, G., Sohn, Y. J., Koch, D., & Vaßen, R. (2017). Application of high-velocity oxygen-fuel (HVOF) spraying to the fabrication of Yb-silicate environmental barrier coatings. *Coatings*, 7(4), 55.
- 35. Bartkowiak, K., Ullrich, S., Frick, T., & Schmidt, M. (2011). New developments of laser processing aluminium alloys via additive manufacturing technique. *Physics procedia*, *12*, 393-401.
- 36. Baufeld, B., Widdison, R., & Dutilleul, T. (2017). Wire based electron beam additive manufacturing. In 70th IIW assembly and international conference Shanghai, China.

- 37. Baufeld, B., Widdison, R., Dutilleul, T., & Bridger, K. (2016). Electron beam additive manufacturing at the Nuclear AMRC. *Electrotechnica & Electronica* (*E*+ *E*), *51*.
- 38. Behera, A., & Behera, A. (2022). Superalloys. *Advanced Materials: An Introduction to Modern Materials Science*, 225-261.
- 39. Belbaki, A., & Mebdoua-Lahmar, Y. (2017). Influence of diverging section length on the supersonic jet delivered from micro-nozzle: Application to cold spray coating process. In *Applied Mechanics, Behavior of Materials, and Engineering Systems: Selected contributions to the 5th Algerian Congress of Mechanics, CAM2015, El-Oued, Algeria, October 25–29* (pp. 465-473). Springer International Publishing.
- 40. Ben Mahmud, T. (2018). Development of Near-Nanostructured Coatings by High Velocity Oxy-Fuel Spraying. *Development*, 2018, 01-04.
- 41. Benenati, G., & Lupoi, R. (2016). Development of a deposition strategy in cold spray for additive manufacturing to minimize residual stresses. *Procedia Cirp*, 55, 101-108.
- 42. Benn, R. C., & Salva, R. P. (2010, October). Additively manufactured INCONEL® alloy 718. In *Proceedings of the 7th International Symposium on Superalloy* (Vol. 718, pp. 455-456).
- 43. Berger, L. M. (2007). Hardmetals as thermal spray coatings. *Powder Metallurgy*, *50*(3), 205-214.
- 44. Berger, L. M. (2015). Application of hardmetals as thermal spray coatings. *International Journal of Refractory Metals and Hard Materials*, 49, 350-364.
- 45. Berthod, P. (2005). Kinetics of high temperature oxidation and chromia volatilization for a binary Ni–Cr alloy. *Oxidation of Metals*, *64*(3), 235-252.
- 46. Bhattiprolu, V. S., Johnson, K. W., Ozdemir, O. C., & Crawford, G. A. (2018). Influence of feedstock powder and cold spray processing parameters on microstructure and mechanical properties of Ti-6Al-4V cold spray depositions. *Surface and Coatings Technology*, *335*, 1-12.
- 47. Biamino, S., Penna, A., Ackelid, U., Sabbadini, S., Tassa, O., Fino, P., ... & Badini, C. (2011). Electron beam melting of Ti–48Al–2Cr–2Nb alloy: Microstructure and mechanical properties investigation. *Intermetallics*, *19*(6), 776-781.
- 48. Bikas, H., Stavropoulos, P., & Chryssolouris, G. (2016). Additive manufacturing methods and modelling approaches: a critical review. *The International Journal of Advanced Manufacturing Technology*, 83, 389-405.
- 49. Bingol, D., Tekin, N., & Alkan, M. (2010). Brilliant Yellow dye adsorption onto sepiolite using a full factorial design. *Applied clay science*, *50*(3), 315-321.

- 50. Bird, R. K., & Hibberd, J. (2009). Tensile Properties and Microstructure of Inconel 718 Fabricated with Electron Beam Freeform Fabrication (EBF (sup 3)) (No. NASA/TM-2009-215929).
- 51. Blazynski, T. Z. (2012). *Explosive welding, forming and compaction*. Springer Science & Business Media.
- 52. Blose, R. E., Walker, B. H., Walker, R. M., & Froes, S. H. (2006). New opportunities to use cold spray process for applying additive features to titanium alloys. *Metal Powder Report*, 61(9), 30-37.
- 53. Bobbio, L. D., Bocklund, B., Liu, Z. K., & Beese, A. M. (2021). Tensile behavior of stainless steel 304L to Ni-20Cr functionally graded material: experimental characterization and computational simulations. *Materialia*, *18*, 101151.
- 54. Borchers, C., Gärtner, F., Stoltenhoff, T., & Kreye, H. (2005). Formation of persistent dislocation loops by ultra-high strain-rate deformation during cold spraying. *Acta Materialia*, *53*(10), 2991-3000.
- 55. Boulos, M. I., Fauchais, P. L., & Pfender, E. (2023). The plasma state. In *Handbook of Thermal Plasmas* (pp. 3-55). Cham: Springer International Publishing.
- 56. Boulos, M. I., Fauchais, P. L., Heberlein, J. V., Boulos, M. I., Fauchais, P. L., & Heberlein, J. V. (2021). Industrial applications of thermal spray technology. *Thermal Spray Fundamentals: From Powder to Part*, 997-1096.
- 57. Boulos, M. I., Fauchais, P. L., Heberlein, J. V., Boulos, M. I., Fauchais, P. L., & Heberlein, J. V. (2021). Combustion Spraying. *Thermal Spray Fundamentals: From Powder to Part*, 235-302.
- 58. Brasil, J. L., Martins, L. C., Ev, R. R., Dupont, J., Dias, S. L., Sales, J. A., ... & Lima, É. C. (2005). Factorial design for optimization of flow-injection preconcentration procedure for copper (II) determination in natural waters, using 2-aminomethylpyridine grafted silica gel as adsorbent and spectrophotometric detection. *International Journal of Environmental Analytical Chemistry*, 85(7), 475-491.
- 59. Brenne, F., Leuders, S., & Niendorf, T. (2017). On the impact of additive manufacturing on microstructural and mechanical properties of stainless steel and Ni-base alloys. *BHM Bergund Hüttenmännische Monatshefte*, *5*(162), 199-202.
- 60. Brenne, F., Taube, A., Pröbstle, M., Neumeier, S., Schwarze, D., Schaper, M., & Niendorf, T. (2016). Microstructural design of Ni-base alloys for high-temperature applications: impact of heat treatment on microstructure and mechanical properties after selective laser melting. *Progress in Additive Manufacturing*, *1*, 141-151.

- 61. Bruera, A., Puddu, P., Theimer, S., Villa-Vidaller, M., List, A., Bolelli, G., ... & Lusvarghi, L. (2023). Adhesion of cold sprayed soft coatings: Effect of substrate roughness and hardness. *Surface and Coatings Technology*, 466, 129651.
- 62. Cai, W., Daehn, G., Vivek, A., Li, J., Khan, H., Mishra, R., & Komarasamy, M. (2018, June). A state-of-the-art review on solid-state metal joining. In *International Manufacturing Science and Engineering Conference* (Vol. 51364, p. V002T04A044). American Society of Mechanical Engineers.
- 63. Cai, Z., Deng, S., Liao, H., Zeng, C., & Montavon, G. (2014). The effect of spray distance and scanning step on the coating thickness uniformity in cold spray process. *Journal of thermal spray technology*, 23, 354-362.
- 64. Cakmak, E., Watkins, T. R., Bunn, J. R., Cooper, R. C., Cornwell, P. A., Wang, Y., ... & Babu, S. S. (2016). Mechanical characterization of an additively manufactured Inconel 718 theta-shaped specimen. *Metallurgical and Materials Transactions A*, 47, 971-980.
- 65. Cao, G. H., Sun, T. Y., Wang, C. H., Li, X., Liu, M., Zhang, Z. X., ... & Chen, G. F. (2018). Investigations of γ' , γ'' and δ precipitates in heat-treated Inconel 718 alloy fabricated by selective laser melting. *Materials Characterization*, *136*, 398-406.
- 66. Cao, J., Liu, F., Lin, X., Huang, C., Chen, J., & Huang, W. (2013). Effect of overlap rate on recrystallization behaviors of Laser Solid Formed Inconel 718 superalloy. *Optics & Laser Technology*, 45, 228-235.
- 67. Caruso, F., Meyer, M. C., & Lupoi, R. (2018). Three-dimensional numerical simulations of the particle loading effect on gas flow features for low pressure cold spray applications. *Surface and Coatings Technology*, *339*, 181-190.
- 68. Cavaliere, P. (2014). Cold spray coating technology for metallic components repairing. In *Through-life Engineering Services: Motivation, Theory, and Practice* (pp. 175-184). Cham: Springer International Publishing.
- 69. Cavaliere, P., & Silvello, A. (2015). Processing conditions affecting residual stresses and fatigue properties of cold spray deposits. *The International Journal of Advanced Manufacturing Technology*, 81, 1857-1862.
- 70. Cavaliere, P., & Silvello, A. (2018). Finite element analyses of pure Ni cold spray particles impact related to coating crack behaviour. *Surface Engineering*, *34*(5), 361-368.
- 71. Champagne Jr, V. K., Ozdemir, O. C., & Nardi, A. (Eds.). (2021). *Practical cold spray*. Cham, Switzerland: Springer International Publishing.

- 72. Champagne, V. K., Helfritch, D. J., Dinavahi, S. P., & Leyman, P. F. (2011). Theoretical and experimental particle velocity in cold spray. *Journal of thermal spray technology*, 20, 425-431.
- 73. Champagne, V. K., West, M. K., Reza Rokni, M., Curtis, T., Champagne, V., & McNally, B. (2016). Joining of cast ZE41A Mg to wrought 6061 Al by the cold spray process and friction stir welding. *Journal of Thermal Spray Technology*, 25, 143-159.
- 74. Champagne, V., & Helfritch, D. (2015). Critical Assessment 11: Structural repairs by cold spray. *Materials Science and Technology*, *31*(6), 627-634.
- 75. Chandrasekhar, S. (2013). *Hydrodynamic and hydromagnetic stability*. Courier Corporation.
- 76. Chang, S. H. (2009). In situ TEM observation of γ' , γ'' and δ precipitations on Inconel 718 superalloy through HIP treatment. *Journal of alloys and compounds*, 486(1-2), 716-721.
- 77. Chavan, N. M., Vinod Kumar, M., Sudharshan Phani, P., Pant, P., & Sundararajan, G. (2019). Influence of nozzle throat cross section on microstructure and properties of cold sprayed coatings. *Journal of Thermal Spray Technology*, 28, 1718-1729.
- 78. Chen, C., Gojon, S., Xie, Y., Yin, S., Verdy, C., Ren, Z., ... & Deng, S. (2017). A novel spiral trajectory for damage component recovery with cold spray. *Surface and Coatings Technology*, 309, 719-728.
- 79. Chen, C., Xie, Y., Yan, X., Yin, S., Fukanuma, H., Huang, R., ... & Liao, H. (2019). Effect of hot isostatic pressing (HIP) on microstructure and mechanical properties of Ti6Al4V alloy fabricated by cold spray additive manufacturing. *Additive manufacturing*, 27, 595-605.
- 80. Chen, C., Xie, Y., Yin, S., Planche, M. P., Deng, S., Lupoi, R., & Liao, H. (2016). Evaluation of the interfacial bonding between particles and substrate in angular cold spray. *Materials Letters*, 173, 76-79.
- 81. Chen, Y. S., & Kim, S. W. (1987). Computation of turbulent flows using an extended kepsilon turbulence closure model (No. NAS 1.26: 179204).
- 82. Cheng, B., & Chou, K. (2015). Geometric consideration of support structures in part overhang fabrications by electron beam additive manufacturing. *Computer-Aided Design*, 69, 102-111.
- 83. Chlebus, E., Gruber, K., Kuźnicka, B., Kurzac, J., & Kurzynowski, T. (2015). Effect of heat treatment on the microstructure and mechanical properties of Inconel 718 processed by selective laser melting. *Materials Science and Engineering: A*, 639, 647-655.

- 84. Choi, Y., Kim, S., Kwon, S. L., Choi, H., & Yun, G. J. (2024). Multi-stage Johnson—Cook Model for Collision Analysis: Impact Experiments and Simulations. *International Journal of Aeronautical and Space Sciences*, 1-16.
- 85. Cinca, N., Drehmann, R., Dietrich, D., Gärtner, F., Klassen, T., Lampke, T., & Guilemany, J. M. (2019). Mechanically induced grain refinement, recovery and recrystallization of cold-sprayed iron aluminide coatings. *Surface and Coatings Technology*, 380, 125069.
- 86. Coddet, P., Verdy, C., Coddet, C., & Debray, F. (2015). Mechanical properties of Cu-0.1 Ag alloys deposited by cold spray with various powder feed rate and heat treatment. *Journal of Thermal Spray Technology*, 24, 119-125.
- 87. Coddet, P., Verdy, C., Coddet, C., Lecouturier, F., & Debray, F. (2014). Comparison of the properties of cold-sprayed Cu-0.5 Cr-0.05 Zr alloys after various heat treatments versus forged and vacuum plasma-sprayed alloys. *Journal of thermal spray technology*, 23, 486-491.
- 88. Cunningham, C. R., Flynn, J. M., Shokrani, A., Dhokia, V., & Newman, S. T. (2018). Invited review article: Strategies and processes for high quality wire arc additive manufacturing. *Additive Manufacturing*, 22, 672-686.
- 89. Dadbakhsh, S., Hao, L., & Sewell, N. (2012). Effect of selective laser melting layout on the quality of stainless steel parts. *Rapid Prototyping Journal*, *18*(3), 241-249.
- 90. Daly, B. J., & Harlow, F. H. (1970). Transport equations in turbulence. *Physics of fluids*, *13*(11), 2634-2649.
- 91. De Bartolomeis, A., Newman, S. T., Jawahir, I. S., Biermann, D., & Shokrani, A. (2021). Future research directions in the machining of Inconel 718. *Journal of Materials Processing Technology*, 297, 117260.
- 92. de Lima, M. S. F., & Sankaré, S. (2014). Microstructure and mechanical behavior of laser additive manufactured AISI 316 stainless steel stringers. *Materials & Design*, 55, 526-532.
- 93. DebRoy, T., Wei, H. L., Zuback, J. S., Mukherjee, T., Elmer, J. W., Milewski, J. O., ... & Zhang, W. (2018). Additive manufacturing of metallic components–process, structure and properties. *Progress in Materials Science*, 92, 112-224.
- 94. Dehmas, M., Lacaze, J., Niang, A., & Viguier, B. (2011). TEM study of high-temperature precipitation of delta phase in Inconel 718 alloy. *Advances in materials science and engineering*, 2011.
- 95. Délery, J., & Dussauge, J. P. (2009). Some physical aspects of shock wave/boundary layer interactions. *Shock waves*, 19(6), 453-468.
- 96. Deng, D. (2018). *Additively Manufactured Inconel 718: Microstructures and Mechanical Properties* (Vol. 1798). Linköping University Electronic Press.

- 97. Deng, D., Moverare, J., Peng, R. L., & Söderberg, H. (2017). Microstructure and anisotropic mechanical properties of EBM manufactured Inconel 718 and effects of post heat treatments. *Materials Science and Engineering: A*, 693, 151-163.
- 98. Deng, D., Peng, R. L., Brodin, H., & Moverare, J. (2018). Microstructure and mechanical properties of Inconel 718 produced by selective laser melting: Sample orientation dependence and effects of post heat treatments. *Materials Science and Engineering: A*, 713, 294-306.
- 99. Deng, D., Peng, R. L., Söderberg, H., & Moverare, J. (2018). On the formation of microstructural gradients in a nickel-base superalloy during electron beam melting. *Materials & Design*, 160, 251-261.
- 100. Derekar, K. S. (2018). A review of wire arc additive manufacturing and advances in wire arc additive manufacturing of aluminium. *Materials science and technology*, *34*(8), 895-916.
- 101. Devasenapathi, A., Ng, H. W., Yu, S. C. M., & Indra, A. B. (2002). Forming near net shape free-standing components by plasma spraying. *Materials Letters*, *57*(4), 882-886.
- 102. Ding, D., Pan, Z., Van Duin, S., Li, H., & Shen, C. (2016). Fabricating superior NiAl bronze components through wire arc additive manufacturing. *Materials*, 9(8), 652.
- 103. Dorfman, M. R. (2018). Thermal spray coatings. In *Handbook of environmental degradation of materials* (pp. 469-488). William Andrew Publishing.
- 104. Dykhuizen, R. C., & Neiser, R. A. (2003). Optimizing the cold spray process. *Thermal Spray 2003: Advancing the Science and Applying the Technology*, 5-8.
- 105. Dykhuizen, R. C., & Smith, M. F. (1998). Gas dynamic principles of cold spray. *Journal of Thermal spray technology*, 7, 205-212.
- 106. Eason, P. D., Kennett, S. C., Eden, T. J., Krull, I., Kowalski, B., & Jones, J. L. (2012). In situ observation of microstrain relief in cold-sprayed bulk copper during thermal annealing. *Scripta Materialia*, *67*(9), 791-794.
- 107. Ekanayake, S., Gear, J. A., & Ding, Y. (2009). Flow simulation of a two dimensional rectangular supersonic convergent divergent nozzle. *ANZIAM Journal*, *51*, C377-C392.
- 108. Elibol, M. (2002). Response surface methodological approach for inclusion of perfluorocarbon in actinorhodin fermentation medium. *Process Biochemistry*, *38*(5), 667-673.
- 109. Estejab, B., & Khalkhali, Z. (2023). Finite element simulation of single-particle impact in polymeric cold spray and comparison to experimental results. *The International Journal of Advanced Manufacturing Technology*, 125(7), 3023-3036.
- 110. Ortega, F., Sova, A., Monzón, M. D., Marrero, M. D., Benítez, A. N., & Bertrand, P. (2015). Combination of electroforming and cold gas dynamic spray for fabrication of rotational

- moulds: feasibility study. *The International Journal of Advanced Manufacturing Technology*, 76, 1243-1251.
- 111. Fang, D., Deng, S., Liao, H., & Coddet, C. (2010). The effect of robot kinematics on the coating thickness uniformity. *Journal of thermal spray technology*, *19*, 796-804.
- 112. Fauchais, P. L., Heberlein, J. V., Boulos, M. I., Fauchais, P. L., Heberlein, J. V., & Boulos, M. I. (2014). Combustion Spraying Systems. *Thermal Spray Fundamentals: From Powder to Part*, 227-303.
- 113. Fauchais, P. L., Heberlein, J. V., Boulos, M. I., Fauchais, P. L., Heberlein, J. V., & Boulos, M. I. (2014). Cold Spray. *Thermal Spray Fundamentals: From Powder to Part*, 305-382.
- 114. Fauchais, P., & Montavon, G. (2007). Plasma spraying: from plasma generation to coating structure. *Advances in Heat Transfer*, 40, 205-344.
- 115. Fauchais, P., & Vardelle, A. (2012). Thermal sprayed coatings used against corrosion and corrosive wear. *Advanced plasma spray applications*, *10*, 34448.
- 116. Feng, K. Y., Liu, P., Li, H. X., Sun, S. Y., Xu, S. B., & Li, J. N. (2017). Microstructure and phase transformation on the surface of Inconel 718 alloys fabricated by SLM under 1050 C solid solution+ double ageing. *Vacuum*, *145*, 112-115.
- 117. Fraunhofer, I. W. S. (2021). Annual report 2019/2020 Fraunhofer IWS, 2020.
- 118. Gan, H. Y., Cheng, M., Guo, Z. X., Tai, Q. A., Kozhevnikova, G., Song, H. W., & Zhang, S. H. (2020). Spheroidization mechanism of lamellar δ phase in Inconel 718 during Delta processing. *Journal of Materials Engineering and Performance*, 29, 3852-3857.
- 119. Gan, J. A., & Berndt, C. C. (2015). Nanocomposite coatings: thermal spray processing, microstructure and performance. *International materials reviews*, 60(4), 195-244.
- 120. Gao, P., Zhang, C., Wang, R., Deng, G., Li, J., & Su, L. (2023). Tamping effect during additive manufacturing of copper coating by cold spray: A comprehensive molecular dynamics study. *Additive Manufacturing*, 66, 103448.
- 121. Garmeh, S., Jadidi, M., Lamarre, J. M., & Dolatabadi, A. (2023). Cold spray gas flow dynamics for on and off-axis nozzle/substrate hole geometries. *Journal of Thermal Spray Technology*, 32(1), 208-225.
- 122. Gärtner, F., Stoltenhoff, T., Voyer, J., Kreye, H., Riekehr, S., & Kocak, M. (2006). Mechanical properties of cold-sprayed and thermally sprayed copper coatings. *Surface and Coatings Technology*, 200(24), 6770-6782.
- 123. Ghelichi, R., Bagherifard, S., Guagliano, M., & Verani, M. (2011). Numerical simulation of cold spray coating. *Surface and Coatings Technology*, 205(23-24), 5294-5301.

- 124. Ghelichi, R., Bagherifard, S., MacDonald, D., Fernandez-Pariente, I., Jodoin, B., & Guagliano, M. (2014). Experimental and numerical study of residual stress evolution in cold spray coating. *Applied Surface Science*, 288, 26-33.
- 125. Gibson, I., Rosen, D. W., Stucker, B., Khorasani, M., Rosen, D., Stucker, B., & Khorasani, M. (2021). *Additive manufacturing technologies* (Vol. 17, pp. 160-186). Cham, Switzerland: Springer.
- 126. Gill, B. J., & Tucker, R. C. (1986). Plasma spray coating processes. *Materials science and technology*, 2(3), 207-213.
- 127. Gilmore, D. L., Dykhuizen, R. C., Neiser, R. A., Smith, M. F., & Roemer, T. J. (1999). Particle velocity and deposition efficiency in the cold spray process. *Journal of thermal spray technology*, 8, 576-582.
- 128. Goldbaum, D., Chromik, R. R., Yue, S., Irissou, E., & Legoux, J. G. (2011). Mechanical property mapping of cold sprayed Ti splats and coatings. *Journal of thermal spray technology*, 20, 486-496.
- 129. Gong, X., & Chou, K. (2016). Microstructures of Inconel 718 by selective laser melting. In *TMS 2015 144 th Annual Meeting & Exhibition: Supplemental Proceedings* (pp. 461-468). Springer International Publishing.
- 130. Gong, X., Wang, X., Cole, V., Jones, Z., Cooper, K., & Chou, K. (2015, June). Characterization of microstructure and mechanical property of Inconel 718 from selective laser melting. In *International Manufacturing Science and Engineering Conference* (Vol. 56826, p. V001T02A061). American Society of Mechanical Engineers.
- 131. Gonzalez, R., Ashrafizadeh, H., Lopera, A., Mertiny, P., & Mcdonald, A. (2016). A review of thermal spray metallization of polymer-based structures. *Journal of Thermal Spray Technology*, 25, 897-919.
- 132. Gribbin, S., Bicknell, J., Jorgensen, L., Tsukrov, I., & Knezevic, M. (2016). Low cycle fatigue behavior of direct metal laser sintered Inconel alloy 718. *International Journal of Fatigue*, 93, 156-167.
- 133. Gribbin, S., Ghorbanpour, S., Ferreri, N. C., Bicknell, J., Tsukrov, I., & Knezevic, M. (2019). Role of grain structure, grain boundaries, crystallographic texture, precipitates, and porosity on fatigue behavior of Inconel 718 at room and elevated temperatures. *Materials Characterization*, 149, 184-197.
- 134. Gross, B. C., Erkal, J. L., Lockwood, S. Y., Chen, C., & Spence, D. M. (2014). Evaluation of 3D printing and its potential impact on biotechnology and the chemical sciences.

- 135. Grujicic, M., Tong, C., DeRosset, W. S., & Helfritch, D. (2003). Flow analysis and nozzle-shape optimization for the cold-gas dynamic-spray process. *Proceedings of the Institution of Mechanical Engineers, Part B: Journal of Engineering Manufacture*, 217(11), 1603-1613.
- 136. Grujicic, M., Zhao, C. L., DeRosset, W. S., & Helfritch, D. (2004). Adiabatic shear instability based mechanism for particles/substrate bonding in the cold-gas dynamic-spray process. *Materials & design*, 25(8), 681-688.
- 137. Gruner, H. (1984). Vacuum plasma spray quality control. *Thin Solid Films*, *118*(4), 409-420.
- 138. Gu, D. D., Meiners, W., Wissenbach, K., & Poprawe, R. (2012). Laser additive manufacturing of metallic components: materials, processes and mechanisms. *International materials reviews*, 57(3), 133-164.
- 139. Gu, Y., Xia, K., Wu, D., Mou, J., & Zheng, S. (2020). Technical characteristics and wear-resistant mechanism of nano coatings: a review. Coatings, 10(3), 233.
- 140. Guddati, S., Kiran, A. S. K., Leavy, M., & Ramakrishna, S. (2019). Recent advancements in additive manufacturing technologies for porous material applications. *The International Journal of Advanced Manufacturing Technology*, *105*, 193-215.
- 141. Guo, D., Kazasidis, M., Hawkins, A., Fan, N., Leclerc, Z., MacDonald, D., ... & Jodoin, B. (2022). Cold spray: Over 30 years of development toward a hot future. *Journal of thermal spray technology*, *31*(4), 866-907.
- 142. Guo, J., Zhou, Y., Liu, C., Wu, Q., Chen, X., & Lu, J. (2016). Wire arc additive manufacturing of AZ31 magnesium alloy: Grain refinement by adjusting pulse frequency. *Materials*, 9(10), 823.
- 143. Guo, M., Yang, Y., Yang, C., & Dai, D. (2024). Effects of structure parameters on performances of laser powder bed fusion processed AlSi10Mg body-centered cubic lattices. *Journal of Laser Applications*, 36(1).
- 144. Guo, N., & Leu, M. C. (2013). Additive manufacturing: technology, applications and research needs. *Frontiers of mechanical engineering*, 8, 215-243.
- 145. Choi, H. J., Lee, M., & Lee, J. Y. (2010). Application of a cold spray technique to the fabrication of a copper canister for the geological disposal of CANDU spent fuels. *Nuclear Engineering and Design*, 240(10), 2714-2720.
- 146. Hanaor, D. A., & Sorrell, C. C. (2011). Review of the anatase to rutile phase transformation. *Journal of Materials science*, 46, 855-874.

- 147. Hanft, D., Exner, J., Schubert, M., Stöcker, T., Fuierer, P., & Moos, R. (2015). An overview of the aerosol deposition method: Process fundamentals and new trends in materials applications. *J. Ceram. Sci. Technol*, *6*(3), 147-182.
- 148. Hasani, N., Dharmendra, C., Sanjari, M., Fazeli, F., Amirkhiz, B. S., Pirgazi, H., ... & Mohammadi, M. (2021). Laser powder bed fused Inconel 718 in stress-relieved and solution heat-treated conditions. *Materials Characterization*, 181, 111499.
- 149. Hassani-Gangaraj, M., Veysset, D., Champagne, V. K., Nelson, K. A., & Schuh, C. A. (2018). Adiabatic shear instability is not necessary for adhesion in cold spray. *Acta Materialia*, *158*, 430-439.
- 150. Hassani-Gangaraj, M., Veysset, D., Nelson, K. A., & Schuh, C. A. (2018). In-situ observations of single micro-particle impact bonding. *Scripta Materialia*, *145*, 9-13.
- 151. Hassani-Gangaraj, M., Veysset, D., Nelson, K. A., & Schuh, C. A. (2016). Supersonic impact of metallic micro-particles. *arXiv preprint arXiv:1612.08081*.
- 152. Hautfenne, C., Nardone, S., & De Bruycker, E. (2017, September). Influence of heat treatments and build orientation on the creep strength of additive manufactured IN718. In *4th international ECCC Conference* (Vol. 1). Düsseldorf, Germany: Steel Institute VDEh.
- 153. Hay, J. C., & Pharr, G. M. (1998). Experimental investigations of the Sneddon solution and an improved solution for the analysis of nanoindentation data. *MRS Online Proceedings Library*, 522, 39-44.
- 154. Hay, J. C., Bolshakov, A., & Pharr, G. M. (1999). A critical examination of the fundamental relations used in the analysis of nanoindentation data. *Journal of materials Research*, 14(6), 2296-2305.
- 155. Hegab, H., Khanna, N., Monib, N., & Salem, A. (2023). Design for sustainable additive manufacturing: A review. *Sustainable Materials and Technologies*, *35*, e00576.
- 156. Heimann, R. B. (1996). Applications of plasma-sprayed ceramic coatings. *Key Engineering Materials*, 122, 399-442.
- 157. Helfritch, D., Stier, O., & Villafuerte, J. (2015). Cold spray economics. *Modern Cold Spray: Materials, Process, and Applications*, 377-401.
- 158. Hellsten, A., Laine, S., Hellsten, A., & Laine, S. (1997). Extension of the k-omega-SST turbulence model for flows over rough surfaces. In 22nd atmospheric flight mechanics conference (p. 3577).
- 159. Henao, J., Poblano-Salas, C., Monsalve, M., Corona-Castuera, J., & Barceinas-Sanchez, O. (2019). Bio-active glass coatings manufactured by thermal spray: A status report. *Journal of Materials Research and Technology*, 8(5), 4965-4984.

- 160. Henriques, V. A. R., Campos, P. P. D., Cairo, C. A. A., & Bressiani, J. C. (2005). Production of titanium alloys for advanced aerospace systems by powder metallurgy. *Materials Research*, *8*, 443-446.
- 161. Hopkinson, N., & Dicknes, P. (2003). Analysis of rapid manufacturing—using layer manufacturing processes for production. *Proceedings of the Institution of Mechanical Engineers, Part C: Journal of Mechanical Engineering Science*, 217(1), 31-39.
- 162. Hosseini, E., & Popovich, V. A. (2019). A review of mechanical properties of additively manufactured Inconel 718. *Additive Manufacturing*, *30*, 100877.
- 163. Huang, R., Sone, M., Ma, W., & Fukanuma, H. (2015). The effects of heat treatment on the mechanical properties of cold-sprayed coatings. *Surface and Coatings Technology*, 261, 278-288.
- 164. Hui, R., Wang, Z., Kesler, O., Rose, L., Jankovic, J., Yick, S., ... & Ghosh, D. (2007). Thermal plasma spraying for SOFCs: Applications, potential advantages, and challenges. *Journal of Power Sources*, 170(2), 308-323.
- 165. Hulka, I. (2013). Microstructural characteristics, wear and corrosion behaviour of HVOF and HVAF sprayed cermet coatings. Timişoara: Editura Politehnica.
- 166. Hull, C. W. (1986). U.S. Patent No. 4,575,330. Washington, DC: U.S. Patent and Trademark Office.
- 167. Hussain, T. (2013). Cold spraying of titanium: a review of bonding mechanisms, microstructure and properties. *Key engineering materials*, 533, 53-90.
- 168. Hussain, T., McCartney, D. G., Shipway, P. H., & Marrocco, T. (2011). Corrosion behavior of cold sprayed titanium coatings and free standing deposits. *Journal of Thermal Spray Technology*, 20, 260-274.
- 169. Hussain, T., McCartney, D. G., Shipway, P. H., & Zhang, D. (2009). Bonding mechanisms in cold spraying: the contributions of metallurgical and mechanical components. *Journal of Thermal Spray Technology*, *18*, 364-379.
- 170. Huynh, L., Rotella, J., & Sangid, M. D. (2016). Fatigue behavior of IN718 microtrusses produced via additive manufacturing. *Materials & Design*, 105, 278-289.
- 171. Yadroitsev, I., Bertrand, P., & Smurov, I. (2007). Parametric analysis of the selective laser melting process. *Applied surface science*, 253(19), 8064-8069.
- 172. Imbriglio, S. I., & Chromik, R. R. (2021). Factors affecting adhesion in metal/ceramic interfaces created by cold spray. *Journal of Thermal Spray Technology*, 1-21.

- 173. Irissou, E., Legoux, J. G., Ryabinin, A. N., Jodoin, B., & Moreau, C. (2008). Review on cold spray process and technology: part I—intellectual property. *Journal of Thermal Spray Technology*, 17, 495-516.
- 174. Ito, K., & Ogawa, K. (2014). Effects of spark-plasma sintering treatment on cold-sprayed copper coatings. *Journal of thermal spray technology*, 23, 104-113.
- 175. Izadi, M., Farzaneh, A., Mohammed, M., Gibson, I., & Rolfe, B. (2020). A review of laser engineered net shaping (LENS) build and process parameters of metallic parts. *Rapid prototyping journal*, 26(6), 1059-1078.
- 176. Longtin, J., Sampath, S., Tankiewicz, S., Gambino, R. J., & Greenlaw, R. J. (2004). Sensors for harsh environments by direct-write thermal spray. *IEEE Sensors Journal*, 4(1), 118-121.
- 177. Kruth, J. P., Levy, G., Klocke, F., & Childs, T. H. (2007). Consolidation phenomena in laser and powder-bed based layered manufacturing. *CIRP annals*, *56*(2), 730-759.
- 178. Jackson, M. A., Van Asten, A., Morrow, J. D., Min, S., & Pfefferkorn, F. E. (2016). A comparison of energy consumption in wire-based and powder-based additive-subtractive manufacturing. *Procedia Manufacturing*, *5*, 989-1005.
- 179. Jahani, B., Brooks, A., & Azarmi, F. (2018). Development of antibacterial surfaces via thermal spray coating techniques. *Biomed. Sci. Instrum*, *54*(1), 116-122.
- 180. Jia, Q., & Gu, D. (2014). Selective laser melting additive manufacturing of Inconel 718 superalloy parts: Densification, microstructure and properties. *Journal of Alloys and Compounds*, 585, 713-721.
- 181. Jiao, L., Chua, Z. Y., Moon, S. K., Song, J., Bi, G., & Zheng, H. (2018). Femtosecond laser produced hydrophobic hierarchical structures on additive manufacturing parts. *Nanomaterials*, 8(8), 601.
- 182. Johnson, A. S., Shao, S., Shamsaei, N., Thompson, S. M., & Bian, L. (2017). Microstructure, fatigue behavior, and failure mechanisms of direct laser-deposited Inconel 718. *Jom*, 69, 597-603.
- 183. Johnson, A. S., Shuai, S., Shamsaei, N., Thompson, S. M., & Bian, L. (2016). Fatigue behavior and failure mechanisms of direct laser deposited Inconel 718.
- 184. Jonda, E., Łatka, L., & Pakieła, W. (2020). Microstructure and selected properties of Cr3C2–NiCr coatings obtained by HVOF on magnesium alloy substrates. *Materials*, *13*(12), 2775.
- 185. Kadyrov, E. (1996). Gas-particle interaction in detonation spraying systems. *Journal of Thermal Spray Technology*, *5*, 185-195.

- 186. Kadyrov, E., & Kadyrov, V. (1995). Gas dynamical parameters of detonation powder spraying. *Journal of Thermal Spray Technology*, *4*, 280-286.
- 187. Kahhal, P., Jo, Y. K., & Park, S. H. (2024). Recent progress in remanufacturing technologies using metal additive manufacturing processes and surface treatment. *International Journal of Precision Engineering and Manufacturing-Green Technology*, 11(2), 625-658.
- 188. Kahlen, F. J., & Kar, A. (2001). Residual stresses in laser-deposited metal parts. *Journal of Laser Applications*, *13*(2), 60-69.
- 189. Kahlen, F. J., & Kar, A. (2001). Tensile strengths for laser-fabricated parts and similarity parameters for rapid manufacturing. *J. Manuf. Sci. Eng.*, 123(1), 38-44.
- 190. Kamaraj, M., & Radhakrishnan, V. M. (2019). Cold spray coating diagram: bonding properties and construction methodology. *Journal of Thermal Spray Technology*, 28, 756-768.
- 191. Kang, Y. J., Yang, S., Kim, Y. K., AlMangour, B., & Lee, K. A. (2019). Effect of post-treatment on the microstructure and high-temperature oxidation behaviour of additively manufactured inconel 718 alloy. *Corrosion Science*, 158, 108082.
- 192. Kanjer, A., Optasanu, V., de Lucas, M. M., Heintz, O., Geoffroy, N., François, M., ... & Lavisse, L. (2018). Improving the high temperature oxidation resistance of pure titanium by shot-peening treatments. *Surface and Coatings Technology*, *343*, 93-100.
- 193. Karimi, M., Fartaj, A., Rankin, G., Vanderzwet, D., Birtch, W., & Villafuerte, J. (2006). Numerical simulation of the cold gas dynamic spray process. *Journal of thermal spray technology*, *15*, 518-523.
- 194. Karthikeyan, J. (2004). Cold spray technology: International status and USA efforts. *Report from ASB Industries Inc., Barbeton, OH*, 44203, 1-14.
- 195. Karthikeyan, J. (2005). COLD SPRAY TECHNOLOGY. Advanced materials & processes, 163(3).
- 196. Kaur, N., Kumar, M., Sharma, S. K., Kim, D. Y., Kumar, S., Chavan, N. M., ... & Singh, H. (2015). Study of mechanical properties and high temperature oxidation behavior of a novel cold-spray Ni-20Cr coating on boiler steels. *Applied Surface Science*, 328, 13-25.
- 197. Kavei, G., Nakaruk, A., & Sorrell, C. C. (2011). Equilibrium state of anatase to rutile transformation for titanium dioxide film prepared by ultrasonic spray pyrolysis technique. *Mater. Sci. Appl*, 2(6), 700-705.
- 198. Kelley, P. F., Saigal, A., & Carter, A. (2016). Fatigue behaviour of direct metal laser sintered Inconel 718. *International Journal of Precision Technology*, 6(3-4), 277-288.
- 199. Kerstens, F., Cervone, A., & Gradl, P. (2021). End to end process evaluation for additively manufactured liquid rocket engine thrust chambers. *Acta Astronautica*, *182*, 454-465.

- 200. Khorram Niaki, M., & Nonino, F. (2017). Additive manufacturing management: a review and future research agenda. *International Journal of Production Research*, *55*(5), 1419-1439.
- 201. Kim, A. (2017). Experimental Analysis and Simulations of the Effects of Deposition Conditions on Deformation Characteristics of Al-6061 Powders in Cold-Spray (Doctoral dissertation, Northeastern University).
- 202. Kim, J., Lee, S., & Lee, C. (2015). Investigating the cause of hindrance to the interfacial bonding of INCONEL 718 layer deposited by kinetic spray process. *Journal of the Korean institute of surface engineering*, 48(6), 275-282.
- 203. Kim, K. H., Kim, J. H., Hong, K. W., Park, J. Y., & Lee, C. B. (2017). Application of high-temperature ceramic plasma-spray coatings for a reusable melting crucible. *Surface and Coatings Technology*, 326, 429-435.
- 204. King, P. C., & Jahedi, M. (2010). Relationship between particle size and deformation in the cold spray process. *Applied Surface Science*, 256(6), 1735-1738.
- 205. King, P. C., Bae, G., Zahiri, S. H., Jahedi, M., & Lee, C. (2010). An experimental and finite element study of cold spray copper impact onto two aluminum substrates. *Journal of thermal spray technology*, *19*, 620-634.
- 206. King, P., Yandouzi, M., & Jodoin, B. (2015). The physics of cold spray. *Modern Cold Spray: Materials, Process, and Applications*, 31-72.
- 207. King, R. B. (1987). Elastic analysis of some punch problems for a layered medium. *International Journal of Solids and Structures*, 23(12), 1657-1664.
- 208. Kirka, M. M., Greeley, D. A., Hawkins, C., & Dehoff, R. R. (2017). Effect of anisotropy and texture on the low cycle fatigue behavior of Inconel 718 processed via electron beam melting. *International Journal of Fatigue*, 105, 235-243.
- 209. Kirka, M. M., Medina, F., Dehoff, R., & Okello, A. (2017). Mechanical behavior of post-processed Inconel 718 manufactured through the electron beam melting process. *Materials Science and Engineering:* A, 680, 338-346.
- 210. Kirka, M. M., Unocic, K. A., Raghavan, N., Medina, F., Dehoff, R. R., & Babu, S. S. (2016). Microstructure development in electron beam-melted Inconel 718 and associated tensile properties. *Jom*, 68(3), 1012-1020.
- 211. Ko, K. H., Choi, J. O., & Lee, H. (2016). The interfacial restructuring to amorphous: A new adhesion mechanism of cold-sprayed coatings. *Materials Letters*, 175, 13-15.
- 212. Konečná, R., Kunz, L., Nicoletto, G., & Bača, A. (2016). Long fatigue crack growth in Inconel 718 produced by selective laser melting. *International Journal of Fatigue*, 92, 499-506.

- 213. Konečná, R., Nicoletto, G., Kunz, L., & Bača, A. (2016). Microstructure and directional fatigue behavior of Inconel 718 produced by selective laser melting. *Procedia Structural Integrity*, 2, 2381-2388.
- 214. Kosarev, V. F., Klinkov, S. V., Alkhimov, A. P., & Papyrin, A. N. (2003). On some aspects of gas dynamics of the cold spray process. *Journal of Thermal Spray Technology*, 12, 265-281.
- 215. Kotoban, D., Grigoriev, S., Okunkova, A., & Sova, A. (2017). Influence of a shape of single track on deposition efficiency of 316L stainless steel powder in cold spray. *Surface and Coatings Technology*, 309, 951-958.
- 216. Kruth, J. P., Froyen, L., Van Vaerenbergh, J., Mercelis, P., Rombouts, M., & Lauwers, B. (2004). Selective laser melting of iron-based powder. *Journal of materials processing technology*, *149*(1-3), 616-622.
- 217. Kruth, J. P., Leu, M. C., & Nakagawa, T. (1998). Progress in additive manufacturing and rapid prototyping. *Cirp Annals*, *47*(2), 525-540.
- 218. Kuerten, J. V., Van der Geld, C. W. M., & Geurts, B. J. (2011). Turbulence modification and heat transfer enhancement by inertial particles in turbulent channel flow. *Physics of fluids*, 23(12).
- 219. Kumar, R., Sharma, S., Singh, J. P., Gulati, P., Singh, G., Dwivedi, S. P., ... & Abbas, M. (2023). Enhancement in wear-resistance of 30MNCRB5 boron steel-substrate using HVOF thermal sprayed WC–10% Co–4% Cr coatings: A comprehensive research on microstructural, tribological, and morphological analysis. *Journal of Materials Research and Technology*, 27, 1072-1096.
- 220. Kumar, S. (2022). Influence of processing conditions on the mechanical, tribological and fatigue performance of cold spray coating: a review. *Surface Engineering*, 38(4), 324-365.
- 221. Kumar, S. P., Elangovan, S., Mohanraj, R., & Ramakrishna, J. R. (2021). A review on properties of Inconel 625 and Inconel 718 fabricated using direct energy deposition. *Materials Today: Proceedings*, 46, 7892-7906.
- 222. Kumar, S., & Kumar, R. (2021). Influence of processing conditions on the properties of thermal sprayed coating: a review. *Surface Engineering*, *37*(11), 1339-1372.
- 223. Kumar, S., & Pandey, S. M. (2022). The Study of Assessment Parameters and Performance Measurement of Cold Spray Technique: A Futuristic Approach Towards Additive Manufacturing. *MAPAN*, *37*(4), 859-879.

- 224. Kumar, S., Ramakrishna, M., Chavan, N. M., & Joshi, S. V. (2017). Correlation of splat state with deposition characteristics of cold sprayed niobium coatings. *Acta Materialia*, *130*, 177-195.
- 225. Kuo, Y. L., & Kakehi, K. (2017). Influence of powder surface contamination in the Ni-based superalloy alloy718 fabricated by selective laser melting and hot isostatic pressing. *Metals*, 7(9), 367.
- 226. Kuo, Y. L., Horikawa, S., & Kakehi, K. (2017). Effects of build direction and heat treatment on creep properties of Ni-base superalloy built up by additive manufacturing. *Scripta Materialia*, 129, 74-78.
- 227. Kuo, Y. L., Horikawa, S., & Kakehi, K. (2017). The effect of interdendritic δ phase on the mechanical properties of Alloy 718 built up by additive manufacturing. *Materials & Design*, 116, 411-418.
- 228. Kuo, Y. L., Kamigaichi, A., & Kakehi, K. (2018). Characterization of Ni-based superalloy built by selective laser melting and electron beam melting. *Metallurgical and Materials Transactions A*, 49, 3831-3837.
- 229. Kurdi, A., Aldoshan, A., Alshabouna, F., Alodadi, A., Degnah, A., Alnaser, H., ... & Basak, A. K. (2023). Investigation into the microstructure and hardness of additively manufactured (3D-Printed) Inconel 718 Alloy. *Materials*, *16*(6), 2383.
- 230. Latief, F. H., Sherif, E. S. M., Wismogroho, A. S., Widayatno, W. B., & Abdo, H. S. (2020). The cyclic oxidation and hardness characteristics of thermally exposed titanium prepared by inductive sintering-assisted powder metallurgy. *Crystals*, *10*(2), 104.
- 231. Lavernia, E. J., & Srivatsan, T. S. (2010). The rapid solidification processing of materials: science, principles, technology, advances, and applications. *Journal of Materials Science*, 45, 287-325.
- 232. Lee, S. C., Chang, S. H., Tang, T. P., Ho, H. H., & Chen, J. K. (2006). Improvement in the microstructure and tensile properties of Inconel 718 superalloy by HIP treatment. *Materials Transactions*, 47(11), 2877-2881.
- 233. Levy, G. N. (2010). The role and future of the laser technology in the additive manufacturing environment. *Physics Procedia*, 5, 65-80.
- 234. Lew, A. J., Buscaglia, G. C., & Carrica, P. M. (2001). A note on the numerical treatment of the k-epsilon turbulence model. *International Journal of Computational Fluid Dynamics*, 14(3), 201-209.
- 235. Leyens, C., & Peters, M. (Eds.). (2006). *Titanium and titanium alloys: fundamentals and applications*. Wiley-vch.

- 236. Li, C. J., Li, W. Y., & Liao, H. (2006). Examination of the critical velocity for deposition of particles in cold spraying. *Journal of Thermal Spray Technology*, *15*, 212-222.
- 237. Li, C. J., Luo, X. T., Dong, X. Y., Zhang, L., & Li, C. X. (2022). Recent research advances in plasma spraying of bulk-like dense metal coatings with metallurgically bonded lamellae. *Journal of Thermal Spray Technology*, 31(1), 5-27.
- 238. Li, J., Longtin, J. P., Tankiewicz, S., Gouldstone, A., & Sampath, S. (2007). Interdigital capacitive strain gauges fabricated by direct-write thermal spray and ultrafast laser micromachining. *Sensors and Actuators A: Physical*, 133(1), 1-8.
- 239. Li, J., Zhang, T., Liao, Z., Wei, Y., Hang, R., & Huang, D. (2023). Engineered functional doped hydroxyapatite coating on titanium implants for osseointegration. *Journal of Materials Research and Technology*.
- 240. Li, K., Chen, W., Gong, N., Pu, H., Luo, J., Zhang, D. Z., & Murr, L. E. (2023). A critical review on wire-arc directed energy deposition of high-performance steels. *Journal of Materials Research and Technology*.
- 241. Li, R. X., Ding, J. B., Zhao, Y. Y., Tian, Q. W., Zhong, X. T., Wang, R. Q., ... & Li, Y. C. (2024). Preliminary Study on the Dynamic Deformation Mechanism of CoCrFeNi High-Entropy Alloy and Its Application in the Shaped Charge Liner. *Journal of Alloys and Compounds*, 175083.
- 242. Li, S., Muddle, B., Jahedi, M., & Soria, J. (2012). A numerical investigation of the cold spray process using underexpanded and overexpanded jets. *Journal of thermal spray technology*, 21, 108-120.
- 243. Li, W. Y., & Gao, W. (2009). Some aspects on 3D numerical modeling of high velocity impact of particles in cold spraying by explicit finite element analysis. *Applied Surface Science*, 255(18), 7878-7892.
- 244. Li, W. Y., & Li, C. J. (2005). Optimal design of a novel cold spray gun nozzle at a limited space. *Journal of Thermal Spray Technology*, *14*, 391-396.
- 245. Li, W. Y., Li, C. J., & Liao, H. (2006). Effect of annealing treatment on the microstructure and properties of cold-sprayed Cu coating. *Journal of Thermal Spray Technology*, 15, 206-211.
- 246. Li, W. Y., Li, C. J., & Liao, H. (2010). Significant influence of particle surface oxidation on deposition efficiency, interface microstructure and adhesive strength of cold-sprayed copper coatings. *Applied Surface Science*, 256(16), 4953-4958.

- 247. Li, W. Y., Zhang, C., Guo, X. P., Zhang, G., Liao, H. L., Li, C. J., & Coddet, C. (2008). Effect of standoff distance on coating deposition characteristics in cold spraying. *Materials & design*, 29(2), 297-304.
- 248. Li, W. Y., Zhang, C., Li, C. J., & Liao, H. (2009). Modeling aspects of high velocity impact of particles in cold spraying by explicit finite element analysis. *Journal of Thermal Spray Technology*, 18, 921-933.
- 249. Li, W., Cao, C., & Yin, S. (2020). Solid-state cold spraying of Ti and its alloys: A literature review. *Progress in Materials Science*, 110, 100633.
- 250. Li, W., Yang, K., Yin, S., Yang, X., Xu, Y., & Lupoi, R. (2018). Solid-state additive manufacturing and repairing by cold spraying: A review. *Journal of materials science* & *technology*, 34(3), 440-457.
- 251. Li, X., Shi, J. J., Wang, C. H., Cao, G. H., Russell, A. M., Zhou, Z. J., ... & Chen, G. F. (2018). Effect of heat treatment on microstructure evolution of Inconel 718 alloy fabricated by selective laser melting. *Journal of Alloys and Compounds*, 764, 639-649.
- 252. Li, Y. J., Dong, T. S., Fu, B. G., Li, G. L., & Liu, Q. (2021). Study of the microstructure and properties of cold sprayed NiCr coating. *Journal of Materials Engineering and Performance*, 30(12), 9067-9077.
- 253. Liu, F., Lin, X., Huang, C., Song, M., Yang, G., Chen, J., & Huang, W. (2011). The effect of laser scanning path on microstructures and mechanical properties of laser solid formed nickel-base superalloy Inconel 718. *Journal of Alloys and Compounds*, 509(13), 4505-4509.
- 254. Liu, F., Lin, X., Leng, H., Cao, J., Liu, Q., Huang, C., & Huang, W. (2013). Microstructural changes in a laser solid forming Inconel 718 superalloy thin wall in the deposition direction. *Optics & Laser Technology*, 45, 330-335.
- 255. Liu, F., Lin, X., Song, M., Zhao, W., Chen, J., & Huang, W. (2011). Effect of intermediate heat treatment temperature on microstructure and notch sensitivity of laser solid formed Inconel 718 superalloy. *Journal of Wuhan University of Technology-Mater. Sci. Ed.*, 26(5), 908-913.
- 256. Liu, F., Lin, X., Yang, G., Song, M., Chen, J., & Huang, W. (2011). Microstructure and residual stress of laser rapid formed Inconel 718 nickel-base superalloy. *Optics & laser technology*, 43(1), 208-213.
- 257. Liu, S., Jiang, T., Fan, M., Tan, G., Cui, S., & Shen, X. (2021). Nanostructure rod-like TiO2-reduced graphene oxide composite aerogels for highly-efficient visible-light photocatalytic CO2 reduction. *Journal of Alloys and Compounds*, 861, 158598.

- 258. Liu, W. C., Yao, M., Chen, Z. L., & Wang, S. G. (1999). Niobium segregation in Inconel 718. *Journal of materials science*, *34*, 2583-2586.
- 259. Liu, Z., Liu, J., Li, H., Wu, Z., Zhong, Y., Ramachandran, C. S., ... & Wang, Q. (2024). Research Progress on Numerical Simulation of the Deposition and Deformation Behavior of Cold Spray Particles. *Coatings*, *14*(7), 913.
- 260. Loke, K., Zhang, Z. Q., Narayanaswamy, S., Koh, P. K., Luzin, V., Gnaupel-Herold, T., & Ang, A. S. M. (2021). Residual stress analysis of cold spray coatings sprayed at angles using through-thickness neutron diffraction measurement. *Journal of Thermal Spray Technology*, *30*, 1810-1826.
- 261. Lu, Y., Wu, S., Gan, Y., Huang, T., Yang, C., Junjie, L., & Lin, J. (2015). Study on the microstructure, mechanical property and residual stress of SLM Inconel-718 alloy manufactured by differing island scanning strategy. *Optics & Laser Technology*, 75, 197-206.
- 262. Luo, X. T., Li, C. X., Shang, F. L., Yang, G. J., Wang, Y. Y., & Li, C. J. (2014). High velocity impact induced microstructure evolution during deposition of cold spray coatings: A review. *Surface and Coatings Technology*, 254, 11-20.
- 263. Lupoi, R., & O'Neill, W. (2011). Powder stream characteristics in cold spray nozzles. *Surface and Coatings Technology*, 206(6), 1069-1076.
- 264. Luttrell, T., Halpegamage, S., Tao, J., Kramer, A., Sutter, E., & Batzill, M. (2014). Why is anatase a better photocatalyst than rutile?-Model studies on epitaxial TiO2 films. *Scientific reports*, *4*(1), 4043.
- 265. Luzin, V., Spencer, K., & Zhang, M. X. (2011). Residual stress and thermo-mechanical properties of cold spray metal coatings. *Acta Materialia*, *59*(3), 1259-1270.
- 266. Lynch, M. E., Gu, W., El-Wardany, T., Hsu, A., Viens, D., Nardi, A., & Klecka, M. (2013). Design and topology/shape structural optimisation for additively manufactured cold sprayed components: This paper presents an additive manufactured cold spray component which is shape optimised to achieve 60% reduction in stress and 20% reduction in weight. *Virtual and Physical Prototyping*, 8(3), 213-231.
- 267. Lyphout, C., Fasth, A., & Nylen, P. (2014). Mechanical property of HVOF inconel 718 coating for aeronautic repair. *Journal of thermal spray technology*, 23, 380-388.
- 268. Lyphout, C., Nylén, P., & Östergren, L. (2011). Relationships between process parameters, microstructure, and adhesion strength of HVOF sprayed IN718 coatings. *Journal of thermal spray technology*, 20, 76-82.
- 269. Lyphout, C., Nylen, P., & Östergren, L. G. (2012). Adhesion strength of HVOF sprayed IN718 coatings. *Journal of thermal spray technology*, *21*, 86-95.

- 270. Rombouts, M., Kruth, J. P., Froyen, L., & Mercelis, P. (2006). Fundamentals of selective laser melting of alloyed steel powders. *CIRP annals*, *55*(1), 187-192.
- 271. Lynch, M. E., Gu, W., El-Wardany, T., Hsu, A., Viens, D., Nardi, A., & Klecka, M. (2013). Design and topology/shape structural optimisation for additively manufactured cold sprayed components: This paper presents an additive manufactured cold spray component which is shape optimised to achieve 60% reduction in stress and 20% reduction in weight. *Virtual and Physical Prototyping*, 8(3), 213-231.
- 272. Ma, M., Wang, Z., & Zeng, X. (2015). Effect of energy input on microstructural evolution of direct laser fabricated IN718 alloy. *Materials Characterization*, 106, 420-427.
- 273. Ma, M., Wang, Z., Wang, D., & Zeng, X. (2013). Control of shape and performance for direct laser fabrication of precision large-scale metal parts with 316L Stainless Steel. *Optics & Laser Technology*, 45, 209-216.
- 274. Ma, W., Xie, Y., Chen, C., Fukanuma, H., Wang, J., Ren, Z., & Huang, R. (2019). Microstructural and mechanical properties of high-performance Inconel 718 alloy by cold spraying. *Journal of Alloys and Compounds*, 792, 456-467.
- 275. MacDonald, D., Fernández, R., Delloro, F., & Jodoin, B. (2017). Cold spraying of armstrong process titanium powder for additive manufacturing. *Journal of thermal spray technology*, 26, 598-609.
- 276. MacDonald, D., Nastic, A., & Jodoin, B. (2018). Understanding adhesion. *Cold-Spray Coatings: Recent Trends and Future Perspectives*, 421-450.
- 277. Madhavadas, V., Srivastava, D., Chadha, U., Raj, S. A., Sultan, M. T. H., Shahar, F. S., & Shah, A. U. M. (2022). A review on metal additive manufacturing for intricately shaped aerospace components. *CIRP Journal of Manufacturing Science and Technology*, *39*, 18-36.
- 278. Mahesh, K., Philip, J. T., Joshi, S. N., & Kuriachen, B. (2021). Machinability of Inconel 718: A critical review on the impact of cutting temperatures. *Materials and Manufacturing Processes*, *36*(7), 753-791.
- 279. Manikandan, S. G. K., Sivakumar, D., & Kamaraj, M. (2019). Welding the Inconel 718 superalloy: Reduction of micro-segregation and laves phases. Elsevier.
- 280. Martina, F., Williams, S. W., & Colegrove, P. (2013). Improved microstructure and increased mechanical properties of additive manufacture produced Ti-6Al-4V by interpass cold rolling.
- 281. Marzbanrad, B., Jahed, H., & Toyserkani, E. (2018). On the evolution of substrate's residual stress during cold spray process: A parametric study. *Materials & Design*, *138*, 90-102.

- 282. Matikainen, V., Koivuluoto, H., Milanti, A., & Vuoristo, P. (2015). Advanced coatings by novel high-kinetic thermal spray processes.
- 283. Mauer, G., Singh, R., Rauwald, K. H., Schrüfer, S., Wilson, S., & Vaßen, R. (2017). Diagnostics of cold-sprayed particle velocities approaching critical deposition conditions. *Journal of Thermal Spray Technology*, 26, 1423-1433.
- 284. Mauer, G., Vaßen, R., & Stöver, D. (2011). Plasma and particle temperature measurements in thermal spray: approaches and applications. *Journal of thermal spray technology*, 20, 391-406.
- 285. Mazhdi, M., & Tafreshi, M. J. (2018). The effects of gadolinium doping on the structural, morphological, optical, and photoluminescence properties of zinc oxide nanoparticles prepared by co-precipitation method. *Applied Physics A*, 124(12), 863.
- 286. Melchels, F. P., Domingos, M. A., Klein, T. J., Malda, J., Bartolo, P. J., & Hutmacher, D. W. (2012). Additive manufacturing of tissues and organs. *Progress in polymer science*, *37*(8), 1079-1104.
- 287. Melentiev, R., Yu, N., & Lubineau, G. (2021). Polymer metallization via cold spray additive manufacturing: A review of process control, coating qualities, and prospective applications. *Additive manufacturing*, 48, 102459.
- 288. Meng, X., Zhang, J., Zhao, J., Liang, Y., & Zhang, Y. (2011). Influence of gas temperature on microstructure and properties of cold spray 304 SS coating. *Journal of materials science & technology*, 27(9), 809-815.
- 289. Menon, N., & Skews, B. W. (2010). Shock wave configurations and flow structures in non-axisymmetric underexpanded sonic jets. *Shock Waves*, 20, 175-190.
- 290. Merchant, V. E., & Hewitt, J. A. (1997). Laser Based Method of Evaluating the Behavior of Surfaces and Surface Treatments at Transient High Temperatures and Pressures (p. 0111). Defence Research Establishment Atlantic.
- 291. Meyer, M. C., Yin, S., McDonnell, K. A., Stier, O., & Lupoi, R. (2016). Feed rate effect on particulate acceleration in cold spray under low stagnation pressure conditions. *Surface and Coatings Technology*, 304, 237-245.
- 292. Meyer, M., Caruso, F., & Lupoi, R. (2018). Particle velocity and dispersion of high Stokes number particles by PTV measurements inside a transparent supersonic Cold Spray nozzle. *International Journal of Multiphase Flow*, *106*, 296-310.
- 293. Meyer, M., Yin, S., & Lupoi, R. (2017). Particle in-flight velocity and dispersion measurements at increasing particle feed rates in cold spray. *Journal of Thermal Spray Technology*, 26, 60-70.

- 294. Milanti, A., Matikainen, V., Bolelli, G., Koivuluoto, H., Lusvarghi, L., & Vuoristo, P. (2016). Microstructure and sliding wear behavior of Fe-based coatings manufactured with HVOF and HVAF thermal spray processes. *Journal of Thermal Spray Technology*, 25, 1040-1055.
- 295. Milewski, J. O., & Milewski, J. O. (2017). Lasers, electron beams, plasma arcs. *Additive Manufacturing of Metals: From Fundamental Technology to Rocket Nozzles, Medical Implants, and Custom Jewelry*, 85-97.
- 296. Mittal, G., & Paul, S. (2022). Suspension and solution precursor plasma and HVOF spray: A review. *Journal of Thermal Spray Technology*, *31*(5), 1443-1475.
- 297. Montavon, G., Sampath, S., Berndt, C. C., Herman, H., & Coddet, C. (1995). Effects of vacuum plasma spray processing parameters on splat morphology. *Journal of Thermal Spray Technology*, *4*, 67-74.
- 298. Moridi, A., Gangaraj, S. H., Vezzu, S., & Guagliano, M. (2014). Number of passes and thickness effect on mechanical characteristics of cold spray coating. *Procedia Engineering*, 74, 449-459.
- 299. Moridi, A., Hassani-Gangaraj, S. M., Guagliano, M., & Dao, M. (2014). Cold spray coating: review of material systems and future perspectives. *Surface Engineering*, *30*(6), 369-395.
- 300. Moroni, M., Castellino, M., & De Girolamo, P. (2022). Numerical and Physical Modeling of Ponte Liscione (Guardialfiera, Molise) Dam Spillways and Stilling Basin. *Hydrology*, 9(12), 214.
- 301. Morrow, W. R., Qi, H., Kim, I., Mazumder, J., & Skerlos, S. J. (2007). Environmental aspects of laser-based and conventional tool and die manufacturing. *Journal of Cleaner Production*, 15(10), 932-943.
- 302. Mostafa, A., Picazo Rubio, I., Brailovski, V., Jahazi, M., & Medraj, M. (2017). Structure, texture and phases in 3D printed IN718 alloy subjected to homogenization and HIP treatments. *Metals*, 7(6), 196.
- 303. Mostaghimi, J., Chandra, S., Ghafouri-Azar, R., & Dolatabadi, A. (2003). Modeling thermal spray coating processes: a powerful tool in design and optimization. *Surface and Coatings Technology*, *163*, 1-11.
- 304. Motyka, M., Nowak, W. J., Wierzba, B., & Chrominski, W. (2020). Characterization of the Interface Between α and β Titanium Alloys in the Diffusion Couple. *Metallurgical and Materials Transactions A*, 51, 6584-6591.
- 305. Mukherjee, T., Zhang, W., & DebRoy, T. (2017). An improved prediction of residual stresses and distortion in additive manufacturing. *Computational Materials Science*, *126*, 360-372.

- 306. Murr, L. E. (2018). A metallographic review of 3D printing/additive manufacturing of metal and alloy products and components. *Metallography, Microstructure, and Analysis*, 7, 103-132.
- 307. Murr, L. E., Gaytan, S. M., Ceylan, A., Martinez, E., Martinez, J. L., Hernandez, D. H., ... & Wicker, R. B. (2010). Characterization of titanium aluminide alloy components fabricated by additive manufacturing using electron beam melting. *Acta materialia*, 58(5), 1887-1894.
- 308. Murr, L. E., Gaytan, S. M., Ramirez, D. A., Martinez, E., Hernandez, J., Amato, K. N., ... & Wicker, R. B. (2012). Metal fabrication by additive manufacturing using laser and electron beam melting technologies. *Journal of Materials Science & Technology*, 28(1), 1-14.
- 309. Murr, L. E., Martinez, E., Amato, K. N., Gaytan, S. M., Hernandez, J., Ramirez, D. A., ... & Wicker, R. B. (2012). Fabrication of metal and alloy components by additive manufacturing: examples of 3D materials science. *Journal of Materials Research and Technology*, *1*(1), 42-54.
- 310. Nadammal, N., Cabeza, S., Mishurova, T., Thiede, T., Kromm, A., Seyfert, C., ... & Bruno, G. (2017). Effect of hatch length on the development of microstructure, texture and residual stresses in selective laser melted superalloy Inconel 718. *Materials & Design*, 134, 139-150.
- 311. Nastic, A., Jodoin, B., Poirier, D., & Legoux, J. G. (2021). Particle temperature effect in cold spray: A study of soft particle deposition on hard substrate. *Surface and Coatings Technology*, 406, 126735.
- 312. Negi, S., Nambolan, A. A., Kapil, S., Joshi, P. S., Karunakaran, K. P., & Bhargava, P. (2020). Review on electron beam based additive manufacturing. *Rapid Prototyping Journal*, 26(3), 485-498.
- 313. Neikov, O. D. (2019). Powders for additive manufacturing processing. *Handbook of Non-Ferrous Metal Powders*, 2, 373-399.
- 314. Neo, R. G., Wu, K., Tan, S. C., & Zhou, W. (2022). Effect of spray distance and powder feed rate on particle velocity in cold spray processes. *Metals*, *12*(1), 75.
- 315. Ni, M., Chen, C., Wang, X., Wang, P., Li, R., Zhang, X., & Zhou, K. (2017). Anisotropic tensile behavior of in situ precipitation strengthened Inconel 718 fabricated by additive manufacturing. *Materials Science and Engineering:* A, 701, 344-351.
- 316. Nikbakht, R., Saadati, M., Kim, H. S., Jahazi, M., & Chromik, R. R. (2024). Multi-scale analysis of microstructural evolution and atomic bonding mechanisms in CoCrFeMnNi highentropy alloys upon cold spray impact. *Journal of Materials Science & Technology*.

- 317. Ning, X. J., Jang, J. H., & Kim, H. J. (2007). The effects of powder properties on in-flight particle velocity and deposition process during low pressure cold spray process. *Applied Surface Science*, 253(18), 7449-7455.
- 318. Ning, X. J., Wang, Q. S., Ma, Z., & Kim, H. J. (2010). Numerical study of in-flight particle parameters in low-pressure cold spray process. *Journal of Thermal Spray Technology*, 19, 1211-1217.
- 319. Nnaji, R. N., Bodude, M. A., Osoba, L. O., Fayomi, O. S. I., & Ochulor, F. E. (2020). Study on high-temperature oxidation kinetics of Haynes 282 and Inconel 718 nickel-based superalloys. *The International Journal of Advanced Manufacturing Technology*, *106*, 1149-1160.
- 320. Oksa, M., Turunen, E., Suhonen, T., Varis, T., & Hannula, S. P. (2011). Optimization and characterization of high velocity oxy-fuel sprayed coatings: techniques, materials, and applications. *Coatings*, *1*(1), 17-52.
- 321. Oliver, W. C., & Pharr, G. M. (1992). An improved technique for determining hardness and elastic modulus using load and displacement sensing indentation experiments. *Journal of materials research*, 7(6), 1564-1583.
- 322. Orme, M. E., Gschweitl, M., Ferrari, M., Vernon, R., Madera, I. J., Yancey, R., & Mouriaux, F. (2017). Additive manufacturing of lightweight, optimized, metallic components suitable for space flight. *Journal of Spacecraft and Rockets*, *54*(5), 1050-1059.
- 323. Osakada, K., & Shiomi, M. (2006). Flexible manufacturing of metallic products by selective laser melting of powder. *International Journal of Machine Tools and Manufacture*, 46(11), 1188-1193.
- 324. Osipovich, K., Kalashnikov, K., Chumaevskii, A., Gurianov, D., Kalashnikova, T., Vorontsov, A., ... & Kolubaev, E. (2023). Wire-feed electron beam additive manufacturing: A review. *Metals*, *13*(2), 279.
- 325. Oyinbo, S. T., & Jen, T. C. (2019). A comparative review on cold gas dynamic spraying processes and technologies. *Manufacturing Review*, *6*, 25.
- 326. Ozdemir, O. C. (2023). Process parameters and control. *Advances in Cold Spray: A Coating Deposition and Additive Manufacturing Process*, 89.
- 327. Ozdemir, O. C., Chen, Q., Muftu, S., & Champagne, V. K. (2019). Modeling the continuous heat generation in the cold spray coating process. *Journal of Thermal Spray Technology*, 28, 108-123.
- 328. Ozdemir, O. C., Widener, C. A., Carter, M. J., & Johnson, K. W. (2017). Predicting the effects of powder feeding rates on particle impact conditions and cold spray deposited coatings. *Journal of Thermal Spray Technology*, 26, 1598-1615.

- 329. Eason, P. D., Fewkes, J. A., Kennett, S. C., Eden, T. J., Tello, K., Kaufman, M. J., & Tiryakioğlu, M. (2011). On the characterization of bulk copper produced by cold gas dynamic spray processing in as fabricated and annealed conditions. *Materials Science and Engineering: A*, 528(28), 8174-8178.
- 330. Eason, P. D., Eden, T. J., Kennett, S. C., & Kaufman, M. J. (2012). A structure property processing comparison of cold rolled pm copper and cold gas dynamically sprayed copper. *J Powder Metall Min*, *1*(101), 2.
- 331. Palodhi, L., Das, B., & Singh, H. (2021). Effect of particle size and morphology on critical velocity and deformation behavior in cold spraying. *Journal of Materials Engineering and Performance*, *30*, 8276-8288.
- 332. Pan, J., Hu, S., Yang, L., Ding, K., & Ma, B. (2016). Numerical analysis of flame and particle behavior in an HVOF thermal spray process. *Materials & Design*, *96*, 370-376.
- 333. Pan, Z., Ding, D., Wu, B., Cuiuri, D., Li, H., & Norrish, J. (2018). Arc welding processes for additive manufacturing: a review. *Transactions on Intelligent Welding Manufacturing: Volume I No. 1 2017*, 3-24.
- 334. Papyrin, A. N., Klinkov, S. V., & Kosarev, V. F. (2003). Modeling of particle-substrate adhesive interaction under the cold spray process. *Thermal Spray 2003: Advancing the Science and Applying the Technology*, 1, 5-8.
- 335. Parimi, L. L., Attallah, M. M., Gebelin, J. C., & Reed, R. C. (2012). Direct laser fabrication of Inconel-718: Effects on distortion and microstructure. *Proceedings of the Superalloys*, 12.
- 336. Parimi, L. L., Ravi, G. A., Clark, D., & Attallah, M. M. (2014). Microstructural and texture development in direct laser fabricated IN718. *Materials Characterization*, 89, 102-111.
- 337. Patel, M., Thomas, J., & Joshi, H. C. (2021). Flow characterization of supersonic gas jets: Experiments and simulations. *Vacuum*, *192*, 110440.
- 338. Patel, R. R., Keshri, A. K., Dulikravich, G. S., & Agarwal, A. (2010). An experimental and computational methodology for near net shape fabrication of thin walled ceramic structures by plasma spray forming. *Journal of Materials Processing Technology*, 210(10), 1260-1269.
- 339. Pathak, S., & Saha, G. C. (2017). Development of sustainable cold spray coatings and 3D additive manufacturing components for repair/manufacturing applications: A critical review. *Coatings*, 7(8), 122.
- 340. Pattison, J., Celotto, S., Khan, A., & O'neill, W. (2008). Standoff distance and bow shock phenomena in the Cold Spray process. *Surface and Coatings Technology*, 202(8), 1443-1454.

- 341. Pattison, J., Celotto, S., Morgan, R., Bray, M., & O'neill, W. (2007). Cold gas dynamic manufacturing: A non-thermal approach to freeform fabrication. *International Journal of Machine Tools and Manufacture*, 47(3-4), 627-634.
- 342. Pawlowski, L. (2008). The science and engineering of thermal spray coatings. John Wiley & Sons.
- 343. Pereira, J. C., Borovkov, H., Zubiri, F., Guerra, M. C., & Caminos, J. (2021). Optimization of thin walls with sharp corners in SS316L and IN718 alloys manufactured with laser metal deposition. *Journal of Manufacturing and Materials Processing*, *5*(1), 5.
- 344. Pérez-Andrade, L. I., Gärtner, F., Villa-Vidaller, M., Klassen, T., Muñoz-Saldaña, J., & Alvarado-Orozco, J. M. (2019). Optimization of Inconel 718 thick deposits by cold spray processing and annealing. *Surface and Coatings Technology*, *378*, 124997.
- 345. Popovich, V. A., Borisov, E. V., Heurtebise, V., Riemslag, T., Popovich, A. A., & Sufiiarov, V. S. (2018). Creep and thermomechanical fatigue of functionally graded Inconel 718 produced by additive manufacturing. In *TMS 2018 147th Annual Meeting & Exhibition Supplemental Proceedings* (pp. 85-97). Springer International Publishing.
- 346. Popovich, V. A., Borisov, E. V., Popovich, A. A., Sufiiarov, V. S., Masaylo, D. V., & Alzina, L. (2017). Functionally graded Inconel 718 processed by additive manufacturing: Crystallographic texture, anisotropy of microstructure and mechanical properties. *Materials & Design*, 114, 441-449.
- 347. Popovich, V. A., Borisov, E. V., Popovich, A. A., Sufiiarov, V. S., Masaylo, D. V., & Alzina, L. (2017). Impact of heat treatment on mechanical behaviour of Inconel 718 processed with tailored microstructure by selective laser melting. *Materials & Design*, 131, 12-22.
- 348. Popovich, V. A., Borisov, E. V., Sufiyarov, V. S., & Popovich, A. A. (2019). Tailoring the properties in functionally graded alloy inconel 718 using additive technologies. *Metal Science and Heat Treatment*, 60, 701-709.
- 349. Prabhakar, P., Sames, W. J., Dehoff, R., & Babu, S. S. (2015). Computational modeling of residual stress formation during the electron beam melting process for Inconel 718. *Additive Manufacturing*, 7, 83-91.
- 350. Prashar, G., & Vasudev, H. (2021). A comprehensive review on sustainable cold spray additive manufacturing: State of the art, challenges and future challenges. *Journal of Cleaner Production*, 310, 127606.
- 351. Prashar, G., Vasudev, H., & Thakur, L. (2021). Thermal Spraying Fundamentals: Process Applications, Challenges, and Future Market. *Thermal Spray Coatings*, 1-36.

- 352. Pröbstle, M., Neumeier, S., Hopfenmüller, J., Freund, L. P., Niendorf, T., Schwarze, D., & Göken, M. (2016). Superior creep strength of a nickel-based superalloy produced by selective laser melting. *Materials Science and Engineering: A*, 674, 299-307.
- 353. Qi, H., Azer, M., & Ritter, A. (2009). Studies of standard heat treatment effects on microstructure and mechanical properties of laser net shape manufactured Inconel 718. *Metallurgical and Materials Transactions A*, 40, 2410-2422.
- 354. Radhakrishna, C. H., & Prasad Rao, K. (1997). The formation and control of Laves phase in superalloy 718 welds. *Journal of Materials Science*, *32*, 1977-1984.
- 355. Raghavan, N., Dehoff, R., Pannala, S., Simunovic, S., Kirka, M., Turner, J., ... & Babu, S. S. (2016). Numerical modeling of heat-transfer and the influence of process parameters on tailoring the grain morphology of IN718 in electron beam additive manufacturing. *Acta Materialia*, 112, 303-314.
- 356. Raghavan, S., Zhang, B., Wang, P., Sun, C. N., Nai, M. L. S., Li, T., & Wei, J. (2017). Effect of different heat treatments on the microstructure and mechanical properties in selective laser melted INCONEL 718 alloy. *Materials and Manufacturing Processes*, 32(14), 1588-1595.
- 357. Raletz, F., Vardelle, M., & Ezo'o, G. (2006). Critical particle velocity under cold spray conditions. *Surface and Coatings Technology*, 201(5), 1942-1947.
- 358. Ramesh, C. S., Devaraj, D. S., Keshavamurthy, R., & Sridhar, B. R. (2011). Slurry erosive wear behaviour of thermally sprayed Inconel-718 coatings by APS process. *Wear*, 271(9-10), 1365-1371.
- 359. Ran, R., Wang, Y., Zhang, Y. X., Fang, F., Wang, H. S., Yuan, G., & Wang, G. D. (2020). Microstructure, precipitates and mechanical properties of Inconel 718 alloy produced by two-stage cold rolling method. *Materials Science and Engineering: A*, 793, 139860.
- 360. Ranjan, P., Warton, W. J., & James, K. A. (2020). A comparison of physics-and correlation-based turbulence models at low Reynolds numbers. *Journal of Aircraft*, *57*(1), 128-142.
- 361. Rao, G. A., Srinivas, M., & Sarma, D. S. (2006). Influence of modified processing on structure and properties of hot isostatically pressed superalloy Inconel 718. *Materials Science and Engineering:* A, 418(1-2), 282-291.
- 362. Raoelison, R. N., Aubignat, E., Planche, M. P., Costil, S., Langlade, C., & Liao, H. (2016). Low pressure cold spraying under 6 bar pressure deposition: Exploration of high deposition efficiency solutions using a mathematical modelling. *Surface and Coatings Technology*, 302, 47-55.

- 363. Rashed, M. G. (2019). *Deformation behaviour of additively manufactured microlattice structures: a micro-structural investigation* (Doctoral dissertation, UNSW Sydney).
- 364. Rathinam, A., Rao, J. R., & Nair, B. U. (2011). Adsorption of phenol onto activated carbon from seaweed: Determination of the optimal experimental parameters using factorial design. *Journal of the Taiwan Institute of Chemical Engineers*, 42(6), 952-956.
- 365. Rayleigh, L. (1892). XVI. On the instability of a cylinder of viscous liquid under capillary force. *The London, Edinburgh, and Dublin Philosophical Magazine and Journal of Science*, 34(207), 145-154.
- 366. Raza, T., Andersson, J., & Svensson, L. E. (2018). Microstructure of selective laser melted alloy 718 in as-manufactured and post heat treated condition. *Procedia Manufacturing*, 25, 450-458.
- 367. Rech, S., Trentin, A., Vezzu, S., Vedelago, E., Legoux, J. G., & Irissou, E. (2014). Different cold spray deposition strategies: single-and multi-layers to repair aluminium alloy components. *Journal of thermal spray technology*, 23, 1237-1250.
- 368. Reddy, C. D., Zhang, Z. Q., Msolli, S., Guo, J., & Sridhar, N. (2021). Impact induced metallurgical and mechanical interlocking in metals. *Computational Materials Science*, 192, 110363.
- 369. Rocha, S. S. D., Adabo, G. L., Henriques, G. E. P., & Nóbilo, M. A. D. A. (2006). Vickers hardness of cast commercially pure titanium and Ti-6Al-4V alloy submitted to heat treatments. *Brazilian dental journal*, *17*, 126-129.
- 370. Romano, J., Ladani, L., Razmi, J., & Sadowski, M. (2015). Temperature distribution and melt geometry in laser and electron-beam melting processes—A comparison among common materials. *Additive Manufacturing*, *8*, 1-11.
- 371. Ruffo, M., Tuck, C., & Hague, R. (2006). Cost estimation for rapid manufacturing-laser sintering production for low to medium volumes. *Proceedings of the Institution of Mechanical Engineers, Part B: Journal of Engineering Manufacture*, 220(9), 1417-1427.
- 372. Rzeszotarska, M., Zasada, D., Płociński, T., Stępniowski, W. J., & Polański, M. (2023). On the influence of manufacturing parameters on the microstructure, mechanical properties and corrosion resistance of AISI 316L steel deposited by laser engineered net shaping (LENS®). *Materials*, 16(5), 1965.
- 373. Cadney, S., Brochu, M., Richer, P., & Jodoin, B. (2008). Cold gas dynamic spraying as a method for freeforming and joining materials. *Surface and Coatings Technology*, 202(12), 2801-2806.

- 374. Saint John, D. B., Joshi, S. B., Simpson, T. W., Qu, M., Rowatt, J. D., & Lou, Y. (2016). A Preliminary Examination of Variability Due to Build Location and Powder Feedstock in Additive Manufacture of Inconel 718 using Laser-Based Powder Bed Fusion.
- 375. Saleh, M., Luzin, V., & Spencer, K. (2014). Analysis of the residual stress and bonding mechanism in the cold spray technique using experimental and numerical methods. *Surface and Coatings Technology*, 252, 15-28.
- 376. Samaee, V., Sandfeld, S., Idrissi, H., Groten, J., Pardoen, T., Schwaiger, R., & Schryvers, D. (2020). Dislocation structures and the role of grain boundaries in cyclically deformed Ni micropillars. *Materials Science and Engineering:* A, 769, 138295.
- 377. Samareh, B., & Dolatabadi, A. (2007). A three-dimensional analysis of the cold spray process: the effects of substrate location and shape. *Journal of thermal spray technology*, *16*, 634-642.
- 378. Samareh, B., Stier, O., Lüthen, V., & Dolatabadi, A. (2009). Assessment of CFD modeling via flow visualization in cold spray process. *Journal of thermal spray technology*, 18, 934-943.
- 379. Sames, W. (2015). Additive manufacturing of Inconel 718 using electron beam melting: processing, post-processing, & mechanical properties (Doctoral dissertation).
- 380. Sames, W. J., Medina, F., Peter, W. H., Babu, S. S., & Dehoff, R. R. (2014, November). Effect of process control and powder quality on Inconel 718 produced using electron beam melting. In 8th international symposium on superalloy 718 and derivatives (pp. 409-423). Hoboken, NJ, USA: John Wiley & Sons, Inc..
- 381. Sames, W. J., Unocic, K. A., Dehoff, R. R., Lolla, T., & Babu, S. S. (2014). Thermal effects on microstructural heterogeneity of Inconel 718 materials fabricated by electron beam melting. *Journal of materials research*, 29(17), 1920-1930.
- 382. Sames, W. J., Unocic, K. A., Helmreich, G. W., Kirka, M. M., Medina, F., Dehoff, R. R., & Babu, S. S. (2017). Feasibility of in situ controlled heat treatment (ISHT) of Inconel 718 during electron beam melting additive manufacturing. *Additive manufacturing*, *13*, 156-165.
- 383. Sampath, S., Dwivedi, G., Valarezo, A., & Choi, B. (2013). Partnership for accelerated insertion of new technology: case study for thermal spray technology. *Integrating Materials and Manufacturing Innovation*, 2, 1-35.
- 384. Sampath, S., Herman, H., & Greenlaw, R. (2003). *U.S. Patent No.* 6,576,861. Washington, DC: U.S. Patent and Trademark Office.
- 385. Schaak, C., Tillmann, W., Schaper, M., & Aydinöz, M. E. (2016). Process gas infiltration in Inconel 718 samples during SLM processing. *RTe Journal*.

- 386. Schmidt, T., Gärtner, F., & Kreye, H. (2003). High strain rate deformation phenomena in explosive powder compaction and cold gas spraying. *Thermal Spray 2003: Advancing the Science and Applying the Technology*, 1, 5-8.
- 387. Schmidt, T., Gärtner, F., Assadi, H., & Kreye, H. (2006). Development of a generalized parameter window for cold spray deposition. *Acta materialia*, *54*(3), 729-742.
- 388. Schubert, C., Van Langeveld, M. C., & Donoso, L. A. (2014). Innovations in 3D printing: a 3D overview from optics to organs. *British Journal of Ophthalmology*, *98*(2), 159-161.
- 389. Schwartz, M. (2010). Coatings (Thermal Spray Processes). In *Innovations in Materials Manufacturing, Fabrication, and Environmental Safety* (pp. 403-462). CRC Press.
- 390. Scrivani, A., Bardi, U., Carrafiello, L., Lavacchi, A., Niccolai, F., & Rizzi, G. (2003). A comparative study of high velocity oxygen fuel, vacuum plasma spray, and axial plasma spray for the deposition of CoNiCrAlY bond coat alloy. *Journal of thermal spray technology*, *12*, 504-507.
- 391. Seede, R., Mostafa, A., Brailovski, V., Jahazi, M., & Medraj, M. (2018). Microstructural and microhardness evolution from homogenization and hot isostatic pressing on selective laser melted Inconel 718: structure, texture, and phases. *Journal of Manufacturing and Materials Processing*, 2(2), 30.
- 392. Semiatin, S. L. (2020). An overview of the thermomechanical processing of α/β titanium alloys: current status and future research opportunities. *Metallurgical and Materials Transactions A*, 51(6), 2593-2625.
- 393. Seng, D. H. L., Zhang, Z., Zhang, Z. Q., Meng, T. L., Teo, S. L., Tan, B. H., ... & Ba, T. (2023). Impact of spray angle and particle velocity in cold sprayed IN718 coatings. *Surface and Coatings Technology*, 466, 129623.
- 394. Sezgin, H., & Berkalp, O. B. (2018). Analysis of the effects of fabric reinforcement parameters on the mechanical properties of textile-based hybrid composites by full factorial experimental design method. *Journal of Industrial Textiles*, 48(3), 580-598.
- 395. Shah, K., ul Haq, I., Khan, A., Shah, S. A., Khan, M., & Pinkerton, A. J. (2014). Parametric study of development of Inconel-steel functionally graded materials by laser direct metal deposition. *Materials & Design* (1980-2015), 54, 531-538.
- 396. Shapiro, A. A., Borgonia, J. P., Chen, Q. N., Dillon, R. P., McEnerney, B., Polit-Casillas, R., & Soloway, L. (2016). Additive manufacturing for aerospace flight applications. *Journal of Spacecraft and Rockets*, 952-959.
- 397. Shassere, B., Greeley, D., Okello, A., Kirka, M., Nandwana, P., & Dehoff, R. (2018). Correlation of microstructure to creep response of hot isostatically pressed and aged electron beam melted Inconel 718. *Metallurgical and Materials Transactions A*, 49, 5107-5117.

- 398. Shayegan, G., Mahmoudi, H., Ghelichi, R., Villafuerte, J., Wang, J., Guagliano, M., & Jahed, H. (2014). Residual stress induced by cold spray coating of magnesium AZ31B extrusion. *Materials & Design*, 60, 72-84.
- 399. Shiomi, M., Osakada, K., Nakamura, K., Yamashita, T., & Abe, F. (2004). Residual stress within metallic model made by selective laser melting process. *CIRP annals*, *53*(1), 195-198.
- 400. Shirazi, S. F. S., Gharehkhani, S., Mehrali, M., Yarmand, H., Metselaar, H. S. C., Kadri, N. A., & Osman, N. A. A. (2015). A review on powder-based additive manufacturing for tissue engineering: selective laser sintering and inkjet 3D printing. *Science and technology of advanced materials*, 16(3), 033502.
- 401. Siegmann, S., & Abert, C. (2013). 100 years of thermal spray: About the inventor Max Ulrich Schoop. *Surface and Coatings Technology*, 220, 3-13.
- 402. Sing, S. L., Tey, C. F., Tan, J. H. K., Huang, S., & Yeong, W. Y. (2020). 3D printing of metals in rapid prototyping of biomaterials: Techniques in additive manufacturing. In *Rapid prototyping of biomaterials* (pp. 17-40). Woodhead Publishing.
- 403. Singh, D. D., Arjula, S., & Reddy, A. R. (2021). Functionally graded materials manufactured by direct energy deposition: a review. *Materials Today: Proceedings*, 47, 2450-2456.
- 404. Singh, R., Rauwald, K. H., Wessel, E., Mauer, G., Schruefer, S., Barth, A., ... & Vassen, R. (2017). Effects of substrate roughness and spray-angle on deposition behavior of cold-sprayed Inconel 718. *Surface and Coatings technology*, *319*, 249-259.
- 405. Singh, R., Schruefer, S., Wilson, S., Gibmeier, J., & Vassen, R. (2018). Influence of coating thickness on residual stress and adhesion-strength of cold-sprayed Inconel 718 coatings. *Surface and Coatings technology*, *350*, 64-73.
- 406. Singh, S., Berndt, C. C., Singh Raman, R. K., Singh, H., & Ang, A. S. (2023). Applications and developments of thermal spray coatings for the iron and steel industry. *Materials*, *16*(2), 516.
- 407. Slama, C., & Abdellaoui, M. (2000). Structural characterization of the aged Inconel 718. *Journal of alloys and compounds*, 306(1-2), 277-284.
- 408. Smith, D. H., Bicknell, J., Jorgensen, L., Patterson, B. M., Cordes, N. L., Tsukrov, I., & Knezevic, M. (2016). Microstructure and mechanical behavior of direct metal laser sintered Inconel alloy 718. *Materials Characterization*, 113, 1-9.

- 409. Snyder, J. C., & Thole, K. A. (2019, June). Effect of additive manufacturing process parameters on turbine cooling. In *Turbo Expo: Power for Land, Sea, and Air* (Vol. 58653, p. V05BT21A002). American Society of Mechanical Engineers.
- 410. Sochalski-Kolbus, L. M., Payzant, E. A., Cornwell, P. A., Watkins, T. R., Babu, S. S., Dehoff, R. R., ... & Duty, C. (2015). Comparison of residual stresses in Inconel 718 simple parts made by electron beam melting and direct laser metal sintering. *Metallurgical and Materials Transactions A*, 46, 1419-1432.
- 411. Sola, A., & Nouri, A. (2019). Microstructural porosity in additive manufacturing: The formation and detection of pores in metal parts fabricated by powder bed fusion. *Journal of Advanced Manufacturing and Processing*, *1*(3), e10021.
- 412. Soller, S., Barata, A., Beyer, S., Dahlhaus, A., Guichard, D., Humbert, E., ... & Zeiss, W. (2016). Selective laser melting (SLM) of Inconel 718 and stainless steel injectors for liquid rocket engines. *Proceedings of the Space Propulsion*.
- 413. Sonar, T., Balasubramanian, V., Malarvizhi, S., Venkateswaran, T., & Sivakumar, D. (2021). An overview on welding of Inconel 718 alloy-Effect of welding processes on microstructural evolution and mechanical properties of joints. *Materials Characterization*, 174, 110997.
- 414. Song, X., Everaerts, J., Zhai, W., Zheng, H., Tan, A. W. Y., Sun, W., ... & Korsunsky, A. M. (2018). Residual stresses in single particle splat of metal cold spray process—Numerical simulation and direct measurement. *Materials Letters*, 230, 152-156.
- 415. Song, X., Zhai, W., Huang, R., Fu, J., Fu, M. W., & Li, F. (2021). Metal-based 3D-printed micro parts & structures. In *Encyclopedia of Materials: Metals and Alloys* (pp. 448-461). Elsevier.
- 416. Sova, A., Grigoriev, S., Okunkova, A., & Smurov, I. (2013). Potential of cold gas dynamic spray as additive manufacturing technology. *The International Journal of Advanced Manufacturing Technology*, 69, 2269-2278.
- 417. Sova, A., Smurov, I., Doubenskaia, M., & Petrovskiy, P. (2018). Deposition of aluminum powder by cold spray micronozzle. *The International Journal of Advanced Manufacturing Technology*, 95, 3745-3752.
- 418. Stevens, E. L., Toman, J., To, A. C., & Chmielus, M. (2017). Variation of hardness, microstructure, and Laves phase distribution in direct laser deposited alloy 718 cuboids. *Materials & design*, 119, 188-198
- 419. Stokes, J., & Looney, L. (2001). HVOF system definition to maximise the thickness of formed components. *Surface and Coatings Technology*, *148*(1), 18-24.

- 420. Stoltenhoff, T., Borchers, C., Gärtner, F., & Kreye, H. (2006). Microstructures and key properties of cold-sprayed and thermally sprayed copper coatings. *Surface and Coatings Technology*, 200(16-17), 4947-4960.
- 421. Stoltenhoff, T., Kreye, H., & Richter, H. J. (2002). An analysis of the cold spray process and its coatings. *Journal of Thermal spray technology*, *11*, 542-550.
- 422. Strondl, A., Fischer, R., Frommeyer, G., & Schneider, A. (2008). Investigations of MX and γ'/γ "precipitates in the nickel-based superalloy 718 produced by electron beam melting. *Materials Science and Engineering: A*, 480(1-2), 138-147.
- 423. Strondl, A., Palm, M., Gnauk, J., & Frommeyer, G. (2011). Microstructure and mechanical properties of nickel based superalloy IN718 produced by rapid prototyping with electron beam melting (EBM). *Materials Science and Technology*, 27(5), 876-883.
- 424. Suárez, A., Veiga, F., Bhujangrao, T., & Aldalur, E. (2022). Study of the Mechanical Behavior of Topologically Optimized Arc Wire Direct Energy Deposition Aerospace Fixtures. *Journal of Materials Engineering and Performance*, 31(8), 6270-6282.
- 425. Sudharshan Phani, P., Srinivasa Rao, D., Joshi, S. V., & Sundararajan, G. (2007). Effect of process parameters and heat treatments on properties of cold sprayed copper coatings. *Journal of Thermal Spray Technology*, *16*, 425-434.
- 426. Suhonen, T., Varis, T., Dosta, S., Torrell, M., & Guilemany, J. M. (2013). Residual stress development in cold sprayed Al, Cu and Ti coatings. *Acta Materialia*, *61*(17), 6329-6337.
- 427. Sui, S., Chen, J., Fan, E., Yang, H., Lin, X., & Huang, W. (2017). The influence of Laves phases on the high-cycle fatigue behavior of laser additive manufactured Inconel 718. *Materials Science and Engineering:* A, 695, 6-13.
- 428. Sun, C., Wang, Y., McMurtrey, M. D., Jerred, N. D., Liou, F., & Li, J. (2021). Additive manufacturing for energy: A review. *Applied Energy*, 282, 116041.
- 429. Sun, W., Tan, A. W. Y., Bhowmik, A., Marinescu, I., Song, X., Zhai, W., ... & Liu, E. (2018). Deposition characteristics of cold sprayed Inconel 718 particles on Inconel 718 substrates with different surface conditions. *Materials Science and Engineering: A*, 720, 75-84.
- 430. Sun, W., Tan, A. W. Y., Wu, K., Yin, S., Yang, X., Marinescu, I., & Liu, E. (2020). Post-process treatments on supersonic cold sprayed coatings: A review. *Coatings*, *10*(2), 123.
- 431. Sundararajan, G., Chavan, N. M., & Kumar, S. (2013). The elastic modulus of cold spray coatings: influence of inter-splat boundary cracking. *Journal of thermal spray technology*, 22, 1348-1357.

- 432. Sundararajan, G., Chavan, N. M., Sivakumar, G., & Sudharshan Phani, P. (2010). Evaluation of parameters for assessment of inter-splat bond strength in cold-sprayed coatings. *Journal of Thermal Spray Technology*, *19*, 1255-1266.
- 433. Sundararajan, G., Rao, D. S., Sivakumar, G., & Joshi, S. V. (2013). Detonation spray coatings. *Encyclopedia of Tribology*, 736-742.
- 434. Svetlizky, D., Zheng, B., Buta, T., Zhou, Y., Golan, O., Breiman, U., ... & Eliaz, N. (2020). Directed energy deposition of Al 5xxx alloy using Laser Engineered Net Shaping (LENS®). *Materials & Design*, 192, 108763.
- 435. Tabbara, H., Gu, S., McCartney, D. G., Price, T. S., & Shipway, P. H. (2011). Study on process optimization of cold gas spraying. *Journal of Thermal Spray Technology*, 20, 608-620.
- 436. Talib, R. J., Saad, S., Toff, M. R. M., & Hashim, H. (2003). Thermal spray coating technology: A review. *Solid State Sci Technol*, *11*(1), 109-117.
- 437. Taminger, K., & Hafley, R. A. (2003, July). Electron beam freeform fabrication: a rapid metal deposition process. In *3rd annual automotive composites conference*.
- 438. Tan, A. W. Y., Sun, W., Phang, Y. P., Dai, M., Marinescu, I., Dong, Z., & Liu, E. (2017). Effects of traverse scanning speed of spray nozzle on the microstructure and mechanical properties of cold-sprayed Ti6Al4V coatings. *Journal of Thermal Spray Technology*, 26, 1484-1497.
- 439. Taylor, K., Jodoin, B., & Karov, J. (2006). Particle loading effect in cold spray. *Journal of Thermal Spray Technology*, 15, 273-279.
- 440. Tayon, W. A., Shenoy, R. N., Redding, M. R., Keith Bird, R., & Hafley, R. A. (2014). Correlation between microstructure and mechanical properties in an Inconel 718 deposit produced via electron beam freeform fabrication. *Journal of Manufacturing Science and Engineering*, 136(6), 061005.
- 441. Tejero-Martin, D., Rezvani Rad, M., McDonald, A., & Hussain, T. (2019). Beyond traditional coatings: A review on thermal-sprayed functional and smart coatings. *Journal of Thermal Spray Technology*, 28, 598-644.
- 442. Thompson, S. M., Bian, L., Shamsaei, N., & Yadollahi, A. (2015). An overview of Direct Laser Deposition for additive manufacturing; Part I: Transport phenomena, modeling and diagnostics. *Additive Manufacturing*, 8, 36-62.
- 443. Tiamiyu, A. A., Sun, Y., Nelson, K. A., & Schuh, C. A. (2021). Site-specific study of jetting, bonding, and local deformation during high-velocity metallic microparticle impact. *Acta Materialia*, 202, 159-169.

- 444. Tian, Y., McAllister, D., Colijn, H., Mills, M., Farson, D., Nordin, M., & Babu, S. (2014). Rationalization of microstructure heterogeneity in INCONEL 718 builds made by the direct laser additive manufacturing process. *Metallurgical and Materials Transactions A*, 45, 4470-4483.
- 445. Tillmann, W., Schaak, C., Nellesen, J., Schaper, M., Aydinöz, M. U., & Hoyer, K. P. (2017). Hot isostatic pressing of IN718 components manufactured by selective laser melting. *Additive Manufacturing*, *13*, 93-102.
- 446. Tillmann, W., Schaak, C., Nellesen, J., Schaper, M., Aydinöz, M. E., & Niendorf, T. (2015). Functional encapsulation of laser melted Inconel 718 by Arc-PVD and HVOF for post compacting by hot isostatic pressing. *Powder Metallurgy*, 58(4), 259-264.
- 447. Torrance, J. W., & Stefanescu, D. M. (2004). Investigation on the effect of surface roughness on the static mechanical properties of thin-wall ductile iron castings. *AFS Trans*, *112*, 757-772.
- 448. Trosch, T., Strößner, J., Völkl, R., & Glatzel, U. (2016). Microstructure and mechanical properties of selective laser melted Inconel 718 compared to forging and casting. *Materials letters*, 164, 428-431.
- 449. Tucho, W. M., Cuvillier, P., Sjolyst-Kverneland, A., & Hansen, V. (2017). Microstructure and hardness studies of Inconel 718 manufactured by selective laser melting before and after solution heat treatment. *Materials Science and Engineering:* A, 689, 220-232.
- 450. Tucker Jr, R. C. (2013). Introduction to thermal spray technology (pp. 3-9). ASM International.
- 451. Unabia, R., Candidato Jr, R., & Pawłowski, L. (2018). Current progress in solution precursor plasma spraying of cermets: a review. *Metals*, 8(6), 420.
- 452. Unocic, K. A., Kolbus, L. M., Dehoff, R. R., Dryepondt, S. N., & Pint, B. A. (2014). High-temperature performance of UNS N07718 processed by additive manufacturing. *NACE corrosion*, 2014.
- 453. Uriondo, A., Esperon-Miguez, M., & Perinpanayagam, S. (2015). The present and future of additive manufacturing in the aerospace sector: A review of important aspects. *Proceedings of the Institution of Mechanical Engineers, Part G: Journal of Aerospace Engineering*, 229(11), 2132-2147.
- 454. Vadla, S. R., & Doom, J. (2018). Analysis of jet characteristics among various cold spray nozzles. *Journal of Thermal Spray and Engineering*, 1(1), 24-31.

- 455. Vafadar, A., Guzzomi, F., Rassau, A., & Hayward, K. (2021). Advances in metal additive manufacturing: a review of common processes, industrial applications, and current challenges. *Applied Sciences*, *11*(3), 1213.
- 456. Valdez, M., Kozuch, C., Faierson, E. J., & Jasiuk, I. (2017). Induced porosity in Super Alloy 718 through the laser additive manufacturing process: Microstructure and mechanical properties. *Journal of Alloys and Compounds*, 725, 757-764.
- 457. Valentin, M., Arnaud, C., & Kling, R. (2019, March). Additive manufacturing by wire based laser metal deposition. In *Laser 3D Manufacturing VI* (Vol. 10909, pp. 86-92). SPIE.
- 458. Van Steenkiste, T., & Smith, J. R. (2004). Evaluation of coatings produced via kinetic and cold spray processes. *Journal of Thermal Spray Technology*, *13*, 274-282.
- 459. Varadaraajan, V., & Mohanty, P. (2017). Design and optimization of rectangular cold spray nozzle: Radial injection angle, expansion ratio and traverse speed. *Surface and Coatings Technology*, *316*, 246-254.
- 460. Vardelle, A., Moreau, C., Akedo, J., Ashrafizadeh, H., Berndt, C. C., Berghaus, J. O., ... & Vuoristo, P. (2016). The 2016 thermal spray roadmap. *Journal of Thermal Spray Technology*, 25, 1376-1440.
- 461. Vardelle, M., Vardelle, A., & Fauchais, P. (1993). Spray parameters and particle behavior relationships during plasma spraying. *Journal of Thermal Spray Technology*, 2, 79-91.
- 462. Vaz, R. F., Garfias, A., Albaladejo, V., Sanchez, J., & Cano, I. G. (2023). A review of advances in cold spray additive manufacturing. *Coatings*, *13*(2), 267.
- 463. Vernhes, L., Lee, D. A., Poirier, D., Li, D., & Klemberg-Sapieha, J. E. (2013). HVOF coating case study for power plant process control ball valve application. *Journal of thermal spray technology*, 22, 1184-1192.
- 464. Vilardell, A. M., Cinca, N., Concustell, A., Dosta, S., Cano, I. G., & Guilemany, J. M. (2015). Cold spray as an emerging technology for biocompatible and antibacterial coatings: state of art. *Journal of Materials Science*, *50*, 4441-4462.
- 465. Villafuerte, J. (2010). Recent trends in cold spray technology: looking at the future. *Surface Engineering*, 26(6), 393-394.
- 466. Viscusi, A., Astarita, A., Gatta, R. D., & Rubino, F. (2019). A perspective review on the bonding mechanisms in cold gas dynamic spray. *Surface Engineering*, *35*(9), 743-771.
- 467. Viswanathan, V., Katiyar, N. K., Goel, G., Matthews, A., & Goel, S. (2021). Role of thermal spray in combating climate change. *Emergent Materials*, 1-15.
- 468. Walker, M. (2018). Microstructure and bonding mechanisms in cold spray coatings. *Materials Science and Technology*, *34*(17), 2057-2077.

- 469. Wang, Q., & Zhang, M. X. (2013). Review on recent research and development of cold spray technologies. *Key Engineering Materials*, *533*, 1-52.
- 470. Wang, X., & Chou, K. (2017). Electron backscatter diffraction analysis of Inconel 718 parts fabricated by selective laser melting additive manufacturing. *Jom*, 69, 402-408.
- 471. Wang, X., & Chou, Y. K. (2015, November). A method to estimate residual stress in metal parts made by Selective Laser Melting. In *ASME International Mechanical Engineering Congress and Exposition* (Vol. 57359, p. V02AT02A015). American Society of Mechanical Engineers.
- 472. Wang, X., Keya, T., & Chou, K. (2016). Build height effect on the Inconel 718 parts fabricated by selective laser melting. *Procedia Manufacturing*, *5*, 1006-1017.
- 473. Wang, Z., Guan, K., Gao, M., Li, X., Chen, X., & Zeng, X. (2012). The microstructure and mechanical properties of deposited-IN718 by selective laser melting. *Journal of alloys and compounds*, *513*, 518-523.
- 474. Watanabe, T., Ikeda, K., Katayama, M., & Inada, Y. (2016, May). In-situ XAFS study for calcination process of Cr catalyst supported on γ-Al2O3 and SiO2. In *Journal of Physics: Conference Series* (Vol. 712, No. 1, p. 012073). IOP Publishing.
- 475. Wei, C., Zhang, Z., Cheng, D., Sun, Z., Zhu, M., & Li, L. (2020). An overview of laser-based multiple metallic material additive manufacturing: from macro-to micro-scales. *International Journal of Extreme Manufacturing*, *3*(1), 012003.
- 476. Williams, S. W., Martina, F., Addison, A. C., Ding, J., Pardal, G., & Colegrove, P. (2016). Wire+ arc additive manufacturing. *Materials science and technology*, *32*(7), 641-647.
- 477. Winnicki, M. (2021). Advanced functional metal-ceramic and ceramic coatings deposited by low-pressure cold spraying: a review. *Coatings*, *11*(9), 1044.
- 478. Winnicki, M., Małachowska, A., Baszczuk, A., Rutkowska-Gorczyca, M., Kukla, D., Lachowicz, M., & Ambroziak, A. (2017). Corrosion protection and electrical conductivity of copper coatings deposited by low-pressure cold spraying. *Surface and Coatings Technology*, *318*, 90-98.
- 479. Winnicki, M., Małachowska, A., Dudzik, G., Rutkowska-Gorczyca, M., Marciniak, M., Abramski, K., ... & Pawłowski, L. (2015). Numerical and experimental analysis of copper particles velocity in low-pressure cold spraying process. *Surface and Coatings Technology*, 268, 230-240.
- 480. Wong, W., Irissou, E., Vo, P., Sone, M., Bernier, F., Legoux, J. G., ... & Yue, S. (2013). Cold spray forming of Inconel 718. *Journal of thermal spray technology*, 22, 413-421.

- 481. Wu, X., Zhang, J., Zhou, X., Cui, H., & Liu, J. (2012). Advanced cold spray technology: Deposition characteristics and potential applications. *Science China Technological Sciences*, *55*, 357-368.
- 482. Xanthopoulou, G., Marinou, A., Vekinis, G., Lekatou, A., & Vardavoulias, M. (2014). Ni-Al and NiO-Al composite coatings by combustion-assisted flame spraying. *Coatings*, 4(2), 231-252.
- 483. Xia, M., Gu, D., Yu, G., Dai, D., Chen, H., & Shi, Q. (2016). Influence of hatch spacing on heat and mass transfer, thermodynamics and laser processability during additive manufacturing of Inconel 718 alloy. *International Journal of Machine Tools and Manufacture*, 109, 147-157.
- 484. Xiao, Q., Tsai, H. M., Papamoschou, D., & Johnson, A. (2009). Experimental and numerical study of jet mixing from a shock-containing nozzle. *Journal of Propulsion and Power*, 25(3), 688-696.
- 485. Xu, Y., Li, W., Qu, L., Yang, X., Song, B., Lupoi, R., & Yin, S. (2021). Solid-state cold spraying of FeCoCrNiMn high-entropy alloy: an insight into microstructure evolution and oxidation behavior at 700-900 C. *Journal of Materials Science & Technology*, 68, 172-183.
- 486. Xu, Z., Hyde, C. J., Tuck, C., & Clare, A. T. (2018). Creep behaviour of inconel 718 processed by laser powder bed fusion. *Journal of Materials Processing Technology*, 256, 13-24.
- 487. Xu, Z., Murray, J. W., Hyde, C. J., & Clare, A. T. (2018). Effect of post processing on the creep performance of laser powder bed fused Inconel 718. *Additive Manufacturing*, 24, 486-497.
- 488. Yadroitsev, I., Krakhmalev, P., Yadroitsava, I., & Du Plessis, A. (2018). Qualification of Ti6Al4V ELI alloy produced by laser powder bed fusion for biomedical applications. *Jom*, 70, 372-377.
- 489. Yadroitsev, I., Yadroitsava, I., Du Plessis, A., & MacDonald, E. (Eds.). (2021). Fundamentals of laser powder bed fusion of metals. Elsevier.
- 490. Yan, M., & Yu, P. (2015). An Overview of densification, microstructure and mechanical property of additively manufactured Ti-6Al-4V—Comparison among selective laser melting, electron beam melting, laser metal deposition and selective laser sintering, and with conventional powder. IntechOpen.
- 491. Yang, Y., Lu, J. B., Luo, Z. Y., & Wang, D. (2012). Accuracy and density optimization in directly fabricating customized orthodontic production by selective laser melting. *Rapid Prototyping Journal*, *18*(6), 482-489.

- 492. Yin, S., & Lupoi, R. (2021). Manufacturing Parameters for Cold Spray Additive Manufacturing. In *Cold Spray Additive Manufacturing: From Fundamentals to Applications* (pp. 53-67). Cham: Springer International Publishing.
- 493. Yin, S., Aldwell, B., & Lupoi, R. (2018). Cold spray additive manufacture and component restoration. *Cold-Spray Coatings: Recent Trends and Future perspectives*, 195-224.
- 494. Yin, S., Cavaliere, P., Aldwell, B., Jenkins, R., Liao, H., Li, W., & Lupoi, R. (2018). Cold spray additive manufacturing and repair: Fundamentals and applications. *Additive manufacturing*, 21, 628-650.
- 495. Yin, S., Cizek, J., Suo, X., Li, W., & Liao, H. (2019). Thermal spray technology. *Advances in Materials Science and Engineering*, 2019.
- 496. Yin, S., Liu, Q., Liao, H., & Wang, X. (2014). Effect of injection pressure on particle acceleration, dispersion and deposition in cold spray. *Computational materials science*, 90, 7-15.
- 497. Yin, S., Meyer, M., Li, W., Liao, H., & Lupoi, R. (2016). Gas flow, particle acceleration, and heat transfer in cold spray: a review. *Journal of Thermal Spray Technology*, 25, 874-896.
- 498. Yin, S., Suo, X., Xie, Y., Li, W., Lupoi, R., & Liao, H. (2015). Effect of substrate temperature on interfacial bonding for cold spray of Ni onto Cu. *Journal of materials science*, *50*, 7448-7457.
- 499. Yin, S., Wang, X. F., Li, W. Y., & Li, Y. (2012). Numerical study on the effect of substrate size on the supersonic jet flow and temperature distribution within the substrate in cold spraying. *Journal of thermal spray technology*, 21, 628-635.
- 500. You, X., Tan, Y., Shi, S., Yang, J. M., Wang, Y., Li, J., & You, Q. (2017). Effect of solution heat treatment on the precipitation behavior and strengthening mechanisms of electron beam smelted Inconel 718 superalloy. *Materials Science and Engineering: A*, 689, 257-268.
- 501. Yu, J., Rombouts, M., Maes, G., & Motmans, F. (2012). Material properties of Ti6Al4V parts produced by laser metal deposition. *Physics Procedia*, *39*, 416-424.
- 502. Zahiri, S. H., Phan, T. D., Masood, S. H., & Jahedi, M. (2014). Development of holistic three-dimensional models for cold spray supersonic jet. *Journal of thermal spray technology*, 23, 919-933.
- 503. Zavalan, F. L., & Rona, A. (2023). A workflow for designing contoured axisymmetric nozzles for enhancing additively manufactured cold spray deposits. *Additive Manufacturing*, 62, 103379.
- 504. Zhai, Y., Lados, D. A., Brown, E. J., & Vigilante, G. N. (2019). Understanding the microstructure and mechanical properties of Ti-6Al-4V and Inconel 718 alloys manufactured by Laser Engineered Net Shaping. *Additive Manufacturing*, 27, 334-344.

- 505. Zhang, D., Niu, W., Cao, X., & Liu, Z. (2015). Effect of standard heat treatment on the microstructure and mechanical properties of selective laser melting manufactured Inconel 718 superalloy. *Materials Science and Engineering: A*, 644, 32-40.
- 506. Zhang, K., Wang, S., Liu, W., & Shang, X. (2014). Characterization of stainless steel parts by laser metal deposition shaping. *Materials & Design*, 55, 104-119.
- 507. Zhang, Q. L., Yao, J. H., & Mazumder, J. (2011). Laser direct metal deposition technology and microstructure and composition segregation of Inconel 718 superalloy. *Journal of Iron and Steel Research, International*, 18(4), 73-78.
- 508. Zhang, Y., Jarosinski, W., Jung, Y. G., & Zhang, J. (2018). Additive manufacturing processes and equipment. In *Additive manufacturing* (pp. 39-51). Butterworth-Heinemann.
- 509. Zhang, Z., Seng, D. H. L., Lin, M., Teo, S. L., Meng, T. L., Lee, C. J. J., ... & Pan, J. (2021). Cold spray deposition of Inconel 718 in comparison with atmospheric plasma spray deposition. *Applied Surface Science*, 535, 147704.
- 510. Zhao, X., Chen, J., Lin, X., & Huang, W. (2008). Study on microstructure and mechanical properties of laser rapid forming Inconel 718. *Materials Science and Engineering: A*, 478(1-2), 119-124.
- 511. Zheng, L., Schmitz, G., Meng, Y., Chellali, R., & Schlesiger, R. (2012). Mechanism of intermediate temperature embrittlement of Ni and Ni-based superalloys. *Critical Reviews in Solid State and Materials Sciences*, *37*(3), 181-214.
- 512. Zhong, M., Yang, L., Liu, W., Huang, T., & He, J. (2005, January). Laser rapid manufacturing of special pattern Inco 718 nickel-based alloy component. In *Lasers in Material Processing and Manufacturing II* (Vol. 5629, pp. 59-66). SPIE.
- 513. Zhou, X. L., Wu, X. K., Guo, H. H., Wang, J. G., & Zhang, J. S. (2010). Deposition behavior of multi-particle impact in cold spraying process. *International Journal of Minerals, Metallurgy, and Materials*, 17(5), 635-640.
- 514. Zitting, A., Paajanen, A., & Penttilä, P. A. (2023). Impact of hemicelluloses and crystal size on X-ray scattering from atomistic models of cellulose microfibrils. *Cellulose*, *30*(13), 8107-8126.

BRIEF BIODATA

Email: parminder.19mez0008@iitrpr.ac.in

D.O.B: 19-04-1989 **Nationality:** Indian

Research Interests: Additive manufacturing; Thermal spraying; Materials science; Finite

element analysis; Fracture mechanics; Superalloys

About the candidate

Parminder Singh is a Ph.D. candidate in the Department of Mechanical Engineering at Indian Institute of Technology, Ropar, Punjab, INDIA. He did his Bachelor of Technology from Punjab Technical University, Jalandhar, Punjab, INDIA. He worked for Defence Research Development Organisation as a Junior Research Fellow in Snow and Avalanche Study Establishment, Chandigarh, INDIA. After that, he was working as an Assistant Engineer in Punjab State Council for Science and Technology, Chandigarh, INDIA. Subsequently, he joined as a Junior Research Fellow in a UAY (Uchchatar Avishkar Yojana) project at Indian Institute of Technology, Ropar, Punjab, INDIA, where he worked under the supervision of Prof. Harpreet Singh for 3 years and 1 month.